Facultat de Física

Departamento de Física Teórica

Ph.D. THESIS:

MIXING OF PSEUDOSCALAR-BARYON AND VECTOR-BARYON IN MESON-BARYON INTERACTION AND THE GENERATION OF RESONANCES

A Thesis submitted by
Eugenio Javier Garzón Alama
for the degree of Doctor of Philosophy in the University of
Valencia

Supervised by:
Eulogio Oset Baguena

"With the lightest meson, with the heaviest baryon,
No Hadron shall escape my sight.
Let those who worship the Quark Model
Beware my power, Chiral Perturbation Theory!"

II

D. Eulogio Oset Báguena, Catedrático de Física Teórica de la Universidad de Valencia,

CERTIFICA: Que la presente Memoria *Mixing of pseudoscalar-baryon and vector-baryon in meson-baryon interaction and the generation of resonances* ha sido realizada bajo mi dirección en el Departamento de Física Teórica de la Universidad de Valencia por Eugenio Javier Garzón Alama como Tesis para obtener el grado de Doctor en Física

Y para que así conste presenta la referida Memoria, firmando el presente certificado.

Fdo: Eulogio Oset Báguena

IV

Contents

Agradecimientos

La vida está compuesta de etapas, etapas que están llenas de momentos, de personas y de metas. Hoy una de esas etapas termina, pero eso no es algo por lo que entristecerse ya que significa que se ha llegado al final con los objetivos cumplidos y que una nueva etapa comienza. Sin embargo, el llegar al final no es el verdadero objetivo, si no que es el recorrer ese camino lo que nos da la auténtica recompensa y lo que nos hace aprender del esfuerzo y del tiempo invertido. Por ello el ver nuestra meta en el horizonte es lo que nos hace avanzar. Lo importante durante todo el camino es estar rodeado de gente que te apoye y que ande contigo. Y por ello quiero agradecer a todas esas personas que han contribuido mucho o poco a que este día haya llegado.

Primero, el que más ha contribuido a que esto salga adelante ha sido Eulogio. El me ha orientado, ayudado y enseñado todo lo que ha hecho posible esta tesis. Gracias a él he podido formarme no solo como científico si no también como persona y de él he aprendido mucho que seguro que me será muy útil en el futuro. Por él he podido viajar, descubrir nuevas culturas y conocer gente interesante. Además me ha enseñado que el esfuerzo y la constancia tiene su recompensa, que hay que defender con firmeza tus convicciones cuando se está seguro de ello, siempre desde el respeto y la humildad. Por todo ello: Gracias Eulogio.

También a mi familia, a mi madre, a mi padre, a mi hermana y a mi abuela, que siempre están ahí y desean lo mejor para mí. Aunque por más que se lo explique, nunca entienden que es eso de "potrones" y quarks que hago, siempre se han interesado y preocupado de como va el trabajo, cuando lees la tesis, te han contestado ya de ese artículo, a donde te manda Eulogio este año, cuando lees la tesis (si, lo he puesto dos veces), vamos lo que es ser una familia que te quiere y se preocupa. Además porque me han dado la oportunidad y los medios de haber podido estudiar, tener una carrera y llegar hasta donde estoy hoy.

A la gente del grupo, en especial a Juan y a Manolo, que han sido como un par de padres extras durante estos años. A Juan por estar siempre tan pendiente y preocupado por mi, preguntándome a todas horas que cómo estaba. A Manolo por todo lo que me ha enseñado de matemáticas o de programación, y por hacer que a partir de las diez, mirara en reloj cada dos por tres esperando escuchar ese "cafeto", que indicaba que íbamos a almorzar y así poder descansar despegando los ojos de la pantalla.

Agradecer también a la gente que de alguna forma u otra ha pasado por el grupo, dejando su huella no solo profesionalmente si no también de forma personal como Kanchan y Alberto, que han sido colegas pero también les considero amigos. Fueron las primeras personas que conocí del grupo y me hablaron de lo bien que te trataban, como en una familia. Y tenían razón. También a Raquel, que se convirtió en una hermana mayor y en una amiga, y que desde el primer viaje a Japón estuvo ahí y me ayudó en lo que necesitaba. Manolo Pavón fue durante un tiempo el compañero de despacho más divertido que se puede pedir, elevando el nivel de "frikismo" en el despacho hasta límites insospechados.

Durante este tiempo también pasaron por el grupo dos chicas que por su sencillez, alegría y bondad, dieron un gran cambio al grupo. Junko con su humildad, era apreciada por todo el grupo y se convirtió en una improvisada profesora de mi rudimentario japonés. Melahat llegó más tarde y su alegría nos inundó a todos. Ha sido una excelente compañera y amiga. Muchos otros como Jorge Martín Camalich, Dani Gamermann, Nacho Ruiz, Ju-Jun Xie, Chu-Wen Xiao, En Wang, Luis Alvarez Ruso, Carlos Hidalgo, Tim Ledwig, también han formado parte de este proyecto. Agradecer también el apoyo de colegas que me ha ayudado de muchas formas diversas, como Angels Ramos, Michael Döring, Laura Tolos, Atsushi Hosaka, Daisuke Jido, Makoto Oka, Tetsuo Hyodo, Bao Xi Sun y Lian Rong Dai.

Poco a poco la gente va llegando a este día y se va marchando, pero otros vienen, y de repente te encuentras con un grupo de gente fantástica donde menos te lo esperas. Francesca se convirtió en una estupenda compañera de despacho con la que compartir risas y miradas de complicidad. También Uchino ha sido un excelente compañero de cervezas, mientras uno al otro nos enseñábamos japonés y español y comentábamos las divertidas diferencias culturales entre Japón y España. Después llegaron Astrid y Jorgivan con los que conecté enseguida y pasamos muy buenos ratos.

Agradecer también a todos mis compañeros de Aikido, que son demasiados para ponerlos a todos aquí, por haber sido el lugar donde poder evadirme de mis problemas y ser gente maravillosa con la que poder practicar y tomarse una cervecita para reponerse después de haberse pasado la tarde haciendo "kokyus".

Mucha gente ha pasado por mi vida durante estos años, pero nadie ha sido tan importante como Laura. A ella quiero agradecerle todo lo que ha hecho por mí durante este tiempo, lo que me ha apoyado y escuchado, y por haber sido mi mejor amiga. También a su familia, a sus padres Lola y Toni, y a sus hermanos, Silvia y Toni, por haber sido durante estos años mi segunda familia y sentirme como uno más. Gracias.

Esta tesis no es solo mía. Cada uno ha puesto una pequeña parte en esta tesis, por ello quiero agradeceros todo el apoyo y el cariño que me habéis dado. Sin vosotros no habría sido posible.

GRACIAS.

<div align="right">

Eugenio Javier Garzón Alama
7 de Mayo de 2014

</div>

Chapter 1

Introduction

In the mid 50s a copious number of particles were found, with no other means of classification than the conservation of some laboriously deduced quantum numbers, so strange at the time that even inspired the name of strangeness in one of the cases. However, in 1961 Gell-Mann proposed a theory [1, 2] that classified baryons and mesons in octets and decuplets of the SU(3) group depending on their isospin and hypercharge. This led to the prediction of the quarks due to the SU(3) flavour symmetry that underlies this theory.

The quark model was very successful, it gave a natural explanation of why there was one octet of baryons with $J^P = 1/2^+$ and a decuplet of $J^P = 3/2^+$. It predicted new particles like the Ω^- with S=-3, discovered in 1965 [3], and allowed to make estimations of masses and magnetic moments of hadrons. Furthermore the quantum number of colour was predicted due to the need of antisymmetry of the Δ^{++} with $J^P = 3/2^+$ wave-function. But some hadrons were found (like $N^*(1440)(J^P = 1/2^+)$ [4], $N^*(1535)(J^P = 1/2^-)$ or $\Lambda(1405)(J^P = 1/2^-)$) that did not fit in octets and decuplets and were assumed to be excited states of other hadrons. The most natural explanation for the excited states was to assume that the constituent quarks were excited to different discrete levels of a strongly attractive potential acting on the quarks. This has been the main line of approach to these hadronic excited states [5, 6, 7]. Yet, it is curious to observe, by looking at the masses of the first baryon excited states, that the quark excitation energies are of the order of 500 MeV. Then one can wonder why are not one or several pions created, before a quark is excited, since it is energetically more favorable. There could be an answer, since in some cases the dynamics would not lead to sufficient attraction to bind these systems. But maybe in some cases the conditions are such that bound states or resonances might emerge from the addition of one or more mesons to the ground state hadrons. To answer this

(a) The $S = 1/2$ baryon octet

(b) The $S = 3/2$ baryon decuplet
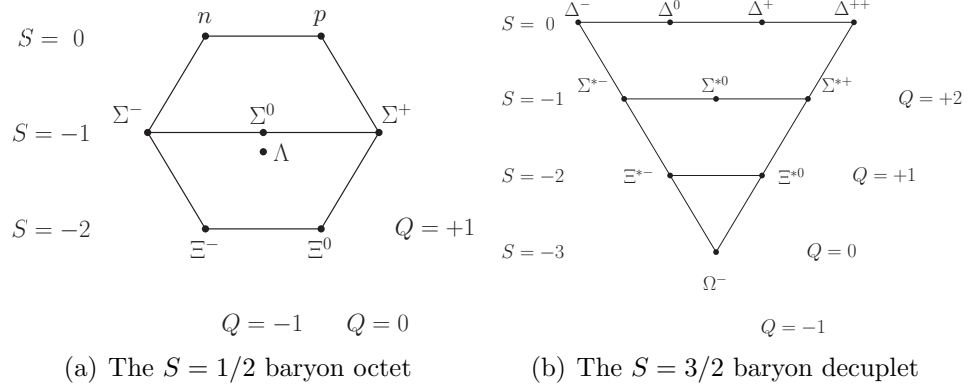
Figure 1.1: The Eightfold Way for baryons.

question one needs to address the dynamics of the interaction of the hadrons in a reliable way, and big steps have been given in this direction.

1.1   Effective Lagrangians and Chiral Perturbation Theory

The idea of Weinberg [8] to describe the low energy Hadron Physic using effective Lagrangians which contain the basic symmetries of QCD has been very fruitful. Including the chiral symmetry contained in the QCD Lagrangian in the effective Lagrangians has led to chiral Lagrangians, which have been systematically studied in Ref. [9]. With these Lagrangians many problems in hadron physics has been studied using perturbative techniques leading to chiral Perturbation Theory (χPT) which has had an undeniable success. However χPT has its limitations, like any theory. In the case of the $\pi\pi$ interaction the perturbative series expansion has its limits in the first singularity, which is the pole corresponding to the σ resonance about 500 MeV of energy. The next step was to combine the information of chiral Lagrangians with the unitarity in coupled channels [10, 11], obtaining a nonperturbative formalism which allows to extend the information contained in the chiral Lagrangians to higher energies, know as Chiral unitary theory, o unitarized chiral perturbation theory, UχPT.

One of the more amazing results of the UχPT theory, is the dynamical generation of resonances, which means that starting with the interaction of meson-meson in coupled channels and using unitary techniques, one obtain the meson-meson collision amplitudes where eventually poles appear that

correspond to bound states or resonances. In this way one can obtain several scalar mesons as σ, $f_0(980)$, $a_0(980)$, etc. in the mesonic channel, and also baryonic resonances with $J^P = 1/2^-$, as $N^*(1535)$, or two $\Lambda(1405)$ [12]. Those states are understood as composite states of meson-meson or meson-baryon, in the same way that the deuteron is a bound state of proton-neutron and not a bag with six uncorrelated quarks. These results break with the simple scheme that mesons are composed of $\bar{q}q$ and baryons by qqq. This theory gives good results for collision amplitudes between mesons and meson-baryon, and also lets one calculate properties of the resonances, like partial decay widths, magnetic moments, helicity amplitudes, and also allows one to face production processes of theses particles successfully.

Recently the interaction of vectors mesons among themselves and with baryons has also been studied. The interaction of vectors is described by another theory, the hidden gauge of Bando et ál. [13], which includes chiral symmetry and leads to the same chiral Lagrangian for the meson-meson interaction, including vector mesons in addition.

1.2 Dynamically generated resonances

The use of chiral Lagrangians in combination with unitary techniques in coupled channels of mesons and baryons has been a very convenient scheme to study the nature of many hadron resonances. The analysis of meson baryon scattering amplitudes shows poles in the second Riemann sheet which are identified with existing baryon resonances. In this way the interaction of the octet of pseudoscalar mesons with the octet of stable baryons has lead to $J^P = 1/2^-$ resonances which fit quite well the spectrum of the known low lying resonances with these quantum numbers, as we can see in Refs. [14, 15, 16, 17, 18, 19, 20, 21, 22]. Similarly, the interaction of the octet of pseudoscalar mesons with the decuplet of baryons also leads to many resonances that can be identified with existing ones of $J^P = 3/2^-$ [23, 24]. Sometimes a new resonance is predicted, as in the case of the $\Lambda(1405)$, where all the chiral approaches find two poles close by, rather than one, a fact that finds experimental support in the analyses of Refs. [25, 26][1]. The nature of the resonances is admittedly more complex than just a molecule of pseudoscalar and baryon, but the success of this picture in reproducing many experimental data on decay and production of the resonances provides support to claim very large components of this character for the resonance wave function.

---

[1]In the next edition of the Particle Data Group, the two $\Lambda(1405)$ states will be officially included.

Much work has been done using pseudoscalar mesons as building blocks, but the consideration of vectors instead of pseudoscalars is only beginning to be exploited. In the baryon sector the interaction of the $\rho\Delta$ has been recently addressed in Ref. [27], where three degenerate N^* states around 1800 MeV and three degenerate Δ states around 1900 MeV, with $J^P = 1/2^-, 3/2^-, 5/2^-$, are found. This work has been recently extended to the SU(3) space of vectors and baryons of the decuplet in Ref. [28] and of the octet in Ref. [29]. The underlying theory for this study is the hidden gauge formalism of Refs. [30, 13, 31], which deals with the interaction of vector mesons and pseudoscalars in a way respecting chiral dynamics, providing the interaction of pseudoscalars among themselves, with vector mesons, and vector mesons among themselves. It also offers a perspective on the chiral Lagrangians as limiting cases at low energies of vector exchange diagrams occurring in the theory. In a more recent work, looking for poles in the πN scattering amplitudes, the ρN channel is also included in Ref. [32] and a resonance around 1700 MeV is dynamically generated, having the strongest coupling to this later channel.

In the meson sector, the interaction of $\rho\rho$ within this formalism has been addressed in Ref. [33], where it has been shown to lead to the dynamical generation of the $f_2(1270)$ and $f_0(1370)$ meson resonances, with a branching ratio for the sensitive $\gamma\gamma$ decay channel in good agreement with experiment as in done in Ref. [34]. This work has been extended to the SU(3) space in Ref. [35] where, in addition to these two resonances, the $f_2'(1525)$, $f_0(1710)$ and other resonances are generated, including the prediction of an h_1 resonance around 1800 MeV for which experimental evidence has been found recently in Ref. [36] from an analysis of the BES experiment on $J/\Psi \to \gamma K^{*0} \bar{K}^{*0}$ [37].

Chapter 2

Formalism

Quantum chromodynamics (QCD) is the theory that underlies the strong interaction describing the interaction between quarks and gluons. This theory is well understood and studied at high energies and has been tested many times experimentally. However at low energies QCD shows a feature called "confinement" that makes that in nature only "colour singlets", also called hadrons, exist such as protons, neutrons, pions, etc. Unfortunately, perturbative methods of QCD cannot be applied at this regime, but big steps in nonperturvative approaches as lattice have been given in the last decade.

Nevertheless effective theories are one of the most powerful tools in the study of hadron physics at low energies. The SU(3) symmetry contained in the QCD Lagrangian, can be extended to the low lying pseudoscalar mesonic states (π, k, η). This extension is understood under the chiral symmetry of the light quarks (u, d, s) which is spontaneously broken leading to the Goldstone bosons and the development of a theory called Chiral Perturbation Theory (χPT) (See Refs. [38, 39] for further details).

The most general, chirally invariant, effective Lagrangian density with the minimal number of derivatives reads

$$\mathcal{L}_{eff} = \frac{f^2}{4} Tr \left(\partial_\mu U \partial^\mu U^\dagger \right) \tag{2.1}$$

where $f \approx 93$ MeV is a free parameter which later on will be related to the pion decay and

$$U(x) = e^{i\sqrt{2}\phi(x)/f} \tag{2.2}$$

First of all, the Lagrangian is invariant under the global $SU(3)_L \times SU(3)_R$

transformations

$$U \quad \rightarrow \quad RUL^{\dagger} \tag{2.3}$$

$$\partial_{\mu}U \quad \rightarrow \quad R\partial_{\mu}UL^{\dagger} \tag{2.4}$$

$$U^{\dagger} \quad \rightarrow \quad LU^{\dagger}R^{\dagger} \tag{2.5}$$

$$\partial_{\mu}U^{\dagger} \quad \rightarrow \quad L\partial_{\mu}U^{\dagger}R^{\dagger} \tag{2.6}$$

So,

$$\mathcal{L}_{eff} \quad \rightarrow \quad \frac{f^2}{4}Tr\left(R\partial_{\mu}UL^{\dagger}L\partial^{\mu}U^{\dagger}R^{\dagger}\right) \tag{2.7}$$

$$= \frac{f^2}{4}Tr\left(R^{\dagger}R\partial_{\mu}U\partial^{\mu}U^{\dagger}\right) = \mathcal{L}_{eff} \tag{2.8}$$

In the $U(x)$ contained in the Lagrangian of Eq. (2.1), $\phi(x)$ is related with the mesons fields and the Gell-Mann matrices as

$$\phi(x) = \sum_{a=1}^{8} \frac{1}{\sqrt{2}}\lambda_a\phi_a(x) = \begin{pmatrix} \phi_3 + \frac{1}{\sqrt{3}}\phi_8 & \phi_1 - i\phi_2 & \phi_4 - i\phi_5 \\ \phi_1 + i\phi_2 & -\phi_3 + \frac{1}{\sqrt{3}}\phi_8 & \phi_6 - i\phi_7 \\ \phi_4 + i\phi_5 & \phi_6 + i\phi_7 & -\frac{2}{\sqrt{3}}\phi_8 \end{pmatrix} \tag{2.9}$$

The coupling of the pseudoscalar meson to the baryon octet of $SU(3)$ is given by

$$\mathcal{L}_{BBP} = \frac{F}{2}\langle\bar{B}\gamma_{\mu}\gamma_5[u^{\mu}, B]\rangle + \frac{D}{2}\langle\bar{B}\gamma_{\mu}\gamma_5\{u^{\mu}, B\}\rangle \tag{2.10}$$

where $F = 0.51$ and $D = 0.75$, and the B is a matrix contains the fields of the baryon octet

$$B = \begin{pmatrix} \frac{1}{\sqrt{2}}\Sigma^0 + \frac{1}{\sqrt{6}}\Lambda & \Sigma^+ & p \\ \Sigma^- & -\frac{1}{\sqrt{2}}\Sigma^0 + \frac{1}{\sqrt{6}}\Lambda & n \\ \Xi^- & \Xi^0 & -\frac{2}{\sqrt{6}}\Lambda \end{pmatrix} \tag{2.11}$$

At lowest order in the pseudoscalar meson field

$$u^{\mu} = -\frac{\sqrt{2}}{f}\partial^{\mu}P \tag{2.12}$$

where for the case of the octet of pseudoscalar meson, the P matrix is

$$P = \begin{pmatrix} \frac{\pi^0}{\sqrt{2}} + \frac{\eta_8}{\sqrt{3}} & \pi^+ & K^+ \\ \pi^- & -\frac{\pi^0}{\sqrt{2}} + \frac{\eta_8}{\sqrt{3}} & K^0 \\ K^- & \bar{K}^0 & -\frac{2}{\sqrt{3}}\eta_8 \end{pmatrix} \tag{2.13}$$

which allows to rewrite the Lagrangian of Eq. (2.10) as

$$\mathcal{L}_{BBP} = -\frac{\sqrt{2}}{f}\frac{D+F}{2}\langle \bar{B}\gamma_\mu\gamma_5\partial^\mu PB\rangle - \frac{\sqrt{2}}{f}\frac{D-F}{2}\langle \bar{B}\gamma_\mu\gamma_5 B\partial^\mu P\rangle \quad (2.14)$$

For a particular case of a pseudoscalar meson P coupling to two baryons B_1 and B_2, the previous Lagrangian can be written in terms of an effective vertex as

$$-it_{B_1B_2P} = \left\{\alpha\frac{(D+F)}{2f} + \beta\frac{(D-F)}{2f}\right\}\vec{\sigma}\vec{k} \quad (2.15)$$

where $\vec{k}$ is the incoming momentum of the meson in the BBP vertex. The coefficients α and β can be found in Appendix D.

2.1 The hidden gauge formalism

The hidden gauge formalism [30, 13, 31, 40] includes the interaction of vector mesons, photons and pseudoscalar mesons. Under this formalism, the Lagrangian is given by

$$\mathcal{L} = \mathcal{L}^{(2)} + \mathcal{L}_{III} \quad (2.16)$$

$$\mathcal{L}^{(2)} = \frac{1}{4}f^2\langle D_\mu U D^\mu U^\dagger + \chi U^\dagger + \chi^\dagger U\rangle \quad (2.17)$$

$$\mathcal{L}_{III} = -\frac{1}{4}\langle V_{\mu\nu}V^{\mu\nu}\rangle + \frac{1}{2}M_V^2\langle\left[V_\mu - \frac{i}{g}\Gamma_\mu\right]^2\rangle \quad (2.18)$$

with the covariant derivative defined as

$$D_\mu U = \partial_\mu U - ieQA_\mu U + ieUQA_\mu, \quad (2.19)$$

where V_μ, A_μ are the vector and photon fields and Q is the charge matrix, $Q = diag(2,-1,-1)/3$. χ stands for the mass matrix. In Eq. (2.18), V_μ is the SU(3) matrix for the nonet of vector mesons

$$V_\mu = \begin{pmatrix} \frac{\rho^0}{\sqrt{2}} + \frac{\omega}{\sqrt{2}} & \rho^+ & K^{*+} \\ \rho^- & -\frac{\rho^0}{\sqrt{2}} + \frac{\omega}{\sqrt{2}} & K^{*0} \\ K^{*-} & \bar{K}^{*0} & \phi \end{pmatrix}_\mu \quad (2.20)$$

and g is the coupling of the theory $g = \frac{M_V}{2f}$ with M_V the vector mass. The interaction of vectors with the photons and pseudoscalars is accounted for by means of Γ_μ

$$\Gamma_\mu = \frac{1}{2}\left[u^\dagger\left(\partial_\mu - ieQA_\mu\right)u + u\left(\partial_\mu - ieQA_\mu\right)u^\dagger\right] \quad (2.21)$$

where the field u is defined as

$$u^2 = U = e^{i\sqrt{2}\phi/f} \tag{2.22}$$

The magnitude $V_{\mu\nu}$ for the vector mesons is given by

$$V_{\mu\nu} = \partial_\mu V_\nu - \partial_\nu V_\mu - ig\,[V_\mu, V_\nu] \tag{2.23}$$

and the second term in the Lagrangian of Eq. (2.18) is given by

$$
\begin{aligned}
\left[V_\mu - \frac{i}{g}\Gamma_\mu\right]^2 &= \left(V_\mu - \frac{e}{g}QA_\mu - \frac{1}{g}\frac{1}{2f^2}\phi e QA_\mu\phi + \frac{1}{g}\frac{1}{4f^2}\phi^2 e QA_\mu \right.\\
&\quad \left. + \frac{1}{g}\frac{1}{4f^2}e QA_\mu\phi^2 - \frac{i}{g}\frac{1}{4f^2}[\phi, \partial_\mu\phi]\right)^2
\end{aligned}
\tag{2.24}
$$

One can obtain from the previous Lagrangian the following interaction terms involving pseudoscalar mesons, vector mesons and photons.

$$\mathcal{L}_{V\gamma} = -M_V^2\frac{e}{g}A_\mu\langle V^\mu Q\rangle \tag{2.25}$$

$$\mathcal{L}_{V\gamma PP} = e\frac{M_V^2}{4gf^2}A_\mu\langle V^\mu(Q\phi^2 + \phi^2 Q - 2\phi Q\phi)\rangle \tag{2.26}$$

$$\mathcal{L}_{VPP} = -i\frac{M_V^2}{4gf^2}\langle V^\mu[\phi, \partial_\mu\phi]\rangle \tag{2.27}$$

$$\mathcal{L}_{\gamma PP} = ieA_\mu\langle Q[\phi, \partial_\mu\phi]\rangle \tag{2.28}$$

$$\widetilde{\mathcal{L}}_{PPPP} = -\frac{1}{8f^2}\langle[\phi, \partial_\mu\phi]^2\rangle. \tag{2.29}$$

The diagrams of these vertices are represented individually in Fig. 2.1.

2.2   Formalism for VV interaction

From the Lagrangian of Eq. (2.18) one can get the interaction of vector mesons among themselves as

$$\mathcal{L}_V = -\frac{1}{4}\langle V_{\mu\nu}V^{\mu\nu}\rangle \tag{2.30}$$

where the symbol $\langle\rangle$ stands for the trace in the SU(3) space and the term $V_{\mu\nu}$ is given in Eq. (2.23)

$$V_{\mu\nu} = \partial_\mu V_\nu - \partial_\nu V_\mu - ig\,[V_\mu, V_\nu] \tag{2.31}$$
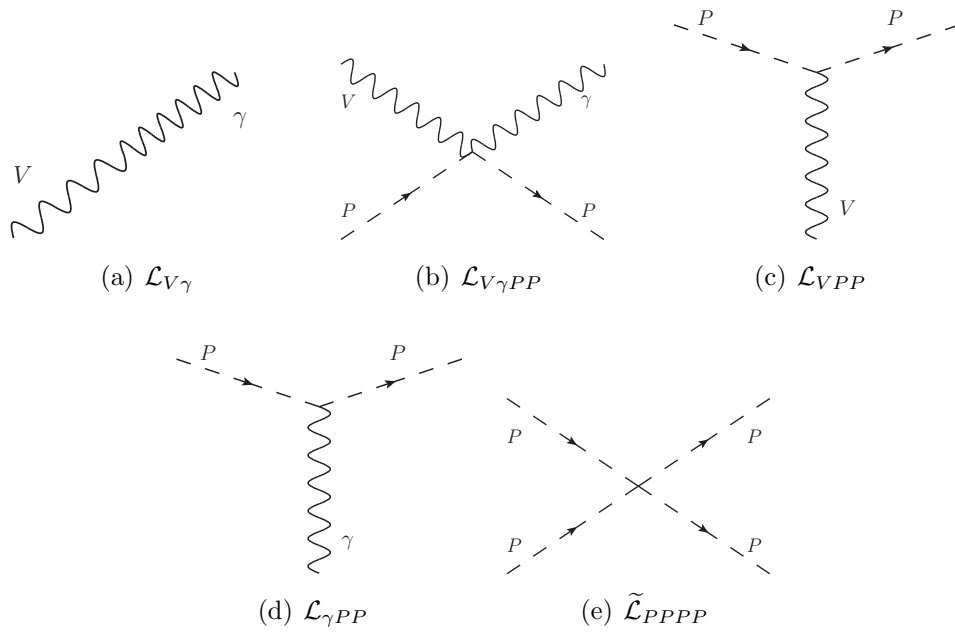
Figure 2.1: Interaction diagrams involving pseudoscalar mesons, vector mesons and photons from the Lagrangian of Eq. (2.16).

The Lagrangian gives two contact terms of four and three vector mesons,

$$\mathcal{L}^{(4V)} = \frac{g^2}{2}\langle V_\mu V_\nu V^\mu V^\nu - V_\nu V_\mu V^\mu V^\nu \rangle \tag{2.32}$$

$$\mathcal{L}^{(3V)} = ig\langle (V^\mu \partial_\nu V_\mu - \partial_\nu V_\mu V^\mu)V^\nu \rangle \tag{2.33}$$

We are interested on the three vector vertex of Fig. 2.2 since it will be used in the vector meson - baryon interaction. The interaction of vector mesons
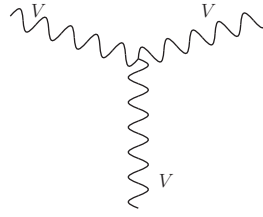
Figure 2.2: Three vector vertex of the Lagrangian of Eq. (2.39).

with the baryon octet is introduced in the same way than the pseudoscalar mesons through the following Lagrangian

$$\mathcal{L}_{BBV} = g\left(\langle \bar{B}\gamma_\mu[V^\mu, B]\rangle + \langle \bar{B}\gamma_\mu B\rangle\langle V^\mu\rangle \right) \tag{2.34}$$

where B is the SU(3) matrix of the baryon octet given in Eq. (2.11). The diagram of this vertex is shown in Fig. 2.3. Furthermore, the interaction
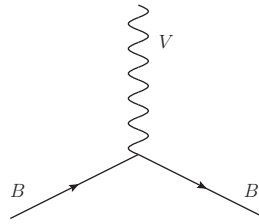
Figure 2.3: Baryon of the octet - vector meson vertex of the Lagrangian of Eq. (2.34).

of vector meson with baryon of the decuplet has been also studied. The Lagrangian for baryon of the decuplet - vector meson interaction is given in Ref. [41] by

$$\mathcal{L} = -i\bar{T}^\mu D_\nu \gamma^\nu T_\mu \tag{2.35}$$

where T^{μ}_{abc} is the spin decuplet field, with a, b, c the $SU(3)$ indices, given by

$$
\begin{array}{llllllll}
T^{111} & = & \Delta^{++}, & T^{112} & = & \frac{1}{\sqrt{3}}\Delta^{+}, & T^{122} & = & \frac{1}{\sqrt{3}}\Delta^{0}, T^{222} = \Delta^{-}, \\
T^{113} & = & \frac{1}{\sqrt{3}}\Sigma^{*+}, & T^{123} & = & \frac{1}{\sqrt{6}}\Sigma^{*0}, & T^{223} & = & \frac{1}{\sqrt{3}}\Sigma^{*-}, \\
T^{133} & = & 6\frac{1}{\sqrt{3}}\Xi^{*0}, & T^{233} & = & \frac{1}{\sqrt{3}}\Xi^{*-}, & T^{333} & = & \frac{1}{\sqrt{3}}\Omega^{-}
\end{array}
\tag{2.36}
$$

The covariant derivative D^{ν} is given by

$$
D^{\nu}T^{\mu}_{abc} = \partial^{\nu}T^{\mu}_{abc} + (\Gamma^{\nu})^{d}_{a}T^{\mu}_{dbc} + (\Gamma^{\nu})^{d}_{b}T^{\mu}_{adc} + (\Gamma^{\nu})^{d}_{c}T^{\mu}_{abd}
\tag{2.37}
$$

where Γ^{ν} is the vector current

$$
\Gamma^{\nu} = -\frac{1}{4f^{2}}\left(V^{\mu}\partial^{\nu}V_{\mu} - \partial^{\nu}V_{\mu}V^{\mu}\right)
\tag{2.38}
$$

2.3 Lagrangians of the meson-baryon interaction

One of the most relevant studies done in this work is the vector meson - baryon interaction where a vector meson is exchanged providing the corresponding potential. For the interaction of the vectors among themselves we have the three vector Lagrangian

$$
\mathcal{L}^{(3V)}_{III} = ig\langle(\partial_{\mu}V_{\nu} - \partial_{\nu}V_{\mu})V^{\mu}V^{\nu}\rangle \ ,
\tag{2.39}
$$

where V_{μ} is the $SU(3)$ matrix for the nonet of the ρ given in Eq. (2.20) and $g = \frac{M_{V}}{2f}$, with f=93 MeV. The Lagrangian of Eq. (2.39) can be rewritten in a more convenient way as follows

$$
\begin{aligned}
\mathcal{L}^{(3V)}_{III} & = ig\langle V^{\nu}\partial_{\mu}V_{\nu}V^{\mu} - \partial_{\nu}V_{\mu}V^{\mu}V^{\nu}\rangle \\
& = ig\langle V^{\mu}\partial_{\nu}V_{\mu}V^{\nu} - \partial_{\nu}V_{\mu}V^{\mu}V^{\nu}\rangle \\
& = ig\langle(V^{\mu}\partial_{\nu}V_{\mu} - \partial_{\nu}V_{\mu}V^{\mu})V^{\nu}\rangle
\end{aligned}
\tag{2.40}
$$

In the same way, the coupling of the vectors to pseudoscalar mesons is given by the Lagrangian of Eq. (2.27)

$$
\mathcal{L}_{VPP} = -ig\langle[P,\partial_{\nu}P]V^{\nu}\rangle \ ,
\tag{2.41}
$$

where here P is the $SU(3)$ matrix of the pseudoscalar mesons of Eq. (2.13). The Lagrangian for the coupling of the vector to the baryon is given in Eq. (2.42) by

$$
\mathcal{L}_{BBV} = g\left(\langle\bar{B}\gamma_{\mu}[V^{\mu},B]\rangle + \langle\bar{B}\gamma_{\mu}B\rangle\langle V^{\mu}\rangle\right) \ ,
\tag{2.42}
$$
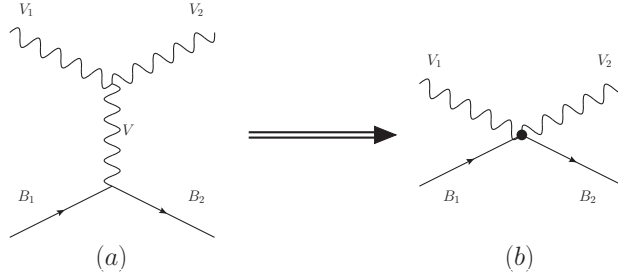
Figure 2.4: Vector meson-baryon interaction: (a) with vector meson exchange (b) contact term.

where B is now the $SU(3)$ matrix of the baryon octet of Eq. (2.11). The interaction has been studied for the baryon octet in Ref. [29] and for baryon decuplet in Ref. [28]. As shown in Ref. [29], the leading term of the $VB \to VB$ interaction involves the three vector vertex of Eq. (2.39), with one vector meson exchanged, and the coupling of this exchanged vector to the baryon, given by Eq. (2.42). In both works, the vector meson exchange diagram of Fig. 2.4(a) becomes the contact term of Fig. 2.4(b) neglecting the three momentum versus the mass of the vector meson exchanged. The potential provided by this term, keeping the dominant γ^0 term in Eq. (2.42), is given by

$$V_{ij} = -C_{ij} \frac{1}{4f^2} \left(k^0 + k'^0 \right) \ \vec{\epsilon}\,\vec{\epsilon}\,' \tag{2.43}$$

where k^0, k'^0 are the energies of the incoming and outgoing vector mesons. The result of Eq. (2.43), with the $\vec{\epsilon}\,\vec{\epsilon}\,'$ factor for the polarization of the vector mesons, stems from considering the three momentum of the external vectors small with respect to the mass of the vector mesons. The explicit factorization of the spin term in the potential produces a degeneracy in the spin of the states found when this potential is used. This is studied in detail in Appendix A. The C_{ij} coefficients for the vector meson - octet baryon for all the states of isospin and strangeness can be found in Appendix A of Ref. [29], where the subindices i and j correspond to the different channels. The V matrix is the potential of the terms shown in Fig. 2.5, where the successive diagrams can be expressed as

$$T = V + V\,G\,V + V\,G\,V\,G\,V + \ldots \tag{2.44}$$

that can be written as

$$T = V + V\,G\,T \tag{2.45}$$

This expression can be resumed as the standard form of the Bethe-Salpeter
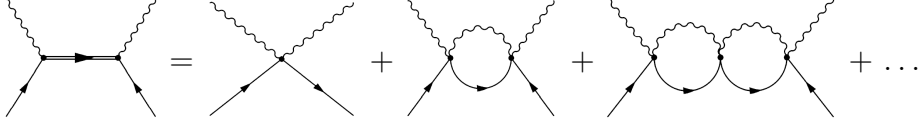
Figure 2.5: First diagrams involved in Bethe-Salpeter equation.

equation given by

$$T = [1 - V\,G]^{-1}\,V \tag{2.46}$$

where G is the loop function of a vector meson and a baryon which is calculated in dimensional regularization, as shown in Refs. [18, 42], and given by

$$
\begin{aligned}
G \;=\;& i2M \int \frac{d^4q}{(2\pi)^4} \frac{1}{(P-q)^2 - M^2 + i\epsilon} \frac{1}{q^2 - m^2 + i\epsilon} \\
=\;& \frac{2M}{16\pi^2} \Bigg\{ a(\mu) + \ln\frac{M^2}{\mu^2} + \frac{m^2 - M^2 + s}{2s} \ln\frac{m^2}{M^2} + \\
& + \frac{q}{\sqrt{s}} \Big[\ln(s - (M^2 - m^2) + 2q\sqrt{s}) + \ln(s + (M^2 - m^2) + 2q\sqrt{s}) \\
& - \ln(-s + (M^2 - m^2) + 2q\sqrt{s}) - \ln(-s - (M^2 - m^2) + 2q\sqrt{s}) \Big] \Bigg\}
\end{aligned}
\tag{2.47}
$$

with μ a regularization scale and $a(\mu)$ the subtraction constant, depending on the channel. There exists a relationship between both parameters μ and α given explicitly by

$$\alpha'(\mu') = \alpha(\mu) + log(\frac{\mu'^2}{\mu^2}) \tag{2.48}$$

This relationship has been studied in detail in Ref. [18], where the authors found, fitting the pole of the $\Lambda(1405)$, that with a regularization scale of $\mu =630$ MeV, the natural value for the subtraction constant α was -2. Using these values, one can choose a value for μ and then work only with the subtraction constant, since there is an unambiguous relationship. In the literature, authors use different regularization scales, emphasizing the need of been able to compare results.

Commonly, the subtraction constant $a(\mu)$ is fitted to get the position of a pole or to reproduce an amplitude. Sometimes, reproducing the data requires fitting a parameter for each channel and other times one global subtraction constant for all channels is enough

We call Eq. (2.46) the onshell factorized Bethe-Salpeter equation (BS), although other forms can be seen in the literature. Eq. (2.46) sums the terms

of the Lippmann-Schwinger equation or ladder terms, but using relativistic kinematics, and in the integral implicit in the VGT term of the BS equation, the V and the T are factorized on shell outside the integral. This is fully justified using the N/D method and dispersion relations as seen in Refs. [43, 18]. This approach neglects in principle the left hand cut in the dispersion relation, although given its weak energy dependence in the physical region of our interest, it is very accurately taken into account by means of the subtraction constant $a(\mu)$ in Eq. (2.47), which is a parameter fitted to the data.

2.4   Convolution of the loop function

In the cases where the iteration of the Bethe-Salpeter equation includes particles that have relatively large widths, as the ρ, K^* meson or Δ, a convolution of the loop function G with the mass distribution is needed. The loop function with the convolution for the case of the ρ meson would be

$$\tilde{G}(s) = \frac{1}{N} \int_{(m_\rho - 2\Gamma_\rho)^2}^{(m_\rho + 2\Gamma_\rho)^2} d\tilde{m}^2 \left(-\frac{1}{\pi}\right) \mathrm{Im} \frac{1}{\tilde{m}^2 - m_\rho^2 + i\tilde{m}\Gamma(\tilde{m})} G(s, \tilde{m}^2, M_B^2)$$
(2.49)

where $\tilde{G}$ is normalized with

$$N = \int_{(m_\rho - 2\Gamma_\rho)^2}^{(m_\rho + 2\Gamma_\rho)^2} d\tilde{m}^2 \left(-\frac{1}{\pi}\right) \mathrm{Im} \frac{1}{\tilde{m}^2 - m_\rho^2 + i\tilde{m}\Gamma(\tilde{m})}$$
(2.50)

Considering the width of the ρ, Γ_ρ=149.4 MeV, the $\Gamma(\tilde{m})$ function is energy dependent and is given in Ref. [35] as

$$\tilde{\Gamma}(\tilde{m}) = \Gamma_\rho \frac{q_{\mathrm{off}}^3}{q_{\mathrm{on}}^3} \theta(\tilde{m} - m_1 - m_2)$$
(2.51)

with $m_1 = m_2 = m_\pi$ for the ρ using

$$q_{\mathrm{off}} = \frac{\lambda^{1/2}(\tilde{m}^2, m_\pi^2, m_\pi^2)}{2\tilde{m}}, \quad q_{\mathrm{on}} = \frac{\lambda^{1/2}(m_\rho^2, m_\pi^2, m_\pi^2)}{2m_\rho}$$
(2.52)

where λ is the Källen function and Γ_ρ is the nominal width of the ρ. We can see in Fig. 2.6 the effects of the convolution of the G function, where the threshold is softened. This can remove some undesirable effects, as cusp in the T matrix, and provide width to the resonances. Nevertheless, the convolution of the G function can, in some cases, make poles disappear.
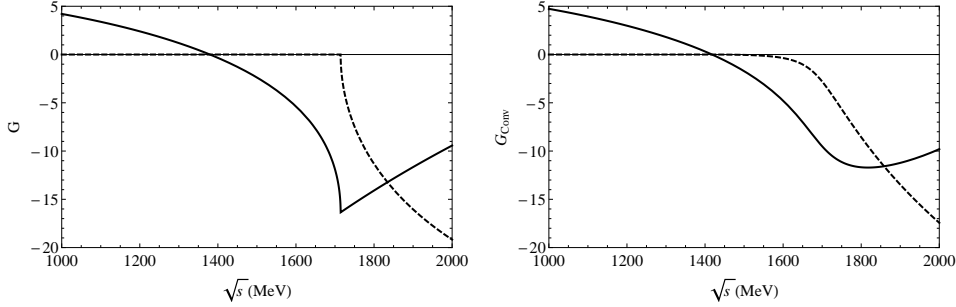
Figure 2.6: G function for ρN with $\alpha = -2.0$ and $\mu = 630$ MeV: Left) G function without convolution. Right) G function with the mass convolution of the ρ with $\Gamma_\rho = 149.4$ MeV.

For the case of the Δ we can proceed similarly. However, the integral over the mass is different since now we integrate with the baryonic propagator.

$$\tilde{G}(s) = \frac{1}{N} \int_{M_\Delta - 2\Gamma_\Delta}^{M_\Delta + 2\Gamma_\Delta} d\tilde{M} \left(-\frac{1}{\pi} \right) \text{Im} \frac{1}{\tilde{M} - M_\Delta + i\frac{\Gamma(\tilde{M})}{2}} G(s, m^2, \tilde{M}^2) \quad (2.53)$$

where $\tilde{G}$ is normalized with

$$N = \int_{M_\Delta - 2\Gamma_\Delta}^{M_\Delta + 2\Gamma_\Delta} d\tilde{M} \left(-\frac{1}{\pi} \right) \text{Im} \frac{1}{\tilde{M} - M_\Delta + i\frac{\Gamma(\tilde{M})}{2}} \quad (2.54)$$

where for the width of the Δ we take $\Gamma_\Delta = 120.0$ MeV, and the Γ function as defined in Eq. (2.51).

2.5 Poles and couplings

Once the scattering matrix is evaluated, some peaks appear that can be associated to states. Next step is to find the poles associated to those peaks, in order to obtain the couplings of these states to the different channels. The method used is to search for poles in the second Riemann sheet, changing the momentum $\vec{q}$ to $-\vec{q}$ in the analytical formula of the G function when $Re(\sqrt{s})$ is over the threshold of the corresponding channel. Using this method one can find poles, as $(M_R + i\Gamma/2)$, where the real part corresponds to the mass of the resonance and the imaginary part is half of the width of this state (the complex conjugate pole at $(M_R - i\Gamma/2)$ also appear).

One of the most powerful method when evaluating the couplings, is to calculate the residue using the residue theorem of the T matrix in a path of

radius r around the pole.

$$\int_0^{2\pi} T(z(\theta))ire^{i\theta}d\theta = 2\pi iRes(T) = 2\pi ig^2 \qquad (2.55)$$

where $z = z_0 + re^{i\theta}$, and $z_0 = M_R + i\Gamma/2$. So, the coupling g_i for a given channel i can be evaluated with

$$g_i^2 = \frac{r}{2\pi}\int_0^{2\pi} T_{ii}(z(\theta))e^{i\theta}d\theta \qquad (2.56)$$

The coupling does not depend on the value of the radius r, but usually it is taken around 1 MeV. However one needs to be careful with poles close to a threshold, as in the case of $X(3872)$, since if the integral path cross the threshold, one will obtain a wrong value for the coupling.

Somehow, the convolution of the G function eventually can make the pole disappear in channels with the ρ meson. In this case one can study the amplitude in the real axis using that near the peak the T matrix will be about

$$T_{ij} = \frac{g_ig_j}{\sqrt{s} - M_R + i\Gamma/2} \qquad (2.57)$$

where M_R is the position of the maximum and Γ the width at half-maximum. The constants g_i and g_j are the couplings of the resonances to the channels i, j. Then one can take the diagonal channel and obtain

$$|g_i|^2 = \frac{\Gamma}{2}\sqrt{|T_{ii}|^2} \qquad (2.58)$$

where the coupling g_i has an arbitrary phase. With one coupling determined, we can obtain the other ones from the T_{ij} matrices using Eq. (2.57), given by

$$g_j = g_i\frac{T_{ij}(\sqrt{(s)} = M_R)}{T_{ii}(\sqrt{(s)} = M_R)} \; . \qquad (2.59)$$

Once we obtain the couplings of the resonances for each channel, we can calculate the partial decay widths using the equation

$$\Gamma_i = \frac{1}{2\pi}\frac{M_B}{M_R}p_i|g_i|^2 \qquad (2.60)$$

In the case of decay channels involving ρ or K^*, resonances that are under their threshold can still get decay width. In these cases the momentum used in the previous equation would be imaginary. Experimentally the decay of the resonance is observed because the width of the vector is big enough to

allow the decay, although the resonance is under the threshold. In order to generate this effect in our calculation of the partial decay width, we make the convolution of the momentum with the mass of the vector mesons. In the case of the ρ one has

$$
\begin{aligned}
\tilde{p} \;=\; & \frac{1}{N} \int_{(m_\rho - 2\Gamma_\rho)^2}^{(m_\rho + 2\Gamma_\rho)^2} d\tilde{m}^2 \left(-\frac{1}{\pi} \right) \mathrm{Im} \, \frac{1}{\tilde{m}^2 - m_\rho^2 + i\tilde{m}\Gamma(\tilde{m})} \\
& \frac{\lambda^{1/2}(M_R^2, \tilde{m}^2, M_N^2)}{2M_R} \theta(M_R - \tilde{m}_\rho - M_N)
\end{aligned}
\tag{2.61}
$$

Here N is the same normalization as used in Eq. (2.50).

Chapter 3

Radiative decay of S=1/2 resonances

3.1 Introduction

In a recent paper [27], the $\rho\Delta$ interaction was studied within the local hidden gauge formalism for the interaction of vector mesons. The results of the interaction gave a natural interpretation for the $\Delta(1930)(5/2^-)$ as a $\rho\Delta$ bound state, which otherwise is extremely problematic in quark models since it involves a $3\hbar\omega$ excitation and appears with much higher mass. At the same time two states with $J^P = 1/2^-$, $3/2^-$ were obtained, degenerate with the $5/2^-$, which could be accommodated with two known Δ states in that energy range. Also, three degenerate N^* states with $1/2^-$, $3/2^-$, $5/2^-$ were obtained, which were more difficult to identify with known resonances since that sector is not so well established. The work of Ref. [27] was extended to the $SU(3)$ sector in Ref. [28] to account for the interaction of vectors of the octet with baryons of the decuplet. In this case ten resonances, all of them also degenerate in the three spin states, were obtained, many of which could be identified with existing resonances, while there were predictions for a few more. At the same time in Ref. [28] the poles and residues at the poles of the resonances were evaluated, providing the coupling of the resonances to the different vector-baryon of the decuplet components.

One of the straightforward tests of these theoretical predictions is the radiative decay of these resonances into photon and the member of the baryon octet or decuplet to which it couples. Radiative decay of resonances into γN is one of the observables traditionally calculated in hadronic models. Work in quark models on this issue is abundant [44, 45, 46, 47, 48, 49, 5, 50, 51, 52, 53, 54, 55, 56, 57, 58]. For resonances which appear as dynamically generated in chiral unitary theories there is also much work done on the radiative decay into γN [16, 59, 60, 61, 62]. Experimental work in this topic is also of current

19

interest [63, 64, 65].

In this chapter we address the novel aspect of radiative decay into a photon and a baryon of the decuplet of the Δ, since the underlying dynamics of the resonances that we study provides this as the dominant mode of radiative decay into photon baryon. This is so, because the underlying theory of the studies of Refs. [27, 28] is the local hidden gauge formalism for the interaction of vector mesons developed in Refs. [30, 13, 31, 40], which has the peculiar feature, inherent to vector meson dominance, that the photons couple to the hadrons through the conversion into a vector meson. In this case a photon in the final state comes from either a ρ^0, ω, ϕ. Thus, the radiative decay of the resonances into γB is readily obtained from the theory by taking the terms with $\rho^0 B$, ωB, ϕB in the final state and coupling the γ to any of the final ρ^0, ω, ϕ vector mesons. This procedure was used in Ref. [34] and provided good results for the radiative decay into $\gamma\gamma$ of the $f_0(1370)$ and $f_2(1270)$ mesons which were dynamically generated from the $\rho\rho$ interaction within the same framework of Ref. [33]. This latter work was also extended to the interaction of vectors with themselves within $SU(3)$, where many other states are obtained which can be also associated with known resonances [35]. The radiative decay of the latter resonances into $\gamma\gamma$ or a γ and a vector has been studied in Ref. [66], with good agreement with experiment when available. Given the success of the theory in its predictions and the good results obtained for the $\gamma\gamma$ decay of the $f_0(1370)$, $f_2(1270)$ and $f_2'(1525)$ mesons, the theoretical framework stands on good foot and the predictions made should be solid enough to constitute a test of the theory by contrasting with experimental data.

The extension of the work of Refs. [27, 28] to the interaction of vector mesons with baryons of the octet of the proton has also been successful [29] and nine resonances, degenerated in spin-parity $1/2^-$ and $3/2^-$, appear dynamically generated in the approach, many of which can be naturally associated to know resonances in the PDG [67]. We study the radiative decay of these resonances into a photon and a baryon of the octet. In this case we can also evaluate helicity amplitudes and compare them with experimental results when available.

The experimental situation in that region of energies is still poor. The PDG [67] quotes many radiative decays of N^* resonances, and of the $A_{1/2}$, $A_{3/2}$ helicity amplitudes for decay of resonances into γN, with N either proton or neutron. However, there are no data to our knowledge for radiative decay into γB, with B a baryon of the decuplet. The reason for it might be the difficulty in the measurement, or the lack of motivation, since there are also no theoretical works devoted to the subject. With the present study we hope to reverse the situation offering a clear motivation for these experiments since

they bear close connection with the nature invoked for these resonances, very different to the ordinary three quark structure of the baryons.

The numbers obtained for the radiative widths are well within measurable range, of the order of 1 MeV, and the predictions are interesting, with striking differences of one order of magnitude between decay widths for different charges of the same resonance.

In the next two Sections we present the framework for the evaluation of amplitudes of radiative decay. In Section 3.4 we show the results obtained for the different resonances generated with the baryon decuplet. Section 3.5 introduces the equations for the baryon octet, which are used to obtain results for the decay width of the resonances dynamically generated with a vector and the baryon octet. In Section 3.6 we present the results for the helicity amplitudes of some resonances used in the previous section, and in Section 3.7 we finish with some conclusions.

3.2   Framework

In Refs. [27, 28], the s-wave scattering amplitudes for vector-decuplet baryon $VB \to V'B'$ are given by

$$t_{VB \to V'B'} = t\, \vec{\epsilon} \cdot \vec{\epsilon}\,' \delta_{m_s, m_s'}, \tag{3.1}$$

where $\vec{\epsilon}$, $\vec{\epsilon}\,'$ refer to the initial and final vector polarization and the matrix is diagonal in the third component of the baryons of the decuplet. The transition is diagonal in spin of the baryon and spin of the vector, and as a consequence in the total spin. To make this property more explicit, we write the states of total spin as

$$|S, M\rangle = \sum_{m_s} \mathcal{C}\left(3/2, 1, S; m_s, M - m_s, M\right) |3/2, m_s\rangle |\vec{\epsilon}_{M - m_s}\rangle \tag{3.2}$$

and

$$\langle S, M| = \sum_{m_s'} \mathcal{C}\left(3/2, 1, S; m_s', M - m_s', M\right) \langle 3/2, m_s'| \langle \vec{\epsilon}^{\,*}_{M - m_s'}|, \tag{3.3}$$

where $\mathcal{C}\left(3/2, 1, S; m_s, M - m_s, M\right)$ are the Clebsch-Gordan coefficients and ϵ_μ the polarization vectors in spherical basis in the Coulomb Gauge and with the photon in the z direction

$$\vec{\epsilon}_+ = -\frac{1}{\sqrt{2}}\left(\vec{\epsilon}_1 + i\vec{\epsilon}_2\right), \quad \vec{\epsilon}_- = \frac{1}{\sqrt{2}}\left(\vec{\epsilon}_1 - i\vec{\epsilon}_2\right), \quad \vec{\epsilon}_0 = \vec{\epsilon}_3. \tag{3.4}$$

We can write Eq. (3.1) in terms of the projectors $|S,M\rangle\langle S,M|$ as

$$t_{VB\to V'B'} = t\,\langle\vec{\epsilon}'|\langle 3/2,m_s'|\sum_{S,M}|S,M\rangle\langle S,M|3/2,m_s\rangle|\vec{\epsilon}\,\rangle. \qquad (3.5)$$

Since the Clebsch-Gordan coefficients satisfy the normalization condition

$$\sum_S \mathcal{C}\left(3/2,1,S;m_s,M-m_s\right)\mathcal{C}\left(3/2,1,S;m_s',M'-m_s'\right) = \delta_{m_s,m_s'}\delta_{M,M'},$$
$$(3.6)$$

we have then

$$\sum_{S,M}|S,M\rangle\langle S,M| = \sum_M\sum_{m_s}|3/2,m_s\rangle\langle 3/2,m_s|\,|\vec{\epsilon}_{M-m_s}\,\rangle\langle\vec{\epsilon}^{\,*}_{M-m_s}| \,(3.7)$$

$$= \sum_{M'}\sum_{m_s}|3/2,m_s\rangle\langle 3/2,m_s|\,|\vec{\epsilon}_{M'}\,\rangle\langle\vec{\epsilon}^{\,*}_{M'}| \equiv 1.$$

We can depict the contribution of a specific resonant state of spin S to the amplitude described by means of Fig. 3.1. Then the amplitude for the tran-
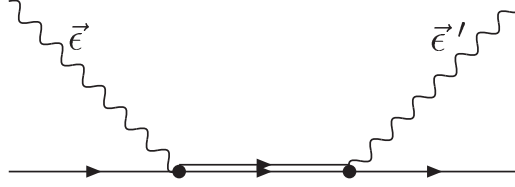
Figure 3.1: Diagram contributing to the vector-baryon interaction via the exchange of a resonance.

sition of the resonance to a final vector-baryon state is depicted by means of Fig. 3.2. As shown is Refs. [27, 28], the $VB \to V'B'$ scattering amplitudes develop poles corresponding to resonances and a resonant amplitude is written as Eq. (3.1) with t given by

$$t_{ij} = \frac{g_i g_j}{\sqrt{s} - M + i\Gamma/2} \qquad (3.8)$$

with g_i and g_j the couplings to the initial and final states. Accordingly, the amplitude for the transition from the resonance to a final state of vector-baryon is given by

$$\begin{aligned}t_{SM\to V'B'} &= g_i\langle\vec{\epsilon}'|\langle 3/2,m_s|S,M\rangle \\ &= g_i\mathcal{C}(3/2,1,S;m_s,M-m_s,M)\langle\vec{\epsilon}'|\vec{\epsilon}_{M-m_s}\rangle. \qquad (3.9)\end{aligned}$$
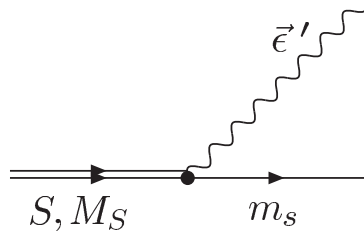
Figure 3.2: Diagram on the decay of the resonance in a decuplet baryon and a vector meson.

The generalization of Eq. (3.9) for the octet is rather obvious, the spin 3/2 becomes now 1/2 and then we have

$$t_{SM \to V'B'} = g_i \mathcal{C}(1/2, 1, S; m_s, M - m_s, M) \langle \vec{\epsilon} \, | \vec{\epsilon}_{M-m_s} \rangle. \qquad (3.10)$$

and the equations which determine the radiative decay width will be identical with this trivial change.

When calculating the decay width of the resonance into VB we will sum $|t|^2$ over the vector and baryon polarization, and average over the resonance polarization M. Thus, we have

$$\frac{1}{2S+1} \sum_{M, \, m_s, \, \vec{\epsilon}} |t_{SM \to V'B'}|^2 \qquad (3.11)$$

$$= |g_i|^2 \frac{1}{2S+1} \sum_{M, \, m_s, \, \vec{\epsilon}} \mathcal{C}(3/2, 1, S; m_s, M - m_s, M)^2 \langle \vec{\epsilon}^*_{M-m_s} | \vec{\epsilon} \, \rangle \langle \vec{\epsilon} \, | \vec{\epsilon}_{M-m_s} \rangle$$

$$= |g_i|^2 \frac{1}{2S+1} \sum_{M'} \sum_{m_s} \frac{2S+1}{3} \mathcal{C}(3/2, S, 1; m_s, -m_s - M', -M')^2 \langle \vec{\epsilon}^*_{M'} | \vec{\epsilon}_{M'} \rangle$$

$$= |g_i|^2 \frac{1}{3} \sum_{M'} \delta_{M'M'}$$

$$= |g_i|^2,$$

where in the first step we have permuted the two last spins in the Clebsch-Gordan coefficients and in the second we applied their orthogonality condition.

We observe that the normalization of the amplitudes is done in a way such that the sum and average of $|t|^2$ is simply the modulus squared of the coupling of the resonance to the final state. The width of the resonance for decay into VB is given in the Mandl and Shaw normalization (See Ref. [68])

by

$$\Gamma \;=\; \frac{M_B}{2\pi M_R}\, q\, |g_i|^2,$$ (3.12)

where q is the momentum of the vector in the resonance rest frame and M_B, M_R the masses of the baryon and the resonance respectively. We should note already that later on when the vector polarizations are substituted by the photon polarizations in the sum over M' in Eq. (3.11) we will get a factor two rather than three, because we only have two transverse polarizations, and then Eq. (3.12) must be multiplied by the factor 2/3.

3.3   Radiative decay

Next we study the radiative decay into $B\gamma$ of the resonances dynamically generated in Ref. [28] with B a baryon of the decuplet. Recalling the results of Ref. [28] we obtained there ten resonances dynamically generated, each of them degenerated in three states of spin, $1/2^-$, $3/2^-$, $5/2^-$. As we have discussed in the former section, the radiative width will not depend on the spin of the resonance, but only on the coupling, which is the same for all three spin states due to the degeneracy. This would be of course an interesting experimental test of the nature of these resonances. In order to proceed
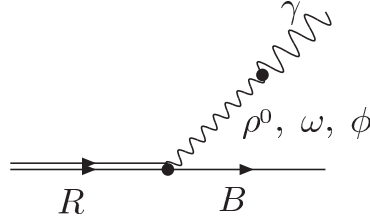
Figure 3.3: Diagram on the radiative decay of the resonance in a baryon and a photon.

further, we use the same formalism of the hidden gauge local symmetry for the vector mesons of Refs. [30, 13, 31, 40]. The peculiarity of this theory concerning photons is that they couple to hadrons by converting first into a vector meson, ρ^0, ω or ϕ. Diagrammatically this is depicted in Fig. 3.3. This idea has already been applied with success to obtain the radiative decay of the $f_2(1270)$, $f_0(1370)$, $f_2'(1525)$ and $f_0(1710)$ resonances into $\gamma\gamma$ in Refs. [34, 66]. In Ref. [34] the question of gauge invariance was addressed and it was shown that the theory fulfills it. In Ref. [69], it is also proved in the case of radiative decay of axial vector resonances.

The amplitude of Fig. 3.3 requires the γV conversion Lagrangian, which comes from Refs. [30, 13, 31] and is given by the Lagrangian of Eq. (2.25) (see Ref. [69] for practical details)

$$\mathcal{L}_{V\gamma} = -M_V^2 \frac{e}{g} A_\mu \langle V^\mu Q \rangle \tag{3.13}$$

with A_μ the photon field, V_μ the $SU(3)$ matrix of vector fields

$$V_\mu \equiv \begin{pmatrix} \frac{1}{\sqrt{2}}\rho^0 + \frac{1}{\sqrt{2}}\omega & \rho^+ & K^{*+} \\ \rho^- & -\frac{1}{\sqrt{2}}\rho^0 + \frac{1}{\sqrt{2}}\omega & K^{*0} \\ K^{*-} & \bar{K}^{*0} & \phi \end{pmatrix}_\mu, \tag{3.14}$$

and Q the charge matrix

$$Q \equiv \begin{pmatrix} 2/3 & 0 & 0 \\ 0 & -1/3 & 0 \\ 0 & 0 & -1/3 \end{pmatrix}. \tag{3.15}$$

In Eq. (3.13), M_V is the vector meson mass, for which we take an average value $M_V = 800$ MeV, e the electron charge, $e^2 = 4\pi\alpha$, and as usual,

$$g = \frac{M_V}{2f}; \quad f = 93 \text{ MeV}.$$

The sum over polarizations in the intermediate vector meson for a fixed final photon polarization, in the product of the $R \rightarrow BV$ transition amplitude of Eq. (3.9) and the $V\gamma$ Lagrangian of Eq. (3.13) converts the polarization vector of the vector meson of the $R \rightarrow BV$ amplitude into the photon polarization of the $R \rightarrow B\gamma$ amplitude, and leads to the equation

$$-it_{\gamma V} D_V = -iM_V^2 \frac{e}{g} \frac{i}{-M_V^2} F_j \tag{3.16}$$

with

$$F_j = \begin{cases} \frac{1}{\sqrt{2}} & \text{for } \rho^0, \\ \frac{1}{3\sqrt{2}} & \text{for } \omega, \\ -\frac{1}{3} & \text{for } \phi. \end{cases} \tag{3.17}$$

and D_V the vector propagator for $p^2 = 0$. Thus, finally our amplitude for the $R \rightarrow B\gamma$ transition, omitting the spin matrix element of Eq. (3.9), $\mathcal{C}(3/2, 1, S; m_s, M - m_s, M)\langle \vec{\epsilon} \,|\vec{\epsilon}_{M-m_s}\rangle$, is given by

$$t_\gamma = -\frac{e}{g} \sum_{j=\rho^0, \, \omega, \, \phi} g_j F_j. \tag{3.18}$$

As discussed in the former section, the radiative decay width will then be given by

$$\Gamma_\gamma = \frac{1}{2\pi} \frac{2}{3} \frac{M_B}{M_R} q \ |t_\gamma|^2. \tag{3.19}$$

The couplings g_j for different resonance and VB with $V = \rho^0$, ω, ϕ and B different baryon of the decuplet can be found in Ref. [28] and we use them here for the evaluation of Γ_γ. The factor $\frac{2}{3}$ in Eq. (3.19) additional to Eq. (3.12) appears because now we have only two photon polarizations and the sum over M' in Eq. (3.11) gives 2 instead of 3 for the case of vector mesons.

3.4   Radiative decays into γ and baryon decuplet

The couplings of the resonances to the different VB channels are given in Ref. [28] in the isospin basis. For the case of ωB and ϕB, there is no change to be done, but for the case of ρB, one must project over the $\rho^0 B$ component. Since this depends on the charge of the resonance R, the radiative decays will depend on this charge, as we will see. We recall that in our phase convention $|\rho^+\rangle = -|1,1\rangle$ of isospin. The information on the resonances and their couplings to different baryons of the decuplet and vector mesons ρ, ω, ϕ for different channels is listed in Table 3.1.

3.4.1 $S = 0, I = 1/2$ channel

A resonance is obtained at $z_R = 1850 + i5 MeV$ which couples to $\Delta\rho$. We have in this case

$$|\Delta\rho, \frac{1}{2}, \frac{1}{2}\rangle = \sqrt{\frac{1}{2}}|\Delta^{++}\rho^-\rangle - \sqrt{\frac{1}{3}}|\Delta^+\rho^0\rangle - \sqrt{\frac{1}{6}}|\Delta^0\rho^+\rangle \tag{3.20}$$

and

$$|\Delta\rho, \frac{1}{2}, -\frac{1}{2}\rangle = \sqrt{\frac{1}{6}}|\Delta^+\rho^-\rangle - \sqrt{\frac{1}{3}}|\Delta^0\rho^0\rangle - \sqrt{\frac{1}{2}}|\Delta^-\rho^+\rangle. \tag{3.21}$$

The coupling of the resonance to ρ^0 is obtained multiplying the coupling of Table 3.1 by the corresponding Clebsch-Gordan coefficient for $\Delta\rho^0$ of Eqs. (3.20, 3.21). Then, by means of Eqs. (3.18, 3.19), one obtains the decay width. In this case since the $\Delta\rho^0$ component is the same for $I_3 = 1/2$ and $I_3 = -1/2$, one obtains the same radiative width for the two channels, which is $\Gamma = 0.722$ MeV.

S, I	Channel			
		$z_R = 1850 + i5$		
0, 1/2	$\Delta\rho$	$4.9 + i0.1$		
		$z_R = 1972 + i49$		
0, 3/2	$\Delta\rho$	$5.0 + i0.2$		
	$\Delta\omega$	$-0.1 + i0.2$		
	$\Delta\phi$	$0.2 - i0.4$		
		$z_R = 2052 + i10$		
-1, 0	$\Sigma\rho$	$4.2 + i0.1$		
		$z_R = 1987 + i1$	$z_R = 2145 + i58$	$z_R = 2383 + i73$
-1,1	$\Sigma\rho$	$1.4 + i0.0$	$-4.3 - i0.7$	$0.4 + i1.1$
	$\Sigma\omega$	$1.4 + i0.0$	$1.3 - i0.4$	$-1.4 - i0.4$
	$\Sigma\phi$	$-2.1 - i0.0$	$-1.9 + i0.6$	$2.1 + i0.6$
		$z_R = 2214 + i4$	$z_R = 2305 + i66$	$z_R = 2522 + i38$
-2, 1/2	$\Xi\rho$	$1.8 - i0.1$	$-3.5 - i1.7$	$0.2 + i1.0$
	$\Xi\omega$	$1.7 + i0.1$	$2.0 - i0.7$	$-0.6 - i0.3$
	$\Xi\phi$	$-2.5 - i0.1$	$-3.0 + i1.0$	$0.9 + i0.4$
		$z_R = 2449 + i7$		
-3, 0	$\Omega\omega$	$1.6 - i0.2$		
	$\Omega\phi$	$-2.4 + i0.3$		

Table 3.1: The couplings g_i of the resonances obtained dynamically to the ρ, ω and ϕ with the baryon decuplet channels of Ref. [28].

3.4.2 $S = 0, I = 3/2$ channel

One resonance is obtained at $z_R = 1972 + i49$ MeV which couples to $\Delta\rho$, $\Delta\omega$ and $\Delta\phi$. The isospin states for $\Delta\rho$ can be written as

$$|\Delta\rho, \frac{3}{2}, \frac{3}{2}\rangle = \sqrt{\frac{3}{5}}|\Delta^{++}\rho^0\rangle + \sqrt{\frac{2}{5}}|\Delta^+\rho^+\rangle, \qquad (3.22)$$

$$|\Delta\rho, \frac{3}{2}, \frac{1}{2}\rangle = \sqrt{\frac{2}{5}}|\Delta^{++}\rho^-\rangle + \sqrt{\frac{1}{15}}|\Delta^+\rho^0\rangle + \sqrt{\frac{8}{15}}|\Delta^0\rho^+\rangle, \; (3.23)$$

$$|\Delta\rho, \frac{3}{2}, -\frac{1}{2}\rangle = \sqrt{\frac{8}{15}}|\Delta^+\rho^-\rangle - \sqrt{\frac{1}{15}}|\Delta^0\rho^0\rangle + \sqrt{\frac{2}{5}}|\Delta^-\rho^+\rangle, \;\; (3.24)$$

$$|\Delta\rho, \frac{3}{2}, -\frac{3}{2}\rangle = \sqrt{\frac{2}{5}}|\Delta^0\rho^-\rangle - \sqrt{\frac{3}{5}}|\Delta^-\rho^0\rangle. \qquad (3.25)$$

Since all the Clebsch-Gordan coefficients to $\Delta\rho^0$ are now different, we obtain different radiative decay width for each charge of the state. The results are $\Gamma = 1.402$ MeV for $I_3 = 3/2$, $\Gamma = 0.143$ MeV for $I_3 = 1/2$, $\Gamma = 0.203$ MeV for $I_3 = -1/2$ and $\Gamma = 1.582$ MeV for $I_3 = -3/2$. It is quite interesting to see that there is an order of magnitude difference between $I = 3/2$ and $I = 1/2$, and this is a clear prediction that could be tested experimentally.

3.4.3 $S = -1, I = 0$ channel

We get a resonance at $z_R = 2052 + i10$ MeV, which couples to $\Sigma^*\rho$. In this case

$$|\Sigma^*\rho, 0, 0\rangle = \sqrt{\frac{1}{3}}|\Sigma^{*+}\rho^-\rangle - \sqrt{\frac{1}{3}}|\Sigma^{*0}\rho^0\rangle - \sqrt{\frac{1}{3}}|\Sigma^{*-}\rho^+\rangle, \qquad (3.26)$$

and the radiative decay obtained is $\Gamma = 0.583$ MeV.

3.4.4 $S = -1, I = 1$ channel

Here we find three resonances at $z_R = 1987 + i1$ MeV, $2145 + i58$ MeV and $2383 + i73$ MeV, which couple to $\Sigma^*\rho$, $\Sigma^*\omega$ and $\Sigma^*\phi$. The relevant isospin states are

$$|\Sigma^*\rho, 1, 1\rangle = \sqrt{\frac{1}{2}}|\Sigma^{*+}\rho^0\rangle + \sqrt{\frac{1}{2}}|\Sigma^{*0}\rho^+\rangle, \qquad (3.27)$$

$$|\Sigma^*\rho, 1, 0\rangle = \sqrt{\frac{1}{2}}|\Sigma^{*+}\rho^-\rangle + \sqrt{\frac{1}{2}}|\Sigma^{*-}\rho^+\rangle, \qquad (3.28)$$

$$|\Sigma^*\rho, 1, -1\rangle = \sqrt{\frac{1}{2}}|\Sigma^{*0}\rho^-\rangle - \sqrt{\frac{1}{2}}|\Sigma^{*-}\rho^0\rangle. \qquad (3.29)$$

The results obtained in this case are summarized in Table 3.2.

I_3	(1987)	(2145)	(2383)
1	0.561	0.399	0.182
0	0.199	0.206	0.277
-1	0.020	2.029	0.537

Table 3.2: The radiative decay widths in units of MeV for the $S = -1, I = 1$ resonances with different isospin projection I_3.

3.4.5 $S = -2, I = 1/2$ channel

Here we also find three states at $z_R = 2214 + i4$ MeV, $2305 + i66$ MeV and $2522 + i38$ MeV, which couple to $\Xi^*\rho$, $\Xi^*\omega$ and $\Xi^*\phi$. The isospin states for $\Xi^*\rho$ are written as

$$|\Xi^*\rho, \frac{1}{2}, \frac{1}{2}\rangle = \sqrt{\frac{2}{3}}|\Xi^{*-}\rho^+\rangle + \sqrt{\frac{1}{3}}|\Xi^{*0}\rho^0\rangle, \tag{3.30}$$

$$|\Xi^*\rho, \frac{1}{2}, -\frac{1}{2}\rangle = -\sqrt{\frac{1}{3}}|\Xi^{*-}\rho^0\rangle + \sqrt{\frac{2}{3}}|\Xi^{*0}\rho^-\rangle. \tag{3.31}$$

The radiative decay widths in this case are shown in Table 3.3.

I_3	(2214)	(2305)	(2522)
1/2	0.815	0.320	0.044
$-1/2$	0.054	1.902	0.165

Table 3.3: The radiative decay widths in units of MeV for the $S = -2, I = 1/2$ resonances with the different isospin projection I_3.

3.4.6 $S = -3, I = 0$ channel

Here we have only one state at $z_R = 2449 + i7$ MeV, which couples to $\Omega\omega$ and $\Omega\phi$. The radiative decay width obtained in this case is $\Gamma = 0.330$ MeV. As

one can see, there is a large variation in the radiative width of the different states, which should constitute a good test for the model when these widths are measured. In Table 3.4 we summarize all the results obtained making an association of our states to some resonances found in the PDG [67].

3.5   Radiative decays into γ and baryon octet

The couplings of the resonances to the different VB channels are given in Ref. [29] in the isospin basis. For the case of ωB and ϕB, there is no change to be done, but for the case of ρB, one must project over the $\rho^0 B$ component. Since this depends on the charge of the resonance R, the radiative decays will depend on this charge, as we will see. We recall that in our phase convention $|\rho^+\rangle = -|1,1\rangle$ of isospin. The information on the resonances and their couplings to different baryons of octet and vector mesons ρ, ω, ϕ for different channels is listed in Table 3.5. We detail the results below and compile them in Table 3.6.

3.5.1 $S = 0, I = 1/2$ channel

Two resonances are obtained at $z_R = 1696$ MeV and $z_R = 1977 + i53$ MeV which couple to ρN, ωN and ϕN. We have in this case

$$|\rho N, \frac{1}{2}, \frac{1}{2}\rangle = -\sqrt{\frac{1}{3}}|\rho^0 p\rangle - \sqrt{\frac{2}{3}}|\rho^+ n\rangle \tag{3.32}$$

$$|\rho N, \frac{1}{2}, -\frac{1}{2}\rangle = \sqrt{\frac{1}{3}}|\rho^0 n\rangle - \sqrt{\frac{2}{3}}|\rho^- p\rangle \tag{3.33}$$

The coupling of the resonance to ρ^0 is obtained multiplying the coupling of Table 3.5 by the corresponding Clebsch-Gordan coefficient for $\rho^0 N$ of Eqs. (3.32, 3.33). Then, by means of Eqs. (3.18, 3.19), one obtains the decay width.

3.5.2 $S = -1, I = 0$ channel

We get three resonances at $z_R = 1784 + i4$ MeV, $z_R = 1906 + i70$ MeV and $z_R = 2158 + i13$ MeV respectively, which couple to $\rho\Sigma$, $\omega\Lambda$ and $\phi\Lambda$. In this case

$$|\rho\Sigma, 0, 0\rangle = \sqrt{\frac{1}{3}}|\rho^-\Sigma^+\rangle - \sqrt{\frac{1}{3}}|\rho^0\Sigma^0\rangle - \sqrt{\frac{1}{3}}|\rho^+\Sigma^-\rangle. \tag{3.34}$$

S, I	Theory	PDG data		Predicted width (KeV) for I_3						
	pole position (MeV)	name	J^P	$-3/2$	-1	$-1/2$	0	$1/2$	1	$3/2$
$0, 1/2$	$1850 + i5$	$N(2090)$	$1/2^-$			722		722		
		$N(2080)$	$3/2^-$							
$0, 3/2$	$1972 + i49$	$\Delta(1900)$	$1/2^-$	1582		203		143		1402
		$\Delta(1940)$	$3/2^-$							
		$\Delta(1930)$	$5/2^-$							
$-1, 0$	$2052 + i10$	$\Lambda(2000)$	$?^?$					583		
$-1, 1$	$1987 + i1$	$\Sigma(1940)$	$3/2^-$		20		199		561	
		$\Sigma(2000)$	$1/2^-$							
	$2145 + i58$	$\Sigma(2250)$	$?^?$		2029		206		399	
	$2383 + i73$	$\Sigma(2455)$	$?^?$		537		277		182	
$-2, 1/2$	$2214 + i4$	$\Xi(2250)$	$?^?$			54		815		
	$2305 + i66$	$\Xi(2370)$	$?^?$			1902		320		
	$2522 + i38$	$\Xi(2500)$	$?^?$			165		44		
$-3, 1$	$2449 + i7$	$\Omega(2470)$	$?^?$				330			

Table 3.4: The predicted radiative decay widths of the ten dynamically generated resonances for different isospin projection I_3. Their possible PDG counterparts are also listed. Note that the $\Sigma(2000)$ could be the spin parter of the $\Sigma(1940)$, in which case the radiative decay widths would be those of the $\Sigma(1940)$.

S, I	Channel			
		$z_R = 1696$	$z_R = 1977 + i53$	
0, 1/2	ρN	$3.2 + i0$	$-0.3 - i0.5$	
	ωN	$0.1 + i0$	$-1.1 - i0.4$	
	ϕN	$-0.2 + i0$	$1.5 + i0.6$	
		$z_R = 1784 + i4$	$z_R = 1906 + i70$	$z_R = 2158 + i13$
-1, 0	$\omega \Lambda$	$1.4 + i0.03$	$0.4 + i0.2$	$-0.3 - i0.2$
	$\rho \Sigma$	$-1.5 + i0.03$	$3.1 + i0.7$	$0.01 - i0.08$
	$\phi \Lambda$	$-1.9 - i0.04$	$-0.6 - i0.3$	$0.5 + i0.3$
		$z_R = 1830 + i40$	$z_R = 1987 + i240$	
-1,1	$\rho \Lambda$	$-1.6 + i0.2$	$-0.3 + i0.9$	
	$\rho \Sigma$	$-1.6 + i0.07$	$2.6 + i0.0$	
	$\omega \Sigma$	$-0.9 + i0.1$	$-0.2 + i0.5$	
	$\phi \Sigma$	$1.2 - i0.2$	$0.2 - i0.7$	
		$z_R = 2039 + i67$	$z_R = 2082 + i31$	
-2, 1/2	$\rho \Xi$	$2.4 + i0.7$	$0.4 + i0.3$	
	$\omega \Xi$	$0.6 - i0.08$	$1.1 + i0.3$	
	$\phi \Xi$	$-0.8 + i0.1$	$-1.6 - i0.4$	

Table 3.5: The couplings g_i of the resonances obtained dynamically to the ρ, ω and ϕ with the baryon octet channels of Ref. [29].

3.5.3 $S = -1, I = 1$ **channel**

Here we find two resonances at $1830 + i40$ MeV and $1987 + i240$ MeV, which couple to $\rho\Lambda$, $\rho\Sigma$, $\omega\Sigma$ and $\phi\Sigma$. The relevant isospin states are

$$|\rho\Sigma, 1, 1\rangle = -\sqrt{\frac{1}{2}}|\rho^0\Sigma^+\rangle - \sqrt{\frac{1}{2}}|\rho^+\Sigma^0\rangle, \tag{3.35}$$

$$|\rho\Sigma, 1, 0\rangle = -\sqrt{\frac{1}{2}}|\rho^+\Sigma^-\rangle - \sqrt{\frac{1}{2}}|\rho^-\Sigma^+\rangle, \tag{3.36}$$

$$|\rho\Sigma, 1, -1\rangle = -\sqrt{\frac{1}{2}}|\rho^-\Sigma^0\rangle + \sqrt{\frac{1}{2}}|\rho^0\Sigma^-\rangle. \tag{3.37}$$

3.5.4 $S = -2, I = 1/2$ **channel**

Here we also find two states at $z_R = 2039 + i67$ MeV and $2082 + i31$ MeV, which couple to $\rho\Xi$, $\omega\Xi$ and $\phi\Xi$. The isospin states for $\rho\Xi$ are written as

$$|\rho\Xi, \frac{1}{2}, \frac{1}{2}\rangle = -\sqrt{\frac{2}{3}}|\rho^+\Xi^-\rangle - \sqrt{\frac{1}{3}}|\rho^0\Xi^0\rangle, \tag{3.38}$$

$$|\rho\Xi, \frac{1}{2}, -\frac{1}{2}\rangle = \sqrt{\frac{1}{3}}|\rho^0\Xi^-\rangle - \sqrt{\frac{2}{3}}|\rho^-\Xi^0\rangle. \tag{3.39}$$

In Table 3.6 we summarize all the results obtained, making an association of our states to some resonances found in the PDG[67]. As one can see, there is a large variation in the radiative width of the different states, which should constitute a good test for the model. For the case of the vector-baryon octet states which decay into γ and a baryon of the octet, it is customary to express the experimental information in terms of helicity amplitudes $A_{1/2}$ and $A_{3/2}$. We evaluate these amplitudes in next section to facilitate the comparison with experiment.

3.6 Helicity amplitudes

Recalling Eq. (3.10) for the dynamically generated states from a vector and a baryon of the octet, we have the two cases $J^P = 1/2^-$ and $J^P = 3/2^-$. The helicity amplitudes with the choice of polarization vectors of Eq. (3.4), which imply the use of the Coulomb Gauge with the photon momentum in

S, I	Theory	PDG data		Predicted width KeV for I_3				
	pole position (MeV)	name	J^P	-1	$-1/2$	0	$1/2$	1
$0, 1/2$	1696	$N(1650)$	$1/2^-$		334		253	
		$N(1700)$	$3/2^-$					
	$1977 + i53$	$N(2080)$	$3/2^-$		196		79	
		$N(2090)$	$1/2^-$					
$-1, 0$	$1784 + i4$	$\Lambda(1690)$	$3/2^-$			65 (166)		
		$\Lambda(1800)$	$1/2^-$					
	$1907 + i70$	$\Lambda(2000)$	$?^?$			321 (21)		
	$2158 + i13$					0 (17)		
$-1, 1$	$1830 + i40$	$\Sigma(1750)$	$1/2^-$	363		69 (240)		7
	$1987 + i240$	$\Sigma(1940)$	$3/2^-$	307		27 (90)		426
		$\Sigma(2000)$	$1/2^-$					
$-2, 1/2$	$2039 + i67$	$\Xi(1950)$	$?^?$		400		89	
	$2082 + i31$	$\Xi(2120)$	$?^?$		212		84	

Table 3.6: The predicted radiative decay widths of the nine dynamically generated resonances for different isospin projection I_3. Their possible PDG counterparts are also listed. The values in the bracket for $I_3 = 0$ denote widths for the radiative decay into $\Lambda\gamma$, while the values outside the bracket denote widths for $\Sigma\gamma$.

the z direction, are defined as

$$A_{1/2}^{N^*} = \sqrt{\frac{2\pi\alpha}{k}}\frac{1}{e}\left\langle N^*, J_z = 1/2|\epsilon_\mu^{(+)}J^\mu|N, J_z = -1/2\right\rangle \qquad (3.40)$$

$$A_{3/2}^{N^*} = \sqrt{\frac{2\pi\alpha}{k}}\frac{1}{e}\left\langle N^*, J_z = 3/2|\epsilon_\mu^{(+)}J^\mu|N, J_z = 1/2\right\rangle \qquad (3.41)$$

where $\alpha = 1/137$, k is the CM photon momentum and $e^2 = 4\pi\alpha$. To accommodate these amplitudes to our Eq. (3.10) we rewrite them taking $\epsilon_\mu^{(+)}J^\mu = -\vec{\epsilon}^{(+)}\vec{J}$, as

$$A_{1/2}^{J=1/2} = -t_\gamma\frac{1}{\sqrt{2k}}\mathcal{C}(1/2, 1, 1/2; m_s, M - m_s, M)\langle\vec{\epsilon}_{M-m_s}|\vec{\epsilon^*}\rangle^* \qquad (3.42)$$

where t_γ is given by Eq. (3.18), with $m_s = -1/2$, $\vec{\epsilon} = \vec{\epsilon}^{(+)}$, which fixes $M - m_s = 1$, and similarly for the other amplitudes. Hence, we obtain

$$A_{1/2}^{J=1/2} = -t_\gamma\frac{1}{\sqrt{2k}}\mathcal{C}(1/2, 1, 1/2; -1/2, 1, 1/2) = \frac{1}{\sqrt{2k}}\sqrt{\frac{2}{3}}t_\gamma \qquad (3.43)$$

$$A_{1/2}^{J=3/2} = -t_\gamma\frac{1}{\sqrt{2k}}\mathcal{C}(1/2, 1, 3/2; -1/2, 1, 1/2) = -\frac{1}{\sqrt{2k}}\sqrt{\frac{1}{3}}t_\gamma \qquad (3.44)$$

$$A_{3/2}^{J=3/2} = -t_\gamma\frac{1}{\sqrt{2k}}\mathcal{C}(1/2, 1, 3/2; 1/2, 1, 1/2) = -\frac{1}{\sqrt{2k}}t_\gamma \qquad (3.45)$$

The ordinary formula to get the radiative decay width in terms of $A_{1/2}$ and $A_{3/2}$ is given in the PDG [67] as

$$\Gamma_\gamma = \frac{k^2}{\pi}\frac{2M_B}{(2J_R + 1)M_R}\left[(A_{1/2})^2 + (A_{3/2})^2\right] \qquad (3.46)$$

One can see that using in Eq. (3.46), the values of the helicity amplitudes obtained in Eqs. (3.43, 3.44, 3.45) one obtains the same result of Eq. (3.19) for both spins of the resonances.

It is interesting to note that the values of $A_{1/2}$ for $J = 1/2$, $3/2$ and $A_{3/2}$ for $J = 3/2$ are all related by the simple relations of Eqs. (3.43, 3.44, 3.45) for these dynamically generated states, and the ratio of $1/\sqrt{3}$ between $A_{1/2}^{J=3/2}$ and $A_{3/2}^{J=3/2}$ is something that could be contrasted with experiment. We compile in Table 3.7 all the results obtained for the resonances that are likely to be associated to states in the PDG for which there are data. The theoretical errors have been obtained by assuming 10% uncertainty in the largest coupling of the resonance to the different channels and 15% in the

PDG data			Helicity amplitudes10^{-3}(GeV$^{-1/2}$)						
name	J^P	Decay	Theory	Exp.[67] PDG	Exp.[70] Barbour	Exp.[71] Devenish	Th.[55]	Th.[72]	Th.[73]
$N(1650)\,1/2^-$		$A^p_{1/2}$	64 ± 7	53 ± 16			5	46	54
		$A^n_{1/2}$	-74 ± 7	$-15\pm\,4$			-16	-58	-35
$N(1700)\,3/2^-$		$A^p_{1/2}$	-46 ± 5	-18 ± 13	-33 ± 21		-13	-3	-33
		$A^p_{3/2}$	-79 ± 9	-2 ± 24	-14 ± 25		-10	15	18
		$A^n_{1/2}$	52 ± 5	0 ± 50	50 ± 42		16	14	-3
		$A^n_{3/2}$	91 ± 9	-3 ± 44	35 ± 30		-42	-23	-30
$N(2080)\,3/2^-$		$A^p_{1/2}$	21 ± 5	$-20\pm\,8$		$26\pm\,52$			
		$A^p_{3/2}$	36 ± 8	17 ± 11		$128\pm\,57$			
		$A^n_{1/2}$	29 ± 5	7 ± 13		$53\pm\,83$			
		$A^n_{3/2}$	50 ± 8	-53 ± 34		100 ± 141			
$N(2090)\,1/2^-$		$A^p_{1/2}$	-30 ± 6						
		$A^n_{1/2}$	-41 ± 6						

Table 3.7: Comparison with experiments and other theoretical works.

other ones. This is only a rough estimate and the uncertainties can easily be double this amount.

We should comment on the signs of the helicity amplitudes. For us they are determined by means of Eqs. (3.43, 3.44, 3.45) in terms of t_γ given in Eq. (3.18). We should mention that the g_j couplings appearing there are all determined with their relative sign, but one of them has an arbitrary sign. Thus we have an arbitrary sign in the helicity amplitudes, but the relative sign between the $A^{J=3/2}_{1/2}$ and $A^{J=3/2}_{3/2}$ is well determined. Within our convention of $SU(3)$ phases also the n and p helicity amplitudes are correlated.

Experimentally the phases of the helicity amplitudes are a subject of convention since there is one phase arbitrary in the non diagonal transition of baryon states. In practice when dealing with physical processes to determine the helicity amplitudes, one has a strong vertex and an electromagnetic one, like $\gamma N \to N^*$ and $N^* \to N\pi$ [74, 75, 76, 77] and one could determine the

sign of the product of these two vertices of some resonances with respect to other ones, with some global phase undetermined. Theoretically one could do a similar thing, but this would require to study the transition amplitude of the VN resonances to πN. This problem is addressed in the present thesis in chapter 4. In view of this, we have chosen two phases to compare with experiment, the one of $A^p_{1/2}$ for $N(1700)$ and that of $A^p_{1/2}$ for $N(2080)$. The choice has been made to agree with the experiments of Barbour and Devenish respectively.

By looking at Table 3.7 we can see that the agreement with the data of $A^p_{1/2}$ for the PDG average of $N^*(1650)$ is good. For the case of $A^n_{1/2}$ the results obtained are larger than experiment but the sign is good. In the case of the $N^*(1700)$, $A^p_{1/2}$ can be considered qualitatively fine within theoretical and experimental errors, $A^p_{3/2}$ seems to be larger than experiment but one can see that individual measurements, as the one of Barbour [70] diverge appreciably from the PDG average values. Similarly $A^n_{1/2}$ would be compatible with experiment within errors and $A^n_{3/2}$ seems also a bit larger, but not qualitatively too off account taken of the large experimental uncertainties. This last magnitude is very relevant since the predictions of the dynamically generated model have opposite sign to all the quark model calculations mentioned in the table. Since a global sign in these non diagonal transitions can always appear in different models, more relevant than the absolute sign is the relative one to $A^n_{1/2}$ which is the same in our case and opposite in Ref. [55, 72]. In Ref. [73] one has the same signs but there is one order of magnitude difference between the two helicity amplitudes, while in our model the ratio is $\sqrt{3}$. It is clear that precise measurements of these magnitudes are very useful to discriminate among models and help us understand better the structure of these resonances.

The case of the $N^*(2080)$ and $N^*(2090)$ is more unclear. The agreement with the PDG average does not seem too good, although the uncertainties are very large, but we find it more appropriate to compare with the results of a single experiment. For this purpose we also show the experimental results of Devenish [71] for the resonances to show that individual measurements are very different from the PDG averages. The agreement with signs of all amplitudes is now good (recall that one theoretical sign is chosen to agree) and also the sizes are similar, account taken of the large experimental uncertainties. Since under the umbrella of the $N^*(2080)$ and $N^*(2090)$ there are apparently different states compiled, it would be possible that the averages of the PDG were not done for different measurements on the same state but for measurements on different states. The experimental situation is hence unclear but the results obtained here should be a motivation for

further reanalysis.

A different way to make the comparison with experiment is to take the relationship of Eqs. (3.43, 3.44, 3.45), tied to the nature of these resonances as dynamically generated from the vector baryon interaction, and extract the only independent amplitude, t_γ, from the experimental data, hence comparing t_γ directly. We have done this and take the data of Barbour and Devenish, for the $N^*(1700)$ and $N^*(2080)$ respectively, to guarantee that they come from the same state. The results are found in Table 3.8. We observe consistency in the sizes and signs (only one sign is chosen theoretically for one amplitude of each resonance), although the experimental errors are still very large. Needless to say that improvements on these measurements would be most welcome.

PDG data			$t_\gamma \, 10^{-3} \, (A_{1/2}^{3/2}/A_{1/2}^{1/2})$		
name	J^P	Decay	Theory	Exp.[70] Barbour	Exp.[71] Devenish
$N(1650)$	$1/2^-$	$A_{1/2}^p$	85 ± 9		
		$\mathbf{A_{1/2}^n}$	$\mathbf{-98 \pm 10}$		
$N(1700)$	$3/2^-$	$A_{1/2}^p$	85 ± 9	60 ± 38	
		$A_{3/2}^p$	85 ± 9	15 ± 26	
		$\mathbf{A_{1/2}^n}$	$\mathbf{-98 \pm 10}$	$\mathbf{-94 \pm 79}$	
		$\mathbf{A_{3/2}^n}$	$\mathbf{-98 \pm 10}$	$\mathbf{-35 \pm 32}$	
$N(2080)$	$3/2^-$	$A_{1/2}^p$	-45 ± 10		-57 ± 116
		$A_{3/2}^p$	-45 ± 10		-164 ± 73
		$\mathbf{A_{1/2}^n}$	$\mathbf{-62 \pm 10}$		$\mathbf{-119 \pm 186}$
		$\mathbf{A_{3/2}^n}$	$\mathbf{-62 \pm 10}$		$\mathbf{-129 \pm 182}$
$N(2090)$	$1/2^-$	$A_{1/2}^p$	-45 ± 10		
		$\mathbf{A_{1/2}^n}$	$\mathbf{-62 \pm 10}$		

Table 3.8: Comparison of t_γ obtained from the theoretical and experimental helicity amplitudes. The numbers in bold characters refer to neutron and the normal ones to the proton.

3.7 Conclusions

In this chapter we have studied the radiative decay into γB, with B a baryon of the octet and decuplet of $SU(3)$, of the dynamically generated resonances obtained within the framework of the local hidden gauge mechanism for vector interactions. The framework is particularly rewarding for the study of such observable, since the photon in the final state appears coupling directly to the vector $V = \rho^0, \ \omega, \ \phi$ in the $R \to BV$ amplitudes which are studied in previous works. The rates obtained are large and the radiative widths are of the order of 1 MeV. On the other hand, one of the appealing features of the results is the large difference, of about one order of magnitude, that one finds between the widths for different charge states of the same particle. Although, such differences are also found in quark models, the precise values are tied to details of the theory, concretely the coupling of the resonances to VB, which sometimes produce large interferences between the different contributions of the three vector mesons to which the photon couples. As a consequence, the radiative decay widths that we have evaluated bear much information on the nature of those resonances, which should justify efforts for a systematic measurement of these observables.

We have studied the decay into γ-baryon octet and γ-baryon decuplet of the states dynamically generated from the vector-baryon octet and vector-baryon decuplet interaction. In the first case one can define the helicity amplitude $A_{1/2}$ and $A_{3/2}$ for the n and p type states of the N^*, which makes the comparison with data more useful. We have found good agreement with data in some cases and rough in others, but we have warned about the large experimental uncertainties and the possibility that the PDG averages are done over different states. Perhaps the most practical way to test the nature of the resonances that we have discussed would be to check experimentally the relationships of Eqs. (3.43, 3.44, 3.45) which relate the spin 1/2 and 3/2 helicity amplitudes for the approximately degenerated spin partners, as we have done. What stands clear from the work and the discussion is that these observables are very useful to help us understand better the nature of the resonances discussed here. Further experimental work is most desirable. The results of this Chapter are published in Ref. [78].

The box diagram

4.1 Introduction

The approach to QCD at low energies using effective Lagrangians [8] has proved very valuable. In particular the implementation of chiral symmetry [79, 80] has been a guiding principle to construct effective Lagrangians which account for the basic symmetries of the strong interaction and take the observable hadrons, mesons and baryons, as basic fields in those Lagrangians. Along this line, the use of chiral Lagrangians in combination with unitary techniques in coupled channels of mesons and baryons has been a very fruitful scheme to study the nature of many hadron resonances. It allows, among many other, to evaluate meson baryon scattering amplitudes, which sometimes show poles in the second Riemann sheet which are identified with existing baryon resonances. They are dynamically generated resonances. In this way the interaction of the octet of pseudoscalar mesons with the octet of stable baryons has lead to $J^P = 1/2^-$ resonances which fit quite well the spectrum of the known low lying resonances with these quantum numbers [14, 15, 16, 17, 18, 19, 20, 21, 22]. Similarly, the interaction of the octet of pseudoscalar mesons with the decuplet of baryons also leads to many resonances that can be identified with existing ones of $J^P = 3/2^-$ [23, 24]. One interesting case is the one of the $\Lambda(1405)$, where all the chiral approaches find two poles close by, which have found experimental support in the analysis of Refs. [25, 26].

Much work has been done using pseudoscalar mesons as building blocks, but the consideration of vectors instead of pseudoscalars is also receiving much attention lately. In the baryon sector the interaction of the $\rho\Delta$ has been recently addressed in Ref. [27], where three degenerate N^* states around 1800 MeV and three degenerate Δ states around 1900 MeV, with $J^P =$

$1/2^-, 3/2^-, 5/2^-$, are found. This work has been recently extended to the $SU(3)$ space of vectors and baryons of the decuplet in Ref. [28]. The underlying theory for this study is the local hidden gauge formalism [30, 13, 31, 40], which deals with the interaction of vector mesons and pseudoscalars in a way respecting chiral dynamics, providing the interaction of pseudoscalars among themselves, with vector mesons, and vector mesons among themselves. The theory provides the chiral Lagrangians as limiting cases at low energies through vector exchange diagrams.

In the same line, the interaction of vector mesons with the octet of baryons has been addressed in Ref. [29], where also many states are dynamically generated which can be associated to known resonances. A few other states remain as predictions or are difficult to associate to the known states which show a large dispersion from different experiments. More recently, work along this line has been done in Ref. [81], and the concrete issue of the mixing of the pseudoscalar-baryon and vector-baryon channels, that we tackle here in the strangeness S=0 sector, has been addressed in Ref. [82] for S=-1.

The next natural step in this direction is to put the pseudoscalar-baryon and vector-baryon states on the same footing and two works have been already done in this direction, the first one using a $SU(6)$ scheme that invokes spin-isospin symmetry [83]. The transition from vector-baryon to pseudoscalar-baryon is implemented in this latter approach through the implicit exchange of an axial vector in the t-channel. Such a term is not present in the local hidden gauge approach, where instead, the exchange of pseudoscalar mesons coming from the vector-pseudoscalar-pseudoscalar vertex is responsible for the transition. The second work [82] investigates the mixing in the strangeness S=-1 sector, using a contact pseudoscalar-vector-baryon term obtained by gauging a theory with pseudoscalars and baryons. In the present work we stick to the standard local hidden gauge formalism in the unitary gauge and study the mixing in a systematic way in order to see modifications to the resonances obtained in the work of Ref. [29] when the pseudoscalar-baryon channels are allowed to couple to the main building blocks of vector-baryon.

The idea has already been used in Ref. [32], in the study of πN scattering at intermediate energies, where the ρN channel is also included and a resonance is dynamically generated around 1700 MeV, which has the strongest coupling to the ρN channel.

The introduction of the pseudoscalar-baryon channels has as a main effect the widening of the resonances found in Ref. [29] and, except in some very particular case, has a negligible effect on the mass of the resonances. The consideration of the pseudoscalar-baryon channels also allows us to determine the partial decay width of the resonance into these channels and,

by comparing with the PDG [67] offers new elements to judge on the most appropriate association of the resonances found in Ref. [29] to the known resonances.

4.2 Formalism

The part of the Lagrangian of the local hidden gauge approach that provides the interaction between vectors and is needed for the study of the vector-baryon interaction of Ref. [29], is the three vector Lagrangian shown in Eq. (2.33)

$$\mathcal{L}_{III}^{(3V)} = ig\langle(\partial_\mu V_\nu - \partial_\nu V_\mu)V^\mu V^\nu\rangle \ , \tag{4.1}$$

where V_μ is the $SU(3)$ matrix for the nonet of the ρ

$$V_\mu = \begin{pmatrix} \frac{\rho^0}{\sqrt{2}} + \frac{\omega}{\sqrt{2}} & \rho^+ & K^{*+} \\ \rho^- & -\frac{\rho^0}{\sqrt{2}} + \frac{\omega}{\sqrt{2}} & K^{*0} \\ K^{*-} & \bar{K}^{*0} & \phi \end{pmatrix}_\mu \ , \tag{4.2}$$

and $g = \frac{M_V}{2f}$, with f=93 MeV. In the same way, the coupling of the vectors to pseudoscalar mesons is given by Lagrangian of Eq. (2.41)

$$\mathcal{L}_{VPP} = -ig\langle[P, \partial_\nu P]V^\nu\rangle \ , \tag{4.3}$$

where here P is the $SU(3)$ matrix of the pseudoscalar mesons,

$$P = \begin{pmatrix} \frac{\pi^0}{\sqrt{2}} + \frac{\eta_8}{\sqrt{6}} & \pi^+ & K^+ \\ \pi^- & -\frac{\pi^0}{\sqrt{2}} + \frac{\eta_8}{\sqrt{6}} & K^0 \\ K^- & \bar{K}^0 & -\frac{2}{\sqrt{6}}\eta_8 \end{pmatrix} \ . \tag{4.4}$$

As shown in Refs. [28, 29] the main source of vector-baryon interaction comes from the exchange of a vector meson in the t-channel between the vector and the baryon. This involves the $\mathcal{L}_{III}^{(3V)}$ Lagrangian of Eq. (4.1) and a Lagrangian for the coupling of the vector to the baryon, given in Eq. (2.34) by

$$\mathcal{L}_{BBV} = g\left(\langle\bar{B}\gamma_\mu[V^\mu, B]\rangle + \langle\bar{B}\gamma_\mu B\rangle\langle V^\mu\rangle\right) \ , \tag{4.5}$$

where B is the $SU(3)$ matrix of the baryon octet

$$B = \begin{pmatrix} \frac{1}{\sqrt{2}}\Sigma^0 + \frac{1}{\sqrt{6}}\Lambda & \Sigma^+ & p \\ \Sigma^- & -\frac{1}{\sqrt{2}}\Sigma^0 + \frac{1}{\sqrt{6}}\Lambda & n \\ \Xi^- & \Xi^0 & -\frac{2}{\sqrt{6}}\Lambda \end{pmatrix} \ . \tag{4.6}$$

For the transitions $VB \to PB$ we need the VPP Lagrangian of Eq. (4.3) and one of the two pseudoscalar mesons is exchanged between the external VP and the baryon. The coupling of the pseudoscalar to the baryon for the two $SU(3)$ octet is given in the Lagrangian of Eq. (2.10) by

$$\mathcal{L}_{BBP} = \frac{F}{2}\langle \bar{B}\gamma_\mu\gamma_5 [u^\mu, B]\rangle + \frac{D}{2}\langle \bar{B}\gamma_\mu\gamma_5 \{u^\mu, B\}\rangle \tag{4.7}$$

where $F = 0.51$, $D = 0.75$ [84] and at lowest order in the pseudoscalar field

$$u^\mu = -\frac{\sqrt{2}}{f}\partial^\mu P \; , \tag{4.8}$$

which allows to rewrite the Lagrangian of Eq. (4.7) as

$$\mathcal{L}_{BBP} = -\frac{\sqrt{2}}{f}\frac{D+F}{2}\langle \bar{B}\gamma_\mu\gamma_5 \partial^\mu P B\rangle - \frac{\sqrt{2}}{f}\frac{D-F}{2}\langle \bar{B}\gamma_\mu\gamma_5 B\partial^\mu P\rangle \; . \tag{4.9}$$

Taking the $SU(3)$ trace for a particular case of two baryons, the previous Lagrangian can be written in terms of an effective vertex as

$$-it_{BBP} = \left\{ \alpha\frac{(D+F)}{2f} + \beta\frac{(D-F)}{2f} \right\} \vec{\sigma}\vec{k} \tag{4.10}$$

where $\vec{k}$ is the incoming momentum of the meson in the BBP vertex. The coefficients α and β, can be found in Appendix D. As shown in Ref. [29], the
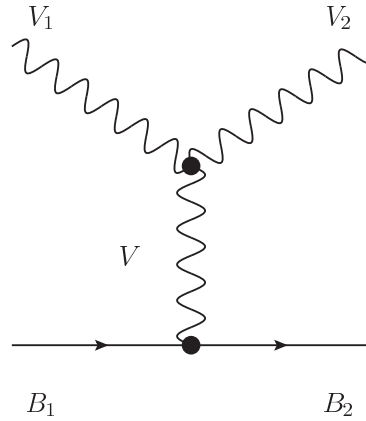

Figure 4.1: Diagram of the $VB \to VB$ interaction mediated by a vector meson.

leading term of the $VB \to VB$ interaction is given by the diagram of Fig. 4.1

which involves the three vector vertex of Eq. (4.1), with one vector meson exchanged, and the coupling of this exchanged vector to the baryon, given by Eq. (4.5). The potential provided by this term, keeping the dominant γ^0 term in Eq. (4.5), is given by

$$V_{ij} = -C_{ij}\frac{1}{4f^2}\left(k^0 + k'^0\right)\,\vec{\epsilon}\,\vec{\epsilon}' \tag{4.11}$$

where k^0, k'^0 are the energies of the incoming and outgoing vector mesons. The result of Eq. (4.11) with the $\vec{\epsilon}\,\vec{\epsilon}'$ factor for the polarization of the vector mesons stems from considering the three momentum of the external vectors small with respect to the mass of the vector mesons [29]. The C_{ij} coefficients can be found in Appendix A of Ref. [29], where the subindex i and j correspond to the different channels for all the states of isospin and strangeness.

However, it is more convenient to work with a relativistic potential as seen in Ref. [42], which is given by

$$V_{ij} = -C_{ij}\frac{1}{4f^2}\left(2\sqrt{s} - M_{B_i} - M_{B_j}\right)\left(\frac{M_{B_i} + E_{B_i}}{2M_{B_i}}\right)^{1/2}\left(\frac{M_{B_j} + E_{B_j}}{2M_{B_j}}\right)^{1/2} \tag{4.12}$$

where M_{B_i}, M_{B_j} are the masses of the initial or final baryons respectively, and E_{B_i}, E_{B_j} their on shell energy.

This potential has been used as the input of the Bethe-Salpeter equation to study the scattering matrix,

$$T = [1 - V\,G]^{-1}\,V \tag{4.13}$$

where G is the loop function of a vector meson and a baryon which is calculated in dimensional regularization, as shown in Refs. [18, 42], and is given by

$$
\begin{aligned}
G &= i2M\int\frac{d^4q}{(2\pi)^4}\frac{1}{(P-q)^2 - M^2 + i\epsilon}\frac{1}{q^2 - m^2 + i\epsilon} \\
&= \frac{2M}{16\pi^2}\left\{a(\mu) + \ln\frac{M^2}{\mu^2} + \frac{m^2 - M^2 + s}{2s}\ln\frac{m^2}{M^2} + \right. \\
&\quad + \frac{q}{\sqrt{s}}\left[\ln(s - (M^2 - m^2) + 2q\sqrt{s}) + \ln(s + (M^2 - m^2) + 2q\sqrt{s})\right. \\
&\quad \left.\left. - \ln(-s + (M^2 - m^2) + 2q\sqrt{s}) - \ln(-s - (M^2 - m^2) + 2q\sqrt{s})\right]\right\}
\end{aligned}
\tag{4.14}
$$

where μ=630 MeV is a regularization scale and $a(\mu)$ a subtraction constant with a value of -2 in Ref. [29], which is considered a natural size in Ref. [18].

In the cases where the iteration of the Bethe-Salpeter equation includes the ρ or K^* mesons, which have a relatively large widths, a convolution of the loop function G with the mass distribution of these vector mesons is needed. So the loop function with the convolution would be

$$\tilde{G}(s) = \frac{1}{N} \int_{(m_i-2\Gamma_i)^2}^{(m_i+2\Gamma_i)^2} d\tilde{m}^2 \left(-\frac{1}{\pi}\right) \text{Im} \frac{1}{\tilde{m}^2 - m^2 + i\tilde{m}\Gamma(\tilde{m})} G(s, \tilde{m}^2, \tilde{M}_B^2)$$

(4.15)

where $\tilde{G}$ is normalized with

$$N = \int_{(m_i-2\Gamma_i)^2}^{(m_i+2\Gamma_i)^2} d\tilde{m}^2 \left(-\frac{1}{\pi}\right) \text{Im} \frac{1}{\tilde{m}^2 - m_i^2 + i\tilde{m}\Gamma(\tilde{m})}$$

(4.16)

considering the masses m_i and the widths of the vectors Γ_i ($i = \rho,\ K^*$) Γ_ρ=149.4 MeV and Γ_{K^*}=50.5 MeV. The $\Gamma(\tilde{m})$ function is energy dependent and is given in Ref. [35] as

$$\tilde{\Gamma}(\tilde{m}) = \Gamma_i \frac{q_{\text{off}}^3}{q_{\text{on}}^3} \theta(\tilde{m} - m_1 - m_2)$$

(4.17)

with $m_1 = m_2 = m_\pi$ for the ρ using that

$$q_{\text{off}} = \frac{\lambda(\tilde{m}^2, m_\pi^2, m_\pi^2)}{2\tilde{m}}, \quad q_{\text{on}} = \frac{\lambda(m_\rho^2, m_\pi^2, m_\pi^2)}{2m_\rho}$$

(4.18)

or $m_1 = m_\pi$ and $m_2 = m_K$ for the K^* using

$$q_{\text{off}} = \frac{\lambda(\tilde{m}^2, m_K^2, m_\pi^2)}{2\tilde{m}}, \quad q_{\text{on}} = \frac{\lambda(m_{K^*}^2, m_K^2, m_\pi^2)}{2m_{K^*}},$$

(4.19)

where λ is the Källen function and Γ_i is the nominal width of the ρ or the K^*. Without these convolutions, the peaks that we find in the scattering matrix in the channels where the ρ or the K^* are involved, have a zero width or are very narrow. But when the loop function G is replaced by the convolution function $\tilde{G}$ using the correspondent mass distribution, those peaks acquire a substantial width.

The $\vec{\epsilon}\vec{\epsilon}'$ factor involving the polarization of the vector mesons factorizes in all the iterations of the potential implicit in the Bethe-Salpeter equations, as a consequence of which there will be a degeneracy in the spin, $1/2^-$, $3/2^-$, for the resonances found for each isospin and strangeness.

Once the scattering matrix is evaluated some peaks appear that can be associated to states. Next step is to find the poles associated to those peaks, in order to obtain the couplings of the different channels to those states. The

method used is to search poles in the second Riemann sheet, changing the momentum $\vec{q}$ to $-\vec{q}$ in the analytical formula of the G function when $Re(\sqrt{s})$ is over the threshold of the corresponding channel. Using this method one can find poles, as $(M_R + i\Gamma/2)$, where the real part correspond to the mass of the resonance and the imaginary part is half of the width of this state. However the convolution of the G function eventually can make the pole disappear in channels with the ρ or the K^* mesons. In this case one can study the amplitude in the real axis using that near the peak the T matrix will be as

$$T_{ij} = \frac{g_i g_j}{\sqrt{s} - M_R + i\Gamma/2} \tag{4.20}$$

where M_R is the position of the maximum and Γ the width at half-maximum. The couplings g_i and g_j are related to the channels which couple to this resonance. Then one can take the diagonal channel where the coupling is largest and obtain

$$|g_i|^2 = \frac{\Gamma}{2} \sqrt{|T_{ii}|^2} \tag{4.21}$$

where the coupling g_i has an arbitrary phase. With one coupling determined, we can obtain the other ones from the T_{ij} matrices using Eq. (4.20), given by

$$g_j = g_i \frac{T_{ij}(\sqrt{(s)} = M_R)}{T_{ii}(\sqrt{(s)} = M_R)} \ . \tag{4.22}$$

This procedure has been used to calculate all the couplings of all the states of the vector-baryon interaction in Ref. [29], so we shall use this method in order to calculate our results in the present work.

Using this formalism, nine resonances are found in Ref. [29], which are associated to known states of the PDG [67], through the isospin and strangeness and the pole position. However, the widths obtained with this approach are smaller than the experimental ones. This result leads us to think that there should be some other mechanisms which contribute to the vector meson - baryon interaction potential. Since vector mesons and baryons couple to pseudoscalar mesons, there can be diagrams where the interaction is mediated by pseudoscalar mesons. The next section is devoted to study such mechanisms.

4.3 The box diagram

In addition to the driving term in the $VB \rightarrow VB$ potential of Eq. (4.12) there are other terms involving the exchange of pseudoscalar mesons that also contribute to this interaction. The idea is that an external vector meson
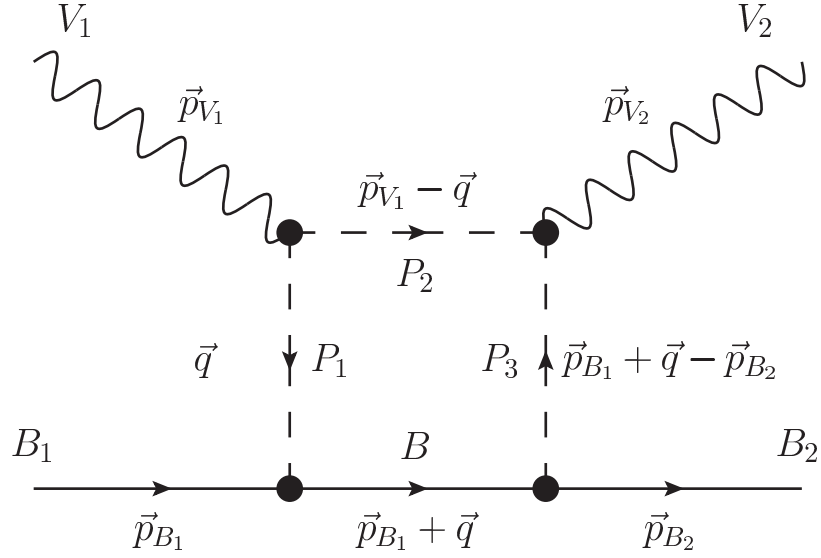
Figure 4.2: Diagram of the $VB \to VB$ interaction mediated by a pseudoscalar meson-baryon loop.

decays into two pseudoscalar mesons, through the Lagrangian of Eq. (4.3), and one of the pseudoscalar mesons is exchanged and absorbed by the baryon. Then a pseudoscalar-baryon state propagates in the intermediate state and the inverse procedure occurs in a second vertex, giving rise to a VB again. The mechanism is depicted in Fig. 4.2 in terms of a Feynman diagram, which gives a contribution to the $VB \to VB$ potential given by

$$
\begin{aligned}
-it_{Box} \;=\; & \int \frac{d^4q}{(2\pi)^4} ig\; C_{V_1}(\vec{p}_{V_1} - \vec{q} - \vec{q}) \cdot \vec{\epsilon}_1 \\
\;=\; & \frac{i}{q^2 - m_1^2 + i\epsilon} ig\; C_{V_2}(\vec{p}_{V_1} - \vec{q} - \vec{p}_{B_1} - \vec{q} + \vec{p}_{B_2}) \cdot \vec{\epsilon}_2 \\
& \frac{i}{(p_{V_1} - q)^2 - m_2^2 + i\epsilon} \frac{i}{(p_{B_1} + q - p_{B_2})^2 - m_3^2 + i\epsilon} \\
& \frac{i}{(p_{B_1} + q)^0 - E_B(\vec{p}_{B_1} + \vec{q}) + i\epsilon} \vec{\sigma} \cdot \vec{q}\, \vec{\sigma} \cdot (-\vec{p}_{B_1} - \vec{q} + \vec{p}_{B_2}) \\
& \{\alpha_1(D + F) + \beta_1(D - F)\} \frac{1}{2f} \\
& \{\alpha_2(D + F) + \beta_2(D - F)\} \frac{1}{2f} \tag{4.23}
\end{aligned}
$$

where q is the loop four-momentum, $\vec{p}_{V_i}$ and $\vec{p}_{B_i}$ are the momenta of the external vector mesons and baryons and m_i are the masses of the three pseudoscalar mesons of the loop. The coefficients of the VPP vertex C_{V_i} are obtained from Eq. (4.3) and the coefficients for the couplings of the pseudoscalars to the baryons, α_i and β_i are shown in Tables D.1 and D.2 of Appendix D.

In other to calculate this integral, we perform analytically the integration over the q^0 component of the four-momentum of the loop. This leads to a residue, which is simplified by eliminating the fallacious poles with no determined position in the complex plane $((x - x_0 + i\epsilon - i\epsilon')^{-1})$, and the result is given in Appendix C.

Consistently with the approximation in Ref. [29] of neglecting the three momentum of the external vectors, we take here the same prescription and set these momenta to zero. The integral simplifies since we can substitute

$$\langle m'|\vec{\sigma}\cdot\vec{q}\,\vec{\sigma}\cdot\vec{q}\,|m\rangle = \langle m'|\vec{q}^{\,2}|m\rangle = \vec{q}^{\,2}\delta_{m'm} \tag{4.24}$$

and

$$q_i q_j \to \frac{1}{3}\vec{q}^{\,2}\delta_{ij} \tag{4.25}$$

The most generic expression for the diagram of Fig. 4.2, is given by

$$
\begin{aligned}
V_{Box} &= -g^2 \frac{C_{V_1} C_{V_2}}{2f^2} \left\{ a(D+F)^2 + b(D-F)^2 + c(D+F)(D-F) \right\} \vec{\epsilon}_1 \vec{\epsilon}_2 \\
&\quad \frac{1}{2\pi^2}\frac{4}{3} \int d|\vec{q}\,| |\vec{q}\,|^6 \left(\frac{\Lambda^2}{\Lambda^2 + |\vec{q}\,|^2} \right)^2 \frac{Num}{Den}
\end{aligned}
\tag{4.26}
$$

where we have introduced the usual form factor accompanying the Yukawa vertex with Λ=1 GeV. The coefficients a, b and c, depend on each state, channel and particles involved in the box diagram, and can be found in Tables of Appendix E. The numerator and denominator (Num and Den) of Eq. (4.26) are given in Appendix C.

We found that for the channels with strangeness it was sufficient to consider only the diagonal terms of the Box diagram, but for the channels with S=0, the consideration of the non-diagonal terms made changes in the $K^*\Lambda \to K^*\Lambda$ amplitude that recommended its explicit consideration. Hence in the case of S=0, the non-diagonal terms are evaluated for the most relevant channels, ρN, $K^*\Lambda$ and $K^*\Sigma$.

This $VB \to VB$ potential modifies the original potential, with only the vector meson exchange, giving a new potential including both interactions.

$$\tilde{V} = V + V_{Box} \tag{4.27}$$

where V (tree level) and V_{Box} are given by Eq. (4.12) and Eq. (4.26) respectively. In Fig. 4.3 we can see a comparison of the real and imaginary parts of the tree level potential and the box potential for the ρN diagonal term. The same figure (right panel) shows the box contribution for the different diagonal terms of all channels that couple to $S = 0$, $I = 1/2$.

The results show that the box potential has a small real part, which is near zero close to the threshold, and an important imaginary part in contrast with the null imaginary part of the tree level potential. It is clear that the total potential will contribute to the scattering matrix generating a widening of the resonances. Using this new potential, we can introduce it in the Bethe-Salpeter equation and recalculate the scattering matrix for all the states and channels. Although there is a Lagrangian which involves the coupling of the
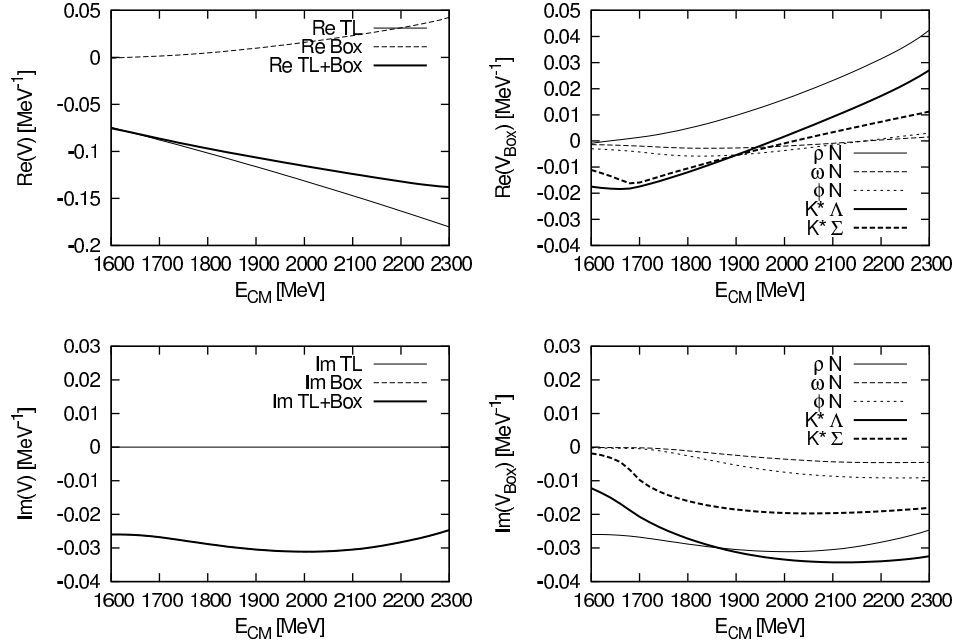
Figure 4.3: Left) Comparison between the tree-level (TL) and the box diagram (Box) potential: (Top) Real part and (Bottom) Imaginary part. Right) Comparison of the box diagram potential between the different channels of the state I=1/2 and S=0: (Top) Real part and (Bottom) Imaginary part.

pseudoscalar mesons connecting the baryon octet and baryon decuplet, in the present work we have neglected the diagrams with a decuplet baryon as an intermediate state since the results of the box integral for these cases are less than 10% of those for the octet baryon in the intermediate state.

One can see qualitatively why this box diagram gives a small contribution

to the real part. For this exercise we select the $\rho^+ n \to \pi^+ n$ vertex, together with the $\rho^+ n \to \rho^+ n$. The π^0 exchange diagram in the first case provides a transition amplitude

$$t_{\rho^+ n \to \pi^+ n} \approx \frac{2\sqrt{2}}{\sqrt{3}} \frac{\vec{q}^{\,2}}{q^{0^2} - \vec{q}^{\,2} - m_\pi^2} g \frac{D + F}{2f} \tag{4.28}$$

while the $\rho^+ n \to \rho^+ n$ gives

$$t_{\rho^+ n \to \rho^+ n} \approx \frac{2m_\rho}{4f^2} \tag{4.29}$$

and we chose q^0, $\vec{q}$ in the π exchange corresponding to the πN on shell situation for $\sqrt{s} \approx 1650$ MeV. We find the $\rho^+ n \to \rho^+ n$ vertex about 4 times bigger than the $\rho^+ n \to \pi^+ n$ one. Yet, one must consider that to get a contribution to $\rho^+ n \to \rho^+ n$, the $\rho^+ n \to \pi^+ n$ terms must be iterated in the box (and multiplied by $G(\pi, n)$) and this further reduces the contribution of the box diagram to the real part of the $VN \to VN$ amplitude. The accurate numerical results can be seen in Fig. 4.3, corroborating the qualitative explanation.

4.4 Contact terms VPBB for the box diagrams
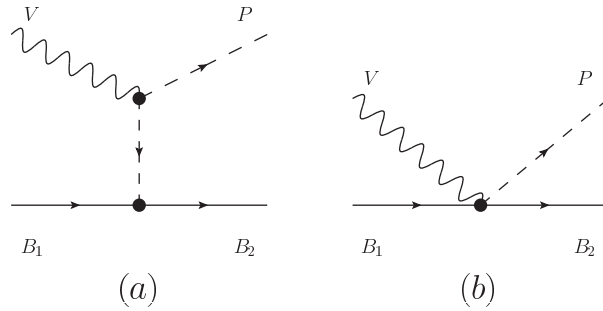

Figure 4.4: Diagram of the $VB \to PB$ vertex: (a) meson exchange (b) contact term.

As we are following the local hidden gauge, there are some other diagrams requested by the gauge invariance of the theory in the presence of baryons. Hence, in addition to the diagram of Fig.4.4 (a), we have to add the diagram

of Fig.4.4 (b). This has been known for long and has been taken into account
in the literature under the denomination of vertex corrections [85, 86, 87, 88,
89, 90, 82]. This diagram of Fig.4.4 (b) corresponds to a contact term of
VPBB and as seen in Ref. [89], the correspondence between the meson in
flight term (Fig.4.4 (a)) and the contact term (Fig.4.4 (b)) is given by:

Meson in flight:

$$
\begin{aligned}
-it_{con} \;=\; & C_V g \vec{\epsilon}\left(\vec{P}_{V_1} + \vec{q} + \vec{q}\right) \frac{1}{(P_{V_1}+q)^2 - m^2} \\
& \{\alpha\,(D+F) + \beta\,(D-F)\} \frac{1}{2f}\vec{\sigma}(\vec{P}_{V_1}+\vec{q}) \qquad (4.30)
\end{aligned}
$$

Contact term:

$$
-it_{con} = C_V g\left\{\alpha\,(D+F) + \beta\,(D-F)\right\} \frac{1}{2f}\vec{\sigma}\vec{\epsilon} \qquad (4.31)
$$

Using this vertex, one has to rewrite Eq. (4.23), to calculate the diagrams of
Fig. 4.5. First of all, we should relabel the momenta of the the box diagram
in a more convenient way,

$$
\begin{aligned}
-it_{Box} \;=\; & \int \frac{d^4q}{(2\pi)^4} igC_{V_1}(-\vec{P}_{V_1} - \vec{q} - \vec{q})\vec{\epsilon}_1\, igC_{V_2}(-\vec{q} - \vec{P}_{V_2} - \vec{q})\vec{\epsilon}_2 \\
& \frac{i}{(P_{V_1}+q)^2 - m_1^2}\frac{i}{q^2 - m^2}\frac{i}{(P_{V_1}-q)^2 - m_3^2} \\
& \frac{i}{(P_{B_1}^0 + P_{V_1}^0 + q^0) - E_{B_1}(\vec{q}) + i\epsilon}\frac{M_{B_1}}{E_{B_1}(q)}\vec{\sigma}(\vec{P}_{V_1}+\vec{q})\vec{\sigma}(-\vec{P}_{V_2}-\vec{q}) \\
& \{\alpha_1(D+F) + \beta_1(D-F)\}\{\alpha_2(D+F) + \beta_2(D-F)\}\frac{1}{4f^2} \\
& \hspace{10cm} (4.32)
\end{aligned}
$$

While the (a) diagram of Fig. 4.5 gives an equal contribution to spin 1/2
and 3/2, the diagrams of Figs. 4.5 (b), (c) and (d) only contribute to spin
1/2. This is because the operator $\vec{\sigma}\vec{\epsilon}$ only couples to spin 1/2. This is done
explicitly in Appendix B, where we show that the matrix element of $\vec{\sigma}\vec{\epsilon}$ is
$\sqrt{3}\,\delta_{J,1/2}$. Intuitively we can see that only J=1/2 is allowed by looking at
the intermediate PB state, necessarily in s-wave because of the $\vec{\sigma}\vec{\epsilon}$ coupling,
hence the total spin J is the spin carried by the nucleon, J=1/2. Using the
vertex of Eq. (4.31) in the expression of the Box given by Eq. (4.32), we can
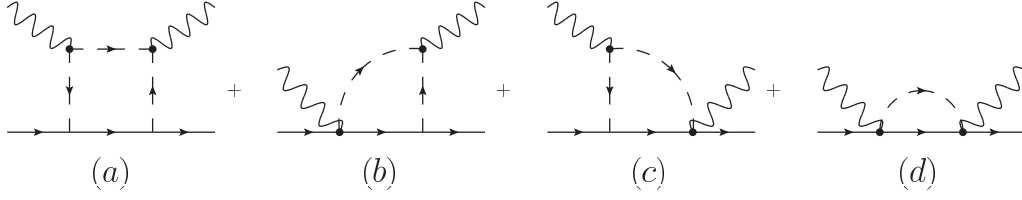
Figure 4.5: Diagrams of the vector-baryon interaction mediated by pseudoscalars channels.

evaluate the diagram (b) of Fig. 4.5, and obtain

$$
\begin{aligned}
-it_{Box}^{CP} =\ & \frac{1}{2f} g C_{V_1} \left\{ \alpha_1 (D+F) + \beta_1 (D-F) \right\} \\
& \frac{1}{2f} g C_{V_2} \left\{ \alpha_2 (D+F) + \beta_2 (D-F) \right\} \\
& \int \frac{d^3 q}{(2\pi)^3} \vec{q}^{\,2} \frac{M_{B_1}}{E_{B_1}(q)} \frac{1}{\omega_2(q)} \frac{1}{\omega_3(q)} \frac{1}{P_{V_2}^0 + \omega_2(q) + \omega_3(q)} \\
& \frac{1}{P_{V_2}^0 - \omega_2(q) - \omega_3(q) + i\epsilon} \frac{1}{P_{B_1}^0 + P_{V_1}^0 - \omega_2(q) - E_{B_1}(q) + i\epsilon} \\
& \frac{1}{P_{B_1}^0 + P_{V_1}^0 - P_{V_2}^0(q) - \omega_3(q) - E_{B_1}(q) + i\epsilon} \left(\frac{\Lambda^2}{\Lambda^2 + \vec{q}^{\,2}} \right)^2 \\
& \left\{ (\omega_2(q) + \omega_3(q))(P_{B_1}^0 - \omega_2(q) - E_{B_1}(q) - \omega_3(q) + P_{V_1}^0) \right. \\
& \left. - \omega_3(q) P_{V_2}^0 \right\}
\end{aligned} \tag{4.33}
$$

In the same way, for the evaluation of the diagram (c) in Fig. 4.5, we substitute the term of the outgoing vector by the contact term. Hence the result

is the same as in Eq. (4.33) changing $\omega_3 \to \omega_1$ and $P_{V_2}^0 \to P_{V_1}^0$, and one gets

$$
\begin{aligned}
-it_{Box}^{PC} =\ & \frac{1}{2f}gC_{V_1}\left\{\alpha_1(D+F)+\beta_1(D-F)\right\} \\
& \frac{1}{2f}gC_{V_2}\left\{\alpha_2(D+F)+\beta_2(D-F)\right\} \\
& \int \frac{d^3q}{(2\pi)^3}\vec{q}^{\,2}\frac{M_{B_1}}{E_{B_1}(q)}\frac{1}{\omega_2(q)}\frac{1}{\omega_1(q)}\frac{1}{P_{V_1}^0+\omega_2(q)+\omega_1(q)} \\
& \frac{1}{P_{V_1}^0-\omega_2(q)-\omega_1(q)+i\epsilon}\frac{1}{P_{B_1}^0+P_{V_2}^0-\omega_2(q)-E_{B_1}(q)+i\epsilon} \\
& \frac{1}{P_{B_1}^0+P_{V_2}^0-P_{V_1}^0-\omega_1(q)-E_{B_1}(q)+i\epsilon}\left(\frac{\Lambda^2}{\Lambda^2+\vec{q}^{\,2}}\right)^2 \\
& \left\{(\omega_2(q)+\omega_1(q))(P_{B_1}^0-\omega_2(q)-E_{B_1}(q)-\omega_1(q)+P_{V_2}^0)\right. \\
& \left.-\omega_1(q)P_{V_1}^0\right\}
\end{aligned}
\tag{4.34}
$$

Finally, the last diagram has two contact terms, as shown in Fig.4.5 (d), and the expression of the t-matrix in this case is given by

$$
\begin{aligned}
-it_{Box}^{CC} =\ & \frac{1}{2f}gC_{V_1}\left\{\alpha_1(D+F)+\beta_1(D-F)\right\} \\
& \frac{1}{2f}gC_{V_2}\left\{\alpha_2(D+F)+\beta_2(D-F)\right\} \\
& 3\int \frac{d^3q}{(2\pi)^3}\frac{M_{B_1}}{E_{B_1}(q)}\frac{1}{2\omega_2(q)} \\
& \frac{1}{P_{B_1}^0+P_{V_1}^0-\omega_2(q)-E_{B_1}(q)+i\epsilon}\left(\frac{\Lambda^2}{\Lambda^2+\vec{q}^{\,2}}\right)^2
\end{aligned}
\tag{4.35}
$$

These diagrams should be included in the potential in order to evaluate the scattering matrix.

$$
\tilde{V} = V + V_{Box} + (V_{Box}^{CP}+V_{Box}^{PC}+V_{Box}^{CC})\delta_{J,1/2}
\tag{4.36}
$$

The presence of the terms V_{Box}^{CP}, V_{Box}^{PC} and V_{Box}^{CC} breaks the degeneracy in total spin J, that one has with the terms V and V_{Box}.

One finds that the contact term, or Kroll-Ruderman in the nomenclature of Ref. [82], is more important than the pseudoscalar exchange, around 1.5-2.5 times bigger depending on the cases, and has opposite sign. In Ref. [82] only this term was used but not the pseudoscalar exchange term. As a consequence, the corrections due to the VB and PB mixing only affect the J=1/2 case in the work of Ref. [82]. As we find here, the corrections from

the mixing due to the pseudoscalar exchange term in J=3/2 are relatively small, justifying its neglect in Ref. [82]. On the other hand for J=1/2, only the contact term is used in Ref. [82] and the destructive interference with the pseudoscalar exchange term is missed. This could justify why the effects due to the mixing in the scattering amplitudes of PB found in Ref. [82] are bigger than those found here for the VB case.

There are other possible couplings in the approach, like the consideration of the tensor coupling for the VBB vertex used in Ref. [81], which was found to have minor effects in the present context in Ref. [91]. Other couplings concerning vectors have also been exploited, like using the anomalous coupling of VVP. This was done in Ref. [27] and found to provide negligible corrections in the problem of $\Delta\rho$ interaction. One exception where this term turned out to be relatively important was in the study of the $\eta'N$ interaction and its mixing with the VB channels. Indeed, the consideration of the anomalous $\eta'K^*\bar{K}^*$ in Ref. [92] was found relatively relevant, but only because the $\eta'PV$ normal coupling of Eq. (4.3) is zero when the η' is considered as a $SU(3)$ singlet in a first approximation.

4.5 Results

The use of the Bethe-Salpeter equation, generates the following scattering matrices for the different states, shown in Figs. 4.6, 4.7, 4.8 and 4.9. We present the results of $|T_{ii}|^2$ as a function of $\sqrt{s}$. We consider interesting the comparison of the scattering matrix obtained using only the potential of the vector interaction, and the new results of the Bethe-Salpeter equation with the combined potential. In all the figures, we present both results, the first one as a dashed line and the last one with a solid line. The most striking feature in all the figures when including the intermediate PB states is, as expected, an increase in the width of the resonances. However, in some cases we also observe a shift of the peak for J=1/2 of some resonances. This is the case for the resonances seen for $J^P = 1/2^-$ in the ρN and $K^*\Lambda$ channels in Fig. 4.6.

In Fig. 4.6 we see two peaks for the state of $S = 0$ and $I = 1/2$, one around 1700 MeV, in channels ρN and $K^*\Lambda$, and another peak near 1980 MeV, which appears in all the channels except for ρN. We can see that the mixing of the PB channels affects differently the two spins, $J^P = 1/2^-$ and $3/2^-$, as a consequence of the extra mechanisms contributing to the $J^P = 1/2^-$ case discussed in the previous section. The effect of the box diagram on the $J^P = 3/2^-$ sector is small, however the PB-VB mixing mechanism are more important in the $J^P = 1/2^-$ sector. The most important feature is a shift
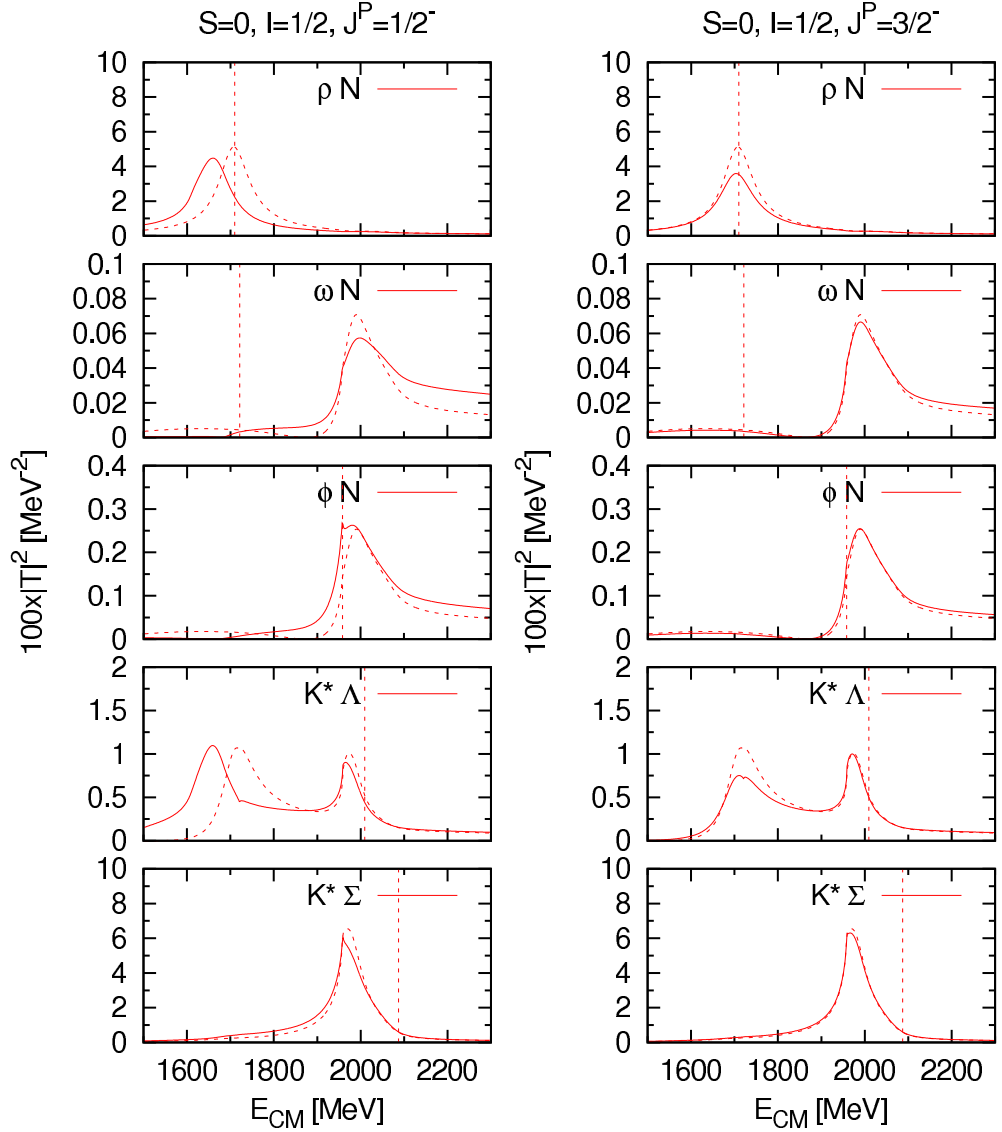
Figure 4.6: $|T|^2$ for the S=0, I=1/2 states. Dashed lines correspond to tree level only and solid lines are calculated including the box diagram potential. Vertical dashed lines indicate the channel threshold.

of the peak around 1700 MeV, which appears now around 1650 MeV. This breaking of the degeneracy is most welcome since this allows us to associate the $1/2^-$ peak found at 1650 MeV with the $N^*(1650)(1/2^-)$ while the peak for $3/2^-$ at 1700 MeV can be naturally associated to the $N^*(1700)(3/2^-)$. We shall discuss the other peak in the next section. Fig. 4.7 shows the results
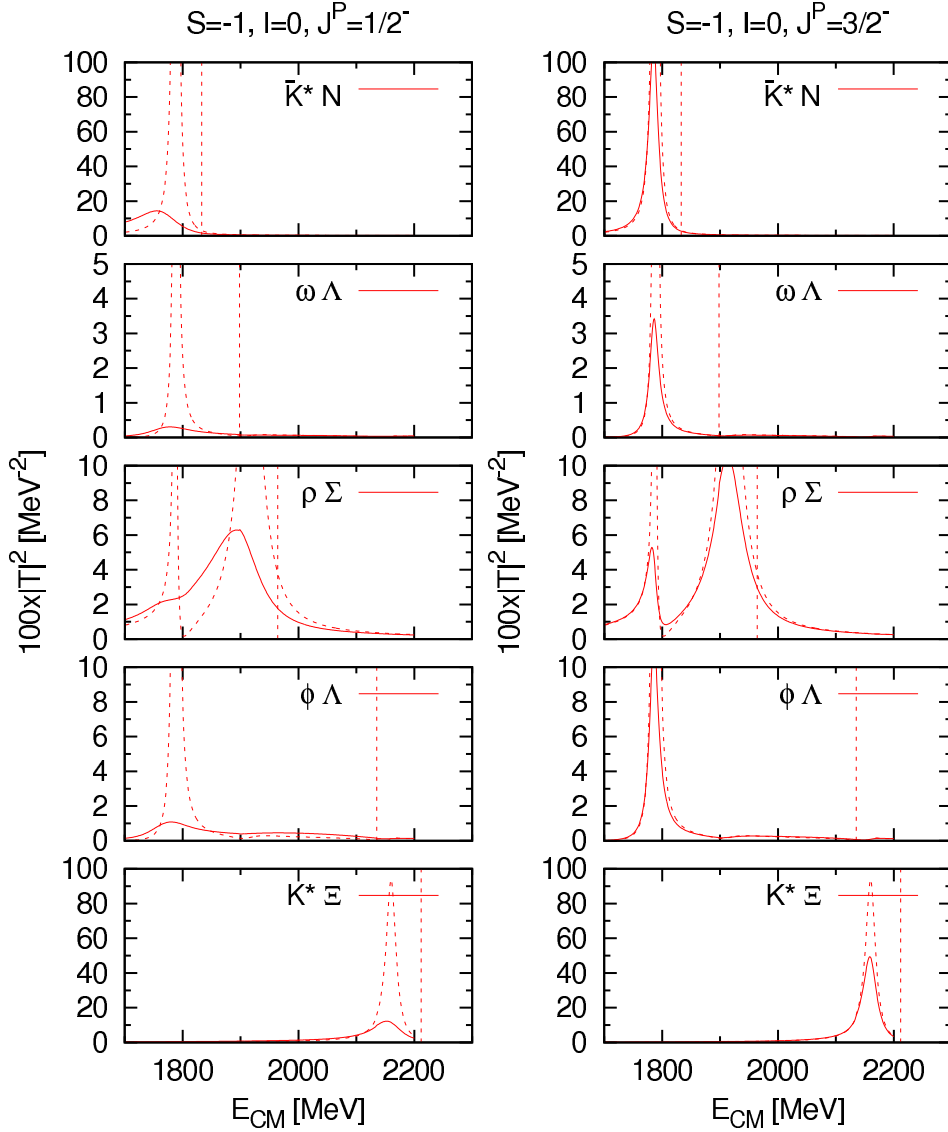
Figure 4.7: $|T|^2$ for the S=-1, I=0 states. Dashed lines correspond to tree level only and solid lines are calculated including the box diagram potential. Vertical dashed lines indicate the channel threshold.

for $S = -1$, with $I = 0$. The left column corresponds to $J^P = 1/2^-$ and the right column to $J^P = 3/2^-$. We can find three peaks for these quantum numbers. The first one around 1780 MeV appears in the channels $\bar{K}^*N$, $\omega\Lambda$, $\rho\Sigma$ and $\phi\Lambda$, but not for the channel $K^*\Xi$. The second peak appears only in the $\rho\Sigma$ channel around 1900 MeV. The third peak is near 2150 MeV, an is

only visible in the $K^*\Xi$ channel. Once again we see the different effects of the PB-VB mixing in $J^P = 1/2^-$ and $3/2^-$. The effects are again small in $J^P = 3/2^-$ but they are sizable for $J^P = 1/2^-$. Indeed, the peak around 1780 MeV is shifted to lower energies and becomes considerably broader. This fact is also most welcome since it provides an explanation on why the width of the $1/2^-$ state is bigger than the corresponding state with $3/2^-$, which is supported by experiment, although the masses of the particles in this high energy region are not well determined. We will come to this issue in the next section. We also observe that the second peak around 1900 MeV is shifted to lower energies and widened for $J^P = 1/2^-$. The third peak is also widened for $1/2^-$ but there is not much change in its position.

Fig. 4.8 contains the results of $|T|^2$ for the quantum numbers S=-1, I=1. The first peak appears in 1830 MeV for the channels $\bar{K}^*N$, $\rho\Lambda$, $\rho\Sigma$, $\omega\Sigma$, $\phi\Sigma$, but not for $K^*\Xi$. With the only consideration of the vector-baryon channel there was a smooth peak around 2000 MeV, visible in the $\rho\Sigma$ and $K^*\Xi$ channels. What we observe here is that the introduction of the pseudoscalar-baryon channels removes the peak in the $\rho\Sigma$ channel and shifts it to a larger energies around 2180 MeV in the $K^*\Xi$ one. Once again we see a stronger widening of the first peak for $J^P = 1/2^-$ and a slight shift to lower energies with respect to the peak for $J^P = 3/2^-$.

In Fig. 4.9 we include the results of S=-2, I=1/2. The results show two peaks very close to each other, one around 2040 MeV and the other one close to 2080 MeV. After the introduction of the PB-VB mixing we observe different features in $J^P = 1/2^-$ and $3/2^-$. Indeed, the two peaks are still visible for $J^P = 3/2^-$ in the $\bar{K}^*\Lambda$ channels, but they separate in the other channels, where only one of them appears in each case. The higher energy resonance shows up in the $\bar{K}^*\Sigma$, $\omega\Xi$ and $\phi\Xi$ channels, and the lower energy resonance shows up only in the $\rho\Xi$ channel. For $J^P = 1/2^-$ the broadening due to the PB-VB mixing removes the two peaks in the $\bar{K}^*\Lambda$ channel and only a broad bump remains, while the two resonances are still visible in the same channels discussed above but the resonances become wider. In the $\bar{K}^*\Sigma$ channel the first peak is also a bit shifted to lower energies.

Using the results of the poles found in this work, we proceed to evaluate the couplings of the different channels to the resonances studied. Those couplings can be found in Tables 4.1 and 4.2, for the resonances found in the scattering matrix. These couplings give us an idea of which are the most important building blocks in each resonance.

Couplings for $J^P = 1/2^-$						
S I						
0 1/2	1690+i24*		1976+i59			
Channels	g_i	$|g_i|$	g_i	$|g_i|$		
ρN	3.1-i1.0	3.2	-0.4-i0.4	0.6		
ωN	0.1-i0.2	0.2	-1.0-i0.4	1.1		
ϕN	-0.1+i0.3	0.3	1.5+i0.4	1.5		
$K^*\Lambda$	1.8-i1.3	2.2	2.1-i1.1	2.4		
$K^*\Sigma$	-0.4-i0.3	0.5	4.0+i0.0	4.0		
S I						
-1 0	1776+i39		1906+i34*		2163+i37	
Channels	g_i	$|g_i|$	g_i	$|g_i|$	g_i	$|g_i|$
$\bar{K}^*N$	3.7-i1.3	4.0	0.1 +i0.3	0.3	0.1 +i0.4	0.4
$\omega\Lambda$	1.5-i0.1	1.5	0.4 +i0.2	0.4	-0.3 -i0.2	0.3
$\rho\Sigma$	-1.3-i0.2	1.3	3.6 -i0.9	3.7	0.0 -i0.1	0.1
$\phi\Lambda$	-2.0-i0.2	2.0	-0.5 -i0.5	0.7	0.4 +i0.2	0.4
$K^*\Xi$	0.2-i0.0	0.2	0.3 +i0.2	0.4	3.4 -i0.5	3.5
S I						
-1 1	1829*		2116*			
Channels	g_i	$|g_i|$	g_i	$|g_i|$		
$\bar{K}^*N$	2.8 +i0.0	2.8	-0.2 +i 0.2	0.3		
$\rho\Lambda$	-2.4 +i0.2	2.4	-0.3 +i 0.4	0.5		
$\rho\Sigma$	-2.2 +i0.1	2.2	2.5 +i 0.0	2.5		
$\omega\Sigma$	-1.3 +i0.1	1.3	-0.2 +i 0.2	0.3		
$K^*\Xi$	0.2 +i0.1	0.2	2.1 -i 0.2	2.1		
$\phi\Sigma$	1.8 -i0.2	1.8	0.2 -i 0.3	0.4		
S I						
-2 1/2	2047+i19*		2084*			
Channels	g_i	$|g_i|$	g_i	$|g_i|$		
$\bar{K}^*\Lambda$	-1.0-i0.2	1.0	-0.1-i0.4	0.5		
$\bar{K}^*\Sigma$	-1.3+i0.2	1.3	2.9+i0.0	2.9		
$\rho\Xi$	2.9-i0.1	2.9	0.0+i0.8	0.8		
$\omega\Xi$	0.4-i0.3	0.5	1.5+i0.3	1.6		
$\phi\Xi$	-0.6+i0.4	0.7	-2.1-i0.4	2.1		

Table 4.1: Couplings constants for the different channels of the resonances found with $J^P = 1/2^-$.

Couplings for $J^P = 3/2^-$						
S I						
0 1/2	1703+i4*		1979 +i56			
Channels	g_i	$|g_i|$	g_i	$|g_i|$		
ρN	2.1-i0.3	2.1	-0.4-i0.5	0.6		
ωN	0.1-i0.1	0.1	-1.1-i0.4	1.2		
ϕN	-0.1+i0.1	0.1	1.5+i0.5	1.6		
$K^*\Lambda$	1.5-i0.3	1.5	2.1-i1.0	2.4		
$K^*\Sigma$	-0.4-i0.0	0.4	4.0+i0.1	4.0		
S I						
-1 0	1786+i11		1916+i13*		2161+i17	
Channels	g_i	$|g_i|$	g_i	$|g_i|$	g_i	$|g_i|$
$\bar{K}^*N$	3.4-i0.3	3.4	0.1 +i0.3	0.4	0.2+i0.3	0.4
$\omega\Lambda$	1.4-i0.0	1.4	0.5 +i0.2	0.5	-0.3-i0.2	0.4
$\rho\Sigma$	-1.3-i0.0	1.3	3.3 -i0.3	3.3	0.0-i0.1	0.1
$\phi\Lambda$	-1.9-i0.0	1.9	-0.7 -i0.3	0.7	0.5+i0.2	0.5
$K^*\Xi$	0.2-i0.0	0.2	0.4 +i0.1	0.4	3.4-i0.5	3.4
S I						
-1 1	1839*		2081*			
Channels	g_i	$|g_i|$	g_i	$|g_i|$		
$\bar{K}^*N$	2.4 +i0.0	2.4	-0.2 -i 0.5	0.5		
$\rho\Lambda$	-2.0 +i0.2	2.0	-0.4 +i 0.7	0.8		
$\rho\Sigma$	-1.9 +i0.1	1.9	3.2 +i 0.0	3.2		
$\omega\Sigma$	-1.1 +i0.1	1.1	-0.2 +i 0.4	0.4		
$K^*\Xi$	0.2 +i0.1	0.2	2.7 -i 0.4	2.7		
$\phi\Sigma$	1.5 -i0.2	1.5	0.3 -i 0.5	0.6		
S I						
-2 1/2	2044+i12*		2082+i5*			
Channels	g_i	$|g_i|$	g_i	$|g_i|$		
$\bar{K}^*\Lambda$	-1.0-i0.2	1.1	-0.3-i0.2	0.4		
$\bar{K}^*\Sigma$	-1.3-i0.1	1.3	1.6-i0.4	1.7		
$\rho\Xi$	2.9-i0.1	2.9	0.5+i0.1	0.6		
$\omega\Xi$	0.4-i0.3	0.5	1.1-i0.1	1.1		
$\phi\Xi$	-0.6+i0.4	0.7	-1.4-i0.2	1.5		

Table 4.2: Couplings constants for the different channels of the resonances found with $J^P = 3/2^-$.
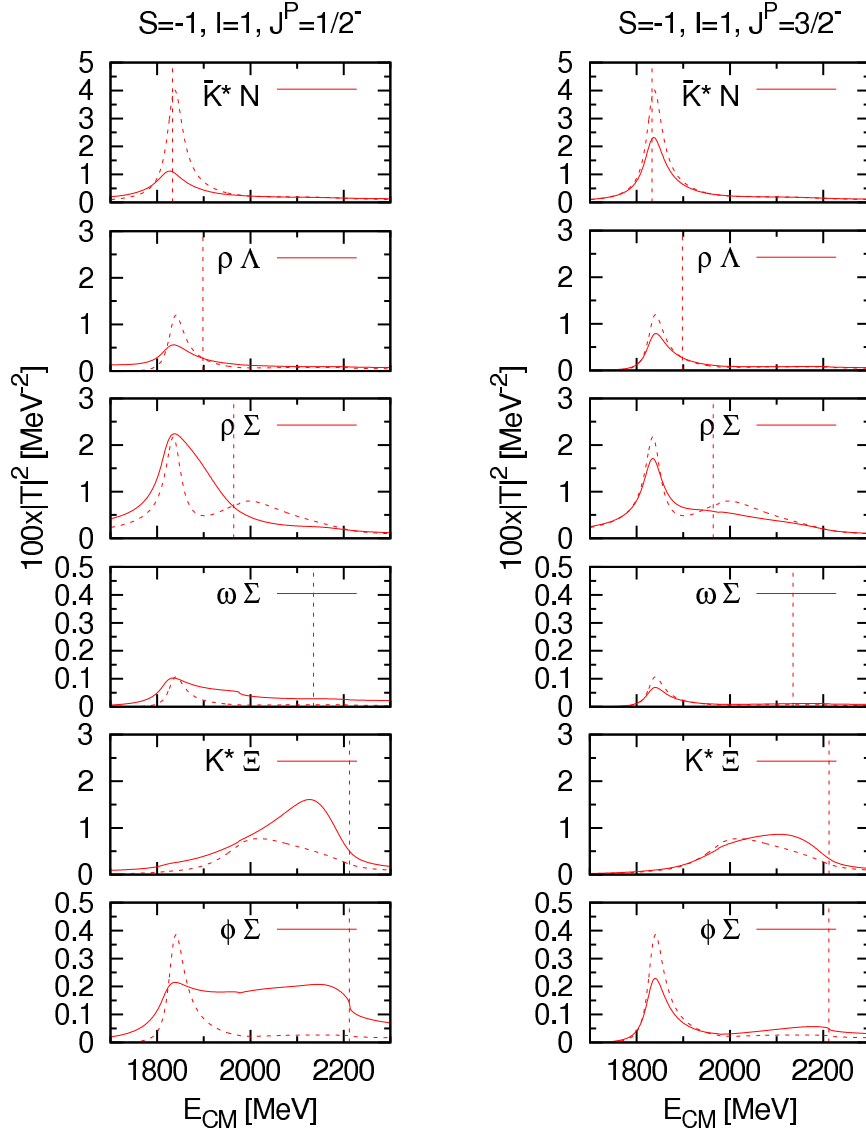
Figure 4.8: $|T|^2$ for the S=-1, I=1 states. Dashed lines correspond to tree level only and solid lines are calculated including the box diagram potential. Vertical dashed lines indicate the channel threshold.

4.6 Comparison to data

In Tables 4.4 and 4.5 we show a summary of the results obtained and the tentative association to known states of the PDG [67]. In Table 4.4 we show the states for $J^P = 1/2^-$ and in Table 4.5 for $J^P = 3/2^-$. For comparison,
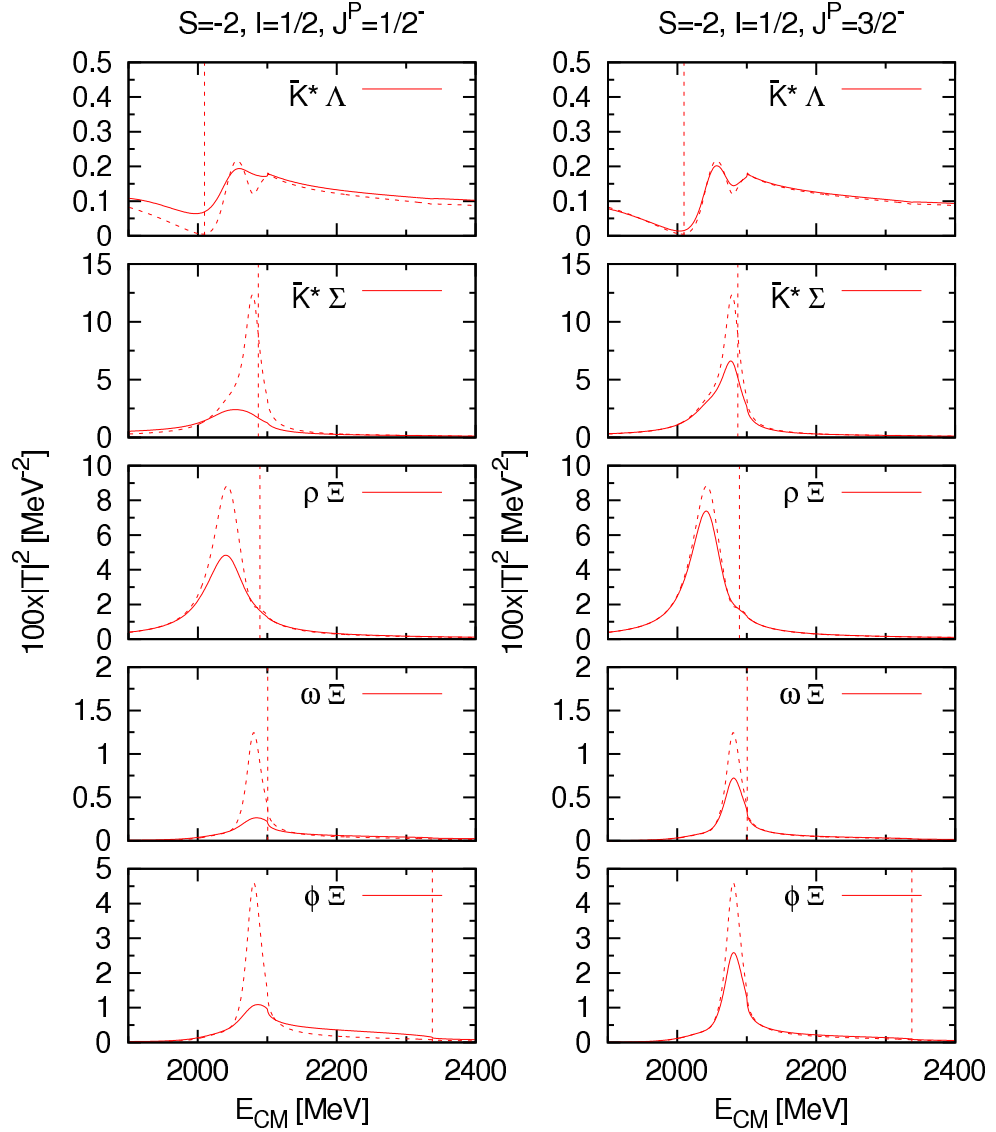
Figure 4.9: $|T|^2$ for the S=-2, I=1/2 states. Dashed lines correspond to tree level only and solid lines are calculated including the box diagram potential. Vertical dashed lines indicate the channel threshold.

the results of Ref. [29] without the mixing are displayed in Table 4.3.

For S=0, I=1/2 we find a state around 1658 MeV with $J^P = 1/2^-$. With fixed ρ mass the peak has a pole associated but with a small imaginary part. Yet, the consideration of the convolution the ρ mass and the pseudoscalar-baryon channels widens the structure considerably becoming an approximate

I, S	Theory			PDG data				
	pole	real axis						
	position	mass	width	name	J^P	status	mass	width
$1/2, 0$	—	1696	92	$N(1650)$	$1/2^-$	$\star\star\star\star$	1645-1670	145-185
				$N(1700)$	$3/2^-$	$\star\star\star$	1650-1750	50-150
	$1977 + i53$	1972	64	$N(2080)$	$3/2^-$	$\star\star$	≈ 2080	180-450
				$N(2090)$	$1/2^-$	$\star$	≈ 2090	100-400
$0, -1$	$1784 + i4$	1783	9	$\Lambda(1690)$	$3/2^-$	$\star\star\star\star$	1685-1695	50-70
				$\Lambda(1800)$	$1/2^-$	$\star\star\star$	1720-1850	200-400
	$1907 + i70$	1900	54	$\Lambda(2000)$	$?^?$	$\star$	≈ 2000	73-240
	$2158 + i13$	2158	23					
$1, -1$	—	1830	42	$\Sigma(1750)$	$1/2^-$	$\star\star\star$	1730-1800	60-160
	—	1987	240	$\Sigma(1940)$	$3/2^-$	$\star\star\star$	1900-1950	150-300
				$\Sigma(2000)$	$1/2^-$	$\star$	≈ 2000	100-450
$1/2, -2$	$2039 + i67$	2039	64	$\Xi(1950)$	$?^?$	$\star\star\star$	1950 ± 15	60 ± 20
	$2083 + i31$	2077	29	$\Xi(2120)$	$?^?$	$\star$	≈ 2120	25

Table 4.3: The properties of the 9 dynamically generated resonances and their possible PDG counterparts.

Breit-Wigner structure with a width of about 98 MeV. This width is compatible with the values of the $N^*(1650)$ $(1/2^-)$ to which the peak obtained would be associated. A similar behavior is seen for $3/2^-$ and we find a state at 1705 MeV which can be associated to the $N^*(1700)$ $(3/2^-)$. In the case of the second peak, the mass found is around 1975 MeV both for $1/2^-$ and $3/2^-$, a bit smaller than the nominal experimental masses of the $N^*(2080)$ $(3/2^-)$ and $N^*(2090)$ $(1/2^-)$ resonances cataloged in the PDG [67]. However, we should note that the masses associated in the PDG are averages done there, but there is a large dispersion of the data for the masses and our calculated results fit well within the experimental masses. The width is also compatible with the experimental results within the large experimental range.

S, I	Theory			PDG data				
	pole position	real axis						
	$M_R + i\Gamma/2$	mass	width	name	J^P	status	mass	width
$0, 1/2$	$1690 + i24^*$	1658	98	$N(1650)$	$1/2^-$	$\star\star\star\star$	1645-1670	145-185
	$1979 + i67$	1973	85	$N(2090)$	$1/2^-$	$\star$	≈ 2090	100-400
$-1, 0$	$1776 + i39$	1747	94	$\Lambda(1800)$	$1/2^-$	$\star\star\star$	1720-1850	200-400
	$1906 + i34^*$	1890	93	$\Lambda(2000)$	$?^?$	$\star$	≈ 2000	73-240
	$2163 + i37$	2149	61					
$-1, 1$	$-$	1829	84	$\Sigma(1750)$	$1/2^-$	$\star\star\star$	1730-1800	60-160
	$-$	2116	200-240	$\Sigma(2000)$	$1/2^-$	$\star$	≈ 2000	100-450
$-2, 1/2$	$2047 + i19^*$	2039	70	$\Xi(1950)$	$?^?$	$\star\star\star$	1950 ± 15	60 ± 20
	$-$	2084	53	$\Xi(2120)$	$?^?$	$\star$	≈ 2120	25

Table 4.4: The properties of the nine dynamically generated resonances and their possible PDG counterparts for $J^P = 1/2^-$. The numbers with asterisk in the imaginary part of the pole position are obtained without the convolution for the vector mass distribution of the ρ and K^*.

In the case of S=-1 and I=0, we found three peaks. A resonance found at 1786 MeV for $3/2^-$ could be associated to $\Lambda(1690)$ with $J^P = 3/2^-$ and the one at 1747 MeV with $1/2^-$ could be associated to the $\Lambda(1800)$ with $J^P = 1/2^-$. Once again, there is a large variation for the masses in the different experiments reported in the PDG under the umbrella of the $\Lambda(1800)$ and the mass that we obtain fits well within these values. For the case of the $\Lambda(1690)$ the dispersion of the masses is much smaller, with the values around 1690 MeV, smaller than our calculated result. The relatively small width of 40 MeV that we obtain is compatible to the experimental widths. For the case of the $\Lambda(1800)$ there is a large variation of the widths, with values as low as 40 or 100 MeV. We also found a state at 1890 MeV for $1/2^-$ and another at 1914 MeV for $3/2^-$ and widths 93 MeV and 59 MeV respectively. They could be associated to the $\Lambda(2000)$ which has an unknown spin in the PDG, but the mass and the width calculated are compatible with this state. A third state is found with a mass around 2150 MeV. More concretely, there is

S, I	Theory			PDG data				
	pole position	real axis						
	$M_R + i\Gamma/2$	mass	width	name	J^P	status	mass	width
$0, 1/2$	$1703 + i4^*$	1705	103	$N(1700)$	$3/2^-$	$\star\star\star$	1650-1750	50-150
	$1979 + i56$	1975	72	$N(2080)$	$3/2^-$	$\star\star$	≈ 2080	180-450
$-1, 0$	$1786 + i11$	1785	19	$\Lambda(1690)$	$3/2^-$	$\star\star\star\star$	1685-1695	50-70
	$1916 + i13^*$	1914	59	$\Lambda(2000)$	$?^?$	$\star$	≈ 2000	73-240
	$2161 + i17$	2158	29					
$-1, 1$	$-$	1839	58	$\Sigma(1940)$	$3/2^-$	$\star\star\star$	1900-1950	150-300
	$-$	2081	270					
$-2, 1/2$	$2044 + i12^*$	2040	53	$\Xi(1950)$	$?^?$	$\star\star\star$	1950 ± 15	60 ± 20
	$2082 + i5^*$	2082	32	$\Xi(2120)$	$?^?$	$\star$	≈ 2120	25

Table 4.5: The properties of the nine dynamically generated resonances and their possible PDG counterparts for $J^P = 3/2^-$. The numbers with asterisk in the imaginary part of the pole position are obtained without the convolution for the vector mass distribution of the ρ and K^*.

the $J^P = 1/2^-$ at 2149 MeV and width 61 MeV and the $J^P = 3/2^-$ partner at 2158 MeV with a smaller width of 29 MeV. We do not find counterparts in the PDG, so these are predictions of the theory.

For S=-1 and I=1, we find two peaks. The first peak for $1/2^-$ with mass 1829 MeV and width 84 MeV can be associated to the $\Sigma(1750)$ $(1/2^-)$ and its partner of $3/2^-$ at 1839 and width 58 MeV can be associated to the $\Sigma(1940)$ $(3/2^-)$. The widths are in good agreement with the experimental results considering the dispersion of data for experiments collected under the same umbrella of this resonance. The second peak has a mass of 2116 MeV and a width of about 200 MeV, and the only state that could correspond to this resonance is $\Sigma(2000)$ $(1/2^-)$ which has an experimental width compatible with that result.

As one can see in Table 4.3, the width provided in Ref. [29] for this state is bigger (240 MeV) than the one reported here. This is a surprise since we should expect an increase of the width from the inclusion of the PB

decay channels. This is the only case where this happens. However, one can understand the reason. In both cases the width is obtained from a visual inspection of $|T|^2$ in the real axis. However, no background determination is done, so this should be taken only as a rough estimate. Indeed, in Fig. 4.8, channel $K^*\Xi$ in left panel, the shape obtained in both cases does not resemble a Breit-Wigner and the association of a width to it has been qualitative. In view of that, we have now put a width of 200-240 MeV which is compatible with the one quoted in Ref. [29] if a similar error band would have been taken in Ref. [29].

Finally, for the case of S=-2 and I=1/2 we found two peaks. For this case it is not clear to which states one can associate them since in this region the states cataloged in the PDG have no determined spin, but the states $\Xi(1950)$ and $\Xi(2120)$ could be associated to those peaks. Both the masses and the widths for both states are compatible with the theoretical results. We should also note that an experimental search devoted to the S=-2 sector is being conducted at Jefferson Lab [93, 94].

4.7   Conclusions

The interaction of vector mesons with the baryon octet using the hidden gauge formalism, produces nine resonances dynamically generated, degenerate in $J^P = 1/2^-$, $3/2^-$, which can be associated to states of the PDG. However the results show that the theoretical widths are significantly smaller than the experimental ones. So, one could think that there is something else involved in the vector meson - baryon octet interaction. Since, pseudoscalar mesons couple both, to vectors and baryons, one can think that it is possible that the interaction is mediated not only by a vector exchange but also by a pseudoscalar exchange.

We found a mechanism, the box diagram involving $V \rightarrow PP$ in two vertices, which is common to $J^P = 1/2^-$ and $3/2^-$ and gives the same contribution in both cases. In addition to this mechanism, there are other ones involving a contact term (vertex correction of the Kroll-Ruderman type) which only contribute for $J^P = 1/2^-$, thus breaking the original degeneracy between these states. The box diagram gives a relatively small contribution, but the terms involving the contact term are more important, producing a widening of the resonance and some times a small shift to smaller energies. In particular we found very rewarding that this splitting leads to a good phenomenological result in the case of the $N^*(1650)(1/2^-)$ and $N^*(1700)(3/2^-)$, which are well reproduced both for the masses and widths. The tendency to have a bigger width in the state of $1/2^-$ than in the partner with $3/2^-$

is also observed in the low lying resonances. For higher mass resonances we noted the difficulty to establish a clean correspondence with particles in the PDG given the large fluctuation of results between different experiments.

The study of the scattering matrix reveals that in fact the widths of the resonances found with this new potential, are bigger than the original ones, and are in a better agreement with the experimental results found in the PDG. Also the couplings are studied, and although the real and imaginary parts are somewhat different from the original ones, the moduli remain very similar for most of the cases.

The formalism done here could be extended to the complementary problem of studying the effect of the vector baryon channels in the resonances which are largely made of pseudoscalar-baryon channels. The interplay of pseudoscalar-baryon, vector-baryon and γ-baryon channels is emerging also as a new experimental line in different reactions, like the photoproduction of $K^*\Lambda$ close to threshold and $K\Lambda$ photoproduction close to the $K^*\Lambda$ threshold [95]. The formalism developed here should be very useful to tackle theoretically these works.

N^* resonances with $J^P = 3/2^-$

5.1 Introduction

The resonance $D_{13}(1520)(3/2^-)$ is catalogued as a four star resonance in the PDG [67]. The $D_{13}(1700)(3/2^-)$ is also catalogued as a three star resonance and has been advocated by many groups, the latest ones [96, 97, 98]. However, the $D_{13}(1700)(3/2^-)$ is not "seen" in the GWU analysis of Ref. [99] nor in former analyses of this group [100]. In a recent unified Chew-Mandelstam SAID analysis of pion photoproduction data the resonance is not needed again [101, 102], and it is also not included in the MAID analysis of photoproduction data [103, 104, 105] where only four star resonances are considered, but it is one of the resonances included in the analysis of the Bonn-Gatchina group [98] and shows more clearly in the analysis of the $(\gamma, \pi^0 \pi^0)$ data in Refs. [106, 107]. One common conclusion from Refs. [96, 106] is the strong coupling of the $D_{13}(1700)(3/2^-)$ state to the $\pi\Delta$ (d-wave) channel, something not intuitive nor expected from ordinary quark models. We should note that, as discussed in Ref. [108] there could be some reason to miss some resonances in the analysis if the resonances are too wide ($\Gamma >$500 MeV) or they posses a small ratio (BR< 4%) to the channel under consideration.

In view of the current discussion about these two resonances, and particularly the doubts casted on the existence of the $D_{13}(1700)(3/2^-)$, we have done a different analysis, purely theoretical, although paying attention to known data on the D_{13} channel. The work consist on taking four coupled channels, also considered in Refs. [96, 100, 99], the ρN (s-wave), πN (d-wave), $\pi\Delta$ (s-wave) and $\pi\Delta$ (d-wave). We look in the region of $\sqrt{s} = 1500 - 1750$ MeV and take the interaction between these channels from the local hidden gauge Lagrangians [30, 13, 31, 40], then solve the Bethe Salpeter equation in coupled channels and from this fully unitary approach we find two res-

onances dynamically generated by the interaction of these channels, which are naturally associated to the $N^*(1520)(3/2^-)$ and $N^*(1700)(3/2^-)$ resonances. The freedom of the theory in the choice of subtraction constants to regularize the loops is used to fit the data on the πN (d-wave) amplitude. The study provides the poles and the residues of the resonances and their coupling to the different channels, widths and partial decay widths. A fair agreement is obtained with phenomenology and the two resonances appear as poles in the complex plane. In particular a relatively strong coupling of the $N^*(1700)(3/2^-)$ to the $\pi\Delta$ (d-wave) suggested in Refs. [96, 106] is confirmed.

The results that we find are also illustrative on why some analyses do not find a compelling need for the $N^*(1700)(3/2^-)$ resonance and we clarify the situation by comparing the amplitudes obtained in this case with the $\pi\pi$ amplitude in the scalar-isoscalar sector, where the $f_0(500)$ and $f_0(980)$ resonances appear. The presence of a first resonance with a width that makes it overlap with a second one with the same quantum numbers has consequences on the second resonance and in the amplitude with these quantum numbers, producing a zero of the πN or $\pi\pi$ amplitudes, respectively, in the vicinity of the second resonance, which makes its coupling to these channels very weak and makes difficult the identification of the $N^*(1700)(3/2^-)$ resonance in the πN channel.

5.2   Formalism

In a nonrelativistic approximation that we follow, Eq. (2.10) provides a vertex

$$-it_{\pi^0 pp} = \frac{F+D}{2f_\pi}\vec{\sigma}\cdot\vec{q} \tag{5.1}$$

where $\vec{q}$ is the incoming momentum of the π^0, and other charge combinations are trivially derived using isospin symmetry. In practice one substitutes $(F+D)/2f_\pi$ by $f_{\pi NN}/m_\pi$ where $f_{\pi NN} = 0.935$, empirically determined. Similarly for the $\pi N\Delta$ transition we take

$$-it_{\pi^+ p\Delta^{++}} = (-)\frac{f_{\pi N\Delta}}{m_\pi}\vec{S}\cdot\vec{q} \tag{5.2}$$

where the minus sign stems from the phase convention $|\pi^+\rangle = -|1,1\rangle$ of isospin, with an empirically value of $f_{\pi N\Delta} = 2.23$. The operator $\vec{S}^+$ is the transition spin operator from spin $1/2$ to $3/2$ normalized such that

$$\langle 3/2M|S_\nu^+|1/2m\rangle = \mathcal{C}(1/2, 1, 3/2; m, \nu, M) \tag{5.3}$$

with S_ν^+ written in spherical basis and $\mathcal{C}(1/2, 1, 3/2; m, \nu, M)$ the Clebsch-Gordan coefficient.

(a) $\rho N(s) \to \rho N(s)$

(b) $\pi\Delta(s) \to \pi\Delta(s)$

(c) $\rho N(s) \to \pi N(d)$

(d) $\rho N(s) \to \pi\Delta(s,d)$

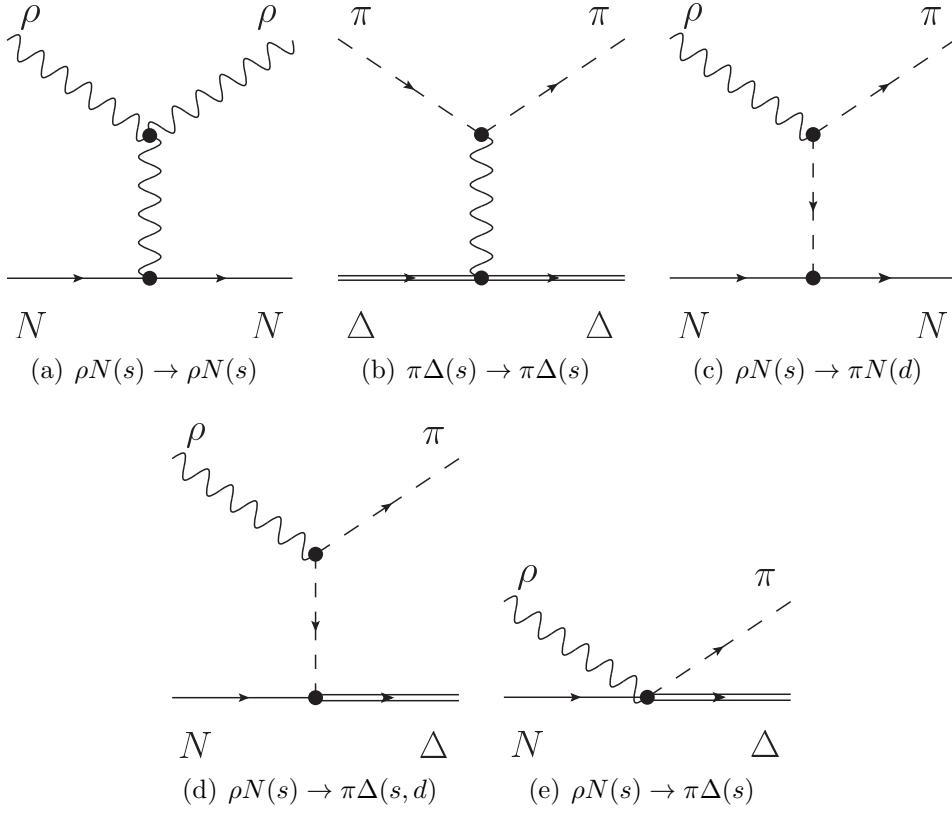(e) $\rho N(s) \to \pi\Delta(s)$

Figure 5.1: Diagrams of the channels involved in the calculation for $N^*(1520)$ and $N^*(1700)$.

5.3 Theoretical Approach

As we have commented in the first section, the channels involved in our study are the ρN (s-wave), πN (d-wave), $\pi\Delta$ (s-wave) and $\pi\Delta$ (d-wave) all of them in isospin $I = 1/2$. In order to develop our calculation, we need the diagrams of the elastic interaction and the transitions diagrams as well. In Fig. 5.1 we show those diagrams. The evaluation of the diagrams shown in Fig. 5.1 leads us to the following vertices for the transitions (See Appendix F for details)

$$t_{\rho N(s) \to \rho N(s)} = -\frac{2}{4f^2}\left(k_\rho^0 + k_\rho'^0\right) \tag{5.4}$$

$$t_{\pi\Delta(s) \to \pi\Delta(s)} = -\frac{5}{4f^2}\left(k_\pi^0 + k_\pi'^0\right) \tag{5.5}$$

$$t_{\rho N(s) \to \pi\Delta(s)} = g\frac{2}{\sqrt{3}}\frac{f_{\pi N\Delta}}{m_\pi}\left\{\frac{\frac{2}{3}\vec{q}^2}{(P_V + q)^2 - m_\pi^2} + 1\right\} \tag{5.6}$$

$$t_{\rho N(s) \to \pi \Delta(d)} = g \frac{2}{\sqrt{3}} \frac{f_{\pi N \Delta}}{m_\pi} \left\{ \frac{\frac{2}{3} \vec{q}^{\,2}}{(P_V + q)^2 - m_\pi^2} \right\} \tag{5.7}$$

$$t_{\rho N(s) \to \pi N(d)} = g(-2\sqrt{6}) \frac{f_{\pi N N}}{m_\pi} \left\{ \frac{\frac{2}{3} \vec{q}^{\,2}}{(P_V + q)^2 - m_\pi^2} \right\} \tag{5.8}$$

where we take $f_{\pi N N} = 0.935$ and $f_{\pi N \Delta} = 2.23$, k_ρ^0 and k_π^0 are the energies of the ρ and the π in the center of mass.

The term of Fig. 5.1(e) is the Kroll-Ruderman term which appears in the $\rho N \to \pi \Delta(s)$ transition. It has the type

$$-it_{KR} = g\sqrt{2} \frac{f_{\pi N \Delta}}{m\pi} \sqrt{\frac{2}{3}} \vec{S}^+ \cdot \vec{\sigma} \tag{5.9}$$

and only involves $L = 0$, providing the term 1 in the bracket of Eq. (5.6).

In order to include the $L = 2$ transitions, we use the same procedure as used in Ref. [109] where the unknown potentials are introduced with a parameter γ and the momenta of the L=2 transition. In our case those channels are $\pi \Delta(d) \to \pi \Delta(d)$, $\pi \Delta(d) \to \pi N(d)$, $\pi N(d) \to \pi N(d)$. With the purpose of working with more suitable parameters γ_{ij}, we normalized them with the pion mass as following.

$$t_{\pi \Delta(d) \to \pi \Delta(d)} = -\frac{\gamma_{33}}{m_\pi^5} q_3^4 \tag{5.10}$$

$$t_{\pi \Delta(d) \to \pi N(d)} = -\frac{\gamma_{34}}{m_\pi^5} q_3^2 q_4^2 \tag{5.11}$$

$$t_{\pi N(d) \to \pi N(d)} = -\frac{\gamma_{44}}{m_\pi^5} q_4^4 \tag{5.12}$$

where q_i are the momenta of each channel. With this notation γ_{ij} have no dimensions and are of the order of 0.01. Note that the L=2 transition leads us to introduce a q^4 term, which at high energies have a very fast grow. To control this divergence we introduce the Blatt-Weisskopf barrier-penetration factors (See Ref. [110]). In the case of $L = 2$, we have a substitution as

$$q^2 \to \frac{x^2}{\sqrt{9 + 3x^2 + x^4}} \tag{5.13}$$

here $x = Rq$ where $R = 0.25$ fm.

We decided to introduce this factor normalized at the energy of 1700 MeV. Let us call $x_{i0} = Rq_{i0}$ with q_{i0} the momentum for a channel i at 1700 MeV. We introduce a factor B_i defined as

$$B_i = \frac{\sqrt{9 + 3x_{i0}^2 + x_{i0}^4}}{\sqrt{9 + 3x_i^2 + x_i^4}} \tag{5.14}$$

So, the potential will be now

$$t_{\pi\Delta(d)\to\pi\Delta(d)} = -\frac{\gamma_{33}}{m_\pi^5}q_3^4 B_3^2 \tag{5.15}$$

$$t_{\pi\Delta(d)\to\pi N(d)} = -\frac{\gamma_{34}}{m_\pi^5}q_3^2 q_4^2 B_3 B_4 \tag{5.16}$$

$$t_{\pi N(d)\to\pi N(d)} = -\frac{\gamma_{44}}{m_\pi^5}q_4^4 B_4^2 \tag{5.17}$$

Using this notation we obtain a more convenient framework for the fit.

5.4 Fitting the data

In order to determine the unknown parameters γ_{ij} we make a fit of the D_{13} partial wave amplitude of πN scattering extracted from experimental data in Ref. [99]. In our case we fit both the real and imaginary parts in an energy range of 1400 to 1800 MeV using the gradient fit method of χ^2. In the fit we have not only the parameters of the transition with L=2, but also the subtraction constants α_i of the loop function. We know that with a regularization scale of $\mu = 630$, the subtraction constant have a natural size of -2 for an s-wave, but as shown in Ref. [109] their fit gives subtraction constants for the d-wave larger than in the case of s-wave amplitudes.

For the analysis of the experimental data we need to normalize the amplitude using Eq. (7) of Ref. [109] which relates our amplitude with the experimental one,

$$\tilde{T}_{ij}(\sqrt{s}) = -\sqrt{\frac{M_i q_i}{4\pi\sqrt{s}}}\sqrt{\frac{M_j q_j}{4\pi\sqrt{s}}}T_{ij}(\sqrt{s}) \tag{5.18}$$

where M and q are the baryon mass an the on-shell momentum of the specific channel.

In Fig. 5.2 we can see the result of the fit, and in Table 5.1 we show the parameters obtained in the fit. For the estimation of the theoretical errors we follow the criteria of Ref. [109] where the authors modify the value of the parameters until the χ^2 increases eight units (which is the procedure to get a 68% confidence level in the case of seven parameters).

In order to give an idea of the quality of the fit and the stability of the results with variations of the parameters we plot in Fig. 5.2 and 5.3 the results obtained increasing or decreasing $\alpha_{\pi\Delta(s)}$ and $\alpha_{\pi N(d)}$, respectively, in $\epsilon(\alpha_{\pi\Delta(s)})$ and $\epsilon(\alpha_{\pi\Delta(s)})$, where ϵ is the error of the parameters that we can see in Table 5.1. As we can see, the fits obtained are still fair.

Figure 5.2: (Solid) Fit to the data of πN (d-wave) of Ref. [99]. (Dashed) Same set of parameters with a variation of $\alpha_{\pi\Delta(s)}$ of its theoretical error.
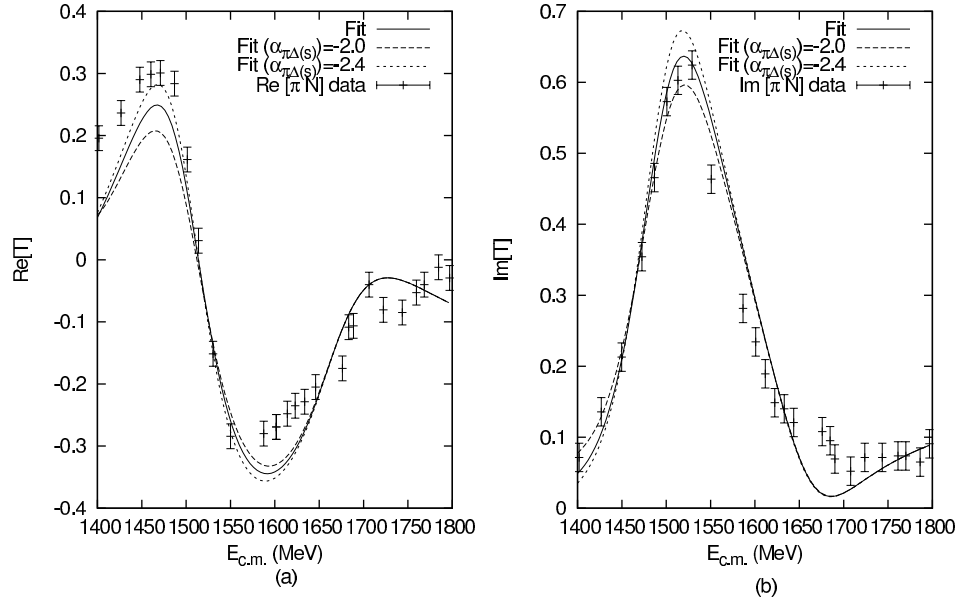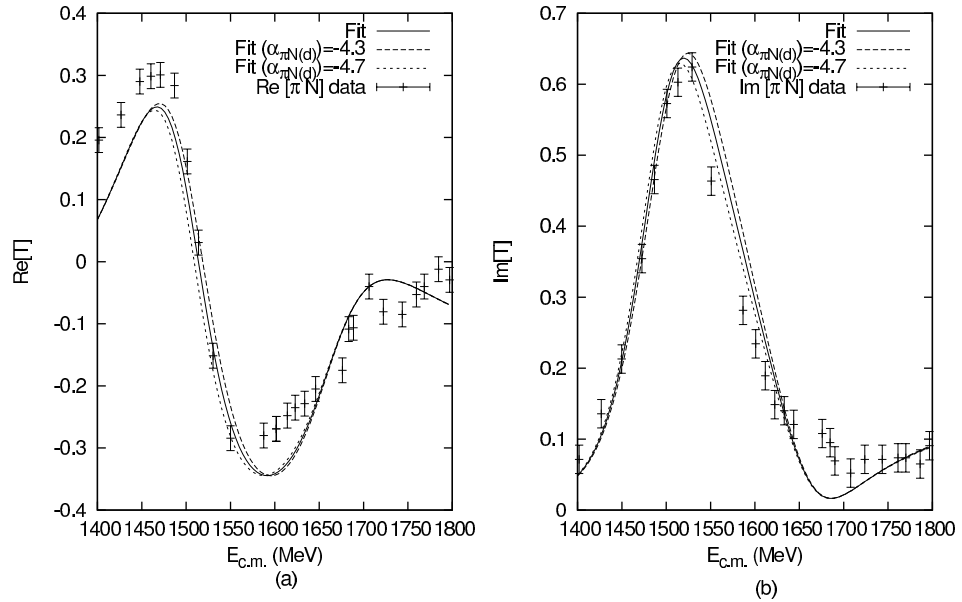

Figure 5.3: (Solid) Fit to the data of πN (d-wave) of Ref. [99]. (Dashed) Same set of parameters with a variation of $\alpha_{\pi N(d)}$ of its theoretical error.

| $\alpha_{\rho N(s)}$	$\alpha_{\pi\Delta(s)}$	$\alpha_{\pi\Delta(d)}$	$\alpha_{\pi N(d)}$	γ_{33}	γ_{34}	γ_{44}
-1.61	-2.2	-4.4	-4.5	0.040	-0.0189	0.0053
0.03	0.2	0.3	0.2	0.002	0.0006	0.0003

Table 5.1: Results of the parameters obtained with the fit. The first row are the parameters and the second row their errors.

5.5 Results

Using the potentials for the transitions shown in the previous section, we construct the scattering t-matrix using the Bethe-Salpeter equation, explained in Eq. (2.46) and the paragraphs that followed. The results for $|T|^2$ are shown in Fig. 5.4 for each diagonal transition. We also include the results of the real and imaginary parts of the t-matrix of the diagonal channels in Fig. 5.5.

  In the analysis of the t-matrix we found two poles that can be associated to the resonances $N^*(1520)$ and $N^*(1700)$ respectively. The poles are found in the second Riemann sheet as explained in section II, and the couplings are obtained through the residues of the poles. These results are compiled in Table 5.2. Using the couplings and Eq. (2.60) one can determine the partial decay widths of the states to each channel. In Table 5.3 we compile the results for the pole positions and the partial decay widths as a function of the α parameters discussed in the former section. As one can see, the results are rather stable. In Tables 5.4 and 5.5 we show these results for the central values, and compare them with the experimental results of the PDG [67]. As the PDG average has big uncertainties, we consider appropriate to include also some single results of the experiments and analysis [96, 111, 112, 107].

   As we can see in Table 5.2, the $N^*(1520)$ couples mostly to the channel ρN, which is closed for the nominal mass of the ρ, but although the mass of the resonance is under the ρN threshold, using Eq. (2.61) we can generate a momentum giving a small partial decay width. In comparison with the experiments, the decay width of ρN to $N^*(1520)$ is smaller but of the same order of magnitude. Note that in experimental analyses one evaluates this rate subtracting the other ones from the total width. In either method the uncertainties for this closed channel are necessarily large. In the case of $N^*(1700)$ the coupling of ρN is smaller but, as we are closer to the threshold, the decay width is of the same order of magnitude as for the $N^*(1520)$. The result for the decay to ρN is in a good agreement with experiment considering the experimental uncertainties.
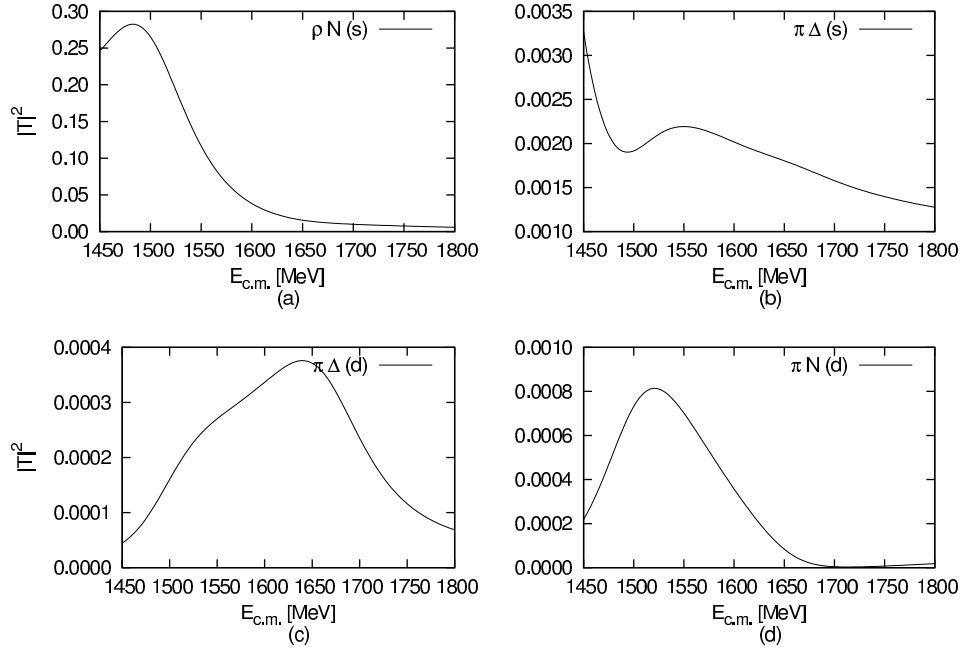
Figure 5.4: Results for the $|T|^2$ matrix of $J^P = 3/2^-$.

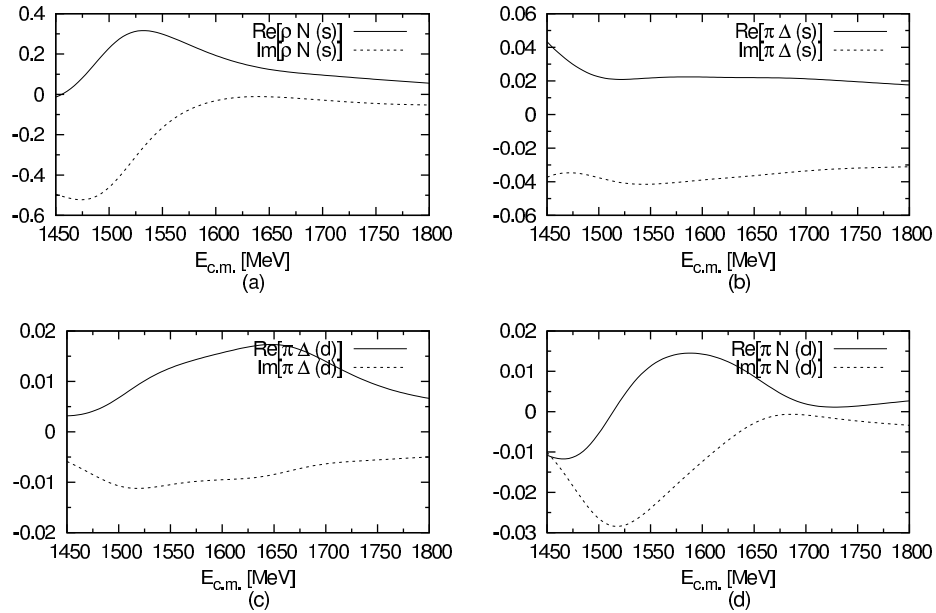
Figure 5.5: Results of real (solid) and imaginary (dashed) parts of T for the diagonal channels.

	$N^*(1520)D_{13}$		$N^*(1700)D_{13}$	
Pole	1467+i83		1665+i78	
Channel	g_i	$|g_i|$	g_i	$|g_i|$
$\rho N(s)$	6.18-1.63i	6.39	1.49+0.42i	1.55
$\pi\Delta(s)$	0.88+0.76i	1.14	-0.39+0.12i	0.41
$\pi\Delta(d)$	-0.75-0.14i	0.77	0.50-0.50i	0.70
$\pi N(d)$	-1.51-0.51i	1.60	-0.09-0.94i	0.94

Table 5.2: Couplings of the resonances for each channel.

The $\pi\Delta$ (s-wave) channel has small couplings for $N^*(1700)$ but, as we are over the threshold, the phase space is big enough to generate a moderate decay width. The results of the branching ratios are in a fair agreement with the experiments within the large uncertainties. For this case the PDG average has a very wide range, but the individual results are more precise. There is a large disagreement with the result of Ref. [98] but it is much closer to the one of Ref. [107] by the same group.

The $\pi\Delta$ (d-wave) channel has the lowest coupling to $N^*(1520)$ but, since it has a large momentum, the partial decay width is bigger than for the ρN channel. The branching ratio for $N^*(1520)$ agrees with experimental results, but in the case of $N^*(1700)$, although the result is compatible with some experimental branching ratios, these results are very different and in some cases have large errors.

Finally, for the channel πN (d-wave), since we fit the amplitude to the data, the result of the branching ratio of $N^*(1520)$ is in a very good agreement with the experimental values. On the other hand, we get a branching ratio of the $N^*(1700)$ for the decay into $\pi\Delta$ (d-wave) which is in line with experimental determinations but about twice as large as the PDG average. Yet, an inspection to Table 5.5 indicates that the dispersion of experimental data for the $N^*(1700)$ is quite large, for what further attention to this resonance should be most welcome.

It is interesting to compare the present results with those of the Jülich group [32, 114]. In those works the authors also consider ρN, πN and $\pi\Delta$ channels, in s or d-waves when allowed for $J^P = 3/2^-, I = 1/2$. The dynamics used in those works in similar to the one used here up to details concerning a contact ρN term, present in Ref. [114] (see Figs. 2 and 3), the

		$N^*(1520)D_{13}$			
$\alpha_{\pi\Delta(s)}$	Pole	$\Gamma_{\rho N(s)}$	$\Gamma_{\pi\Delta(s)}$	$\Gamma_{\pi\Delta(d)}$	$\Gamma_{\pi N(d)}$
-2.0	(1467.76,85.18)	4.96	19.85	7.88	62.90
-2.2	(1467.45,83.06)	5.09	18.37	8.25	65.38
-2.4	(1466.12,77.99)	5.47	14.36	9.09	71.18
$\alpha_{\pi N(d)}$	Pole	$\Gamma_{\rho N(s)}$	$\Gamma_{\pi\Delta(s)}$	$\Gamma_{\pi\Delta(d)}$	$\Gamma_{\pi N(d)}$
-4.3	(1472.40,86.88)	5.58	17.55	7.83	66.68
-4.5	(1467.45,83.06)	5.09	18.37	8.25	65.38
-4.7	(1462.78,79.49)	4.61	19.16	8.63	64.00
		$N^*(1700)D_{13}$			
$\alpha_{\pi\Delta(s)}$	Pole	$\Gamma_{\rho N(s)}$	$\Gamma_{\pi\Delta(s)}$	$\Gamma_{\pi\Delta(d)}$	$\Gamma_{\pi N(d)}$
-2.0	(1665.75,77.69)	7.97	4.79	13.28	28.26
-2.2	(1665.53,77.83)	8.02	4.51	13.36	28.54
-2.4	(1665.00,78.30)	8.06	3.64	13.28	28.78
$\alpha_{\pi N(d)}$	Pole	$\Gamma_{\rho N(s)}$	$\Gamma_{\pi\Delta(s)}$	$\Gamma_{\pi\Delta(d)}$	$\Gamma_{\pi N(d)}$
-4.3	(1663.37,78.19)	8.20	4.78	13.26	30.33
-4.5	(1665.53,77.83)	8.02	4.51	13.36	28.54
-4.7	(1667.52,77.40)	7.85	4.26	13.43	26.88

Table 5.3: Comparison of the pole position and partial decay widths varying the values of $\alpha_{\pi\Delta(s)}$ and $\alpha_{\pi N(d)}$ in their error range.

$N^*(1520)D_{13}$							
		Briet-Wigner		Branching ratio ($\Gamma_i/\Gamma(\%)$)			
	Pole	Mass (MeV)	Γ (MeV)	$\rho N_{(s)}$	$\pi\Delta_{(s)}$	$\pi\Delta_{(d)}$	$\pi N_{(d)}$
This work	(1467,83)			5.09	18.37	8.25	65.38
PDG[67]	(1510,55)	1515-1525	100-125	15-25	10-20	10-15	55-65
Manley92[96]		1524±4	124±8	21±4	5±3	15±4	59±3
Manley12[113]	(1501,56)	1512.6±0.5	117±1	20.9±0.7	9.3±0.7	6.3±0.5	62.7±0.5
Cutkosky79[111]	(1510,57)	1525±15	125±25				58±3
Vrana00[112]	(1504,56)	1518±3	125±4	9±1	15±2	11±2	63±2
Toma08[107]	(1509,57)	1520±10	125±15	13±5	12±4	14±5	58±8
Anisovich12[98]	(1507,56)	1517±3	114±4		19±4	9±2	62±3
Ardnt06[99]	(1515,57)	1514.5±0.2	103.6±0.4				63.2±0.1

Table 5.4: Results of the partial decay widths for the $N^*(1520)$ resonance.

		$N^*(1700)D_{13}$					
		Briet-Wigner		Branching ratio ($\Gamma_i/\Gamma(\%)$)			
	Pole	Mass	Γ	$\rho N_{(s)}$	$\pi\Delta_{(s)}$	$\pi\Delta_{(d)}$	$\pi N_{(d)}$
		(MeV)	(MeV)				
This work	(1665,78)			8.02	4.51	13.36	28.54
PDG [67]	(1700,75)	1650-1750	100-250	<35	10-90	<20	12±5
Manley92 [96]		1737±44	249±218	13±17	5±10	80±19	1±2
Manley12 [113]	(1662,55)	1665±3	56±8	38±6	31±9	3±2	2.8±0.5
Cutkosky79 [111]	(1660,38)	1670±25	80±40				11±5
Vrana00 [112]	(1704,78)	1736±33	175±133	7±1	11±1	79±56	4±1
Toma08 [107]	(1710,78)	1740±20	180±30	20±15	10±5	20±11	8^{+8}_{-4}
Anisovich12 [98]	(1770,210)	1790±40	390±140		72±23	≤10	12±5

Table 5.5: Results of the partial decay widths for the $N^*(1700)$ resonance.

Kroll-Ruderman term for $\rho N \to \pi\Delta(s)$ not considered in Refs. [32, 114] and the use of form factors in those works while we use dimensional regularization. In all cases we adhere to the dynamics of local hidden gauge approach. One novelty in our work is that the $N^*(1520)$ is dynamically generated in our approach, while in Refs. [32, 114] is an input resonance. The $N^*(1520)$ was obtained as a dynamically generated state in Ref. [28] using coupled channels and input from chiral Lagrangians. In the present case we have taken only the main $\pi\Delta(s)$ channel, but it is well known that effects of other channels can be incorporated by small changes in the subtraction constants of dimensional regularization, which in the present problem we have left as free parameters.

The other novelty is the $N^*(1700)$ that we also obtain as dynamically generated with our input. It is interesting to remark that in the work of Refs. [32, 114], with the input of non pole terms there was also a state around 1700 MeV which was dynamically generated and a pole could be seen in the third Riemann sheet defined there. However, when the pole terms were added, the pole in the amplitude faded away in that approach. In our work the pole appears around 1665 MeV together with the one for the $N^*(1520)$. The unitarization of the driving terms in all the channels that we consider, including the transition between all of them, generates in our case the two poles and their interference is responsible for the vanishing amplitude of $\pi N(\mathrm{d})$ around 1700 MeV, which is consistent with the experiment. However, physical traces experimentally identifiable as a peak, remain in the $\pi\Delta(\mathrm{d})$ channel as one can see in Fig.5.4, hence, the more intuitive picture of a peak in a cross section is also seen here but only in the $\pi N(\mathrm{d})$ channel. Actually in Refs. [96, 110], the most characteristic feature attributed to the $N^*(1700)$ was its large coupling to $\pi N(\mathrm{d})$.

We should also mention that there are other works that mix pseudoscalars and vectors [81, 82, 115] and others that also include decuplet of baryons [83], this latter one invoking $SU(6)$ spin-isospin symmetry. In our approach we have followed strictly the local hidden gauge formalism that has proved to be very successful in a variety of processes (see recent review of Ref. [116]).

5.6 Conclusions

We have done a theoretical study for the meson-baryon scattering in the region of $\sqrt{s} = 1400 - 1800$ MeV with $J^P = 3/2^-$. We considered the standard coupled channels used in the most complete experimental analyses, ρN (s-wave), $\pi\Delta$ (s-wave), $\pi\Delta$ (d-wave) and πN (d-wave). The interaction of these channels was taken from the local hidden gauge approach and the loops

were regularized using dimensional regularization with subtraction constant of natural size. These constants were varied within a moderate range to obtain a good fit to the πN (d-wave) data. After this, the rest are predictions of the theory.

The first important theoretical finding is that the model obtained, after fitting exclusively the πN (d-wave) extracted from data, produces two poles: one around 1480 MeV that we associate to the $N^*(1520)(3/2^-)$ and another around 1670 MeV that we associate to the $N^*(1700)(3/2^-)$. It is worth noting that the presence of the two poles is rather solid, since they remain by making changes in the parameters that do not spoil massively the agreement with the πN (d-wave) experimental data. This is an interesting aspect to mention, because, undoubtedly, the analysis of data done in Refs. [99, 100, 101] correlates more experimental information than just this amplitude. Yet, what we are finding is that constrains from unitarity, analyticity and chiral dynamics in coupled channels, together with the information of the πN D_{13} amplitude induced from experiment, had as a consequence the appearance of the two poles.

With the model obtained we determined partial decay widths to all the channels. We found an excellent agreement with experiments for the data on the $N^*(1520)(3/2^-)$ and rough to fair for the $N^*(1700)(3/2^-)$. Yet, we noticed the large dispersions of experimental data for the $N^*(1700)(3/2^-)$. The study done here gives a boost to the existence of the $N^*(1700)$ which has been questioned in some recent experimental analyses. In view of this extra support for the $N^*(1700)$ and the large dispersion of the data, further experimental studies concentrating in this energy region for the quantum numbers $(3/2^-)$ of this resonance should be encouraged.

Chapter 6

N^* resonances with $J^P = 1/2^-$

6.1 Introduction

Partial wave analyses of πN data [99, 101] have provided us with much data
on amplitudes, cross sections and resonance properties. It has also been the
subject of intense theoretical investigations (see Refs. [117, 118] for recent
updates on the subject). The introduction of the chiral unitary techniques
to study these reactions in Ref. [14] resulted in surprising news that the
$N^*(1535)$ resonance was dynamically generated from the interaction of me-
son baryon, with a price to pay: coupled channels had to be introduced.
Some of the channels were closed at certain energies, like the $K\Lambda$ and $K\Sigma$ in
the region of the $N^*(1535)$, but they were shown to play a major role in the
generation of this resonance, to the point of suggesting in Ref. [14] that the
$N^*(1535)$ could qualify as a quasibound state of $K\Lambda$ and $K\Sigma$. Work on this
issue followed in Ref. [119], corroborating the main findings of Ref. [14], and
posteriorly in Refs. [21, 23, 19, 120]. In the chiral unitary approach the loops
of the Bethe-Salpeter equation must be regularized, and this is done with
cut offs or using dimensional regularization. The cut off, or equivalently the
subtraction constants in dimensional regularization in the different channels
should be of "natural size", as discussed in Ref. [18], if one wishes to claim
that the resonances have been generated dynamically from the interaction.
However, this is not the case of the $N^*(1535)$, where different cut offs in
Ref. [14], or different subtraction constants in Ref. [119] for different chan-
nels must be used. This is unlike the case of the $\Lambda(1405)$, where an unique
cut off in all channels leads to a good reproduction of the data [17, 18, 20, 12].
This fact was interpreted in Ref. [120] as a manifestation of the nature of the
two resonances, where the $\Lambda(1405)$ would be largely dynamically generated,
while the $N^*(1535)$ would contain a nonnegligible component of a genuine

state, formed with dynamics different than pseudoscalar meson interaction. One might think of remnants of an original seed of three constituent quarks, but this is not necessarily the case. It could also be due to the missing of important channels different than pseudoscalar-baryon. Actually this has been a source of investigation recently, where the mixing of pseudoscalar-baryon and vector-baryon channels has lead to interesting results and some surprises. In Ref. [121] the vector-baryon interaction was studied using the method developed in Ref. [29] but mixing also pseudoscalar-baryon components. It was found that that the mixing produced a shift of some of the resonance positions of Ref. [29] and produced some increase in the width. Similar results have been obtained recently in Refs. [81, 82, 115]. One of the interesting outcomes of this line of research was to see that the consideration of the πN(d-wave), ρN, $\pi\Delta$(s and d waves) in the sector of spin-parity $3/2^-$ with chiral dynamics led to a good reproduction of the πN data in d-waves and to the generation of the $N^*(1520)$ and $N^*(1700)$ resonances [122]. In the present work we want to extend the results of Ref. [122] to the sector of $1/2^-$, with the aim to see if the mixture of the pseudoscalar-baryon and vector-baryon channels can remove the pathology observed by the need of different subtraction constants in different channels. We will show that this is the case and then we shall be able to conclude that the missing components of the wave function in the $N^*(1535)$ noted in Ref. [120] are due to vector-baryon and additional $\pi\Delta$ states that we shall also mix in the present coupled channel approach.

6.2   Formalism

The most important coupled channels of $N^*(1535)$ and $N^*(1650)$ are πN, ηN, $K\Lambda$, $K\Sigma$, ρN and $\pi\Delta$ (d-wave). Some of the matrix elements of the interaction between these channels have been well studied as the $PB \to PB$ transition mediated by a vector meson exchange addressed in Ref. [119]. The diagram involved in this transition is show in Fig. 2.4 and the potential of this transition is given by

$$V_{ij} = -C_{ij}\,\frac{1}{4f^2}\,\left(k^0 + k'^0\right) \tag{6.1}$$

The PB transition coefficients are taken from Ref. [119]. However, since those coefficients are in charge basis we need to convert them to isospin basis, as show in Table 6.1. Similarly, the $\rho N \to \rho N$ transition has been studied in Chapter 4 and the coefficients are given in Appendix A of Ref. [29].

	πN	ηN	$k\Lambda$	$k\Sigma$
πN	2	0	$\frac{3}{2}$	$-\frac{1}{2}$
ηN		0	$-\frac{3}{2}$	$-\frac{3}{2}$
$K\Lambda$			0	0
$K\Sigma$				2

Table 6.1: Coefficients of PB transition with $I = 1/2$

The transition to $VB \to PB$ is implemented following the formalism described in Chapter 5, where the interaction is mediated by a pseudoscalar meson as shown in Fig. 5.1(c). Furthermore we also include the Kroll-Ruderman term shown in Fig. 5.1(e). The evaluation of the diagrams shown in Fig. 5.1 leads us to the following vertices for the transitions (See Appendix F for details)

$$t_{\rho N(s) \to \pi N(s)} = -2\sqrt{6}g\frac{D+F}{2f}\left\{\frac{\frac{2}{3}\vec{q}^{\,2}_{\pi N}}{(P_V + q_{\pi N})^2 - m_\pi^2} + 1\right\} \tag{6.2}$$

$$t_{\rho N(s) \to \eta N(s)} = 0 \tag{6.3}$$

$$t_{\rho N(s) \to K\Lambda(s)} = -\frac{1}{2}\sqrt{6}g\frac{D+3F}{2f}\left\{\frac{\frac{2}{3}\vec{q}^{\,2}_{K\Lambda}}{(P_V + q_{K\Lambda})^2 - m_K^2} + 1\right\} \tag{6.4}$$

$$t_{\rho N(s) \to K\Sigma(s)} = -\frac{1}{2}\sqrt{6}g\frac{D-F}{2f}\left\{\frac{\frac{2}{3}\vec{q}^{\,2}_{K\Sigma}}{(P_V + q_{K\Sigma})^2 - m_K^2} + 1\right\} \tag{6.5}$$

$$\tag{6.6}$$

where we take $F = 0.51$ and $D = 0.75$, an q_i is the momentum of the pseudoscalar meson in the center of mass. The factor 1 that appears inside the braces corresponds to the Kroll-Ruderman vertex. In comparison with the results of Ref. [123], where the authors only take into account the Kroll-Rudermann term, we obtain the same coefficients for the $PB \to VB$ transition.

Moreover we find interesting to include the contribution to the s-wave from the $s-$ and $u-$channels containing the nucleon propagator, shown in Fig. 6.1, given by

$$t_{\pi N \to N \to \pi N} = (E_\pi)^2 \left(\frac{D+F}{2f}\right)^2 \left(\frac{3}{\sqrt{s}+M_N} - \frac{1}{\sqrt{s}-2E_\pi+M_N}\right) \tag{6.7}$$
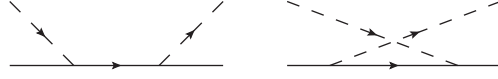
Figure 6.1: Diagrams of $s-$ and $u-$channels exchange with the nucleon propagator.

$$t_{\eta N \to N \to \eta N} = (E_\eta)^2 \left(\frac{1}{\sqrt{3}} \frac{D - 3F}{2f} \right)^2 \left(\frac{1}{\sqrt{s} + M_N} + \frac{1}{\sqrt{s} - 2E_\eta + M_N} \right)$$
(6.8)

This is easily obtained by separating the relativistic nucleon propagator into positive and negative energy components

$$\frac{\slashed{p} + m}{p^2 - m^2} = \frac{M}{E(\vec{p})} \sum_r \left\{ \frac{u_r(\vec{p}) \bar{u}_r(\vec{p})}{p^0 - E(\vec{p}) + i\epsilon} + \frac{v_r(-\vec{p}) \bar{v}_r(-\vec{p})}{p^0 + E(\vec{p}) - i\epsilon} \right\}$$
(6.9)

Then the positive energy part contributes to p-wave and the negative energy part to s-wave. We should note that these terms, as well as a possible isoscalar seagull contribution [124, 125] give a very small contribution.

On the other hand we have the transition of $\rho N \to \pi \Delta(d)$ that has been already studied in Chapter 5. The diagram of this transition is given in Fig. 5.1(d) and the evaluation of this diagram gives the transition of Eq. (5.7) given by

$$t_{\rho N(s) \to \pi \Delta(d)} = g \frac{2}{\sqrt{3}} \frac{f_{\pi N \Delta}}{m_\pi} \left\{ \frac{\frac{2}{3} \vec{q}^2}{(P_V + q)^2 - m_\pi^2} \right\}$$
(6.10)

Here we do not have the 1 factor from the Kroll-Ruderman term since this transition only involves $L = 2$.

As done in Chapter 5 the transitions involving $L = 2$ are introduced with a parameter γ. This is done for the diagonal transition $\pi \Delta(d) \to \pi \Delta(d)$ and for the transition channel that we consider relevant $\pi \Delta(d) \to \pi N(s)$.

$$t_{\pi \Delta(d) \to \pi \Delta(d)} = -\frac{\gamma_0}{m_\pi^5} q_{\pi \Delta}^4$$
(6.11)

$$t_{\pi \Delta(d) \to \pi N(s)} = -\frac{\gamma_1}{m_\pi^3} q_{\pi \Delta}^2$$
(6.12)

The parameters are normalized with the corresponding power of the pion mass to be dimensionless. Both are parametrized, but since the $\pi \Delta(d) \to \pi \Delta(d)$ transition are both d-wave channels, the potential has four momenta while the transition $\pi \Delta(d) \to \pi N(s)$ is a transition from s-wave to d-wave has only two momenta. As done before, the divergence of the momenta is controlled with the Blatt-Weisskopf barrier-penetration factors of Eq. (5.14).

μ[MeV]	$a_{N\pi}$	$a_{N\eta}$	$a_{\Lambda K}$	$a_{\Sigma K}$	$a_{N\rho}$	$a_{\Delta\pi}$	γ_0	γ_1
M_B	-1.203	-2.208	-1.985	-0.528	-0.493	-1.379	0.595	1.47
630	-2.001	-3.006	-3.128	-1.799	-1.291	-2.720	0.595	1.47

Table 6.2: Parameters obtained with the fit. The first row are the parameters with a regularization scale μ that corresponds to the mass of the baryon of each channel. Second row is the same results but with the natural regularization scale $\mu = 630$ MeV. The parameters γ_i are not changed.

6.3 Fitting the data

We have some unknown parameters in our theory that we need to determine fitting the data. First we have the subtraction constant for each channel which, are expected to be around -2 with a regularization scale of $\mu = 630$ MeV. We have also two undetermined parameters in the potential γ_0 and γ_1 corresponding to the transition of $\pi\Delta(d) \rightarrow \pi\Delta(d)$ and $\pi\Delta(d) \rightarrow \pi N$. We perform a fit of the S_{11} partial wave amplitude of the πN scattering data extracted from experimental data of Ref. [126]. We need to normalize the amplitude of the T-matrix using Eq. (7) of Ref. [109], which relates our amplitude with the experimental one by

$$\tilde{T}_{ij}(\sqrt{s}) = -\sqrt{\frac{M_i q_i}{4\pi\sqrt{s}}}\sqrt{\frac{M_j q_j}{4\pi\sqrt{s}}}T_{ij}(\sqrt{s}) \qquad (6.13)$$

where M is the mass of the baryon for the specific channel and q is the on-shell momentum. In Fig. 6.2 we show the fit of both the real and imaginary parts of the $\tilde{T}$ for the diagonal channel of πN.

In Table 6.2 we show the results obtained with the fit. As we commented before, we have used a regularization scale different for each channel, corresponding to the mass of the baryon of that channel. We consider interesting to show also the subtraction constant with a regularization scale of $\mu = 630$ MeV, using Eq. (2.48), in order to compare them with other results found in the bibliography. It is interesting to see that the introduction of the ρN and $\pi\Delta$ channels has had an important qualitative effect in the subtraction constants, which now are all negative and of the same order of magnitude, while in Ref. [119] some of the subtraction constants were even positive.
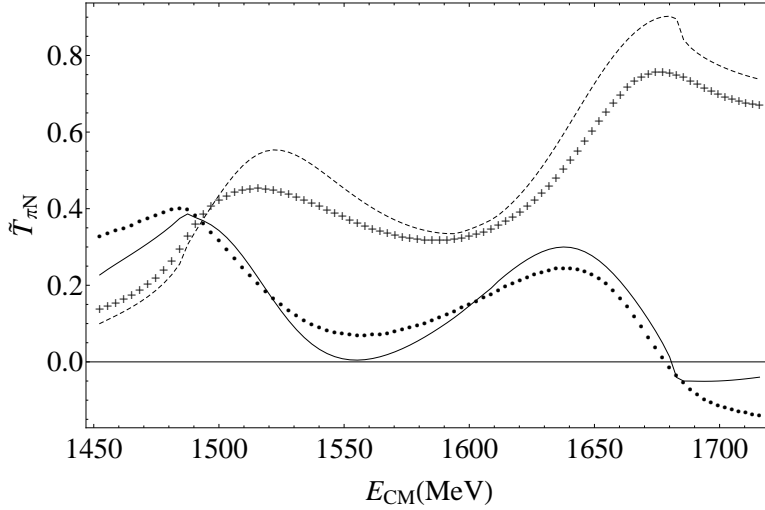
Figure 6.2: Fit to the data extracted from Ref. [126]. We show the real part (circles) and imaginary part (cross) of the data and the result of our fit of $\tilde{T}_{\pi N}$ for real (solid) and imaginary (dashed) parts.

6.4   Results

Using the parameters determined with the fit, we evaluate the T matrix using the Bethe-Salpeter equation and show in Fig. 6.3 the result of $|T|^2$ for all the diagonal channels. Analysing the T matrix, using the method explained in detail in Chapter 2, we found two poles that can be associated to the resonances $N^*(1535)$ and $N^*(1650)$. This is a remarkable novelty, since in Ref. [119] the $N^*(1535)$ appears but not the $N^*(1650)$. The poles are used to calculate the couplings of all channels to each resonances. These results are compiled in Table 6.3. With the couplings one can determine the decay width and branching ratio to each channel of both resonances. The results of the branching ratios for the resonances $N^*(1535)$ and $N^*(1650)$ are shown in Tables 6.4 and 6.5 respectively. In the Tables we show the position of the poles and the branching ratios for each channel found in this work. We compare them with the experimental results of the PDG [67], and as the PDG average has big uncertainties we also compare them with single results of the experiments and analysis [111, 98, 112, 107].

Looking at Table 6.3 we see that the channel the ρN channel has the strongest coupling to $N^*(1535)$ but the resonance is below the threshold, however due to the width of the ρ we can generate enough phase space using Eq. (2.61) and obtain a small width, but in a very good agreement with
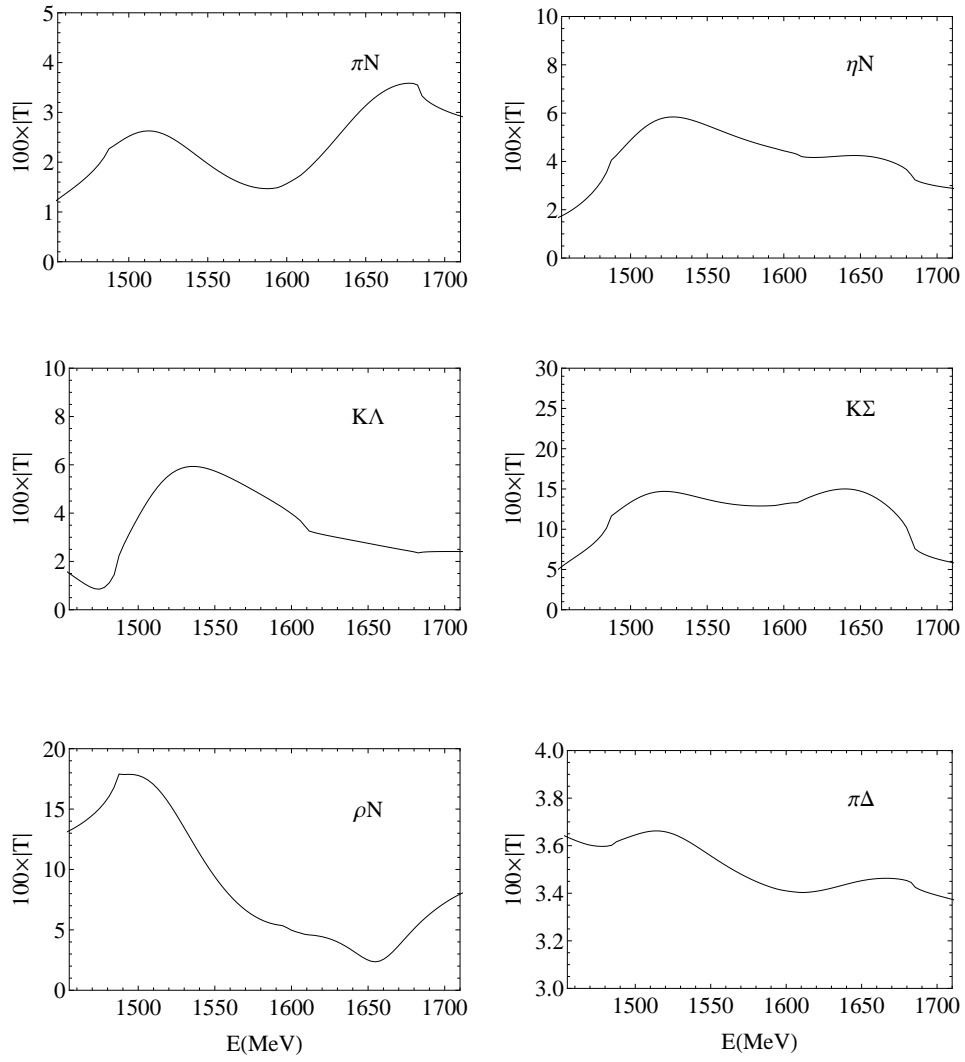
Figure 6.3: Results of the $|T|^2$ matrix for the diagonal channels.

	$N^*(1535)$			$N^*(1650)$		
Channel	g_i	$\|g_i\|$	$g_i G_i$	g_i	$\|g_i\|$	$g_i G_i$
$N\pi$	1.03 +i 0.21	1.05	- 6.68 -i 24.29	1.37 +i 0.54	1.47	2.52 -i 36.51
$N\eta$	1.40 +i 0.78	1.60	-30.50 -i 29.20	1.08 -i 0.60	1.24	-33.89 -i 2.51
ΛK	1.71 +i 0.48	1.78	-38.06 -i 14.50	0.10 -i 0.68	0.69	- 9.96 +i 17.67
ΣK	1.70 +i 1.24	2.10	1.58 -i 2.77	3.21 -i 1.34	3.47	-28.75 -i 13.14
$N\rho$	2.96 +i 0.11	2.96	17.71 -i 2.61	0.94 +i 1.51	1.78	7.83 -i 2.25
$\Delta\pi$	0.31 -i 0.04	0.31	- 8.17 -i 3.20	0.31 +i 0.03	0.31	- 6.03 -i 6.72

Table 6.3: Couplings of the different channels to each resonance

the experimental results. The $K\Sigma$ channel has a coupling as big as the ρN but as the resonance is below the threshold it has not phase space to decay. Similarly the coupling to channel $K\Lambda$ is big but again there is not phase space for decay. On the other hand the $\pi\Delta$ channel has a very small coupling but around 200 MeV of phase space, so this gives it a small branching ratio which agrees with the experimental values. The other channels πN and ηN have smaller couplings but since they have much momentum to decay they have big branching ratios in good agreement with the experimental results. Concerning the width of the $N^*(1535)$ in Table 6.4 we should note that, although the theoretical width obtained from the pole in the complex plane is smaller than the experimental one, the apparent width from $\mathrm{Im}\tilde{T}_{\pi N}$ in the real axis, seen in Fig. 6.2, is much closer to the experiment.

For the case of $N^*(1650)$ the $K\Sigma$ channel has now the biggest coupling to this resonance, but as the resonance is below the threshold it has no phase space for decay. The same as before happens to the ρN channel, the small momentum generated with the mass convolution of the ρ gives a small width but in fair agreement with the experimental value. Although the channels πN, ηN and $\pi\Delta$ have smaller couplings, due to the huge phase space that they have, the branching ratios are quite big, which is in a very good agreement with the experimental results of PDG, but with single experiments as well. Now, the $K\Lambda$ channel is open and the value found for the branching ratio is in good agreement with the only experimental value available of Ref. [98].

We consider interesting to include in Table 6.3 the value of the wave

$N^*(1535)\ J^P = 1/2^-$						
	Theory	PDG	Cutkosky [111]	Anisovich [98]	Vrana [112]	Thoma [107]
Re(Pole)	1508.1	$1490 - 1530$	1510 ± 50	1501 ± 4	1525	$1508 \ ^{+}_{-} \ ^{10}_{30}$
2Im(Pole)	90.3	$90 - 250$	260 ± 80	134 ± 11	102	165 ± 15
Channel	Branching Ratio [$\Gamma_i/\Gamma(\%)$]					
Nπ(1077)	58.6	$35 - 55$	50 ± 10	54 ± 5	$35 \ \pm \ 8$	37 ± 9
Nη(1487)	37.0	42 ± 10		33 ± 5	$51 \ \pm \ 5$	40 ± 10
ΛK(1609)	0.0	-				
ΣK(1683)	0.0	-				
Nρ(1714)	1.0	2 ± 1			$2 \ \pm \ 1$	
$\Delta\pi$(1370)	3.3	$0 - 4$		2.5 ± 1.5	$1 \ \pm \ 1$	23 ± 8

Table 6.4: Results for the pole position and branching ratios for the different channels of $N^*(1535)\ J^P = 1/2^-$ and comparison with experimental results.

function in coordinate space at the origin, defined in Ref. [127] as

$$(2\pi)^{3/2}\,\psi(\vec{0}) = g_i G_i(z_R) \qquad (6.14)$$

where the G function is evaluated in the pole. This magnitude represents the wave function at the origin for s-wave channels. For d-wave channels the wave function goes as r^2 at the origin and vanishes. The magnitude gG then represents the relative strength of the channel for coupling of the resonance to external sources [128]. The results show information about how relevant is each channel for the resonances. The first surprise is to see that, although the $K\Sigma$ channel has the second biggest coupling, the value of the wave function at the origin reveals that this channel is not relevant in the $N^*(1535)$. We also see that the most important channels are the ηN and πN, as one can expect of the experimental results of the branching rations. Moreover the $K\Lambda$ channel has an important contribution but since it is under the threshold this fact is not noticeable experimentally. For the $N^*(1650)$ case the πN channel is now the most important but ηN channel is very important as well. However we can see that now the $K\Sigma$ has a very important contribution since the pole is very close to the $K\Sigma$ threshold. The $K\Lambda$ has a moderate relevance and this is in agreement with the experimental results for the width. The ρN and $\pi\Delta$ channels have a small relative contribution and this is in good agreement with experimental values.

6.5   Conclusions

We have studied the meson-baryon interaction with $J^P = 1/2^-$ including the coupled channels considered in the experimental analysis, πN, ηN, $K\Lambda$, $K\Sigma$, ρN and $\pi\Delta$ (d-wave). We have studied the interaction using the hidden gauge formalism, where the interaction is mediated by the exchange of vector mesons. Other extensions of this formalism involving pseudoscalar and vector mesons are also used as explained in the text. The loops are regularized using dimensional regularization with subtraction constants for each channel. These constants are treated as free parameters and fitted to reproduce the experimental data of the S_{11} πN scattering data extracted from Ref. [126].

Two poles are found and the couplings for each channel, as well as the wave function at the origin, are calculated. These couplings are used to obtain the branching ratios of all channels to both resonances. The results are then compared with several experimental values and there is a good agreement for most of them. It must be noted that the consideration of the ρN and $\pi\Delta$ channels has had an important qualitative change with respect to the work of Ref. [119] where only the pseudoscalar-baryon octet channels

$N^*(1650)\ J^P = 1/2^-$						
	Theory	PDG	Cutkosky [111]	Anisovich [98]	Vrana [112]	Thoma [107]
Re(Pole)	1672.3	$1640 - 1670$	1640 ± 20	1647 ± 6	1663	1645 ± 15
2Im(Pole)	158.2	$100 - 170$	150 ± 30	103 ± 8	240	187 ± 20
Channel	Branching Ratio [$\Gamma_i/\Gamma(\%)$]					
Nπ	58.9	$50 - 90$	65 ± 10	51 ± 4	74 ± 2	70 ± 15
Nη	27.6	$5 - 15$		18 ± 4	6 ± 1	15 ± 6
ΛK	5.7	-		10 ± 5		
ΣK	0.0	-				
Nρ	5.6	1 ± 1			1 ± 1	
$\Delta\pi$	2.2	$0 - 25$		19 ± 9	2 ± 1	10 ± 5

Table 6.5: Results for the pole position and branching ratios for the different channels of $N^*(1650)\ J^P = 1/2^-$ and comparison with experimental results.

were considered. The first one is that now we are able to generate both the $N^*(1535)$ and the $N^*(1650)$ resonances, while in Ref. [119] only the $N^*(1535)$ appeared. The second one is that now the subtraction constants are all negative and of natural size. From the perspective of Ref. [120] we can say that the conclusion in Ref. [120] that the $N^*(1535)$ had an important component of a genuine state in the wave function, can be translated now by stating that the missing components can be filled up by the ρN and $\pi \Delta$ channels that we have found here.

Limits to the Fixed Center Approximation to Faddeev equations: the case of the $\phi(2170)$.

7.1 Introduction

The Faddeev equations to address the interaction of three body systems [129] are very simple conceptually and formally, yet very difficult to solve exactly. Most of the work done with Faddeev equations involve approximations, like the use of separable potentials and energy independent kernels. The Alt-Grassberger-Sandras (AGS) approach [130] follows this line and is widely used. Recently, studies of three hadron systems, two mesons and one baryon [131, 132], or three mesons [133] have been done by means of a different approach to the Faddeev equations which relies upon the on shell two body scattering matrices. The method involves approximations of a different kind, derived from the observation that the ratio of the diagrams involving four and three interactions are similar to the ratios of diagrams with three and two interactions. It was shown in Refs. [131, 132] that the low lying $1/2^+$ excited baryons, except the Roper $N^*(1440)$ which is certainly a very complex object, stemmed from the interaction of two pseudoscalar mesons and one baryon. Similarly, the study of the $\phi K \bar{K}$ system in Ref. [133] showed that the resonance $X(2175)$ was naturally described in terms of those components with the $K\bar{K}$ pair forming mostly an $f_0(980)$ state.

   The discovery of the $X(2175)$ at BABAR [134, 135] with mass $M_X = 2175 \pm 10 \pm 15$ MeV and width $\Gamma_X = 58 \pm 16 \pm 20$ MeV [134] in the $e^+e^- \to \phi(1020)\,f_0(980)$ reaction, was followed by its observation at BES in $J/\Psi \to \eta\,\phi(1020)\,f_0(980)$ decay with $M_X = 2186 \pm 10 \pm 6$ MeV and

$\Gamma_X = 65 \pm 23 \pm 17$ MeV [136]. The Belle Collaboration has performed the most precise measurements up to now of the reactions $e^+e^- \to \phi(1020)\pi^+\pi^-$ and $e^+e^- \to \phi(1020)f_0(980)$ finding $M_X = 2079 \pm 13^{+79}_{-28}$ MeV and $\Gamma_X = 192 \pm 23^{+25}_{-61}$ MeV [137]. The width obtained is larger than in previous measurements but the errors are larger. A combined fit to both BABAR and Belle data on $e^+e^- \to \phi(1020)\pi^+\pi^-$ and $e^+e^- \to \phi(1020)f_0(980)$ has been done in Ref. [138], with the results of $M_X = 2171^{+0.59}_{-0.49}$ MeV and $\Gamma_X = 164^{+69}_{-80}$ MeV. The $X(2175)$ has been renamed in the Particle Data Book (PDG) [67] as the $\phi(2170)$ and we shall use this nomenclature from here on.

The $\phi(2170)$ is one of the states recently found which does not stand a clean comparison with predictions of conventional quark model states [139]. Much theoretical activity has been developed around the $\phi(2170)$ resonance, suggesting it to be a tetraquark [140, 141, 142], or the lightest hybrid $s\bar{s}g$ state [143]. Other works point out at the difficulties encountered trying to interpret the state in terms of already known structures [144, 145, 146].

One appealing idea to interpret this resonance was given in Ref. [133]. The fact that the resonance is seen in its decay into ϕ and $f_0(980)$ suggest that the state could be a strongly bound system of $\phi K\bar{K}$, since in chiral unitary theories the $f_0(980)$ appears as a resonance of the $\pi\pi$ and $K\bar{K}$ channels, mostly the $K\bar{K}$ one [11, 147, 148, 149]. In Ref. [133] the Faddeev equations for the $\phi K\bar{K}$, $\phi\pi\pi$ system were used and the resulting structure was a resonant state of that system with energy and width inside the range given by the experimental ones and where the $K\bar{K}$ pair was strongly correlated around the $f_0(980)$. The Faddeev equations used for this problem relied upon the chiral unitary two body amplitudes evaluated on shell, once it was proved that the unphysical off shell part of the amplitudes cancel exactly with the explicit three body terms provided by the same chiral Lagrangians [131, 132][1].

In view of the technical difficulties to solve the full Faddeev equations one might resort to use a different approximation to these equations, and one of them which is technically very easy is the Fixed Center Approximation (FCA). The basic idea is that one has collisions of one particle against a bound cluster of two other particles, which is not much altered by the interaction with the third particle. The FCA has been used in many problems [150, 151, 152, 153, 154, 155, 156, 157, 158, 159] and is accepted as an accurate tool in the study of bound systems, when the particle interacting with the cluster is lighter than the others and the cluster is relatively strongly bound. Yet, in some cases where the interacting particle is heavier than the

---

[1]This holds in the SU(3) limit. In Ref. [131] it was mentioned that it holds for low momentum transfers, but in Ref. [132] it was shown that actually this condition is unnecessary.

constituents of the cluster one can still get a qualitative picture from the FCA. This is indeed the case for the $NK\bar{K}$ bound system, with the $K\bar{K}$ making the cluster, which was studied in Ref. [160] and results in qualitative agreement with those of Faddeev equations of Ref. [161] were found. Thus, there is no universal rule and for this purpose it is worth to study other systems and other conditions to better understand the limits of the FCA.

More recently, FCA has been also used to study the interaction of systems with several ρ mesons [162] or of one K^* and several ρ mesons [163], and in the study of the $K\bar{K}N$ [160], the $\bar{K}NN$ [164] and the $\pi\rho\Delta$ systems [165], where the last two particles make the cluster. In the case of the $K\bar{K}N$ state one is fortunate to be able to compare with the full Faddeev results of Ref. [161, 166], as well as with the variational calculations of Ref. [167], and the results of the FCA prove to be rather accurate. Similarly the $\bar{K}NN$ system has been studied with the FCA and chiral dynamics and the results are remarkably similar to those obtained in Ref. [168] with a variational calculation, or those of Ref. [169] with Faddeev equations when a kernel incorporating the energy dependence of chiral dynamics is used. In view of this success, it is also important to recall the limits to its application and we do this in the present paper by choosing a particular case, the $\phi K\bar{K}$ system, for which results with the full Faddeev equations are available from Ref. [133].

Recently, a different technical approach has been proposed in Ref. [170] to study the $\phi K\bar{K}$ system, leading to the $\phi(2170)$, and further work along these lines has been done in Ref. [171], hinting at a possible resonant state of the $\phi a_0(980)$, for which no trace was found using the Faddeev equations in Ref. [133]. We shall discuss this work here and the problems encountered in that approach.

7.2 Fixed center approximation formalism to the $\phi f_0(980)$ scattering

By analogy to Refs. [150, 151, 152, 153] we shall study the scattering of a ϕ with a molecular state of $K\bar{K}$. The ϕ scatters and rescatters with the K, $\bar{K}$ of the $f_0(980)$ molecule and the K, $\bar{K}$ states are kept unchanged in their wave function of the bound state. Diagrammatically we have the series of terms depicted in Fig. 7.1. Symbolically these terms can be summed by means of two partition functions T_1 (for ϕK) and T_2 (for $\phi\bar{K}$), where T_1 sums all the diagrams where the ϕ interacts first with the K and T_2 those where the ϕ
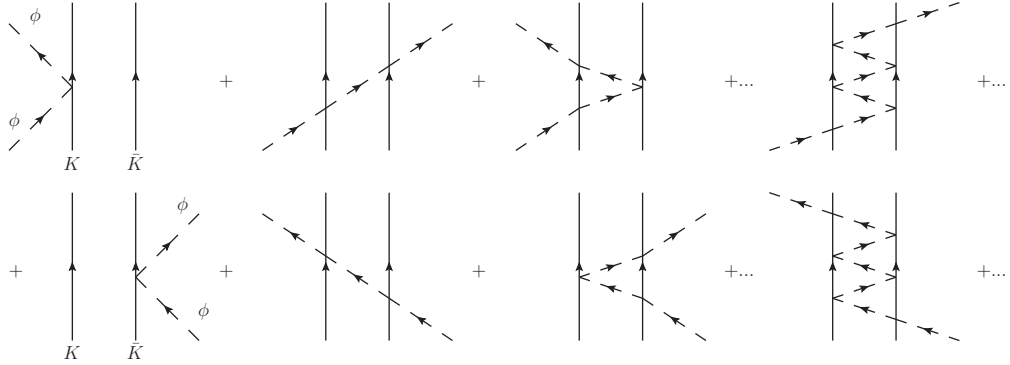
Figure 7.1: Diagrammatic representation of the fixed center approximation to the Faddeev equations.

interacts first with the $\bar{K}$. The FCA equations are

$$
\begin{aligned}
T_1 &= t_1 + t_1 G T_2 \\
T_2 &= t_2 + t_2 G T_1 \\
T &= T_1 + T_2
\end{aligned}
\tag{7.1}
$$

where T is the total $\phi f_0(980)$ T-matrix, G is the propagator for the ϕ between the K, $\bar{K}$ components of the f_0 (see Eq. (7.14) later on) and t_1, t_2 stand for the ϕK and $\phi \bar{K}$ two body t-matrices. In order to see the precise meaning and normalizations entering Eq. (7.1) we follow closely the approach of Ref. [162]. The formalism is easier here since ϕK and $\phi \bar{K}$ have the same amplitude and there is only one isospin state $I = 1/2$. We follow Eqs. (19) to (39) of Ref. [162] substituting the $f_2(\rho\rho)$ by the $f_0(980)(K\bar{K})$ and the external ρ^+ by the ϕ (see also the approach for the K^* multirho states in Ref. [163]). The S matrix for single scattering, first diagram of Fig. 7.1, is given by

$$
\begin{aligned}
S^{(1)} &= -i t_1 F_{f_0}\left(\frac{\vec{k} - \vec{k}'}{2}\right) \frac{1}{\mathcal{V}^2} \frac{1}{\sqrt{2\omega_{p_1}}} \frac{1}{\sqrt{2\omega_{p_1'}}} \frac{1}{\sqrt{2\omega_k}} \frac{1}{\sqrt{2\omega_{k'}}} \\
&\quad (2\pi)^4 \delta(k + K_{f_0} - k' - K'_{f_0}),
\end{aligned}
\tag{7.2}
$$

where $\mathcal{V}$ stands for the volume of a box where we normalize to unity our plane wave states, ω_{p_1}, $\omega_{p_1'}$, are the energies of the initial and final kaon of the f_0 and ω_k, $\omega_{k'}$ the initial and final energy of the ϕ. The symbols k, k', K_{f_0}, K'_{f_0} stand for the four momenta of the initial, final ϕ and initial, final f_0. In Eq. (7.2), $F_{f_0}\left(\frac{\vec{k}-\vec{k}'}{2}\right)$ is the form factor of the $f_0(980)$ as a bound state of $K\bar{K}$.

The double scattering term of Fig. 7.1 gives rise to an S matrix

$$
\begin{aligned}
S^{(2)} &= -i(2\pi)^4\delta(k + K_{f_0} - k' - K'_{f_0})\frac{1}{\mathcal{V}^2}\frac{1}{\sqrt{2\omega_k}}\frac{1}{\sqrt{2\omega_{k'}}}\frac{1}{\sqrt{2\omega_{p_1}}}\frac{1}{\sqrt{2\omega_{p'_1}}} \\
&\quad \times \frac{1}{\sqrt{2\omega_{p_2}}}\frac{1}{\sqrt{2\omega_{p'_2}}}\int\frac{d^3q}{(2\pi)^3}F_{f_0}\left(\vec{q} - \frac{\vec{k} + \vec{k}'}{2}\right)\frac{1}{q^{02} - \vec{q}^{\,2} - m_\phi^2 + i\epsilon}t_1t_2.
\end{aligned}
\tag{7.3}
$$

where $q^0 = (s + m_\phi^2 - M_{f_0}^2)/(2\sqrt{s})$ is the ϕ energy in the ϕf_0 center of mass frame, and ω_{p_2}, $\omega_{p'_2}$, are the energies of the initial and final antikaon.

For scattering at low energies $\vec{k}$, $\vec{k}'$ will be zero and the form factor in the single scattering can be ignored, while the one entering Eq. (7.3) can be replaced by $F_{f_0}(q)$. The evaluation of this form factor is rendered very easy, and practical for the developments that follow, by using the approach of Ref. [127] where a potential in S-wave of the type

$$
V = v\theta(\Lambda - q)\theta(\Lambda - q')
\tag{7.4}
$$

is used in momentum space to obtain a certain bound state (the f_0 for instance). In Eq. (7.4) v is a momentum independent function (although it can depend on the energy), and Λ a cut off in the modulus of the momenta q, q'. Following Ref. [11] we take 1 GeV for it. As shown in Ref. [127], the Quantum Mechanical problem with this potential leads to the same scattering matrix obtained in the chiral unitary approach using the on shell factorization [11, 17, 18][2].

By following Ref. [127] we find the relative wave function of $K\bar{K}$ in momentum space

$$
\langle\vec{p}|\psi\rangle = v\frac{\theta(\Lambda - p)}{E - \omega_K(\vec{p}_1) - \omega_K(\vec{p}_2)}\int_{k<\Lambda}d^3k\langle\vec{k}|\psi\rangle,
\tag{7.5}
$$

which is given in coordinate space by

$$
\langle\vec{x}|\psi\rangle = \int\frac{d^3p}{(2\pi)^{3/2}}e^{i\vec{p}\vec{x}}\langle\vec{p}|\psi\rangle.
\tag{7.6}
$$

The form factor of the bound $K\bar{K}$ state is then given by

$$
F_{f_0}(q) = \frac{1}{\mathcal{N}}\int_{\substack{p<\Lambda \\ |\vec{p}-\vec{q}|<\Lambda}}d^3p\frac{1}{M_{f_0} - 2\omega_K(\vec{p})}\frac{1}{M_{f_0} - 2\omega_K(\vec{p} - \vec{q})},
\tag{7.7}
$$

---

[2]In Ref. [127] a non relativistic Quantum Mechanical formulation is done but its relativistic extension with the same kernel of Eq. (7.4) to match the field theoretical treatment of the chiral unitary approach is straightforward.

where the normalization factor $\mathcal{N}$ is

$$\mathcal{N} = \int_{p<\Lambda} d^3p \frac{1}{(M_{f_0} - 2\omega_K(\vec{p}))^2}.\tag{7.8}$$

We will have to face a small technical detail since the field normalization factors in Eqs. (7.2) and (7.3), $(2\omega_i)^{-1/2}$, are different, and also different than those appearing in the ϕf_0 scattering problem in the Mandl and Shaw normalization that we follow [68], which are

$$S = -iT_{\phi f_0}(s)\frac{1}{\mathcal{V}^2}\frac{1}{\sqrt{2\omega_k}}\frac{1}{\sqrt{2\omega_{k'}}}\frac{1}{\sqrt{2\omega_{f_0}}}\frac{1}{\sqrt{2\omega_{f_0'}}}(2\pi)^4\,\delta(k + K_{f_0} - k'^0 - K'_{f_0})\tag{7.9}$$

Taking this into account, Eqs. (7.1) can be reformulated, in the absence of the form factor in the single scattering, as

$$T^{(K)}(s) = \frac{M_{f_0}}{m_K}t_{\phi K}(s') + \frac{M_{f_0}}{m_K}t_{\phi K}(s')\tilde{G}_0 T^{(\bar{K})}$$

$$T^{(\bar{K})}(s) = \frac{M_{f_0}}{m_K}t_{\phi\bar{K}}(s') + \frac{M_{f_0}}{m_K}t_{\phi\bar{K}}(s')\tilde{G}_0 T^{(K)}\tag{7.10}$$

$$T_{\phi f_0} = T^{(K)} + T^{(\bar{K})},\quad T^{(K)} = T^{(\bar{K})}\tag{7.11}$$

such that

$$T_{\phi f_0} = 2\frac{M_{f_0}}{m_K}t_{\phi K}(s')\frac{1}{1 - \frac{M_{f_0}}{m_K}t_{\phi K}(s')\tilde{G}_0}\tag{7.12}$$

Technically, one should have the ratio of energies instead of that of the masses in Eqs. (7.10), but the ratios are nearly the same and we keep this form, as in Ref. [162], for the FCA equations.

In the case of the form factor in the single scattering term (the form factor is always present in the rescattering terms in $\tilde{G}_0$) we find

$$T_{\phi f_0} = 2\frac{M_{f_0}}{m_K}t_{\phi K}(s')\left[F_{f_0}\left(\frac{\vec{k} - \vec{k}'}{2}\right) - 1 + \frac{1}{1 - \frac{M_{f_0}}{m_K}t_{\phi K}(s')\tilde{G}_0}\right]\tag{7.13}$$

with

$$\tilde{G}_0 \equiv \frac{1}{2M_{f_0}}\int\frac{d^3q}{(2\pi)^3}F_{f_0}\left(\vec{q} - \frac{\vec{k} + \vec{k}'}{2}\right)\frac{1}{q^{02} - \vec{q}^2 - m_\phi^2 + i\epsilon}.\tag{7.14}$$

and

$$s' = s'_{\phi K} = (k + p_1)$$
$$= (k + p_1 + p_2 - p_2)^2 = s + m_K^2 - 2\sqrt{s}p_2^0$$
$$= m_\phi^2 + m_K^2 + \frac{1}{2}(s - m_\phi^2 - m_{f_0}^2)\tag{7.15}$$

in the ϕf_0 center of mass frame where $s = (k + p_1 + p_2)^2$, $p_2^0 = E_{f_0}^{CM}/2$.

7.3   Field theoretical calculation

In order to make a connection with Refs. [170, 171], let us follow their approach and evaluate the diagram of Fig. 7.2.
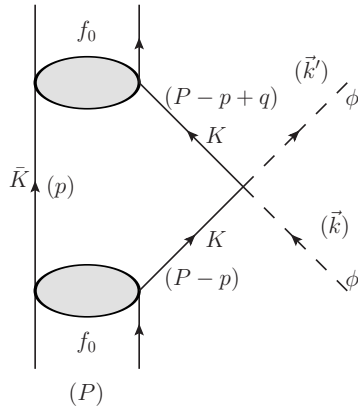

Figure 7.2: Loop diagram considered to evaluate the amplitude in Refs. [170, 171].

To facilitate comparison with the results obtained in Ref. [127] we use non relativistic propagators for the particles. The extension of both formalism to the relativistic case is straightforward but unnecessary for the result that we shall obtain. The amplitude stemming from the diagram of Fig. 7.2 is

$$-iT^{(FT)} = (-ig)^2 \int \frac{d^4p}{(2\pi)}(-i\tilde{t}_{\phi K})\frac{i}{p^0 - \omega_{\bar{K}}(\vec{p}) + i\epsilon}\frac{i}{P^0 - p^0 - \omega_K(\vec{p}) + i\epsilon}$$
$$\times \frac{i}{P^0 - p^0 + q^0 - \omega_K(\vec{P} - \vec{p} + \vec{q}) + i\epsilon} \quad (7.16)$$

conveniently regularized, for instance with a cut off, where $q = k - k'$ and g is the coupling of the state f_0 to the $K\bar{K}$ channel (g^2 is the residue of the $K\bar{K} \to K\bar{K}$ amplitude at the pole of the f_0 resonance, see Ref. [127] for details). The amplitude $\tilde{t}_{\phi K}$ in Eq. (7.16) has a different normalization than the $t_{\phi K}$ used in the rest of the paper to connect with the formalism of Ref. [162]. If we take $\vec{P} = 0$ (the f_0 momentum) and $\vec{q} = 0$, the former

equation can be written as

$$T^{(FT)} = -ig^2 \tilde{t}_{\phi K} \frac{\partial}{\partial P^0} \int \frac{d^4 p}{(2\pi)} \frac{1}{p^0 - \omega_{\bar{K}}(\vec{p}) + i\epsilon} \frac{1}{P^0 - p^0 - \omega_K(\vec{p}) + i\epsilon}$$

$$= -g^2 \tilde{t}_{\phi K} \frac{\partial}{\partial P^0} G(P^0, K\bar{K}) \tag{7.17}$$

where G is the $K\bar{K}$ propagator or the loop function for $K\bar{K}$ intermediate states. By using the result of Ref. [127], assuming V of Eq. (7.4) independent of energy (see Eq. (41) of that work, $P^0 \equiv E$)

$$g^2 = -\left(\frac{dG(E)}{dE} \right)^{-1}_{E=E_{f_0}} \tag{7.18}$$

we obtain the remarkable result for $\vec{q} = 0$

$$T^{(FT)} = \tilde{t}_{\phi K} \tag{7.19}$$

which is nothing but the expression of the impulse approximation. The loop of Fig. 7.2 in field theory implements the impulse approximation used in more conventional approaches.

There is still more to it. Let us perform the p^0 integration in the center of mass frame of ϕf_0. We have

$$T^{(FT)} = \tilde{t}_{\phi K} g^2 \int d^3 p \frac{1}{P^0 - \omega_{\bar{K}}(\vec{p}) - \omega_K(\vec{P} - \vec{p}) + i\epsilon}$$

$$\frac{1}{P^0 - \omega_{\bar{K}}(\vec{p}) - \omega_K(\vec{P} - \vec{p} + \vec{q}) + i\epsilon} \tag{7.20}$$

where g^2, according to Eq. (7.18), is the inverse of the $\int d^3 p$ integral of Eq. (7.20) for $\vec{q} = 0$. Eq. (7.20) resembles much Eq. (7.7) that provides the form factor of the f_0. One can prove that this corresponds to Eq. (7.7) using $\vec{q} \to \vec{q}' = \frac{\vec{k} - \vec{k}'}{2}$, as obtained in Eq. (7.2), by adding to P^0 in the second factor of Eq. (7.20) the recoil energy of the final f_0, $\vec{q}^2/2m_{f_0}$. This equivalence is proved in detail in section IV of Ref. [128]. A different derivation of the same results can be seen in Ref. [172] (see also Ref. [173] for a relativistic formulation).

After this discussion about the meaning of the field theoretical approach of Refs. [170, 171], the FCA goes beyond the impulse approximation by taking into account rescattering of the ϕ with the K and $\bar{K}$ of the f_0. The rescattering is done zigzagging from one K to the $\bar{K}$ and viceversa. Successive
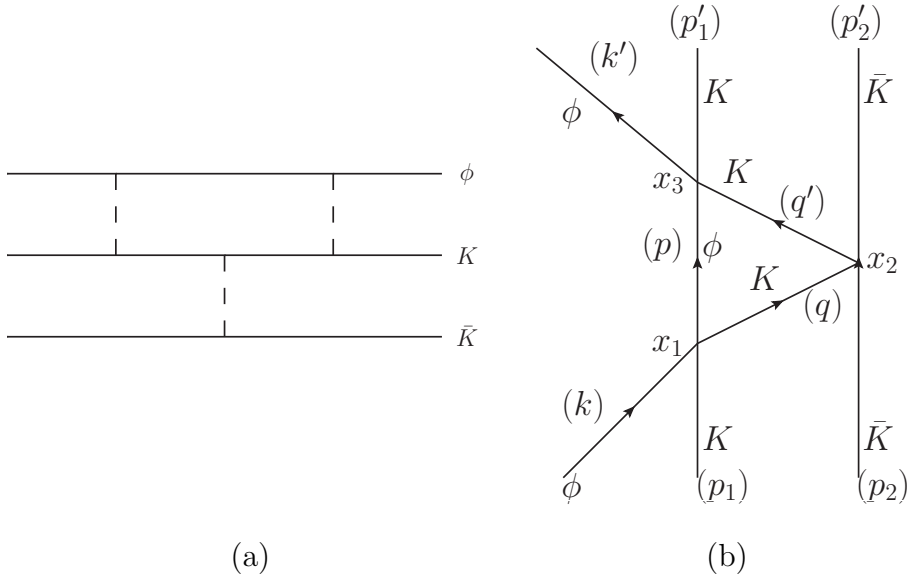
Figure 7.3: Diagrammatic representation of one of the terms of the Faddeev equations in which the f_0 is excited in the intermediate state: a) Typical Faddeev diagram; b) Diagrammatic representation of a) in terms of a field theoretical Feynman diagram.

scatterings of the ϕ on the same particle are forbidden since this leads to diagrams already accounted in the ϕK ($\phi\bar{K}$) scattering matrix and, thus, one would be double counting. In Refs. [170, 171] one is not considering the series implicit in the FCA except for the first term. However, another series of terms is considered as we shall explain in the next section.

7.4 Beyond the FCA: excitation of the f_0 in intermediate states

The FCA does not allow for f_0 excitation in the intermediate propagation of the ϕf_0 states. Since for the $\phi(2170)$ one has about 170 MeV of excitation with respect to the ϕf_0 at rest, it looks very unlikely that the f_0 is not excited in the intermediate states. An intuitive view can be also obtained by recalling that the ϕ has bigger mass than the K and in its collision with the f_0 it could easily break this lighter system. To find the explicit answer one resorts to the Faddeev equations and looks for terms where the f_0 can be broken in intermediate states. We must have in mind that when one has

multiple scattering in the FCA, the $K\bar{K}$ interaction is never used explicitly. Yet, it is implicitly taken into account by using the wave function of the $K\bar{K}$ system. Hence, in the second diagram of Fig. 7.1, the ϕ collides with the K, leaving its wave function unchanged, then it propagates and collides with the $\bar{K}$, leaving it also in its original state. This mechanism corresponds to a diagram of the Faddeev expansion with two interactions of the ϕ in which the initial and final $K\bar{K}$ states do not have the possibility of being excited in the intermediate state. We can go one step ahead in the Faddeev series of diagrams and see if the $K\bar{K}$ interaction, in connection with the double scattering of the ϕ with the K and the $\bar{K}$, can lead to a break up of the $K\bar{K}$ system once there is sufficient energy for this excitation. This is depicted in the diagram shown in Fig. 7.3.

The S matrix for the diagram of Fig. 7.3 is given by

$$
S^{(3)} = \frac{1}{\sqrt{2\omega_k}} \frac{1}{\sqrt{2\omega_{k'}}} \frac{1}{\sqrt{2\omega_{p_1}}} \frac{1}{\sqrt{2\omega_{p_1'}}} \frac{1}{\sqrt{2\omega_{p_2}}} \frac{1}{\sqrt{2\omega_{p_2'}}} \int d^4x_1 \int d^4x_2 \int d^4x_3
$$

$$
\times \int \frac{d^4q}{(2\pi)^4} \int \frac{d^4q'}{(2\pi)^4} \int \frac{d^4p}{(2\pi)^4} (-it_{\phi K}(s'))(-it_{K\bar{K}}(s''))(-it_{\phi K}(s'))
$$

$$
\times \frac{ie^{iq(x_1-x_2)}}{q^2 - m_K^2 + i\epsilon} \frac{ie^{iq'(x_2-x_3)}}{q'^2 - m_K^2 + i\epsilon} \frac{ie^{ip(x_1-x_3)}}{p^2 - m_\phi^2 + i\epsilon} e^{ik'^0 x_3^0} e^{ip_1'^0 x_3^0} e^{ip_2'^0 x_2^0}
$$

$$
\times e^{-ik^0 x_1^0} e^{-ip_1^0 x_1^0} e^{-ip_2^0 x_2^0} \frac{1}{\sqrt{\mathcal{V}}} e^{-i\vec{k}'\vec{x}_3} \varphi_1(x_3)\varphi_2(x_2) \frac{1}{\sqrt{\mathcal{V}}} e^{i\vec{k}\vec{x}_1} \varphi_1(x_1)\varphi_2(x_2)
$$

$$
\tag{7.21}
$$

where

$$
\begin{aligned}
s'' &= (q + p_2)^2 = (k + p_1 - p + p_2)^2 = (k + P - p)^2 \\
&= s - m_\phi^2 - 2\sqrt{s}\,\omega_\phi(\vec{p})
\end{aligned}
\tag{7.22}
$$

with P the momentum of the f_0. By performing the x_1^0, x_2^0, x_3^0, p^0, q'^0, p'^0 integrations, making the change of variables

$$
\vec{x}_1 - \vec{x}_2 = \vec{r} \qquad\qquad \vec{x}_3 - \vec{x}_2 = \vec{r}' \tag{7.23}
$$

$$
\frac{1}{2}(\vec{x}_1 + \vec{x}_2) = \vec{R} \qquad\qquad \frac{1}{2}(\vec{x}_3 + \vec{x}_2) = \vec{R} + \frac{\vec{r}'}{2} - \frac{\vec{r}}{2} \tag{7.24}
$$

and using that

$$
\varphi_1(\vec{x}_1)\varphi_2(\vec{x}_2) = \frac{1}{\sqrt{\mathcal{V}}} e^{i\vec{P}(\frac{\vec{x}_1+\vec{x}_2}{2})} \varphi(\vec{r}) = \frac{1}{\sqrt{\mathcal{V}}} e^{i\vec{P}\vec{R}} \varphi(\vec{r}) \tag{7.25}
$$

$$
\varphi_1^*(\vec{x}_3)\varphi_2^*(\vec{x}_2) = \frac{1}{\sqrt{\mathcal{V}}} e^{-i\vec{P}(\frac{\vec{x}_3+\vec{x}_2}{2})} \varphi^*(\vec{r}) = \frac{1}{\sqrt{\mathcal{V}}} e^{-i\vec{P}'\vec{R}} e^{-i\vec{P}'\frac{\vec{r}'}{2}} e^{i\vec{P}'\frac{\vec{r}}{2}} \varphi^*(\vec{r}') \tag{7.26}
$$

we can perform the d^3x_i integrals and the three $\int d^3q$, $\int d^3q'$, $\int d^3p$ integrals of Eq. (7.21) and we obtain

$$
-it^{(3)} = -i \int \frac{d^3q'}{(2\pi)^3} \int \frac{d^3p}{(2\pi)^3} t_{\phi K}(s') t_{K\bar{K}}(s'') t_{\phi K}(s') \frac{1}{2\omega_K(\vec{q})} \frac{1}{2\omega_K(\vec{q}')}
$$
$$
\times \frac{1}{2\omega_\phi(\vec{p})} \frac{1}{k^0 + p_1^0 - \omega_\phi(\vec{p}) - \omega_K(\vec{q}) + i\epsilon} \frac{1}{k'^0 + p'^0_1 - \omega_\phi(\vec{p}) - \omega_K(\vec{q}') + i\epsilon}
$$
$$
\times \tilde{\varphi}\left(\vec{p} + \vec{q} - \frac{\vec{P}'}{2} - \frac{\vec{k} + \vec{k}'}{2}\right) \tilde{\varphi}\left(\vec{p} + \vec{q}' - \frac{\vec{P}'}{2} - \frac{\vec{k} + \vec{k}'}{2} + \frac{\vec{k} - \vec{k}'}{2}\right)
$$
$$
\tag{7.27}
$$

As we can see, the amplitude $t_{K\bar{K}}(s'')$ has appeared with argument s'', which depends on the integration variables, as shown in Eq. (7.22). In Eq. (7.26) we have used the complex conjugate of the wave function for formal reasons, although they are real here. For the general case of wave functions and form factors where the system is unbound see section IV of Ref. [128].

The amplitude obtained in Eq. (7.27) can be compared directly to the double scattering term of Eq. (7.3),

$$
-it^{(2)} = -it_{\phi K}(s') 2M_{f_0} \tilde{G}_0 t_{\phi K}(s') \tag{7.28}
$$

The factor $[t_{\phi K}(s')]^2$ is the same in both equations and we can remove it for the purpose of comparison of the two amplitudes.

7.5 Results

In the calculations we have taken $t_{\phi K}$ from the work of Ref. [174], where the t matrix is obtained in the chiral unitary approach with the ϕK and its coupled channels. We show in Fig. 7.4 the results for the squared ϕf_0 amplitude, $|T_{\phi f_0}|^2$, obtained with Eq. (7.12), which omits the form factor in the impulse approximation term, and neglecting the $(\vec{k} + \vec{k}')/2$ in the argument of the form factor in the $\tilde{G}_0$ function. We can see that the $|T_{\phi f_0}|^2$ goes down when approaching the threshold of ϕf_0 and then rises again. We find no sign that there should be a peak around 2170 MeV. On the other hand, the form factor is here very important since $\vec{k}$ is quite large, of the order of 420 MeV/c for $\sqrt{s} = 2170$ MeV. In the next step we take into account the form factor but project the amplitude over S-wave by integrating over $\int d\Omega(\hat{k}')$ the form factor, both in the single scattering term and in $\tilde{G}_0$. The results can be seen in Fig. 7.5. We see that the net effect of the form factor has been a drastic reduction of $|T_{\phi f_0}|^2$ beyond the threshold. Below the threshold we have taken

$\vec{k} = \vec{k}' = 0$ as usually done in these calculations. This is based on the fact that, even if the $\phi K \bar{K}$ system were bound, there is a distribution of real momenta in the wave function, but the momenta are small. One can take a different approach and extrapolate the formula of the form factor below threshold introducing purely imaginary ϕ momenta. While one can debate which approach is more physical, it is irrelevant in the present case where we look at the behavior above threshold.

Once again we can see that there is no trace of a peak around $\sqrt{s} = 2170$ MeV when we include the form factor. This is in contrast with the clear peak seen for the $|T_{\phi f_0}|^2$ with the full Faddeev equations, as seen in Fig.1 of Ref. [133]. After this is done, we proceed to evaluate the contribution
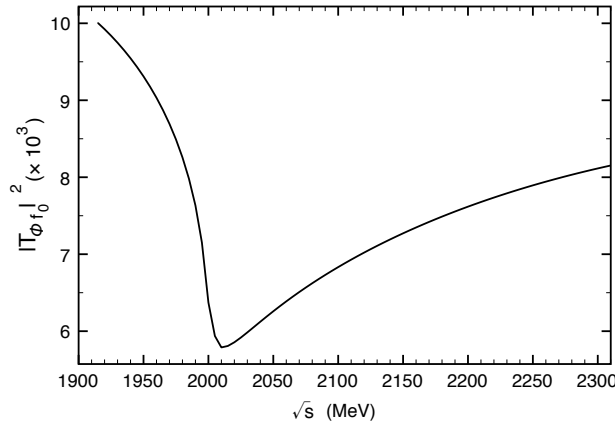

Figure 7.4: Amplitude squared for the $\phi f_0(980)$ interaction without including the form factor F_{f_0}.

from the diagram of Fig. 7.3. In Fig. 7.6 (up) we compare the contribution of this diagram, which now allows for f_0 excitation, with the FCA double scattering. In Fig. 7.6 (down) we show the ratio of the two body term of the FCA to the three body diagram of Fig. 7.3. We should note that for the case of the two body FCA we have two possibilities, when one starts the ϕ interaction from the K or from the $\bar{K}$, but in the case of Fig. 7.3 we have four possibilities, where the ϕ interacts at the beginning and at the end with either the K or the $\bar{K}$. The relative factor of two in the three body amplitude is incorporated in the figure.

What one can see in Fig. 7.6 is that the three body diagram of Fig. 7.3 with intermediate f_0 excitation is of the same size around $\sqrt{s} = 2170$ MeV than the double scattering term of the FCA, which has no intermediate f_0 excitation. We can see in the figure, comparing real and imaginary parts, that the two mechanisms have amplitudes with opposite signs for the real parts in
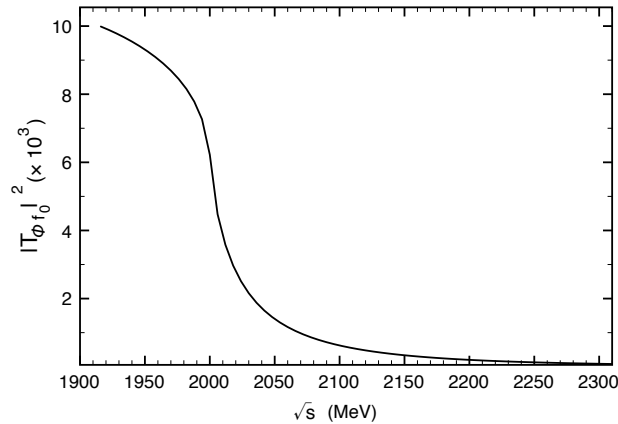
Figure 7.5: Amplitude squared for the $\phi f_0(980)$ interaction including the form factor F_{f_0}.

the region of interest to us. Their simultaneous consideration would change drastically the results obtained from the double scattering contribution of the FCA alone. Yet, when one evaluates the Faddeev integral equations one does not know how much contribution one obtains from such mechanism and this is an information that the present work has provided for the case of the ϕf_0 interaction, which should serve as reference for other possible cases where there is also plenty of excitation energy available. Note that the fact that in intermediate states of the multiple scattering the $K\bar{K}$ system is excited does not invalidate that we call this state a ϕf_0 system, since asymptotically in the scattering we have indeed ϕf_0 in that picture. This is the same as we would have in the π elastic scattering with a nucleus in the Δ region where in intermediate states nucleons can be excited to Δ states.

At low energies close to threshold, and more clearly below it, the two body FCA amplitude dominates over the excitation term. A more appropriate approach in that region would consist of using a complete set of $K\bar{K}$ states which contained the bound $K\bar{K}$ state and their orthogonal states in the continuum, instead of the basis of plane waves used here. Since the plane waves still have an overlap to the bound wave function, it is logical to think that the use of that alternative basis would give a smaller contribution for the excited states, emphasizing more the role of the ground state of the f_0, accounted by the FCA. This numerical finding is in the line with analytical studies of πd and $\bar{K}d$ which show that the contribution of the diagram of Fig. 7.3 should vanish at threshold in the limit of $m_K \to \infty$ [175, 158]. At higher energies, where many states can be excited, the use of the set of plane waves for the wave functions becomes progressively more accurate, making
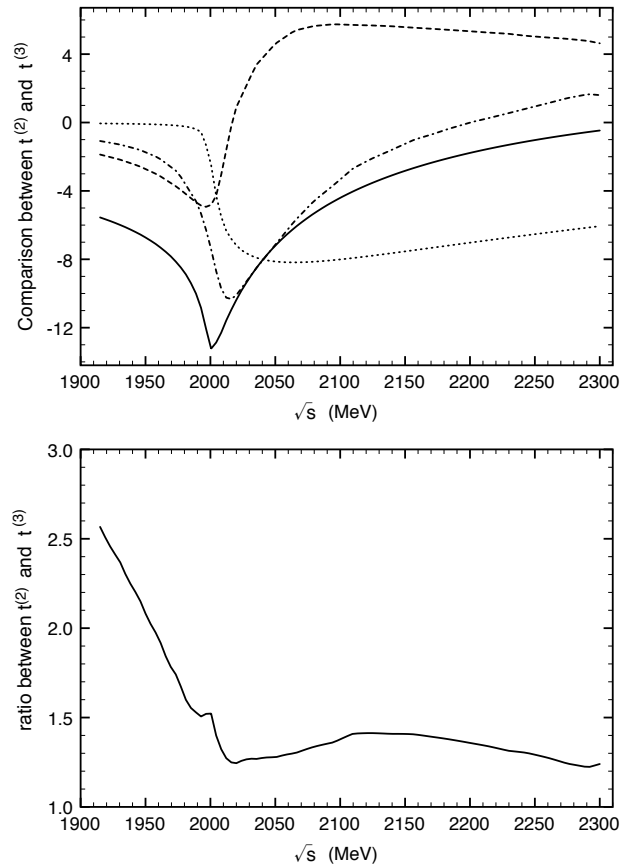
Figure 7.6: Comparison of the amplitudes $t^{(2)}$ and $t^{(3)}$. (Up) The solid and dotted line correspond to the real and imaginary part, respectively, of the $t^{(2)}$ amplitude, while the dashed and dash-dotted line are the real and imaginary part, respectively, of the $t^{(3)}$ amplitude, both divided by $t_{\phi K}(s')t_{\phi K}(s')$, in units of MeV. (Down) Ratio of the modulus of the amplitudes $t^{(2)}$ and $t^{(3)}$.

our results more realistic in the region of 170 MeV excitation.

It is interesting to note that in Refs. [170, 171] the term discussed here of Fig. 7.3 is formally taken into account even if the formalism looks quite different[3]. It is also iterated with multiple steps that have the f_0 ϕ in the intermediate states. Yet, the formalism of Refs. [170, 171] requires to regularize a loop function for the f_0 ϕ propagator, for which one has no input from the derivation of the $K\phi$ and $K\bar{K}$ amplitudes. Thus, one introduces unknown elements at this point, essentially the subtraction constant of a dispersion relation, which is treated as a free parameter in Refs. [170, 171][4]. Furthermore the $K\phi$ interaction, which in the present work is taken from the chiral unitary approach of Ref. [174], is considered in terms of an extra free parameter in Ref. [170], which is adjusted to the data of $\phi(2170)$ production. At this point it is important to note that the use of the fitted ϕK in Ref. [170] results in a $|T_{\phi f_0}|^2$ value at $\sqrt{s} \approx 2170$ MeV about two orders of magnitude bigger than if the ϕK amplitude provided by the chiral unitary approach of Ref. [174] was used, which is corroborated by the authors of Ref. [170]. The approach is thus quite different from the Faddeev approach, where the result is fixed before hand from the elementary $K\phi$ and $K\bar{K}$ scattering amplitudes. Since two free parameters are used in Refs. [170], the approach can provide a fit to the data but it is not a predictive scheme for the present problem.

7.6 Conclusions

The fixed center approximation to the Faddeev equations, when two particles are clustered into a bound system, has been often used and proved to be a good approximations in the low energy regime, close to threshold of the constituent particles or below. One particular feature of this approximation is that the cluster of the two particles is not excited in the intermediate states, which can be a good approximation if there is no energy available to excite it. One could hope that it could still be a good approximation if one goes above the threshold, and as usual one does not know the answer until one has checked it. This is what we have done in this work and we have chosen the case of a problem of current interest, the case of the $\phi(2170)$ particle as a resonant state of the ϕ and $f_0(980)$ states. In this case the $\phi f_0(980)$

---

[3]We are indebted to J. A. Oller and L. Alvarez Ruso for clarifying this point to us.

[4]One might argue that the Faddeev equations of Refs. [131, 132, 133] also need of an extra regularization factor for the genuine Faddeev loops. In Refs. [131, 132, 133] a cut off of around 1 GeV was used, but only for the purpose of showing the independence of the results with respect to this parameter, since those loops contain three propagators and are convergent without the need of extra cutoffs.

system appears with 170 MeV of excitation, so a priory it looks unlikely that the f_0 would not be excited in intermediate states. Yet, it is worth seeing what happens in detail. What we find is that the FCA does not lead to any structure in the region of the $\phi(2170)$, nor close by, unlike by solving the Faddeev equations. On the other hand we determined the contribution of Faddeev diagrams where the f_0 is allowed to be excited in the intermediate states, with terms that involve explicitly the $K\bar{K}$ interaction between two ϕK or $\phi\bar{K}$ collisions. What we found is that this new mechanism is of the same order of magnitude as the ϕK double scattering from the FCA series. Furthermore, we also find that the terms have a strong destructive interference. In view of this, any reliable approach to the problem should take this feature into account. One might think of improving the FCA to include these inelastic excitations, but the problem becomes very involved with the higher iterations and ultimately turns out into a problem far more complicated than the use of the Faddeev equations from the beginning. Hence, from the practical point of view it does not pay to try to simplify the Faddeev equations in favor of a modified FCA once there is a large excitation energy.

The main message from this work is, hence, a warning not to use the FCA for unbound systems, particularly when the scattering particle has a bigger mass than the constituents of the cluster. It also served to show that for bound energies the FCA is a more realistic approach. Finally, the detailed calculation performed here and comparison to the approach of Refs. [170, 171] served to show that those work incorporate some of the relevant mechanisms of the Faddeev equations, but having to rely on fitting parameters, unlike the Faddev approach, does not lead to a predictive tool for these three body systems. The results of this Chapter are published in Ref. [176].

Strategies for an accurate determination of the X(3872) energy from QCD lattice simulations

8.1 Introduction

The X(3872) state, observed for the first time by Belle [177], has been found in many other experiments and is the paradigm of the charmonium states of non-conventional nature (see Refs. [178, 179] for recent reviews on the issue). Although for some time the quantum numbers were not well determined and both, the $J^{PC} = 1^{++}$ and 2^{-+} states were candidates, theoretical papers showed a preference for the 1^{++} state [180, 181, 182, 183, 184], which has been recently confirmed by the LHCb [185].

The search for this state in lattice QCD simulations has also run parallel and several works have been devoted to this task [186, 187, 188, 189], finding one state close to the experimental one. Yet, it was too difficult to unambiguously determine whether one had a bound state or simply $D\bar{D}^*$ scattering states which appear at around the same energy. An important step forward has been given very recently in Ref. [190], where a bound state is obtained in a dynamical $N_f = 2$ lattice simulation with 11 ± 7 MeV below the $D\bar{D}^*$ threshold and quantum numbers 1^{++}. Improvements on this can be done in the future using larger boxes and smaller pion masses. The work of Ref. [190] makes use of the technique proposed in Ref. [191], where the presence of a bound state comes accompanied by a sign change of the scattering length with respect to an attractive potential which does not bind. This observation is useful and has also been applied in Ref. [192].

The purpose of the present paper is to find a strategy to determine accurately the binding energy of the X(3872) in lattice QCD simulations. A precise determination, with an energy about 0.2 MeV below the $D^0\bar{D}^{*0}$ threshold, requires to differentiate between the u and d quark masses in order to account for the 7 MeV difference between the neutral and charged components of the wave function [193, 127]. The small binding of the state with respect to the $D^0\bar{D}^{*0}$ threshold, much smaller than the difference of masses between the $D^0\bar{D}^{*0}$ and D^+D^{*-} components, makes this consideration imperative in order to get a precise value of the binding energy and unambiguously determine the bound state character of the X(3872). In fact, when this is done, energy levels can be associated to either $D^0\bar{D}^{*0}$ or $D^+\bar{D}^{*-}$.

The strategy used here follows closely the work of Ref. [194] using coupled channels, where the energy levels related to the scalar mesons were investigated. It studies the levels of two-meson interaction in a finite box and tackles the inverse problem of deriving phase shifts from pseudolattice data using Lüscher formalism [195] and different strategies. The case of bound states is studied along similar lines in Ref. [196], where the combination of Lüscher formalism and methods related to those used in Refs. [197, 198] allow a precise determination of binding energies of hidden charm states. Thus, in order to have an accurate measurement of the binding energy of the X(3872), we present a method using different number of levels, different box sizes and determine the precision required for the lattice energies.

8.2   The X(3872) in the continuum limit

In this section we discuss briefly the dynamical generation of the X(3872) in the continuum limit. All the details are in Refs. [183, 193, 199]. The pseudoscalar - vector interaction can be studied through the hidden gauge Lagrangian [30, 13], which contains interaction between vectors and with pseudoscalar mesons,

$$\mathcal{L}_{III} = -\frac{1}{4}\langle V_{\mu\nu}V^{\mu\nu}\rangle + \frac{1}{2}M_V^2\langle[V_\mu - \frac{i}{g}\Gamma_\mu]\rangle \qquad (8.1)$$

where $V_{\mu\nu} = \partial_\mu V_\nu - \partial_\nu V_\mu - ig[V_\mu, V_\nu]$, and $g = \frac{M_V}{2f}$. The model is based on vector-meson exchange, see Fig. 8.1. From the above equation, the lower and upper vertices needed to evaluate the amplitude of the diagram depicted in Fig. 8.1 are obtained using the terms

$$\mathcal{L}_{PPV} = -ig\langle V^\mu[P, \partial_\mu P]\rangle, \qquad \mathcal{L}_{3V} = ig\langle (V^\mu\partial_\nu V_\mu - \partial_\nu V_\mu V^\mu)V^\nu\rangle \ , \quad (8.2)$$

where V_μ, P are the matrices of the 16-plet of vector, pseudoscalar mesons [193].
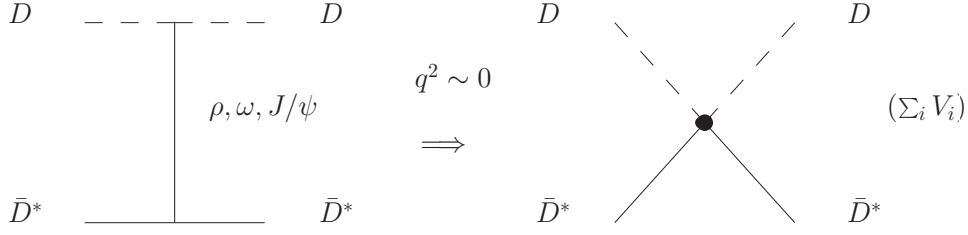
Figure 8.1: Point-like pseudoscalar - vector interaction.

In fact, the combination of both terms in Eq. (8.2), for s-wave, when the momenta q^2 exchanged in the propagator of the vector meson exchanged can be neglected against $-M_V^2$, leads to a point-like interaction, and is equivalent to using the Lagrangian,

$$\mathcal{L}_{PPVV} = -\frac{1}{4f^2} Tr\left(J_\mu \mathcal{J}^\mu\right). \tag{8.3}$$

with $J_\mu = (\partial_\mu P)P - P\partial_\mu P$ and $\mathcal{J}_\mu = (\partial_\mu \mathcal{V}_\nu)\mathcal{V}^\nu - \mathcal{V}_\nu \partial_\mu \mathcal{V}^\nu$, see Refs. [174, 193]. In Ref. [193], the currents in Eq. (8.3) are separated for heavy and light vector-meson-exchange, introducing the breaking parameters,

$$\gamma = \left(\frac{m_{8*}}{m_{3*}}\right)^2 = \frac{m_L^2}{m_H^2} \qquad \psi = \left(\frac{m_{8*}}{m_{1*}}\right)^2 = \frac{m_L^2}{m_{J/\psi}^2} \ ,$$

with $m_{8*} = m_L = 800$ MeV, $m_{3*} = m_H = 2050$ MeV and $m_{1*} = m_{J/\psi} = 3097$ MeV. This gives, $\gamma = 0.14$ and $\psi = 0.07$. Because of the smallness of the breaking parameters, the light and heavy sector are almost disconnected, and the transition potential between those is very small. Also, for light mesons, $f = f_\pi = 93$ MeV, and for heavy ones, $f = f_D = 165$ MeV, is used. Thus, the amplitude of the process $V_1(k)P_1(p) \to V_2(k')P_2(p')$, is given by

$$V_{ij}(s,t,u) = \frac{\xi_{ij}}{4f_i f_j}(s-u)\,\vec{\epsilon}\cdot\vec{\epsilon}' \tag{8.4}$$

with $s-u = (k+k')(p+p')$, which must be projected in s-wave [193, 174], and i, j refer to the particle channels. Working in the charge basis, we have the channels $\frac{1}{\sqrt{2}}(\bar{K}^{*-}K^+ - c.c.)$, $\frac{1}{\sqrt{2}}(\bar{K}^{*0}K^0 - c.c.)$, $\frac{1}{\sqrt{2}}(D^{*+}D^- - c.c.)$, $\frac{1}{\sqrt{2}}(D^{*0}\bar{D}^0 - c.c.)$ and $\frac{1}{\sqrt{2}}(D_s^{*+}D_s^- - c.c.)$, and the matrix ξ can be written in this basis as

$$\xi = \begin{pmatrix} -3 & -3 & 0 & -\gamma & \gamma \\ -3 & -3 & -\gamma & 0 & \gamma \\ 0 & -\gamma & -(1+\psi) & -1 & -1 \\ -\gamma & 0 & -1 & -(1+\psi) & -1 \\ \gamma & \gamma & -1 & -1 & -(1+\psi) \end{pmatrix}. \tag{8.5}$$

Eq. (8.4) is the input of the Bethe Salpether equation,

$$T = (I - VG)^{-1}V\,\vec{\epsilon}\cdot\vec{\epsilon}'\;. \tag{8.6}$$

Here G a diagonal matrix of the two-meson loop function for each channel. Usually it is evaluated with dimensional regularization and depends on the parameter α [193] (μ is a scale mass, fixed a priori)

$$
\begin{aligned}
G = G^{DR}(\sqrt{s}) \;=\;\; & \frac{1}{16\pi^2}\Big\{\alpha(\mu) + \ln\frac{m_1^2}{\mu^2} + \frac{m_2^2 - m_1^2 + s}{2s}\ln\frac{m_2^2}{m_1^2} + \\
& + \frac{q}{\sqrt{s}}\Big[\ln(s - (m_2^2 - m_1^2) + 2q\sqrt{s}) + \ln(s + (m_2^2 - m_1^2) + 2q\sqrt{s}) \\
& - \ln(-s + (m_2^2 - m_1^2) + 2q\sqrt{s}) - \ln(-s - (m_2^2 - m_1^2) + 2q\sqrt{s})\Big]\Big\}
\end{aligned}
\tag{8.7}
$$

One can also evaluate the G function with a cuttoff,

$$G = G^{co}(P_0 = \sqrt{s}) = \int_{q<q_{max}}\frac{d^3q}{(2\pi)^3}\frac{\omega_1 + \omega_2}{2\omega_1\omega_2}\frac{1}{(P^0)^2 - (\omega_1 + \omega_2)^2 + i\epsilon} \tag{8.8}$$

The calculation in Ref. [193] is redone to get a binding energy more realistic at 0.2 MeV with respect to the channel $D^{*0}\bar{D}^0 - c.c.$ [199], where the masses of the mesons are taken from the PDG [67]. The free parameter, α, is fixed for the light channels, $\alpha_L = -0.8$ [193, 174], but the pole position of the X(3872) is not sensitive to that, since its mass is far away from these thresholds. For the heavy channels, the value $\alpha_H = -1.265$ is needed for such binding energy (μ is taken equal to 1500 MeV in all channels). In Table 8.1, a summary of the pole position and couplings of the resonance to each channel is given.

The Weinberg compositeness condition [200] can be generalized for dynamically generated resonances from several channels [127],

$$-\sum_i g_i^2 \frac{\partial G}{\partial s} = 1\;, \tag{8.9}$$

being $s = P_0^2$, the squared of the initial energy in the center-of-mass frame, and $|g_i|$, the couplings in Table 8.1. Each term in Eq. (8.9) gives the probability of finding the i channel in the wave function, which are 0.86 for $D^{*0}\bar{D}^0 - c.c$, 0.124 for $D^{*+}D^- - c.c$ and 0.016 for $D_s^{*+}D_s^- - c.c.$ However, this is different from the wave function at the origin $(2\pi)^{3/2}\psi(0)_i = g_i G_i$, which usually enters the evaluation of observables and are nearly equal [127].

$\sqrt{s_0} = (3871.6 - i0.001)$ MeV	
Channel	$\lvert g_i \rvert$ [MeV]
$\frac{1}{\sqrt{2}}(K^{*-}K^+ - c.c)$	53
$\frac{1}{\sqrt{2}}(\bar{K}^{*0}K^0 - c.c)$	49
$\frac{1}{\sqrt{2}}(D^{*+}D^- - c.c)$	3638
$\frac{1}{\sqrt{2}}(D^{*0}\bar{D}^0 - c.c)$	3663
$\frac{1}{\sqrt{2}}(D_s^{*+}D_s^- - c.c)$	3395

Table 8.1: Couplings of the pole at $\sqrt{s_0}$ MeV to the channel i.

8.3 Formalism in finite volume

We follow the formalism used Ref. [194] where the infinite volume amplitude T is replaced by the amplitude $\tilde{T}$ in a finite box of size L and $G(P^0)$ in Eqs. (8.7) and (8.8) is replaced by the finite volume loop function denoted with $\tilde{G}$, given by the discrete sum over eigenstates of the box

$$\tilde{G}(P^0) = \frac{1}{L^3} \sum_{\vec{q_i}} I(P^0, \vec{q_i}) \tag{8.10}$$

with

$$I(P^0, \vec{q_i}) = \frac{\omega_1(\vec{q_i}) + \omega_2(\vec{q_i})}{2\omega_1(\vec{q_i})\omega_2(\vec{q_i})} \frac{1}{(P^0)^2 - (\omega_1(\vec{q_i}) + \omega_2(\vec{q_i}))^2} \tag{8.11}$$

where $\omega_i = \sqrt{m_i^2 + |\vec{q_i}|^2}$ is the energy and the momentum $\vec{q}$ is quantized as

$$\vec{q_i} = \frac{2\pi}{L}\vec{n_i} \tag{8.12}$$

corresponding to the periodic boundary conditions. Here the vector $\vec{n}$, denotes the three dimension vector of all integers ($\mathbb{Z}^3$). This form produces a degeneracy for the set of three integer numbers which has the same modulus. And we can write the modulus of the momentum as

$$|\vec{q_i}| = \frac{2\pi}{L}\sqrt{m_i} \tag{8.13}$$

where m_i stands for the natural numbers ($\mathbb{N}$), and the multiplicity of the degeneracy is conveniently introduced in Eq. (8.10). The sum over the momenta is done until a q_{max}, so the three dimension sum over $\vec{n_i}$ in Eq. (8.10)

becomes a one dimension sum over m_i to an n_{max} in a symmetric box

$$n_{max} = \frac{q_{max} L}{2\pi} \tag{8.14}$$

When the dimensional regularization is used in the infinite volume case, as in section II, there is no trace of q_{max} (α is related to q_{max}). Thus the equivalent formalism in finite volume should also be made independent of q_{max} and related to α. This is done in Ref. [201] with the result

$$
\begin{aligned}
\tilde{G} &= G^{DR} + \lim_{q_{max} \to \infty} \left(\frac{1}{L^3} \sum_{q < q_{max}} I(P^0, \vec{q}) - \int_{q < q_{max}} \frac{d^3 q}{(2\pi^3)} I(P^0, \vec{q}) \right) \\
&\equiv G^{DR} + \lim_{q_{max} \to \infty} \delta G
\end{aligned} \tag{8.15}
$$

where $\delta G \equiv \tilde{G} - G^{co}$, and G^{co} is given explicitly by the formula of Eq. (8.16) [148]. Here $I(P^0, \vec{q})$ is the factor given in Eq. (8.11)

$$
\begin{aligned}
G^{co} &= \frac{1}{32\pi^2} \left[-\frac{\Delta}{s} log \frac{M_1^2}{M_2^2} + \frac{\nu}{s} \left\{ log \frac{s - \Delta + \nu \sqrt{1 + \frac{M_1^2}{q_{max}^2}}}{-s + \Delta + \nu \sqrt{1 + \frac{M_1^2}{q_{max}^2}}} \right. \right. \\
&\quad \left. + log \frac{s + \Delta + \nu \sqrt{1 + \frac{M_2^2}{q_{max}^2}}}{-s - \Delta + \nu \sqrt{1 + \frac{M_2^2}{q_{max}^2}}} + 2\frac{\Delta}{s} log \frac{1 + \sqrt{1 + \frac{M_1^2}{q_{max}^2}}}{1 + \sqrt{1 + \frac{M_2^2}{q_{max}^2}}} \right\} \\
&\quad \left. - 2 log \left[\left(1 + \sqrt{1 + \frac{M_1^2}{q_{max}^2}} \right) \left(1 + \sqrt{1 + \frac{M_1^2}{q_{max}^2}} \right) \right] + log \frac{M_1^2 M_2^2}{q_{max}^4} \right]
\end{aligned} \tag{8.16}
$$

where $\Delta = M_2^2 - M_1^2$ and $\nu = \sqrt{[s - (M_1 + M_2)^2][s - (M_1 - M_2)^2]}$.

In Fig. 8.2 we show that δG converges as $q_{max} \to \infty$. In practice, one can take an average for different values between q_{max} =1500-2500 MeV and one sees that it reproduces fairly well the limit of $q_{max} \to \infty$. In the present case we use $f_D = 160$ MeV in the potential V. We have used $f_D = 160$ MeV here instead of the $f_D = 165$ MeV of Ref. [183], which provides a fair average of the present values, f_D and f_{D_s}, from lattice QCD calculations [202, 203, 204, 205, 206, 207, 208]. The use of f_D or f_{D_s} in the calculations instead of simply f_π is not clearly justified. From the perspective of heavy quark spin symmetry, (HQSS), and the local hidden gauge approach [30, 13], the dominant terms go with the exchange of light vectors [209], so the use of f_π would be more appropriated. However this uncertainty is not a problem
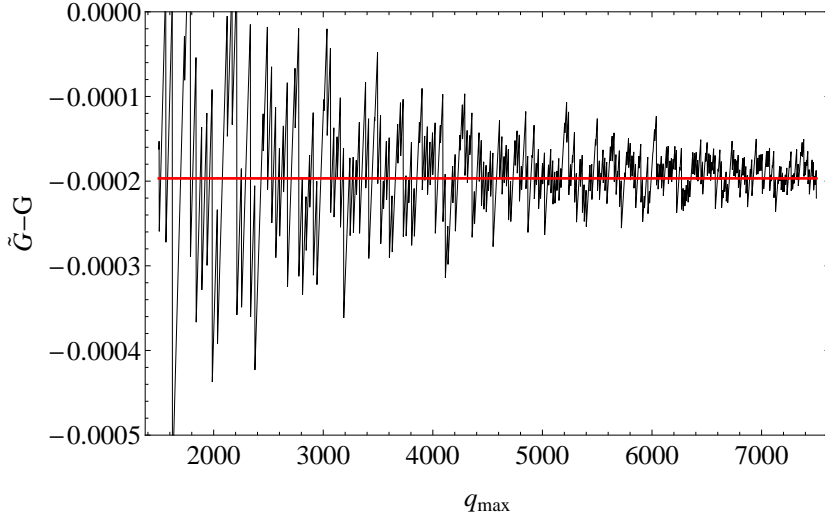
Figure 8.2: Representation of $\delta G = \tilde{G} - G$ for $D^+ D^{*-}$ in function of q_{max} for $\sqrt{s} = 3850$ MeV. The thick line represents the average of δG for different values of q_{max} between 1500 and 2500 MeV.

since in the calculation one finally tunes the subtraction constant α_H to obtain the experimental binding, and the change in the value of f_π for f_D and f_{D_s} is compensated by small changes in α_H as shown in Refs. [210, 211][1].

The Bethe-Salpeter equation in finite volume, can be written as,

$$\tilde{T} = (I - V\tilde{G})^{-1}V \tag{8.17}$$

or

$$\tilde{T}^{-1} = V^{-1} - \tilde{G} \tag{8.18}$$

The energy levels in the box in the presence of interaction V correspond to the condition

$$det(I - V\tilde{G}) = 0. \tag{8.19}$$

In a single channel, Eq. (8.19) leads to poles in the $\tilde{T}$ amplitude when $V^{-1} = \tilde{G}$. In Fig. 8.3 we show this result for one channel, where one can see the asymptotes corresponding to the energies in the free case. As a consequence, an infinite number of poles are predicted for a particular size of the box. Furthermore, for one channel, we can write the amplitude in infinite volume

---

[1]This issue has been recently clarified in Ref. [212], where the use of the impulse approximation at the quark level, with the heavy quarks acting as spectators, leads to the Weinberg-Tomozawa interaction that we have obtained here using f_π.
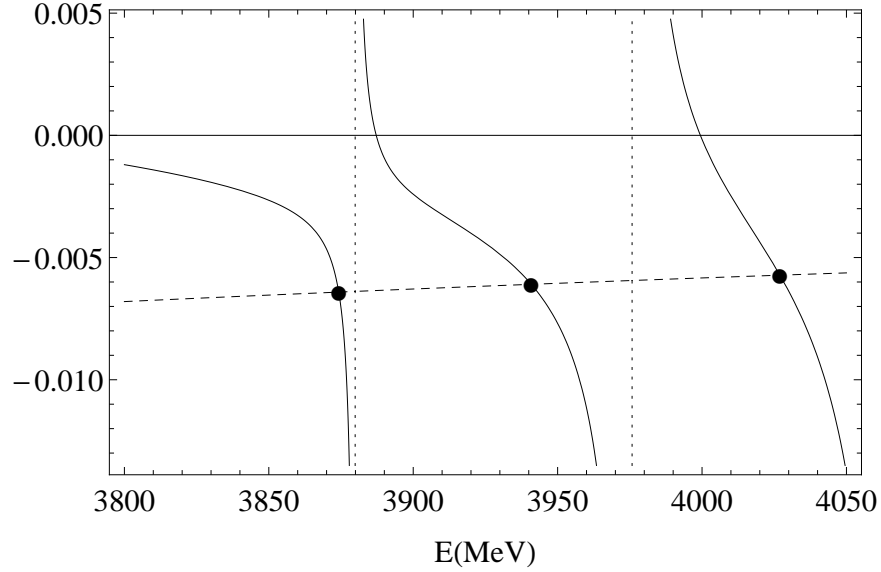
Figure 8.3: $\tilde{G}$(solid) and V^{-1}(dashed) energy dependence of D^+D^{*-} for $Lm_\pi = 2.0$. Black dots correspond to energies ($E \equiv P^0$) where $V^{-1} = \tilde{G}$. Vertical dotted lines are the free energies in the box for D^+D^{*-}.

T for the energy levels (E_i) as

$$T = (\tilde{G}(E_i) - G(E_i))^{-1}. \tag{8.20}$$

These energies have a dependence on L as shown in Fig. 8.4, where the energies are determined for the two first levels corresponding to the channels D^+D^{*-} and $D^0\bar{D}^{*0}$. In Fig. 8.4, the two first free energy levels are also shown with dotted lines. It is interesting to note that at $L = 2$ fm (corresponding to $Lm_\pi = 1.4$, in our scale, with m_π the physical mass of the pion.) where the lattice simulation has been done in Ref. [190][2], the difference of energies between the two levels in our case is 137 MeV while it is about 161 MeV in Ref. [190]. This is an important down shift of about 60 MeV with respect to the difference of the free levels of 194 MeV. This indicates that both approaches have an attractive interaction with, remarkably, about the same strength. The down shift is also seen in the individual level, as we can see in the Fig. 8.4. Furthermore, the values of our energies for the $D^0\bar{D}^{*0}$ channel at $Lm_\pi = 1.4$ for the two lowest levels in the $D^0\bar{D}^{*0}$ state are about 3860 MeV and 3997 MeV. These also compare very well with the values for the first two levels of Ref. [190], (3853 ± 8) MeV and (4014 ± 11) MeV.

---

[2]Note that in Ref. [190] a value of m_π of 266 MeV is used, hence comparison should

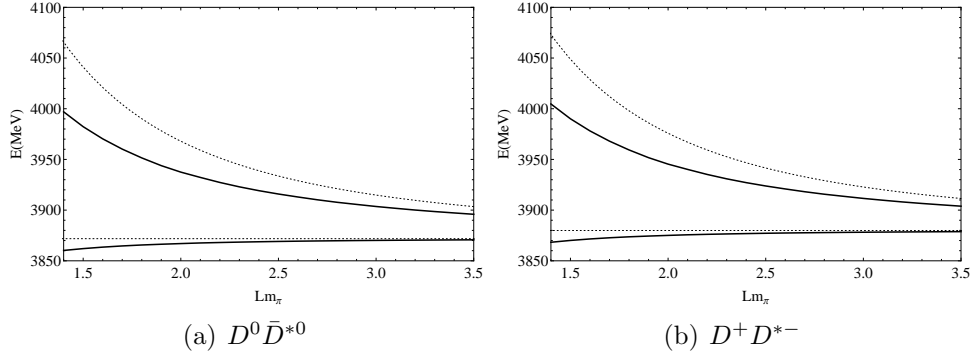(a) $D^0\bar{D}^{*0}$ (b) D^+D^{*-}

Figure 8.4: L dependence of the energies of the poles for the two first levels of a single channel. Dotted lines correspond to the free energies. The value of m_π in the scale is that of the free pion mass.

8.4 Two channel case

In the previous section we have shown the results for the single channels, D^+D^{*-} or $D^0\bar{D}^{*0}$, scattering in a finite box. Next step is to combine the two channels. In the work of Ref. [183] (see also Refs. [193, 199]), a pole at $\sqrt{s} = 3871.6$ MeV is obtained using a subtraction constant of $\alpha_H = -1.265$, with a binding energy of 0.2 MeV with respect to the neutral channel. When we address the inverse problem in the next section, for the sake of simplicity, we take only two channels, D^+D^{*-} and $D^0\bar{D}^{*0}$, reevaluating the coupled channel calculation explained in section II (see Table 8.1). Then, a new value $\alpha_H = -1.153$ is needed in order to get the same position of the pole. The novelty of this study is the inclusion of two channels in the finite box, where the energies are found using the condition of Eq. (8.19). As one can see in Fig. 8.5, we have now two curves for each level, when for a single channel we had only one trajectory. This feature is understood looking into Fig. 8.5, where the free energies for the channels D^+D^{*-} and $D^0\bar{D}^{*0}$ (dotted lines) correspond to the position of the asymptotic lines of Fig. 8.3 for each L. New asymptotes appear with respect to Fig. 8.3, corresponding to the free energies of the $D^0\bar{D}^{*0}$ channel. Since the determinant of Eq. (8.19) has a zero between two asymptotes, the number of bound states in the box is now doubled. It is interesting to note, by looking at Figs. 8.4 and 8.5, that the nondiagonal transition potential between the D^+D^{*-} and $D^0\bar{D}^{*0}$ has a repulsive effect among the levels, which are now more separated than in Fig. 8.4.

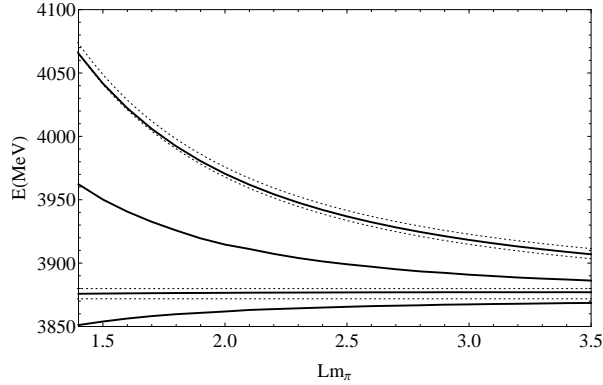be done using the same L not Lm_π, to avoid confusion.

Figure 8.5: L dependence of the energies of the poles for the two first levels of $D^+ D^{*-}$ and $D^0 \bar{D}^{*0}$. Dotted lines correspond to the free energies.

8.5   The inverse problem

Once we have determined the dependence of poles of $\tilde{T}$ with L using the potential for the DD^*, we want now to study the inverse problem. The idea is that QCD lattice data can be used to determine bound states of the $D\bar{D}^*$ system. For this purpose we assume that the lattice data are some discrete points on the energy trajectories obtained by us. Starting with a set of synthetic data of energy and L, we wish to determine the potential which generates them. Thus, simulating Lattice data, we evaluate the potential, and furthermore, by means of Eq. (8.6) we determine the pole position of the X(3872) in infinite volume with this potential. This study is very useful since we can estimate the uncertainties in the pole depending on the errors of the lattice data.

Thus, we generate a set of data for several values of L and a fixed value of the subtraction constant $\alpha = -1.153$. In this case we generate 5 points in a range of $Lm_\pi = [1.5, \ 3.5]$ and take 4 levels, this corresponds to $n=0$ and 1 in the momentum for both channels $D^+ D^{*-}$ and $D^0 \bar{D}^{*0}$. In addition, we simulate uncertainties in the obtained data, moving randomly by 1 MeV the centroid of the energies, then we assign an error of 2 MeV to these data. In Fig. 8.6 we show the simulated set of data.

The second step is to choose the potential. We have chosen a potential with linear dependence in $\sqrt{s}$. This is given by

$$V_i = a_i + b_i \left(\sqrt{s} - \sqrt{s^{th}} \right) \tag{8.21}$$

where $\sqrt{s^{th}} = m_{D^0} + m_{\bar{D}^{0*}}$ is the energy of the first threshold, and $i=1$,
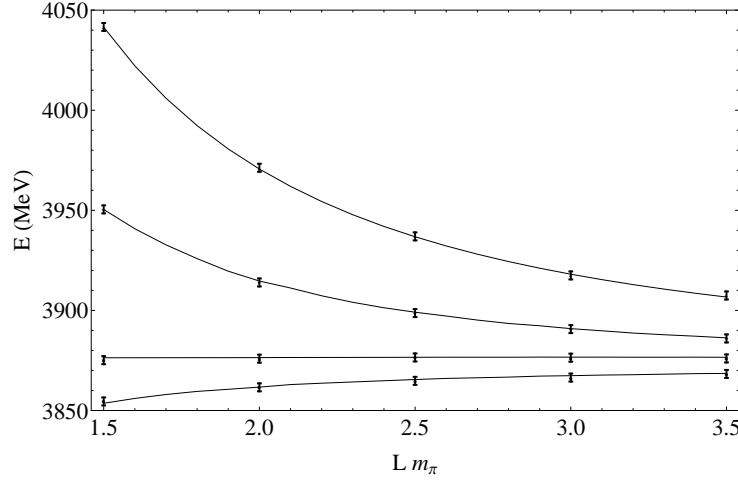
Figure 8.6: Fit to the data. Dots with error bar are the synthetic data generated as explained in the text. Solid lines show the results obtained using the potential fitted to the synthetic data.

2 and 3 are the indices for each channel ($i=1$ for D^+D^{*-}, $i=2$ for $D^0\bar{D}^{*0}$ and $i=3$ for the nondiagonal potential). Therefore, there are six parameters to determine in the potential. With all these ingredients, we do the fit, evaluating those values of the parameters in Eq. (8.21) that minimize the χ^2 function. In Fig. 8.6 we show the result of this fit together with the error band, which is obtained in the standard method [194] varying randomly the parameters of the potential in a moderate range (10% change) and choosing the set of parameters that satisfy the condition $\chi^2 \leq \chi^2_{min} + 1$. With these sets of parameters we determine the binding energy of the system with its dispersion from the pole of $T = (V^{-1} - G^{DR})^{-1}$. In both $\tilde{T}$ and T we need a value of α to determinate $\tilde{G}$ or G^{DR}. The interesting thing that we observe is that the results for the binding energy are essentially independent of the choice of α. Changes in α revert on changes of V that compensate for it. We made choices of α_H between -1.2 and -2.2.

8.6 Results

In the previous section we have commented our aim to determine the binding energy of the system with its uncertainty depending on the set of data chosen in the analysis. We choose several sets of data from Fig. 8.6, varying also their assumed errors, and show the results obtained for the energy of the bound state in Table 8.2. We have fitted the first two levels ($n=0$ and 1)
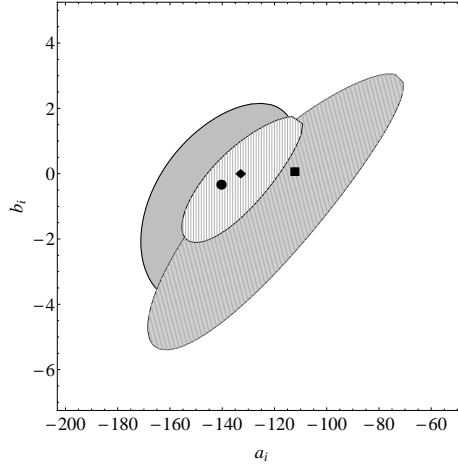
Figure 8.7: Contour plot for the χ^2 representing $\chi^2 \leq \chi^2_{min} + 1$. Each area correspond to a pair of parameters $\{a_i, b_i\}$ for the same potential. Points correspond to values of the parameters in the χ^2 minimum. (Circle and grey area are for a_1 and b_1, Square and diagonal lined area are for a_2 and b_2 and Diamond and vertical lined area are for a_3 and b_3.)

for both channels $D^+ D^{*-}$ and $D^0 \bar{D}^{*0}$ which gives four branches (B) in the data. The first option is taking only the first level with $n=0$, so we have only two branches, which is more realistic for Lattice results. With this choice we also consider several options of the number of points (P) on Lm_π. Then we take 5 points (Lm_π=1.5, 2.0, 2.5, 3.0 and 3.5) in one case and 3 points in another one (Lm_π=1.5, 2.5 and 3.5). The last option that we consider is a modification of the error bars of the energies (ΔE) and the variation in the position of the centroid (ΔC). We choose a first set of high precision with ΔE=2 MeV and ΔC=1 MeV and a second, less accurate, set with ΔE=5 MeV and ΔE=2 MeV. We have done the fits for different possible combinations of these variations in the data set up. The results of the fits are shown in Table 8.2, where the first four columns determine the chosen set up of the synthetic data. The next columns are the fitted parameters, value of χ^2 and pole position. The energy values in the "Pole" column correspond to the pole positions of the T matrix using the G^{DR} loop function of Eq. (8.7) together with the parametrized potential of Eq. (8.21). To test the stability of the pole with the parameters, we vary randomly the parameters by 10%. If the new χ^2 calculated with those parameters is less than the χ^2 obtained in the fit plus one, we determine the pole position, otherwise it will be discarded. We iterate several times until we get 20 or 30 values of the pole positions. Then, we calculate the mean value of those pole

Data				Parameters						Results			
B	P	ΔE	ΔC	a_1	a_2	a_3	b_1	b_2	b_3	χ^2	Pole	Mean Pole	σ
4	5	2	1	-140.18	-112.08	-132.81	-0.310	0.074	0.012	2.32	3871.51	3871.49	0.07
4	5	5	2	-140.18	-112.08	-132.81	-0.310	0.074	0.012	0.79	3871.51	3871.25	0.38
4	3	2	1	-133.01	-131.92	-124.60	-0.242	0.048	-0.075	1.02	3871.44	3871.49	0.18
4	3	5	2	-120.09	-98.19	-150.94	-0.377	-0.075	0.102	0.28	3871.41	3871.15	0.49
2	5	2	1	-176.08	-154.11	-89.26	9.92	7.01	-8.72	0.259	3871.70	3871.47	0.30
2	5	5	2	-158.49	-152.15	-103.23	4.56	6.58	-6.74	0.982	3871.34	3871.30	0.43
2	3	2	1	-132.74	-176.62	-105.53	3.23	0.84	-3.36	0.074	3870.51	3870.48	0.61
2	3	5	2	-226.57	-194.51	-32.74	31.81	13.28	-18.89	0.942	3869.49	3870.37	1.06

Table 8.2: All possible set up changing number of branches (B), number of points (P), energy error bar (ΔE) and centroid of the energies (ΔC) and their set of parameters fitted. The columns denoted as Results are the χ^2 obtained in the fit, the pole is determined with the parameters, and the mean pole and the dispersion are calculated as explained in the text. The results are for $\alpha = -1.25$. As noted in the text, the use of different values of α change the potential but not the binding energy. Note that we quote values of total χ^2 not the reduced one, which is always much smaller than 1.

positions and their dispersion.

The results are in the line with what one should expect: fewer branches, fewer points or bigger errors reverts into a higher dispersion in the binding energy. Since it is difficult for Lattice simulations to calculate higher levels, we have also done the test for the first level of energies for both channels, and in all cases the dispersion of the pole is higher than in the case where two levels are taken into account. Since the experimental errors in the binding of the $X(3872)$ are of the order of 0.20 MeV, the exercise done is telling the level of precision demanded for the Lattice data if the experimental precision is to be matched.

So far we have assumed that the $X(3872)$ is a dynamically generated state. This is a rather generalized assumption in hadronic physics as discussed in the Introduction, but it is also substantiated by the work of Ref. [190]. Indeed in this paper the use of an interpolator operator of $c\bar{c}$ alone does not show the $X(3872)$ but the explicit consideration of $D\bar{D}^*$ together with $c\bar{c}$ shows clearly the signal for it.

If we wished to show that the $X(3872)$ is dynamically generated we could repeat the procedure done in Section IV of Ref. [201]. We do not wish to repeat that here, since our concern is to see strategies to analyse lattice data leading to the precise determination of the binding of the $X(3872)$. However we still find interesting the following exercise. Let us assume that the $X(3872)$ was a state largely genuine, like the ρ meson (See Refs. [43, 213, 214]). We can generate it with the Bethe Salpeter equation using a potential containing a CDD pole [215] of the type

$$V = V_M + \frac{g_{CDD}^2}{s - s_{CDD}} \tag{8.22}$$

As an exercise we shall assume this potential to be same for the diagonal D^+D^{*-}, $D^0\bar{D}^{*0}$ and the transition from $D^+D^{*-} \rightarrow D^0\bar{D}^{*0}$. To ensure a dominance of the genuine component we take V_M to be about 1/10 of the one needed to generate dynamically the state $X(3872)$, $\sqrt{s_{CDD}}$ to be 20 MeV above the $D^0\bar{D}^{*0}$ threshold and then we find $g_{CDD} = 4620$ MeV, which is adjusted to get the binding of the $X(3872)$ at 3871.6 MeV. Then we get the levels of Fig. 8.8. As one can see, the two lower levels have not changed appreciably with respect to Fig. 8.5, but the two upper ones have somewhat changed at small values of L. Nevertheless, the changes found in the two lower levels are sufficient to provide some information on the nature of the state. Indeed, we next repeat the inverse problem, but analysing the results in Fig. 8.8 as "pseudodata" in terms of the potential of Eq. (8.21), since a priori we do not know the structure of the potential of Eq. (8.22). We take only the two lowest levels as in the lower part of Table 8.2, and the case of
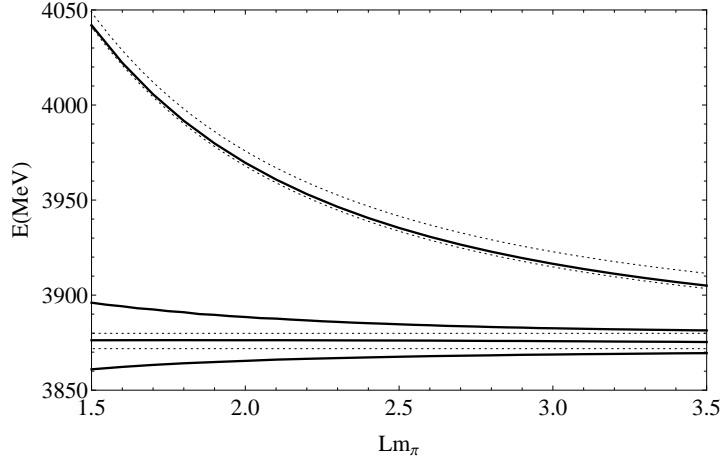
Figure 8.8: L dependence of the energies of the poles for the two first levels of D^+D^{*-} and $D^0\bar{D}^{*0}$ using the CDD pole potential. Dotted lines correspond to the free energies.

$B = 2$, $P = 5$, $\Delta E = 2$, $\Delta C = 1$. With a fit to these data we obtain now a mean pole at 3871.2 MeV and $\sigma = 0.4$ MeV. Furthermore, we obtain a set of coefficients of Eq. (8.21) with larger b_i as compared to those of the analysis of Fig. 8.6. It is then interesting to note that even if our potential in the inverse problem does not explicitly have a CDD pole, a stronger energy dependence with large b_i leads to

$$-\sum_{i=1}^{2} g_i^2 \frac{\partial G_i}{\partial s} = 1 - Z = 0.51 \tag{8.23}$$

indicating that the state has a large genuine component $Z \simeq 0.5$. In spite of not using the form of the potential of Eq. (8.22) that generated the levels of Fig. 8.8, we still find Z quite different from zero, and very close to the value that we get from the sum rule in the infinite volumen case using the potential of Eq. (8.22), $Z = 0.63$. These values are in contrast with the case studied before where $X(3872)$ was generated by the potential of Ref. [183], where we obtain

$$-\sum_{i=1}^{2} g_i^2 \frac{\partial G_i}{\partial s} = 1 - Z = 0.97 \tag{8.24}$$

Therefore, the possible lattice data would be able even to tell the nature of the generated states by the present inverse problem. It is also worth noting that in our analysis we have not considered channels like $J/\psi\omega$ which
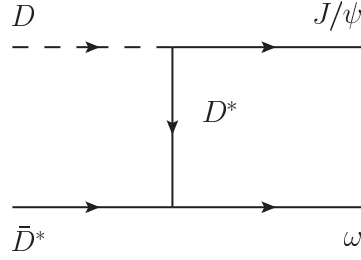
Figure 8.9: Mechanism for the transition from $D\bar{D}^*$ to $J/\psi\omega$.

certainly couple to the $D\bar{D}^*$ state. Indeed, within the local hidden gauge approach, that allows to extrapolate results of chiral dynamics to the heavy quark sector, we have a mechanism that connects these states, as show in Fig. 8.9. The diagram of Fig. 8.9 has a standard three vector vertex and a VVP (upper one) which requires an anomalous coupling that involves three momenta and furthermore requires the exchange of a heavy vector, with the subsequence reduction of the strength in the vector exchange, because of the large D^* mass. All these factors make this term subdominant in the large heavy quark mass, m_Q, counting when using heavy quark spin symmetry. As shown in Ref. [209] this term would vanish in the $m_Q \to \infty$ limit and is very small in practice. This justifies the neglect of this channel in the study that we have done. It is quite interesting to see that in the work of Ref. [190] considering or not the $J/\psi\omega$ channel does not practically change the results concerning the $X(3872)$, from where the authors conclude that "the $J/\psi\omega$ is not significantly coupled to the rest of the system".

To finalize, we would like to make an exercise of potential value to lattice QCD practitioners. Most likely, electromagnetic effects would be neglected in some lattice QCD simulations, eventually increasing the gap between the D^+D^{*-} and $D^0\bar{D}^{*0}$ masses. To estimate the effects of that approximation on the binding energy of the $X(3872)$ we have done the following exercises:

1. We increase m_{D^+} and $m_{D^{*-}}$ by one MeV each. Then we find that the energy of the $X(3872)$ changes from 3871.6 MeV to 3871.7 MeV. As one can see, the change in the energy, $\Delta E = 0.1$ MeV, has been much smaller than the change in the D^+D^{*-} mass of 2 MeV. This somehow indicates the larger weight of the $D^0\bar{D}^{*0}$ state in the mass of the system.

2. Similarly we decrease the mass of the D^0 and $\bar{D}^{*0}$ by one MeV each. Then we find an energy for the $X(3872)$ of 3869.8 MeV. This is a decrease for the energy of 1.8 MeV, nearly the 2 MeV change of the

$D^0\bar{D}^{*0}$ mass. Once again, this is telling us that the $D^0\bar{D}^{*0}$ state is mostly responsible for the mass of the $X(3872)$.

8.7 Conclusions

We have studied the $X(3872)$ state using the coupled channels D^+D^{*-} and $D^0\bar{D}^{*0}$ in a finite box. This is done for a small binding energy. In the direct problem, we have reproduced the energy dependence with the size of the box L in the two channel case. We obtain two energy curves for each level corresponding to the neutral and charged channels. On the other hand, we have addressed the inverse problem, obtaining the potential from the simulated lattice data with the aim of using it to evaluate the pole position in the infinite box case. The fit of the different setups give us an idea of what one should expect when analysing Lattice data. First one needs that the fit should be good enough, that is, a chi square function should be sufficiently small, in order to reproduce the small binding energies. In addition, we have observed that in order to get a good precision in the binding energy, one does not need to extract the lattice data with very small errors. Indeed, even with errors in the data points of 5 MeV, one can obtain the binding energy with 1 MeV (or even smaller value) precision. However, by looking at rows two and three of Table 8.2 it also becomes clear that very high precision in the binding energy requires small errors in the Lattice data. As seen in Fig. 8.6, this is necessary to distinguish between the levels of D^+D^{*-} and $D^0\bar{D}^{*0}$ at large L. From a practical point of view, knowing that it is difficult to get four levels in actual Lattice calculations, it is rewarding to see that with only two levels one can get quite an accurate value for the binding, provided the levels are evaluated at several values of L with enough precision. We also showed that having precise data even allowed us to obtain information on the dynamically generated nature of the $X(3872)$ state. We hope that this work gives a reference in the study of Lattice QCD for best strategies in order to obtain optimum values of the binding of the $X(3872)$ state. The results of this Chapter are published in Ref. [216].

Chapter 9

Conclusions

During this Thesis we have used Chiral Perturbation Theory and its extensions with the Hidden Gauge Formalism to face many problems in hadron physics. Mainly, we have studied the meson-baryon interaction to describe hadronic resonances and their properties, such as mass, width, partial decay widths, radiative decay and helicity amplitudes. The study of the vector meson - baryon interaction has been extended mixing pseudoscalar mesons with vector mesons in an approach that allows a better understanding of the nature of those hadronic states. We have used this formalism to calculate the transition diagrams to obtain the amplitudes in coupled channels that are included in the V potential matrix. Then we have used the Bethe-Salpeter equation to calculate the unitarized T-matrix using the G function, dimensional regularized with a subtraction constant. We look for poles in the complex plane changing to the second Riemann sheet and then we calculate the couplings for each channel that are determined as the residues of the poles. This procedure has been used to study N^* states with $J^P = 1/2^-$ and $3/2^-$ with much success, and we have shown that the mixing of the interaction of pseudoscalar meson - baryon with vector meson has been crucial when one tries to reproduce the experimental widths and branching ratios. Other problems involving meson - meson interaction with the few body approach or the finite volume have also been studied. We detail in the following the conclusions of the work done in this Thesis:

- **Radiative decay.** We have studied the radiative decay of $J^P = 1/2^-$ and $3/2^-$ dynamically generated resonances obtained with the hidden gauge formalism for the interaction of vector mesons with baryons of the octet and the decuplet of SU(3). The framework used takes into account that the photon couples to the resonance converting first into a vector meson ρ^0, ω or ϕ. Using this mechanism we have calculated

the radiative decay widths of these resonances to γB with B a baryon of the octet or the decuplet. We have obtained the decay widths of each third component of isospin I_3 for all the possible combinations of strangeness and isospin. The values of the decay widths are of the order of 1 MeV and one of the relevant features of the results is the large difference, of about one order of magnitude, between the widths of the different charge states of the same resonance. This result is a very useful information which should constitute a good test for the model. We have also calculated the helicity amplitudes of the N^* resonances previously studied. One can define the helicity amplitude $A_{1/2}$ and $A_{3/2}$ for the n and p, which makes the comparison with experimental data easier. Moreover we can now separate spin $J^P = 1/2^-$ and $3/2^-$ for the resonances which is useful in order to compare with data. It is interesting to note that the equations for the helicity amplitudes predict a ratio between $A_{1/2}^{J=3/2}$ and $A_{3/2}^{J=3/2}$ of $1/\sqrt{3}$, which is something that could be contrasted with experiment. We have done this and the results are in good agreement with data in some cases where comparison can be done.

- **The box diagram.** In this work we have studied the vector meson with baryon octet interaction using the hidden gauge formalism which produces nine dynamically generated resonances, degenerate for the quantum numbers $J^P = 1/2^-$ and $3/2^-$. However, the results for the widths found in this study are significantly smaller that the experimental values. This lead us to think that there could be another mechanism involved in the generation of those resonances that has not been taken into account. Since pseudoscalar mesons couple both to vector mesons and baryons, one can think that pseudoscalar mesons can play a role as intermediate states. This mechanism has been taken into account with a box diagram where a pseudoscalar meson and a baryon are the intermediate states. The idea is that the external vector meson decays into two pseudoscalar mesons, and one of them is exchanged and absorbed by the external baryon, so we have an intermediate state which propagates. Then the inverse mechanism occurs and we have again a vector meson and a baryon as final state. The integral of this box diagram is evaluated for each of the possible intermediate states for all the channels. Another important piece for the box is not only the meson exchange but also the Kroll-Ruderman vertex. Moreover this mechanism has an important consequence: since the Kroll-Ruderman term only contributes for $J^P = 1/2^-$, it allows to break the original degeneracy.

The addition of the box diagram to the potential produces a rewarding effect, widening the resonances and in some cases producing a small shift of the position of the peak. This is particularly clear in the the $S = 0$ sector where the $N^*(1650)(1/2^-)$ and the $N^*(1700)(3/2^-)$ degeneracy is broken and the masses and the widths for both states are well reproduced. In the other sectors the widths are also bigger and in better agreement with the results of the PDG than the original ones. The new couplings found, although they are somewhat different from the original ones, the moduli remain very similar for most of the cases.

- N^* **resonances with** $J^P = 3/2^-$**.** The $N^*(1520)(3/2^-)$ is catalogued as a four-star resonance in the PDG and the $N^*(1700)(3/2^-)$ is catalogued as a three-star resonance, however, this later state is not found in some recent analysis but it is included in others. In view of this apparent disagreement we have studied the D_{13} partial wave amplitude of πN scattering extracted from experimental data in order to find out the existence or not of the $N^*(1700)$. We have studied the mixing of pseudoscalar mesons - baryon interaction with vector mesons - baryon interaction with $J^P = 3/2^-$ including the coupled channels ρN (s-wave), πN (d-wave), $\pi \Delta$ (s-wave) and $\pi \Delta$ (d-wave). The novelty of this work is that using the transition of the box, where the pseudoscalar meson - baryon was the intermediate state, we can evaluate the transition of $VB \rightarrow PB$, beyond the consideration of only the Kroll-Ruderman term as done in other works.
  We have fitted the real and the imaginary parts of the T-matrix to the D_{13} partial wave amplitude of πN scattering data in the region of $\sqrt{s} = 1400 - -1800$ MeV, taking as free parameters the subtraction constants for each channel and three parameters of the d-wave transitions. All the subtraction constants obtained are of natural size. The first important result is that, if we want to reproduce the data, two poles appear and it is worth noting that the presence of two poles is rather solid, since moderate changes in the parameters do not spoil the results of the poles. We have also determined the partial decay widths to all channels and have found an excellent agreement for the branching ratios of $N^*(1520)$ and a fair agreement for $N^*(1700)$.

- N^* **resonances with** $J^P = 1/2^-$**.** We have extended the previous study to the $J^P = 1/2^-$ sector, including other meson-baryon channels as ηN, $K\Lambda$ and $K\Sigma$. Some other works trying to describe the $N^*(1535)(1/2^-)$ as a dynamically generated resonance using coupled channels involving pseudoscalar mesons - baryon interaction found that

some of the subtraction constants were quite different from the "natural size" and in some cases even positive. Moreover the $N^*(1650)$ state was not found using this former formalism. In this work we have included channels of vector meson - baryon interaction and the $\pi\Delta$ (d-wave) channel which provide the missing elements that allow to get a more realistic picture.

We have used the πN, ηN, $K\Lambda$, $K\Sigma$, ρN and $\pi\Delta$ (d-wave) in coupled channels to fit the experimental data of the S_{11} πN scattering. The subtraction constant obtained from the fit are now all negative and of natural size. Moreover the consideration of the ρN and $\pi\Delta$ channels has an important qualitative change, now we are able to generate both the $N^*(1535)$ and the $N^*(1650)$ resonances which is an important success of the mixing of pseudoscalar and vector mesons. We can conclude that the important component of a genuine state in the wave function of the $N^*(1535)$ claimed in other works, can be translated now by stating that the missing components can be filled up by the ρN and $\pi\Delta$ channels that we have found here.

- **Limits to the Fixed Center Approximation.** The fixed center approximation to the Faddeev equations is a good approximation when two particles are clustered in a bound system and a third particle leads also to binding with the components of the cluster. This approximation is valid when the two bound particles of the cluster are not excited in an intermediate state, which is most likely when there is no energy available to excite it. This will happen if the state is bound with respect to the mass of the three particles. The case of our study is the $\phi(2170)$ particle as a resonant state of the ϕ and $f_0(980)$ states. In this case the $\phi f_0(980)$ system has 170 MeV of excitation, so there is plenty of energy to excite the f_0 in intermediate states. Our analysis does not lead to any peak structure around the $\phi(2170)$. Moreover we have determined the contribution of the Faddeev diagram that involves the $K\bar{K}$ interaction with the collision of ϕK or $\phi\bar{K}$, and which is responsible for the failure of the FCA. We have found that this mechanism is of the same order of magnitude as the ϕK double scattering from the FCA series. Furthermore, those two mechanisms have amplitudes with opposite signs and their simultaneous consideration would change drastically the results obtained from the double scattering contribution of the FCA alone. In view of this, any approach to this problem should take into account this fact. However, if one tries to improve the FCA including these inelastic excitations, one would face a problem involving higher iterations which would become a more complicated problem

than the use of Faddeev equations from the beginning.

- **Binding energy of** $X(3872)$**.** We have approached the problem of accurately determining the binding energy of the $X(3872)$ in the finite volume. The $X(3872)$ is a resonance dynamically generated with the coupled channels D^+D^{*-} and $D^0\bar{D}^{*0}$ with a binding energy close to the $D^0\bar{D}^{*0}$ threshold. We have studied the DD^* system in the finite box using the hidden gauge formalism in SU(4) for the interaction of the components and then we have studied the scattering amplitude in a finite volume, finding discrete energy levels depending on the size of the box L. The first relevant finding is that we obtain a splitting of the energy levels depending on the size of the box, in contrast to what happens when one considers a single channel system. This is understood by looking at the $\tilde{G}$ function were the free energies appear as asymptotes, so with two channels new asymptotes show up, and as we get an energy level between two adjacent asymptotes, new levels will appear.

  After that, we have studied the inverse problem. We generate pseudo-data emulating the data that would be provided by lattice practitioners. Then we fit the data with a generic energy dependent potential and we get the binding energy which provides the fitted potential. The study consists in seeing the uncertainty of the binding energy depending on the number of points obtained with different box sizes, errors of the energy levels, number of levels, etc. The conclusions extracted of the analysis show that even with errors in the data points of 5 MeV, one can get a binding energy with a precision of 1 MeV, which is very rewarding. Moreover we have observed that with only the first level of the box, that is two trajectories, one can get a good precision whenever enough points for different size of the box L are provided. The idea has been to shed light to produce optimal strategies for a precise determination of the binding energy in future lattice analyses. Finally we have studied the nature of the $X(3872)$ state as a dynamically generated resonance and show that such information can be obtained from Lattice data.

Resumen en español

10.1 Introducción

A mediados de los años 50 se encontraron un gran número de partículas, sin otro tipo de clasificación que unos números cuánticos complicadamente deducidos de una forma tan extraña que por aquel entonces inspiraron el nombre de uno de ellos. Sin embargo, en 1961 Gell-Mann propuso un teoría [1, 2] que clasificaba los bariones y mesones en octetes y decupletes dependiendo de su isospin e hipercarga. Esto llevó a la predicción de los quarks debido a la simetría SU(3) de sabor que subyace en esta teoría.

El modelo de quark tuvo mucho éxito ya que daba una explicación natural a por qué había un octete de bariones con $J^P = 1/2^+$ y un decuplete con $J^P = 3/2^+$. También predijo nuevas partículas como la Ω^- con S=-3, descubierta en 1965 [3] y permitió hacer estimaciones de masas y momentos magnéticos de los hadrones. Por otra parte, se predijo el número cuántico del color debido a la necesidad de antisimetría de la función de onda de la Δ^{++} con $J^P = 3/2^+$. Sin embargo se encontraron algunos hadrones como la $N^*(1440)(J^P = 1/2^+)$[4], $N^*(1535)(J^P = 1/2^-)$ o $\Lambda(1405)(J^P = 1/2^-)$ que parecían no encajar en los octetes y decupletes, y por ello se supuso que eran estados excitados de los hadrones.

La explicación más intuitiva para los estados excitados era suponer que los quarks constituyentes eran excitados a un nivel diferente de un fuerte potencial atractivo que actuaba sobre los quarks. Esta fue la linea de estudio de estos estados hadrónicos excitados [5, 6, 7]. Aun así, era curioso observar mirando la masa de los primeros bariones excitados, que las energías de excitación de los quarks eran del orden de 500 MeV. Por ello nos podríamos preguntar por qué no se creaban varios piones en vez que un quark fuera excitado, ya que energéticamente era más favorable. Debía de haber alguna

respuesta, ya que en algunos casos la dinámica del sistema no tenía atracción suficiente como para ligar estos estados. Pero quizás en algunos casos las condiciones eran tales que estados ligados o resonancias podrían aparecer al añadir uno o más mesones al estado hadrónico fundamental. Para responder a esta pregunta se necesitaba abordar la dinámica de la interacción de hadrones de una forma correcta, y muchos pasos se dieron en esa dirección.

10.1.1 Lagrangianos efectivos y Teoría de Perturbaciones Quiral

La idea de Weinberg [8] de describir la física hadrónica a bajas energías usando Lagrangianos quirales que contienen las simetrías básicas de QCD ha sido muy fructífera. La introducción de la simetría quiral, contenida en QCD, en los Lagrangianos efectivos condujo a los Lagrangianos Quirales, que han sido estudiados en detalle en la Ref. [9]. Con estos Lagrangianos se han estudiado muchos problemas de la física hadrónica usando técnicas perturbativas que dio lugar a la Teoría de Perturbaciones Quiral (χPT) la cual ha tenido un éxito innegable. Sin embargo, χPT tiene sus limitaciones, como toda otra teoría. En el caso de la interacción $\pi\pi$ la expansión en serie perturbativa tiene su límite en la primera singularidad, la cual corresponde al polo de la resonancia σ, alrededor de los 500 MeV de energía. El siguiente paso fue combinar la información de los Lagrangianos Quirales con la unitariedad de los canales acoplados [10, 11]. Se obtiene así un formalismo no perturbativo que permite extender la información contenida en los Lagrangianos Quirales a energías más altas, conocido como Teoría Unitaria Quiral o Teoría de Perturbaciones Quiral Unitarizada, UχPT.

Uno de los resultados más espectaculares de UχPT, es la generación dinámica de resonancias, lo cual significa que empezando con la interacción mesón-mesón en canales acoplados y usando técnicas unitarias, se obtienen las amplitudes de colisión mesón-mesón en las cuales pueden aparecer polos que correspondes a estados ligados o resonancias. De este modo se pueden obtener diversos mesones escalares como σ, $f_0(980)$, $a_0(980)$, etc. en los canales mesónicos, y también resonancias bariónicas con $J^P = 1/2^-$, como la $N^*(1535)$, o dos polos para la $\Lambda(1405)$ [12]. Se entiende que estos estados son estados compuestos por mesón-mesón o mesón-barión, de la misma manera que el deuterón es un estado compuesto de protón-neutrón y no un grupo de seis quarks descorrelacionados. Estos resultados rompen con el esquema de que los mesones están compuestos por $q\bar{q}$ y los bariones por qqq. Esta teoría produce buenos resultados para las amplitudes de colisión entre mesones y para mesón-barión, y también permite calcular propiedades

de las resonancias, como anchuras parciales de desintegración, momentos
magnéticos, amplitudes de helicidad, y además permite abordar procesos de
producción de esas partículas satisfactoriamente.

Recientemente la interacción entre vectores y de vectores con bariones está
siendo estudiada. La interacción de vectores está descrita por otra teoría, el
hidden gauge de Bando et al. [13], la cual incluye la simetría quiral y conduce
al mismo Lagrangiano Quiral para la interacción mesón-mesón incluyendo
además los mesones vectoriales.

10.1.2 Resonancias dinámicamente generadas

El uso de los Lagrangianos Quirales en combinación con técnicas unitarias en
canales de mesones y bariones ha sido un esquema muy conveniente para el
estudio de la naturaleza de muchas resonancias hadrónicas. El análisis de las
amplitudes de dispersión mesón-barión contienen polos en la segunda hoja
de Riemann que se identifican con resonancias bariónicas. De este modo la
interacción del octete de mesones pseudoescalares con el octete de bariones
ha llevado a las resonancias con $J^P = 1/2^-$ las cuales encajan bastante bien
con el espectro conocido de resonancias con esos números cuánticos, como se
puede ver en las Refs. [14, 15, 16, 17, 18, 19, 20, 21, 22]. De forma similar,
la interacción del octete de mesones pseudoescalares con el decuplete de bar-
iones también ha llevado a muchas resonancias que pueden ser identificadas
con las ya existentes con $J^P = 3/2^-$ [23, 24]. De vez en cuando se predice
una nueva resonancia, como en el caso de la $\Lambda(1405)$, donde el análisis quiral
encuentra dos polos cerca uno del otro, en vez de solo uno, hecho que ha hal-
lado apoyo experimental en los análisis de las Refs. [25, 26]. La naturaleza
de las resonancias es más compleja que solo una molécula de un mesón pseu-
doescalar y un barión, pero el éxito de esta visión al reproducir tantos datos
experimentales de desintegración y producción de resonancias, proporciona
un soporte para reivindicar que en la función de onda de la resonancia existe
una gran componente de esta índole.

Se ha realizado mucho trabajo usando mesones pseudoescalares como blo-
ques fundamentales, pero el considerar mesones vectoriales en vez de mesones
pseudoescalares está solo empezado a ser explotado. En el sector bariónico
la interacción de $\rho\Delta$ ha sido recientemente abordada en la Ref. [27], donde
se han encontrado tres estados degenerados N^* entorno a los 1800 MeV y
tres estados degenerados Δ sobre los 1900 MeV con $J^P = 1/2^-$, $3/2^-$, $5/2^-$.
Este trabajo ha sido recientemente extendido al espacio SU(3) de vectores
con bariones del decuplete en la Ref. [28] y con bariones del octete en la
Ref. [29]. La teoría que subyace en este estudio es el formalismo de hidden
gauge de las Refs. [30, 13, 31], el cual trata la interacción de los mesones vec-

toriales y pseudoescalares respetando la dinámica quiral, proporcionando la interacción de mesones pseudoescalares entre ellos, con mesones vectoriales y de los mesones vectoriales entre ellos mismos. En un trabajo reciente en la Ref. [32], el análisis de polos en las amplitudes de dispersión de πN, también incluye el canal ρN y genera dinámicamente una resonancia en torno a los 1700 MeV, la cual tiene un fuerte acoplamiento a este último canal.

En el sector mesónico, con este formalismo la interacción $\rho\rho$ se ha llevado a cabo en la Ref. [33], donde se ha llegado a la generación dinámica de las resonancias mesónicas $f_2(1270)$ y $f_0(1370)$, con una anchura de desintegración al canal $\gamma\gamma$ en concordancia con el experimento realizado en la Ref. [34].

10.2   Formalismo

La Cromodinámica Cuántica (QCD) es la teoría que subyace bajo la interacción fuerte y describe la interacción entre quarks y gluones. Esta teoría esta bien entendida y estudiada a altas energías y ha sido probada muchas veces experimentalmente. QCD presenta una propiedad denominada "confinamiento" que hace que en la naturaleza solo existan "singletes de color", también llamados hadrones tales como protones, neutrones, piones, etc. Los quarks individuales están confinados en los hadrones y no pueden escapar. Hay otra propiedad de QCD, "libertad asintótica" que dice que a altas transferencias de momento los quarks se comportan como libres y los cálculos perturbativos de QCD son posibles. Sin embargo a bajas energías la "running coupling constant", o constante efectiva de la teoría, crece rápidamente. Desafortunadamente, los métodos perturbativos de QCD no pueden ser aplicados en este régimen, pero por otro lado, en la última década se han hecho grandes avances en estudios no-perturbativos como Lattice o reglas de suma de QCD.

No obstante, las teorías efectivas son una de las herramientas más útiles en el estudio de física hadrónica a bajas energías. La simetría de SU(3) contenida en el Lagrangiano de QCD, puede ser extendida a los estados mesónicos de más baja energía (π, k, η). Esto es entendido bajo la simetría quiral de los quarks ligeros (u, d, s) la cual está rota espontáneamente lo que lleva a los bosones de Goldstone y al desarrollo de una teoría llamada Teoría Quiral Perturbativa (χPT) (Ver las Refs. [38, 39] para más detalles).

La densidad Lagrangiana efectiva más general, que es invariante bajo transformaciones quirales, con el mínimo número de derivadas viene dada por

$$\mathcal{L}_{eff} = \frac{f^2}{4} Tr \left(\partial_\mu U \partial^\mu U^\dagger \right) \qquad (10.1)$$

donde $f \approx 93$ MeV es un parámetro libre el cual más adelante estará relacionado con la constante de desintegración del pión y

$$U(x) = e^{i\sqrt{2}\phi(x)/f} \tag{10.2}$$

Primero podemos comprobar que el Lagrangiano es invariante bajo la transformación global $SU(3)_L \times SU(3)_R$

$$U \rightarrow RUL^\dagger \tag{10.3}$$
$$\partial_\mu U \rightarrow R\partial_\mu UL^\dagger \tag{10.4}$$
$$U^\dagger \rightarrow LU^\dagger R^\dagger \tag{10.5}$$
$$\partial_\mu U^\dagger \rightarrow L\partial_\mu U^\dagger R^\dagger \tag{10.6}$$

Así pues,

$$\mathcal{L}_{eff} \rightarrow \frac{f^2}{4}Tr\left(R\partial_\mu UL^\dagger L\partial^\mu U^\dagger R^\dagger\right) \tag{10.7}$$

$$= \frac{f^2}{4}Tr\left(R^\dagger R\partial_\mu U\partial^\mu U^\dagger\right) = \mathcal{L}_{eff} \tag{10.8}$$

En $U(x)$ del Lagrangiano de la Eq. (10.1), $\phi(x)$ está relacionada con el campo de los mesones y las matrices de Gell-Mann mediante

$$\phi(x) = \sum_{a=1}^{8} \frac{1}{\sqrt{2}}\lambda_a\phi_a(x) = \begin{pmatrix} \phi_3 + \frac{1}{\sqrt{3}}\phi_8 & \phi_1 - i\phi_2 & \phi_4 - i\phi_5 \\ \phi_1 + i\phi_2 & -\phi_3 + \frac{1}{\sqrt{3}}\phi_8 & \phi_6 - i\phi_7 \\ \phi_4 + i\phi_5 & \phi_6 + i\phi_7 & -\frac{2}{\sqrt{3}}\phi_8 \end{pmatrix} \tag{10.9}$$

que en términos de los campos de mesones es

$$P = \begin{pmatrix} \frac{\pi^0}{\sqrt{2}} + \frac{\eta_8}{\sqrt{3}} & \pi^+ & K^+ \\ \pi^- & -\frac{\pi^0}{\sqrt{2}} + \frac{\eta_8}{\sqrt{3}} & K^0 \\ K^- & \bar{K}^0 & -\frac{2}{\sqrt{3}}\eta_8 \end{pmatrix} \tag{10.10}$$

El acoplamiento de los mesones pseudoescalares al octete de bariones de $SU(3)$ viene dado por

$$\mathcal{L}_{BBP} = \frac{F}{2}\langle\bar{B}\gamma_\mu\gamma_5[u^\mu, B]\rangle + \frac{D}{2}\langle\bar{B}\gamma_\mu\gamma_5\{u^\mu, B\}\rangle \tag{10.11}$$

donde $F = 0.51$ y $D = 0.75$, y B es una matriz que contiene los campos del octete de bariones

$$B = \begin{pmatrix} \frac{1}{\sqrt{2}}\Sigma^0 + \frac{1}{\sqrt{6}}\Lambda & \Sigma^+ & p \\ \Sigma^- & -\frac{1}{\sqrt{2}}\Sigma^0 + \frac{1}{\sqrt{6}}\Lambda & n \\ \Xi^- & \Xi^0 & -\frac{2}{\sqrt{6}}\Lambda \end{pmatrix} \tag{10.12}$$

Al orden más bajo en el campo de mesones pseudoescalares

$$u^{\mu} = -\frac{\sqrt{2}}{f}\partial^{\mu}P \tag{10.13}$$

donde para el caso del octete de mesones pseudoescalares, la matriz P está dad por ϕ de la Eq. (10.10), lo cual nos permite reescribir el Lagrangiano de la Eq. (10.11) como

$$\mathcal{L}_{BBP} = -\frac{\sqrt{2}}{f}\frac{D+F}{2}\langle\bar{B}\gamma_{\mu}\gamma_5\partial^{\mu}PB\rangle - \frac{\sqrt{2}}{f}\frac{D-F}{2}\langle\bar{B}\gamma_{\mu}\gamma_5 B\partial^{\mu}P\rangle \tag{10.14}$$

Para un caso particular de un mesón pseudoescalar P, el cual se acopla a dos bariones B_1 y B_2, el Lagrangiano anterior se puede escribir en términos de un vértice efectivo como

$$-it_{B_1B_2P} = \left\{\alpha\frac{(D+F)}{2f} + \beta\frac{(D-F)}{2f}\right\}\vec{\sigma}\vec{k} \tag{10.15}$$

donde $\vec{k}$ es el momento entrante del mesón en el vértice BBP. Los coeficientes α y β pueden encontrarse en el Apéndice D.

10.2.1   El formalismo de hidden gauge

El formalismo de hidden gauge [30, 13, 31, 40] incluye la interacción de mesones vectoriales, fotones y mesones pseudoescalares. El Lagrangiano de este formalismo viene dado por

$$\mathcal{L} = \mathcal{L}^{(2)} + \mathcal{L}_{III} \tag{10.16}$$

$$\mathcal{L}^{(2)} = \frac{1}{4}f^2\langle D_{\mu}UD^{\mu}U^{\dagger} + \chi U^{\dagger} + \chi^{\dagger}U\rangle \tag{10.17}$$

$$\mathcal{L}_{III} = -\frac{1}{4}\langle V_{\mu\nu}V^{\mu\nu}\rangle + \frac{1}{2}M_V^2\langle\left[V_{\mu} - \frac{i}{g}\Gamma_{\mu}\right]^2\rangle \tag{10.18}$$

donde la derivada covariante está definida como

$$D_{\mu}U = \partial_{\mu}U - ieQA_{\mu}U + ieUQA_{\mu}, \tag{10.19}$$

donde V_{μ}, A_{μ} son los campos de vectores y fotones y Q es la matriz de carga, $Q = diag(2, -1, -1)/3$. χ corresponde a la matriz de masas. En la Eq. (10.18), V_{μ} es la matriz SU(3) para el nonete de mesones vectoriales

$$V_{\mu} = \begin{pmatrix} \frac{\rho^0}{\sqrt{2}} + \frac{\omega}{\sqrt{2}} & \rho^+ & K^{*+} \\ \rho^- & -\frac{\rho^0}{\sqrt{2}} + \frac{\omega}{\sqrt{2}} & K^{*0} \\ K^{*-} & \bar{K}^{*0} & \phi \end{pmatrix}_{\mu} \tag{10.20}$$

y g es el acoplamiento de la teoría $g = \frac{M_V}{2f}$ con M_V la masa del vector. La interacción de los vectores con los fotones y los pseudoescalares se tiene en cuenta por medio de Γ_μ

$$\Gamma_\mu = \frac{1}{2}\left[u^\dagger\left(\partial_\mu - ieQA_\mu\right)u + u\left(\partial_\mu - ieQA_\mu\right)u^\dagger\right] \tag{10.21}$$

donde el campo u está definido como

$$u^2 = U = e^{i\sqrt{2}\phi/f} \tag{10.22}$$

La magnitud $V_{\mu\nu}$ para los mesones vectoriales viene dada por

$$V_{\mu\nu} = \partial_\mu V_\nu - \partial_\nu V_\mu - ig\left[V_\mu, V_\nu\right] \tag{10.23}$$

y el segundo término en el Lagrangiano de la Eq. (10.18) viene dado por

$$
\begin{aligned}
\left[V_\mu - \frac{i}{g}\Gamma_\mu\right]^2 &= \left(V_\mu - \frac{e}{g}QA_\mu - \frac{1}{g}\frac{1}{2f^2}\phi eQA_\mu\phi + \frac{1}{g}\frac{1}{4f^2}\phi^2 eQA_\mu\right. \\
&\quad \left. + \frac{1}{g}\frac{1}{4f^2}eQA_\mu\phi^2 - \frac{i}{g}\frac{1}{4f^2}\left[\phi, \partial_\mu\phi\right]\right)^2
\end{aligned}
\tag{10.24}
$$

Del Lagrangiano anterior se pueden obtener los siguientes términos de interacción entre mesones pseudoescalares, mesones vectoriales y fotones.

$$\mathcal{L}_{V\gamma} = -M_V^2\frac{e}{g}A_\mu\langle V^\mu Q\rangle \tag{10.25}$$

$$\mathcal{L}_{V\gamma PP} = e\frac{M_V^2}{4gf^2}A_\mu\langle V^\mu(Q\phi^2 + \phi^2 Q - 2\phi Q\phi)\rangle \tag{10.26}$$

$$\mathcal{L}_{VPP} = -i\frac{M_V^2}{4gf^2}\langle V^\mu[\phi, \partial_\mu\phi]\rangle \tag{10.27}$$

$$\mathcal{L}_{\gamma PP} = ieA_\mu\langle Q[\phi, \partial_\mu\phi]\rangle \tag{10.28}$$

$$\widetilde{\mathcal{L}}_{PPPP} = -\frac{1}{8f^2}\langle[\phi, \partial_\mu\phi]^2\rangle. \tag{10.29}$$

Los diagramas de estos vértices están representados individualmente en la Fig. 10.1.

10.2.2 Formalismo para la interacción VV

Partiendo del Lagrangiano de la Eq. (10.18) se puede obtener la interacción entre mesones vectoriales como

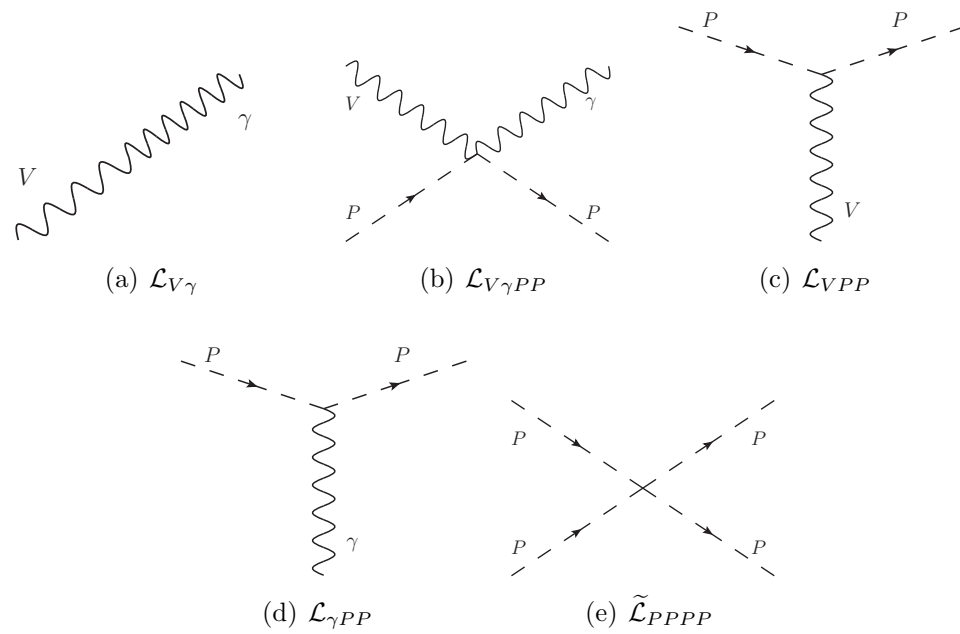$$\mathcal{L}_V = -\frac{1}{4}\langle V_{\mu\nu}V^{\mu\nu}\rangle \tag{10.30}$$

Figure 10.1:   Diagramas de interacción que involucran mesones pseudoescalares, mesones vectoriales y fotones del Lagrangiano de la Eq. (10.16).
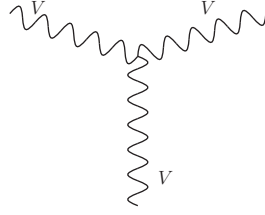
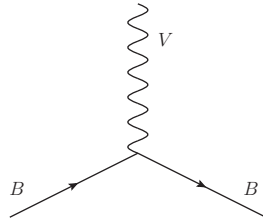Figure 10.2: Vértice de tres vectores del Lagrangiano de la Eq. (10.39).

Figure 10.3: Vértice del mesón vectorial con el octete de bariones del Lagrangiano de la Eq. (10.34).

el símbolo $\langle\rangle$ se refiere a la traza en el espacio de SU(3) donde el término $V_{\mu\nu}$ viene dado en la Eq. (10.23)

$$V_{\mu\nu} = \partial_\mu V_\nu - \partial_\nu V_\mu - ig\left[V_\mu, V_\nu\right] \tag{10.31}$$

Este Lagrangiano genera dos términos de contacto, uno de tres y otro de cuatro mesones vectoriales

$$\mathcal{L}^{(4V)} = \frac{g^2}{2}\langle V_\mu V_\nu V^\mu V^\nu - V_\nu V_\mu V^\mu V^\nu\rangle \tag{10.32}$$

$$\mathcal{L}^{(3V)} = ig\langle(V^\mu\partial_\nu V_\mu - \partial_\nu V_\mu V^\mu)V^\nu\rangle \tag{10.33}$$

Estamos interesados en el vértice de tres vectores de la Fig. 10.2 ya que será usado en la interacción mesón vectorial - barión. La interacción de mesones vectoriales con el octete de bariones se introduce de la misma manera que con los mesones pseudoescalares, usando el siguiente Lagrangiano

$$\mathcal{L}_{BBV} = g\left(\langle\bar{B}\gamma_\mu[V^\mu, B]\rangle + \langle\bar{B}\gamma_\mu B\rangle\langle V^\mu\rangle\right) \tag{10.34}$$

donde B es la matriz SU(3) del octete de bariones dada en la Eq. (10.12). El diagrama de este vértice se muestra en la Fig. 10.3. Además, la interacción de los mesones vectoriales con el decuplete de bariones ha sido estudiada

usando el Lagrangiano para la interacción de los mesones vectoriales con el decuplete de bariones, dado en la Ref. [41] por

$$\mathcal{L} = -i\bar{T}^\mu D_\nu \gamma^\nu T_\mu \tag{10.35}$$

donde T^μ_{abc} son los campos de spin del decuplete, siendo a, b, c los índices SU(3), tales que

$$
\begin{aligned}
T^{111} &= \Delta^{++}, & T^{112} &= \tfrac{1}{\sqrt{3}}\Delta^+, & T^{122} &= \tfrac{1}{\sqrt{3}}\Delta^0, & T^{222} &= \Delta^-, \\
T^{113} &= \tfrac{1}{\sqrt{3}}\Sigma^{*+}, & T^{123} &= \tfrac{1}{\sqrt{6}}\Sigma^{*0}, & T^{223} &= \tfrac{1}{\sqrt{3}}\Sigma^{*-}, \\
T^{133} &= 6\tfrac{1}{\sqrt{3}}\Xi^{*0}, & T^{233} &= \tfrac{1}{\sqrt{3}}\Xi^{*-}, & T^{333} &= \tfrac{1}{\sqrt{3}}\Omega^-
\end{aligned}
\tag{10.36}
$$

La derivada convariante D^ν es

$$D^\nu T^\mu_{abc} = \partial^\nu T^\mu_{abc} + (\Gamma^\nu)^d_a T^\mu_{dbc} + (\Gamma^\nu)^d_b T^\mu_{adc} + (\Gamma^\nu)^d_c T^\mu_{abd} \tag{10.37}$$

donde Γ^ν es la corriente vectorial

$$\Gamma^\nu = -\frac{1}{4f^2}\left(V^\mu \partial^\nu V_\mu - \partial^\nu V_\mu V^\mu\right) \tag{10.38}$$

10.2.3   Lagrangianos de la interacción mesón-barión

Uno de los estudios más relevantes realizados en este trabajo, es la interacción de los mesones vectoriales con los bariones cuando se intercambia un mesón vectorial. Para la interacción entre mesones vectoriales, tenemos el Lagrangiano de tres vectores

$$\mathcal{L}^{(3V)}_{III} = ig\langle(\partial_\mu V_\nu - \partial_\nu V_\mu)V^\mu V^\nu\rangle \ , \tag{10.39}$$

donde V_μ es la matriz $SU(3)$ del nonete de ρ dado por la Eq. (10.20) y $g = \frac{M_V}{2f}$, con f=93 MeV. El Lagrangiano de la Eq. (10.39) puede ser reescrito de una forma más conveniente de la siguiente forma

$$
\begin{aligned}
\mathcal{L}^{(3V)}_{III} &= ig\langle V^\nu \partial_\mu V_\nu V^\mu - \partial_\nu V_\mu V^\mu V^\nu\rangle \\
&= ig\langle V^\mu \partial_\nu V_\mu V^\nu - \partial_\nu V_\mu V^\mu V^\nu\rangle \\
&= ig\langle(V^\mu \partial_\nu V_\mu - \partial_\nu V_\mu V^\mu)V^\nu\rangle
\end{aligned}
\tag{10.40}
$$

De la misma manera, el acoplamiento de los vectores a los pseudoescalares viene dado por el Lagrangiano de la Eq. (10.27)

$$\mathcal{L}_{VPP} = -ig\langle[P, \partial_\nu P]V^\nu\rangle \ , \tag{10.41}$$
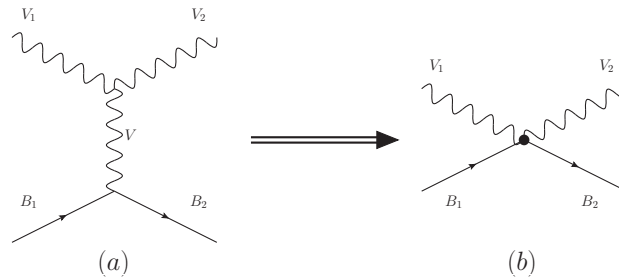
Figure 10.4: Interación mesón vectorial-barión: (a) mediante el intercambio de un mesón vectorial (b) término de contacto.

donde aquí P es la matriz $SU(3)$ de los mesones pseudoescalares de la Eq. (10.10). El Lagrangiano para el acoplamiento de los mesones vectoriales a los bariones viene dado en la Eq. (10.34) donde B es la matriz $SU(3)$ del octete de bariones de la Eq. (10.12). Esta interacción se ha estudiado para el caso del octete de bariones en la Ref. [29] y para el caso del decuplete de bariones en la Ref. [28]. Como se muestra en la Ref. [29], el término dominante para la interacción $VB \to VB$ involucra el vértice de tres vectores de la Eq. (10.39), donde uno de los vectores se intercambia, y el acoplamiento del vector intercambiado al barión viene dado en la Eq. (10.34). En ambos trabajos, el diagrama de intercambio del mesón vectorial de la Fig. 10.4(a) se convierte en el término de contacto de la Fig. 10.4(b) despreciando el trimomento frente a la masa del mesón vectorial que se intercambia. Manteniendo el término dominante γ^0 en la Eq. (10.34) el potencial dado por este término es

$$V_{ij} = -C_{ij} \frac{1}{4f^2} \left(k^0 + k'^0 \right) \ \vec{\epsilon}\vec{\epsilon}' \tag{10.42}$$

donde k^0, k'^0 son las energías de los mesones vectoriales entrante y saliente respectivamente. El resultado de la Eq. (10.42), con el factor $\vec{\epsilon}\vec{\epsilon}'$ para la polarización de los mesones vectoriales, se obtiene al considerar el trimomento de los vectores externos pequeño con respecto a la masa de los mesones vectoriales. La factorización explícita del término de spin en el potencial, produce una degeneración del spin de los estados que se encuentran cuando se usa este potencial. Este hecho esta estudiado en detalle en el Apéndice A. Los coeficientes C_{ij} del potencial mesón vectorial - barión del octete para todos los estados de isospin y extrañeza, se pueden encontrar en el Apéndice A de la Ref. [29], donde los subíndices i y j corresponden a los diferentes canales. La matriz V es el potencial de los términos que se muestran en la
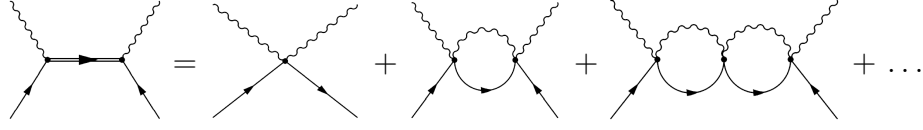
Figure 10.5: Primeros diagramas involucrados en la ecuación de Bethe-Salpeter.

Fig. 10.5, donde los diagramas sucesivos se pueden expresar como

$$T = V + V\,G\,V + V\,G\,V\,G\,V + \dots \tag{10.43}$$

que puede ser reescrito como

$$T = V + V\,G\,T \tag{10.44}$$

Esta expresión se puede expresar en la forma estándar de la ecuación de Bethe-Salpeter dada por

$$T = [1 - V\,G]^{-1}\,V \tag{10.45}$$

donde G es la función loop de un mesón vectorial y un barión, la cual esta calculada con regulación dimensional, como se muestra en las Refs. [18, 42], y viene dada por

$$
\begin{aligned}
G &= i2M \int \frac{d^4q}{(2\pi)^4} \frac{1}{(P-q)^2 - M^2 + i\epsilon} \frac{1}{q^2 - m^2 + i\epsilon} \\
&= \frac{2M}{16\pi^2} \left\{ a(\mu) + \ln\frac{M^2}{\mu^2} + \frac{m^2 - M^2 + s}{2s} \ln\frac{m^2}{M^2} + \right. \\
&\quad + \frac{q}{\sqrt{s}} \left[\ln(s - (M^2 - m^2) + 2q\sqrt{s}) + \ln(s + (M^2 - m^2) + 2q\sqrt{s}) \right. \\
&\quad \left. \left. - \ln(-s + (M^2 - m^2) + 2q\sqrt{s}) - \ln(-s - (M^2 - m^2) + 2q\sqrt{s}) \right] \right\}
\end{aligned}
\tag{10.46}
$$

con μ una escala de regularización y $a(\mu)$ la constante de substracción, que depende del canal. Existe una relación entre estos dos parámetros μ y α la cuál viene dada explícitamente por

$$\alpha'(\mu') = \alpha(\mu) + log(\frac{\mu'^2}{\mu^2}) \tag{10.47}$$

Esta relación se ha estudiado en detalle en la Ref. [18], donde, ajustando el polo de la $\Lambda(1405)$, los autores encuentran que con una escala de regularización de $\mu =$630 MeV, el valor natural para la constante de substracción α

es -2. Usando estos valores, se puede fijar un valor para μ y después trabajar solo con la constante de substracción, ya que existe una relación inequívoca. En la literatura, diversos autores usan diferentes escalas de regularización, lo que hace necesario el ser capaz de comparar resultados mediante esta relación.

Comúnmente, la constante de substracción α se ajusta para obtener la posición del polo o para reproducir una amplitud. A veces, para reproducir los datos se necesita una constante de substracción diferente para cada canal, pero en otros casos, un constante de substracción global es suficiente.

La Eq. (10.45) es la llamada ecuación factorizada on shell Bethe-Salpeter (BS), a pesar de que se puede encontrar con otros nombres en la literatura. La Eq. (10.45) suma los términos de la ecuación de Lippmann-Schwinger o términos escalera, pero usando cinemática relativista, y en la integral implícita del término VGT de la ecuación Bethe-Salpeter, los términos V y T están factorizados fuera de la integral. Esto está justificado usando el método N/D y las relaciones de dispersión usadas en las Refs. [43, 18].

10.2.4 Convolución de la función loop

En los casos en los que la iteración de la ecuación Bethe-Salpeter involucra partículas que tienen una anchura considerablemente grande, como la ρ, el mesón K^* o la Δ, es necesario hacer una convolución de la función loop respecto a la distribución de masa. La función loop con la convolución para el caso del mesón ρ es

$$\tilde{G}(s) = \frac{1}{N_\rho} \int_{(m_\rho - 2\Gamma_\rho)^2}^{(m_\rho + 2\Gamma_\rho)^2} d\tilde{m}^2 \left(-\frac{1}{\pi}\right) \text{Im} \frac{1}{\tilde{m}^2 - m_\rho^2 + i\tilde{m}\Gamma(\tilde{m})} G(s, \tilde{m}^2, M_B^2)$$
(10.48)

donde $\tilde{G}$ está normalizada con

$$N_\rho = \int_{(m_\rho - 2\Gamma_\rho)^2}^{(m_\rho + 2\Gamma_\rho)^2} d\tilde{m}^2 \left(-\frac{1}{\pi}\right) \text{Im} \frac{1}{\tilde{m}^2 - m_\rho^2 + i\tilde{m}\Gamma(\tilde{m})}$$
(10.49)

Considerando que la anchura de la ρ es Γ_ρ=149.4 MeV, la función $\Gamma(\tilde{m})$ depende de la energía y viene dada en la Ref. [35] como

$$\tilde{\Gamma}(\tilde{m}) = \Gamma_\rho \frac{q_{\text{off}}^3}{q_{\text{on}}^3} \theta(\tilde{m} - m_1 - m_2)$$
(10.50)

con $m_1 = m_2 = m_\pi$ para la ρ usando que

$$q_{\text{off}} = \frac{\lambda^{1/2}(\tilde{m}^2, m_\pi^2, m_\pi^2)}{2\tilde{m}}, \quad q_{\text{on}} = \frac{\lambda^{1/2}(m_\rho^2, m_\pi^2, m_\pi^2)}{2m_\rho}$$
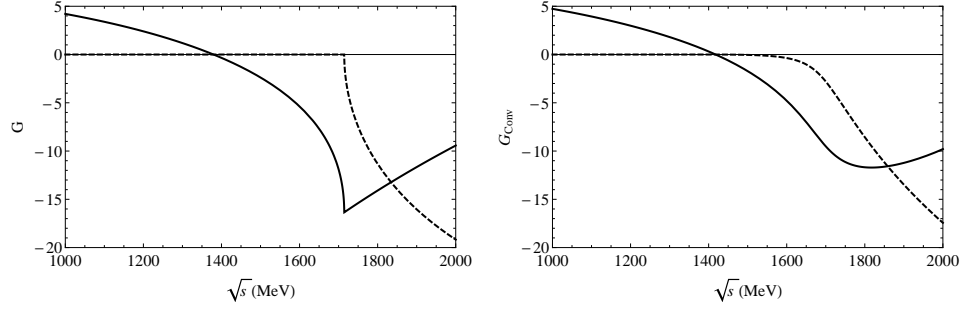(10.51)

Figure 10.6: Función G para ρN con $\alpha = -2.0$ y $\mu = 630$ MeV: Izquierda) Función G sin convolución. Derecha) Función G con convolución de la ρ con $\Gamma_\rho = 149.4$ MeV.

donde λ es la función de Källen y Γ_ρ es la anchura de la ρ. Podemos ver en la Fig. 10.6 los efectos de la convolución de la función G, en la que se aprecia que el umbral se ha suavizado. Esto puede eliminar efectos indeseables como picos en la matriz T, además de generar anchura en las resonancias. Sin embargo, en algunos casos la convolución de la función G puede hacer que los polos desaparezcan.

Para el caso de la Δ podemos proceder de forma similar. Sin embargo, la integral de la masa es diferente ya que ahora integramos un propagador bariónico.

$$\tilde{G}(s) = \frac{1}{N_\Delta} \int_{M_\Delta - 2\Gamma_\Delta}^{M_\Delta + 2\Gamma_\Delta} d\tilde{M} \left(-\frac{1}{\pi}\right) \operatorname{Im} \frac{1}{\tilde{M} - M_\Delta + i\frac{\Gamma(\tilde{M})}{2}} G(s, m^2, \tilde{M}^2)$$
(10.52)

donde $\tilde{G}$ está normalizada con

$$N_\Delta = \int_{M_\Delta - 2\Gamma_\Delta}^{M_\Delta + 2\Gamma_\Delta} d\tilde{M} \left(-\frac{1}{\pi}\right) \operatorname{Im} \frac{1}{\tilde{M} - M_\Delta + i\frac{\Gamma(\tilde{M})}{2}}$$
(10.53)

donde para la anchura de la Δ tomamos $\Gamma_\Delta = 120.0$ MeV, y la función Γ está definida como en la Eq. (10.50).

10.2.5   Polos y acoplamientos

Una vez se ha evaluado la matriz T, aparecen picos que pueden ser asociados a estados. El siguiente paso es encontrar los polos que generan esos picos con el fin de obtener los acoplamientos de estos estados a los diferentes canales. El método empleado es buscar polos en la segunda hoja de Riemann cambiando

el momento $\vec{q}$ a $-\vec{q}$ en la fórmula analítica de la función G cuando $Re(\sqrt{s})$ está por encima del umbral para el canal correspondiente. Usando este método se pueden encontrar polos de la forma $(M_R + i\Gamma/2)$, donde la parte real corresponde a la masa de la resonancia y la parte imaginaria es la mitad de la anchura de este estado.

Uno de los métodos más poderosos cuando se evalúan acoplamientos, es calcular el residuo usando el teorema del residuo en la matriz T en un camino de radio r alrededor del polo

$$\int_0^{2\pi} T(z(\theta))ire^{i\theta}d\theta = 2\pi iRes(T) = 2\pi ig^2 \tag{10.54}$$

donde $z = z_0 + re^{i\theta}$, y $z_0 = M_R + i\Gamma/2$. Así pues, el acoplamiento g_i para un determinado canal i puede ser evaluado con

$$g_i^2 = \frac{r}{2\pi} \int_0^{2\pi} T_{ii}(z(\theta))e^{i\theta}d\theta \tag{10.55}$$

El acoplamiento no depende del valor del radio r, pero generalmente se toma un valor de 1 MeV. Sin embargo hace falta ser cuidadoso con los polos cercanos al umbral, como en el caso de la $X(3872)$, ya que si la integral de camino cruza el umbral, se obtendrá un valor erróneo para el acoplamiento.

En algunos casos, la convolución de la función G puede hacer que el polo desaparezca en canales con el mesón ρ. En este caso se puede estudiar la amplitud en el eje real usando que cerca del pico, la matriz T será de la forma

$$T_{ij} = \frac{g_i g_j}{\sqrt{s} - M_R + i\Gamma/2} \tag{10.56}$$

donde M_R es la posición del máximo y Γ la anchura. Las constantes g_i y g_j son los acoplamientos de la resonancia a los canales i, j. Se puede tomar el canal diagonal y obtener que

$$|g_i|^2 = \frac{\Gamma}{2}\sqrt{|T_{ii}|^2} \tag{10.57}$$

donde el acoplamiento g_i tiene una fase arbitraria. Con un acoplamiento determinado, se pueden obtener los otros a partir de los elementos de matriz T_{ij} usando la Eq. (10.56), mediante

$$g_j = g_i \frac{T_{ij}(\sqrt{(s)} = M_R)}{T_{ii}(\sqrt{(s)} = M_R)} \ . \tag{10.58}$$

Una vez hemos obtenido los acoplamientos de la resonancia a cada canal, podemos calcular las anchuras parciales de desintegración utilizando la ecuación

$$\Gamma_i = \frac{1}{2\pi}\frac{M_B}{M_R}p_i|g_i|^2 \tag{10.59}$$

En el caso de una desintegración donde un mesón ρ o K^* esté involucrado, incluso resonancias que estén por debajo del umbral pueden tener una anchura de desintegración. En estos casos, el momento que se usa en la ecuación anterior sería imaginario. Experimentalmente se observa la desintegración de la resonancia a estos canales debido a que la anchura del mesón vectorial es suficientemente grande como para permitir la desintegración, a pesar de que la resonancia se encuentre por debajo del umbral. Con el fin de generar este efecto en nuestro cálculo de la anchura parcial de desintegración, hacemos la convolución del momento con la masa del mesón vectorial. Para el caso de la ρ tendríamos que

$$
\begin{aligned}
\tilde{p} \;=\; & \frac{1}{N_\rho} \int_{(m_\rho - 2\Gamma_\rho)^2}^{(m_\rho + 2\Gamma_\rho)^2} d\tilde{m}^2 \left(-\frac{1}{\pi}\right) \mathrm{Im} \frac{1}{\tilde{m}^2 - m_\rho^2 + i\tilde{m}\Gamma(\tilde{m})} \\
& \frac{\lambda^{1/2}(M_R^2, \tilde{m}^2, M_N^2)}{2M_R} \theta(M_R - \tilde{m}_\rho - M_N)
\end{aligned}
\tag{10.60}
$$

Donde N_ρ es la misma normalización usada en la Eq. (10.49).

10.3 Conclusiones

Durante esta Tesis, hemos usado la Teoría Quiral de Perturbaciones y sus extensiones con el formalismo Hidden Gauge para abordar varios problemas de la física hadrónica. Principalmente, hemos estudiado la interacción mesón-barión para describir resonancias hadrónicas y sus propiedades, como masa, anchura, anchuras parciales de desintegración, desintegración radiativa y amplitudes de helicidad. Se ha extendido el estudio de la interacción mesón vectorial - barión mezclando mesones pseudoescalares con mesones vectoriales con un enfoque que permite entender mejor la naturaleza de esos estados hadrónicos. Hemos usado este formalismo para calcular los diagramas de transición y así obtener las amplitudes en canales acoplados usados en la matriz potencial V. Luego hemos usado la ecuación Bethe-Salpeter para calcular la matriz unitarizada T usando la función G, regularizada dimensionalmente con una constante de substracción. A continuación buscamos polos en el plano complejo cambiando a la segunda hoja de Riemann y para después calcular los acoplamientos a cada canal que son obtenidos mediante el residuo de los polos. Este procedimiento se ha empleado para estudiar los estados N^* con $J^P = 1/2^-$ y $3/2^-$ con mucho éxito, y hemos mostrado que la mezcla de la interacción de mesones pseudoescalares - barión con mesones vectoriales es crucial cuando se intenta reproducir las anchuras experimentales. Se han estudiado otros casos de la interacción mesón - mesón como

interacción de varios cuerpos o volumen finito. Detallamos en los siguientes apartados las conclusiones del trabajo realizado en esta Tesis:

- **Desintegración radiativa.** Hemos estudiado la desintegración radiativa de las resonancias dinámicamente generadas con $J^P = 1/2^-$ y $3/2^-$ obtenidas con el formalismo hidden gauge para la interacción de los mesones vectoriales con bariones del octete y del decuplete de SU(3). El formalismo tiene en cuenta que el fotón se acopla a las resonancias convirtiéndose primero en un mesón vectorial ρ^0, ω or ϕ. Usando este mecanismo hemos calculado las anchuras de desintegración radiativa de esas resonancias a γB donde B es un barión del octete o del decuplete. Hemos obtenido las anchuras de desintegración para cada tercera componente de isospin I_3 y para todas las posibles combinaciones de extrañeza e isospin. Los valores de las anchuras de desintegración son del orden de 1 MeV y uno de los resultados más relevantes es la gran diferencia, de hasta un orden de magnitud, entre anchuras con diferentes estados de carga para una misma resonancia. Este resultado da una información muy valiosa lo cual constituye una buena prueba para el modelo.
  También hemos calculado las amplitudes de helicidad para las resonancias N^* anteriormente estudiadas. Se puede definir las amplitudes de helicidad $A_{1/2}$ y $A_{3/2}$ para n y p, lo cual hace más fácil la comparación con los datos experimentales. Además ahora podemos separar los spines $J^P = 1/2^-$ y $3/2^-$ para las resonancias lo que es útil para comparar con los datos. Es interesante notar que las ecuaciones para las amplitudes de helicidad predicen una relación entre $A_{1/2}^{J=3/2}$ y $A_{3/2}^{J=3/2}$ de $1/\sqrt{3}$, que es algo que puede ser contrastado con el experimento. Hemos hecho esto y los resultados están de acuerdo con los datos en los casos en los que la comparación puede hacerse.

- **El diagrama de caja.** En este trabajo hemos estudiado la interacción de los mesones vectoriales con el octete de bariones usando el formalismo hidden gauge, el cual genera nueve resonancias dinámicamente generadas, que están degeneradas en los números cuánticos $J^P = 1/2^-$ y $3/2^-$. Sin embargo, los resultados para las anchuras encontrados en ese estudio, eran significativamente menores que los valores experimentales. Esto nos llevó a pensar que podría haber otro mecanismo involucrado en la generación de esas resonancias que no había sido tenido en cuenta. Ya que los mesones pseudoescalares se acoplan a los mesones vectoriales y a los bariones, se podría pensar que los mesones pseudoescalares juegan un papel como estados intermedio. Este mecanismo

se llevo a cabo con un diagrama de caja donde un mesón pseudoescalar y un barión eran los estados intermedios. La idea es que un mesón vectorial externo, se desintegra en dos mesones pseudoescalares y uno de ellos es intercambiado y absorbido por el barión externo, así pues tenemos un estado intermedio que se propaga. Después ocurre el mecanismo inverso para finalmente tener el mesón vectorial y el barión en el estado final. Hemos evaluado la integral para este diagrama de caja para todos los posibles estados intermedios y para todos los canales. Otra pieza importante para la caja, a parte del intercambio de un mesón, es el vértice de Kroll-Ruderman. Además este mecanismo tiene un consecuencia importante: dado que el término de Kroll-Ruderman solo contribuye a $J^P = 1/2^-$, es posible romper la degeneración original.

El añadir el diagrama de caja al potencial produce un efecto beneficioso, ya que hace más anchas las resonancias y en algunos casos produce un pequeño desplazamiento del pico. Este hecho es particularmente visible en el sector con $S = 0$ donde la degeneración de la $N^*(1650)(1/2^-)$ y de la $N^*(1700)(3/2^-)$ se rompe y las masas y las anchuras para los dos estados son correctamente determinados. En otros sectores, las anchuras son también mayores y con una mejor concordancia con los datos experimentales del PDG que los resultados originales. Los nuevos acoplamientos calculados, a pesar de ser un poco diferentes a los originales, en modulo permanecen muy similares para la mayoría de los casos.

- **Resonancias N^* con $J^P = 3/2^-$.** La $N^*(1520)(3/2^-)$ está catalogada como una resonancia de cuatro estrellas en el PDG y la $N^*(1700)(3/2^-)$ está catalogada como una resonancia de tres estrellas, sin embargo esta resonancia no se encuentra en algunos análisis recientes, pero si se encuentra en otros. A la vista de esta aparente contradicción, hemos estudiado la amplitud en ondas parciales D_{13} de la dispersión πN extraída de datos experimentales con el fin de averiguar si la $N^*(1700)$ existe o no. Hemos estudiado la mezcla de la interacción de mesones pseudoescalares - barión con la interacción de mesones vectoriales - barión con $J^P = 3/2^-$ incluyendo los canales ρN (onda s), πN (onda d), $\pi \Delta$ (onda s) y $\pi \Delta$ (onda d). La novedad de este trabajo es que usando la transición del diagrama de caja, donde un mesón pseudoescalar y un barión era el estado intermedio, podemos calcular la transición $VB \to PB$, más allá de solo considerar el término Kroll-Ruderman como ha sido hecho en otros trabajos.

  Hemos ajustado las partes real e imaginaria de la matriz T a la amplitud en ondas parciales D_{13} de la dispersión πN en la región de

$\sqrt{s} = 1400 - -1800$ MeV, tomando como parámetros libres las constantes de substracción para cada canal y tres parámetros de las transiciones en onda d. Todas las constantes de substracción obtenidas son de la escala natural. El primer resultado importante es que si queremos reproducir los datos, dos polos aparecen y merece la pena destacar que la presencia de los dos polos es bastante sólida, ya que cambios moderados en los parámetros no estropean los resultados de los polos. También hemos determinado las anchuras parciales de desintegración para todos los canales y hemos encontrado unos resultados en excelente concordancia con los resultados experimentales de la $N^*(1520)$ y de la $N^*(1700)$.

- **Resonancias N^* con $J^P = 1/2^-$.** Hemos extendido el estudio anterior al sector de $J^P = 1/2^-$, incluyendo otros canales mesón-barión como ηN, $K\Lambda$ y $K\Sigma$. Algunos trabajos que intentan describir la $N^*(1535)(1/2^-)$ como una resonancia dinámicamente generada usando canales acoplados en la interacción mesón pseudoescalar-barión encuentran que algunas de las constantes de substracción son bastante diferentes a la escala natural y en algunos casos incluso positivas. Además el estado $N^*(1650)$ no se encontraba usando ese formalismo. En este trabajo hemos incluido los canales de interacción de mesón vectorial - barión y el canal $\pi\Delta$ (onda d) los cuales proporcionan las piezas que faltaban para obtener un formalismo más realista.
  Hemos usado los canales acoplados πN, ηN, $K\Lambda$, $K\Sigma$, ρN y $\pi\Delta$ (onda d) para ajustar los datos experimentales S_{11} de la dispersión πN. Las constantes de substracción obtenidas con el ajuste ahora son todas negativas y de la escala natural. Además el haber incluido los canales ρN y $\pi\Delta$ tiene una consecuencia importante ya que ahora podemos generar ambas resonancias, la $N^*(1535)$ y la $N^*(1650)$ lo cual es un éxito importante de la mezcla de mesones pseudoescalares y vectoriales. Podemos concluir que la componente de la función de onda de un estado genuino de la $N^*(1535)$ que era apoyada por otros trabajos, puede ser traducida en que habían componentes que faltaban, como los canales ρN y $\pi\Delta$.

- **Límites de la Aproximación de Fixed Center.** La aproximación de Fixed Center a las ecuaciones de Faddeev es una buena aproximación cuando dos de las partículas están ligadas en un cluster y no son excitadas en un estado intermedio, lo cual es común cuando no hay energía disponible para excitarlo. Esto ocurrirá si el estado esta ligado con respecto a la masa de las tres partículas. El caso que estudiamos es el de la $\phi(2170)$ como un estado resonante de la ϕ y de la

$f_0(980)$. En este caso el sistema $\phi\, f_0(980)$ tiene 170 MeV de excitación así que hay energía suficiente para excitar el $f_0(980)$ en un estado intermedio. Nuestro análisis no produce ningun pico para la $\phi(2170)$. Además hemos determinado la contribución del diagrama de Faddeev que involucra la interacción de $K\bar{K}$ con una colisión de ϕK o $\phi\bar{K}$, lo que es responsable del fracaso de la aproximación de fixed center para este caso. Hemos encontrado que este mecanismo es del mismo orden de magnitud que la doble interacción de ϕK en la serie de FCA. Además estos dos mecanismos tienen amplitudes con signo opuesto y el considerarlas simultáneamente podría cambiar drásticamente los resultados obtenidos únicamente de la contribución de doble interacción de FCA. A la vista de este resultado, cualquier análisis de este problema debe tener en cuenta este hecho. Sin embargo, si se intenta mejorar el FCA incluyendo estas excitaciones inelásticas, nos encontraríamos con un problema que involucraría más iteraciones convirtiéndose en un problema más complicado que si se usaran las ecuaciones de Faddeev desde un principio.

- **Energía de enlace de la $X(3872)$.** Hemos abordado el problema de determinar con precisión la energía de enlace de la $X(3872)$ en el volumen finito. La $X(3872)$ es una resonancia dinámicamente generada en los canales acoplados $D^+ D^{*-}$ y $D^0 \bar{D}^{*0}$ con una energía de enlace cercana al umbral de $D^0 \bar{D}^{*0}$. Hemos estudiado el sistema DD^* en volumen finito usando el formalismo hidden gauge en SU(4) para la interacción de sus componentes y hemos estudiado la amplitud de interacción a volumen finito, encontrando unos niveles de energía discretos que dependen del tamaño del volumen de la caja L. El primer resultado relevante es que obtenemos un desdoblamiento de los niveles de energía dependiendo del tamaño de la caja, en contraste con lo que ocurre cuando se usa solo un único canal. Esto se entiende mirando a la función $\tilde{G}$ donde las energías libres aparecen como asíntotas, así que si tenemos dos canales, aparecen nuevas asíntotas, y como encontramos un nivel de energía entre dos asíntotas adyacentes, aparecen nuevos niveles de energía.

  Después de esto hemos estudiado el problema inverso. Hemos generado pseudodatos que emulan los datos que sería obtenidos por estudios realizados con Lattice. A continuación ajustamos estos datos con un potencial genérico que depende de la energía y obtenemos la energía de enlace que genera el potencial ajustado a los datos. El estudio consiste en ver la incertidumbre con la que se determina la energía de enlace dependiendo del número de puntos del tamaño de la caja, los errores en

los niveles de energía, número de niveles, etc. La conclusión que se extrae de este análisis es que incluso con errores en los datos de 5 MeV, se puede obtener la energía de enlace con una precisión inferior a 1 MeV. Además hemos observado que incluso únicamente usando el primer nivel de la caja, se puede tener buena precisión cuando se dispone de suficientes puntos diferentes para el tamaño de la caja L. El objetivo ha sido dar una idea de las estrategias óptimas para determinar con precisión la energía de enlace en futuros análisis de Lattice. Finalmente hemos estudiado la naturaleza de la $X(3872)$ como un estado dinámicamente generado y hemos mostrado diversas informaciones al respecto que pueden obtenerse de los datos de Lattice.

Spin degeneracy of VB considering the $VB \rightarrow VB$ transition

Let us evaluate the transition operator of the vector meson-octet baryon with a pseudoscalar meson-octet baryon as an intermediate state. We want to evaluate both $J = 1/2$ and $3/2$. The initial VB state should be

$$|JM\rangle = \sum_m \mathcal{C}\left(1/2, 1, J; m, M - m, M\right) |1/2m\rangle \, |\vec{\epsilon}_{M-m}\rangle \qquad \text{(A.1)}$$

where

$$\vec{\epsilon}_\mu = \begin{cases} -\frac{1}{\sqrt{2}}(\vec{\epsilon}_1 + i\vec{\epsilon}_2) \\ \vec{\epsilon}_3 \\ \frac{1}{\sqrt{2}}(\vec{\epsilon}_1 - i\vec{\epsilon}_2) \end{cases} \qquad \mu = 1, \ 0, \ -1 \qquad \text{(A.2)}$$
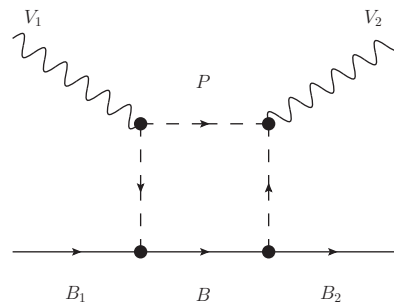

Figure A.1: Vector meson-octet baryon interaction with pseudoscalar meson as intermediate state.

We are going to use the text book of Rose "Elementary Theory of Angular Momentum"[217]. The operator in the baryon sector will be

$$\vec{\sigma} \cdot \vec{q}\, \vec{\epsilon} \cdot \vec{q} \tag{A.3}$$

That is

$$\vec{\epsilon} \cdot \vec{q} \rightarrow \vec{\epsilon}_{M-m} \cdot \vec{q} \rightarrow q_{M-m} \tag{A.4}$$

In Rose (4.3.5) we can find a relation of the momentum with the spherical harmonics given by

$$q_{M-m} = \left(\frac{4\pi}{3}\right)^{1/2} q Y_{1,M-m}\left(\hat{q}\right) \tag{A.5}$$

And for the spinor operator we have

$$\vec{\sigma}\vec{q} = \sum_{\mu}(-1)^{\mu}\sigma^{\mu}q_{-\mu} = \sum_{\mu}(-1)^{\mu}\sigma^{\mu}Y_{1,-\mu}\left(\hat{q}\right)\left(\frac{4\pi}{3}\right)^{1/2}q \tag{A.6}$$

Let $|1/2, m'\rangle$ be the spin state of the intermediate B. Using the Wigner-Eckart theorem we have

$$
\begin{aligned}
\langle 1/2m'|\sigma_{\mu}|1/2m\rangle &= \mathcal{C}\left(1/2, 1, 1/2; m, \mu, m'\right)\langle||\sigma_{\mu}||\rangle & (A.7)\\
&= \mathcal{C}\left(1/2, 1, 1/2; m, \mu, m'\right)\sqrt{3} & (A.8)
\end{aligned}
$$

where we have used Rose (5.2) $\langle||\sigma_{\mu}||\rangle = 2\left[\frac{1}{2}(\frac{1}{2}+2)\right]^{1/2} = \sqrt{3}$. Now we have, using Rose (4.32),

$$
\begin{aligned}
Y_{1,-\mu}\left(\hat{q}\right)Y_{1,M-m} &= \sum_{L}\left[\frac{3 \cdot 3}{4\pi(2L+1)}\right]^{1/2}\mathcal{C}\left(1, 1, L; 0, 0, 0\right)\\
&\quad \mathcal{C}\left(1, 1, L; -\mu, M-m, M-m-\mu\right)\\
&\quad Y_{L,M-m-\mu}\left(\hat{q}\right) & (A.9)
\end{aligned}
$$

Recall $\mathcal{C}\left(j_1, j_2, j_3; 0, 0, 0\right) = 0$ unless $j_1 + j_2 + j_3 =$even (Rose (3.22)). In this case $L = 0$ and 2 for parity reasons. This has to be so because

$$q_i q_j \rightarrow \frac{1}{3}\vec{q}^2\delta_{ij} + \left(q_i q_j - \frac{1}{3}\vec{q}^2\delta_{ij}\right) \tag{A.10}$$

Now we have

$$
\begin{aligned}
\sum_{m} \quad &\mathcal{C}\left(1/2, 1, J; m, M-m, M\right)\mathcal{C}\left(1/2, 1, 1/2; m, \mu, m'\right)\\
&\mathcal{C}\left(1, 1, L; -\mu, M-m, M-m-\mu\right) \tag{A.11}
\end{aligned}
$$

then $m + \mu = m' \Rightarrow \mu = m' - m$. So

$$\sum_m \mathcal{C}\left(1/2, 1, J; m, M - m, M\right) \mathcal{C}\left(1/2, 1, 1/2; m, m' - m, m'\right)$$
$$\mathcal{C}\left(1, 1, L; m - m', M - m, M - m'\right) \tag{A.12}$$

We would use Rose (6.5a) to convert this sum into one Racah coefficient and another Clebsch-Gordan coefficient. Rose (6.5a) tells

$$\sum_{\mu_2} \mathcal{C}\left(j_1, j_2, j'; \mu_1, \mu_2\right) \mathcal{C}\left(j', j_3, j; \mu_1 + \mu_2, \mu_3\right) \mathcal{C}\left(j_2, j_3, j''; \mu_2, \mu_3\right)$$
$$= R_{j''j'}\mathcal{C}\left(j_1, j'', j; \mu_1, \mu_2 + \mu_3\right) \tag{A.13}$$

where $\mu_2 + \mu_3$ must be kept fixed. This tells us that we should put the term $\mathcal{C}\left(1/2, 1, J; m, M - m, M\right)$ in third place, $\mu_2 \equiv m$ and $\mu_3 \equiv M - m$, then $\mu_2 + \mu_3 \equiv M$ fixed. We need to reorder, using Rose (3.17b),

$$\mathcal{C}\left(1/2, 1, 1/2; m, m' - m, m'\right) \rightarrow (-1)^{1/2-m} \left(\frac{2}{3}\right)^{1/2} \mathcal{C}\left(1/2, 1/2, 1; m', -m\right) \tag{A.14}$$

then using Rose (3.16a)

$$= (-1)^{1/2-m} \left(\frac{2}{3}\right)^{1/2} (-1)^{1/2+1/2-1}\mathcal{C}\left(1/2, 1/2, 1; -m', m\right) \tag{A.15}$$

finally we get that $j_1 = 1/2$, $j_2 = 1/2$, $j_3 = 1$, $j = 1$, $j'' = J$ and $\mu_1 = -m'$.

$$\sum_m \mathcal{C}\left(1/2, 1/2, 1; -m', m\right) \mathcal{C}\left(1, 1, L; m - m', M - m\right)$$
$$\mathcal{C}\left(1/2, 1, J; m, M - m\right) (-1)^{1/2-m} \left(\frac{2}{3}\right)^{1/2} (-1)^{m'-m} \left(\frac{4\pi}{3}\right)$$
$$q^2 \sqrt{3} \frac{3}{[4\pi(2L+1)]^{1/2}} \mathcal{C}\left(1, 1, L; 0, 0, 0\right) Y_{L,M-m'}(\hat{q})$$
$$= (-1)^{1/2-m'} \left(\frac{2}{3}\right)^{1/2} \left(\frac{4\pi}{3}\right) q^2 \sqrt{3} \frac{3}{[4\pi(2L+1)]^{1/2}}$$
$$R_{J,1}\mathcal{C}\left(1/2, J, L; -m', M\right) \mathcal{C}\left(1, 1, L; 0, 0, 0\right) Y_{L,M-m'}(\hat{q}) \tag{A.16}$$

Using Rose (3.16c)

$$\mathcal{C}\left(1/2, J, L; -m', M\right) = (-1)^{1/2+m'} \left(\frac{2L+1}{2J+1}\right)^{1/2} \mathcal{C}\left(1/2, L, J; -m', m' - M\right) \tag{A.17}$$

and then with Rose (3.16a)

$$= (-1)^{1/2+m'} \left(\frac{2L+1}{2J+1} \right)^{1/2} (-1)^{1/2+L-J} \mathcal{C} \left(1/2, L, J; m', M-m' \right) \quad \text{(A.18)}$$

then

$$\begin{aligned} R_{J,1} &= [(2J+1)(3)] \, W(1/2, 1/2, L, 1; 1, J) \\ {}^{(6.10b)} &= [(2J+1)(3)] \, (-1)^{1+J-1/2-1} W(1, 1/2, L, J; 1/2, 1) \quad \text{(A.19)} \end{aligned}$$

Altogether we get

$$(-1)^{1+L} q^2 \sqrt{6} \sqrt{4\pi} W(1, 1/2, L, J; 1/2, 1) \mathcal{C} \left(1, 1, L; 0, 0, 0 \right)$$
$$Y_{L,M-m'}(\hat{q}) \mathcal{C} \left(1/2, L, J; m', M-m' \right) \quad \text{(A.20)}$$

Thus

$$\text{if } J = 1/2, \ L = 0, 1 \Rightarrow \text{but only } L = 0$$
$$\text{if } J = 3/2, \ L = 1, 2 \Rightarrow \text{but only } L = 2$$

Now let us consider the box diagram of Fig. A.1. So we will have.

$$\sum_{m'} \int d^3 q \quad \mathcal{C} \left(1/2, L, J; m', M-m' \right) \mathcal{C} \left(1/2, L', J'; m', M'-m' \right)$$
$$Y_{L,M-m'}(\hat{q}) Y^*_{L',M'-m'}(\hat{q}) \quad \text{(A.21)}$$

As expected

$$\int d\Omega Y_{L,M-m'}(\hat{q}) Y^*_{L',M'-m'} = \delta_{L,L'} \delta_{M,M'} \quad \text{(A.22)}$$

and so

$$\sum_{m'} \mathcal{C} \left(1/2, L, J; m', M-m' \right) \mathcal{C} \left(1/2, L, J'; m', M-m' \right) = \delta_{J,J'} \quad \text{(A.23)}$$

We can thus omit the coefficients of $Y_{L,M-m'}$ and the Clebsch-Gordan but since we have to integrate over $\int d^3 q$ later, we should put the factor $\frac{1}{4\pi}$. Hence, the box will give us

$$\frac{1}{4\pi} \int d^3 6 q^4 4\pi \mathcal{C} \left(1/2, 1, L; 0, 0, 0 \right)^2 W(1, 1/2, L, J; 1/2, 1)^2$$
$$= \int d^3 q^4 6 \mathcal{C} \left(1/2, 1, L; 0, 0, 0 \right)^2 W(1, 1/2, L, J; 1/2, 1)^2 \quad \text{(A.24)}$$

We need only two cases

$$J = 1/2, \ L = 0$$
$$J = 1/2, \ L = 2$$

$$\text{(A.25)}$$

We get the Racah coefficients from Table I.3 of the appendix of Rose. For the case of $J = 1/2$ and $L = 0$, using Eqs. (6.10a) and (6.10b) of Rose

$$
\begin{aligned}
W(1, 1/2, 0, 1/2; 1/2, 1) &= \text{phase } W(1, 1/2, 1, 1/2; 1/2, 0) \\
&= \text{phase } W(1, 1, 1/2, 1/2; 0, 1/2) \\
&= \text{phase } \frac{\delta_{1,1}\delta_{1/2,1/2}}{(3 \cdot 2)^{1/2}}
\end{aligned}
\tag{A.26}
$$

where the *phase* does not play a role since one needs W^2 at the end, and for the Clebsch-Gordan coefficient

$$\mathcal{C}\left(1, 1, 0; 0, 0, 0\right) = -\frac{1}{\sqrt{3}} \tag{A.27}$$

all together

$$\int d^3q^4 6 \left(-\frac{1}{\sqrt{3}}\right)^2 \left(\frac{1}{\sqrt{6}}\right)^2 = \int d^3q^4 \frac{1}{3} \tag{A.28}$$

In the case of $J = 1/2$ and $L = 2$,

$$
\begin{aligned}
W(1, 1/2, 2, 3/2; 1/2, 1) &= \text{phase } \left[\frac{(\frac{1}{2} + \frac{3}{2} + \frac{1}{2})(\frac{1}{2} + \frac{3}{2} - 1 + 1)}{(2 \cdot 3 \cdot 4 \cdot 5)}\right]^{1/2} \\
&= \text{phase } \left[\frac{5 \cdot 2}{(2 \cdot 3 \cdot 4 \cdot 5)}\right]^{1/2} = \text{phase } \frac{1}{\sqrt{12}} \\
W(1, 1/2, 2, 3/2; 1/2, 1)^2 &= \frac{1}{12}
\end{aligned}
\tag{A.29}
$$

and for the Clebsch-Gordan coefficient

$$\mathcal{C}\left(1, 1, 2; 0, 0, 0\right) = \sqrt{\frac{2}{3}} \tag{A.30}$$

all together

$$\int d^3q^4 6 \left(\sqrt{\frac{2}{3}}\right)^2 \left(\frac{1}{\sqrt{12}}\right)^2 = \int d^3q^4 6 \frac{2}{3}\frac{1}{12} = \int d^3q^4 \frac{1}{3} \tag{A.31}$$

The degeneracy is not broken, which was easy to see in retrospective. Indeed we had

$$\sigma_l \sigma_m \equiv \delta_{lm} + i\varepsilon_{lms}\sigma_s \quad \rightarrow \quad \begin{array}{l} \epsilon_i q_i \epsilon'_j q_j q_l \sigma_l q_m \sigma_m \\ \epsilon_i q_i \epsilon'_j q_j (\delta_{lm} + i\varepsilon_{lms}\sigma_s) q_m q_l \\ \epsilon_i \epsilon'_j q_i q_j \vec{q}^2 \\ \frac{1}{3}\vec{\epsilon}\vec{\epsilon}' \vec{q}^2 \vec{q}^2 \end{array} \qquad (A.32)$$

which is independent of spin, so we get the same result for $J = 1/2$ and $3/2$.

B

Matrix elements of the $\vec{\sigma}\ \vec{\epsilon}$ operator

Let us evaluate the matrix element

$$\langle 1/2m'|\vec{\sigma}\ \vec{\epsilon}\,|JM\rangle \tag{B.1}$$

where

$$|JM> = \sum_m \mathcal{C}(1/2, 1, J; m, M - m, M)|1/2, m> |\vec{\epsilon}_{M-m}> \tag{B.2}$$

and, as usual,

$$\vec{\epsilon}_\mu = \begin{cases} -\frac{1}{\sqrt{2}}(\vec{\epsilon}_1 + i\vec{\epsilon}_2) \\ \qquad\qquad \vec{\epsilon}_3 \qquad \mu = 1,\ 0,\ -1 \\ \frac{1}{\sqrt{2}}(\vec{\epsilon}_1 - i\vec{\epsilon}_2) \end{cases} \tag{B.3}$$

Hence the matrix element can be written as

$$\begin{aligned}
\langle 1/2m'|\vec{\sigma}\ \vec{\epsilon}\,|JM\rangle &= \sum_m \mathcal{C}(1/2, 1, J; m, M - m, M)\,\langle 1/2m'|\vec{\sigma}\vec{\epsilon}_{M-m}|1/2, m\rangle \\
&= \sum_m \mathcal{C}(1/2, 1, J; m, M - m, M)\,\langle 1/2m'|\sigma_{M-m}|1/2, m\rangle
\end{aligned} \tag{B.4}$$

Using the Wigner-Eckart theorem one obtains

$$\langle 1/2m'|\sigma_{M-m}|1/2, m\rangle = \sqrt{3}\,\mathcal{C}(1/2, 1, 1/2; m, M - m, m') \tag{B.5}$$

from where we get that $m' \equiv M$. Substituting this result in Eq. (B.4) we obtain

$$\sum_m \mathcal{C}(1/2, 1, J; m, M - m, M)\sqrt{3}\,\mathcal{C}(1/2, 1, 1/2; m, M - m, M) = \sqrt{3}\,\delta_{J,1/2} \tag{B.6}$$

Hence, only $J = 1/2$ contributes and $m' = M$, and thus

$$\langle 1/2m'|\vec{\sigma}\,\vec{\epsilon}\,|JM\rangle = \sqrt{3}\,\delta_{J,1/2}\delta_{m',M} \qquad\qquad \text{(B.7)}$$

Expression of the Box diagram integral

The integral of the box diagram of Eq. (4.26) contains a function which comes from the propagator of the three mesons and the baryon of the loop. This expression can be simplified in order to cancel the fallacious poles which appear when one integrates the zero component of the four-momentum using Cauchy's Theorem. The sum of the residues terms leads to a long expression that is given below.

$$
\begin{aligned}
Den \;=\; & (-2\omega_1 + i\epsilon)(-P_V^0 - \omega_1 - \omega_2 + i\epsilon)(\alpha - \omega_3 - \omega_1 + i\epsilon) \\
& (\beta - \omega_1 + i\epsilon)(P_V^0 - \omega_2 - \omega_1 + i\epsilon)(-2\omega_2 + i\epsilon) \\
& (P_V^0 + \alpha - \omega_2 - \omega_3 + i\epsilon)(\beta + P_V^0 - \omega_2 + i\epsilon)(-\alpha - \omega_3 - \omega_1 + i\epsilon) \\
& (-2\omega_3 + i\epsilon)(-\alpha - P_V^0 - \omega_3 - \omega_2 + i\epsilon)(\beta - \alpha - \omega_3 + i\epsilon) \qquad \text{(C.1)}
\end{aligned}
$$

where

$$
\omega_i = \sqrt{|\vec{q}|^2 + m_i^2}, \qquad \alpha = P_{B_1}^0 - P_{B_2}^0, \qquad \beta = P_{B_1}^0 - E_B(\vec{q}),
$$

and

$$
P_{B_i}^0 = \frac{s + M_{B_i}^2 - M_{V_i}^2}{2\sqrt{s}}, \qquad P_{V_i}^0 = \frac{s + M_{V_i}^2 - M_{M_i}^2}{2\sqrt{s}}, \qquad E_B(\vec{q}) = \sqrt{|\vec{q}|^2 + M_B^2}.
$$

$$
\begin{aligned}
Num \;=\; & {P_V^0}^3 \omega_2(\omega_1^2 + \omega_3(\alpha - \beta + \omega_3) + \omega_1(-\beta + 2\omega_3)) \\
& -{P_V^0}^2 \omega_2((-2\alpha - \beta + \omega_2)\omega_3(\alpha - \beta + \omega_3) + \omega_1^2(-\beta + \omega_2 + 2\omega_3) \\
& +\omega_1(\beta^2 - 2(\alpha + \beta)\omega_3 + 2\omega_3^2 + \omega_2(-\beta + 2\omega_3))) \\
& -P_V^0 \omega_2(\omega_1^4 + \omega_1^3(-\beta + 2\omega_2 + 2\omega_3) \\
& +\omega_3(\alpha - \beta + \omega_3)(-(\alpha(\alpha + 2\beta)) \\
& +\omega_2^2 + \omega_3^2 + 2\omega_2(\alpha + \omega_3)) + \omega_1(4\omega_2\omega_3(\alpha - \beta + \omega_3) \\
& +2\omega_3(\alpha + \omega_3)(\alpha - \beta + \omega_3) + \omega_2^2(-\beta + 2\omega_3)) \\
& +\omega_1^2(\omega_2^2 + 2\omega_3(\alpha - \beta + \omega_3) + \omega_2(-2\beta + 4\omega_3))) \\
& +(\omega_1 + \omega_2)((-\beta + \omega_2)\omega_3(\alpha - \beta + \omega_3)(-\alpha^2 + \omega_2^2 + 2\omega_2\omega_3 + \omega_3^2) \\
& +\omega_1^3(\omega_2^2 + \omega_3(\alpha - \beta + \omega_3) + \omega_2(-\beta + 2\omega_3)) \\
& +\omega_1^2(-\beta + \omega_2 + 2\omega_3)(\omega_2^2 \\
& +\omega_3(\alpha - \beta + \omega_3) + \omega_2(-\beta + 2\omega_3)) + \omega_1(\omega_2^3(-\beta + 2\omega_3) \\
& +\omega_2\omega_3(-2\alpha^2 - \alpha\beta + 3\beta^2 + 2\alpha\omega_3 - 7\beta\omega_3 + 4\omega_3^2) \\
& +\omega_2^2(\beta^2 + (\alpha - 5\beta)\omega_3 + 5\omega_3^2) \\
& +\omega_3(\alpha^2(-\alpha + \beta) - (\alpha^2 + 2\alpha\beta - 2\beta^2)\omega_3 + (\alpha - 3\beta)\omega_3^2 + \omega_3^3)))
\end{aligned}
$$

$$(C.2)$$

Coefficients of the Baryon octet - pseudoscalar mesons interaction

The coefficients of the BBP interaction, α and β, are related to the BBP vertex of Eq. (4.10)

$$-it_{BBP} = \left\{ \alpha \frac{(D+F)}{2f_\pi} + \beta \frac{(D-F)}{2f_\pi} \right\} \vec{\sigma} \vec{k} \qquad (D.1)$$

and are given in Tables D.1 and D.2.

Coefficients α for $(D+F)/2f$
η_8	$\bar{n}\ n$	$\bar{p}\ p$	$\bar{\Sigma}^-\ \Sigma^-$	$\bar{\Sigma}^+\ \Sigma^+$	$\bar{\Sigma}^0\ \Sigma^0$	$\bar{\Lambda}\ \Lambda$	$\bar{\Xi}^0\ \Xi^0$	$\bar{\Xi}^-\ \Xi^-$
	$\frac{1}{\sqrt{3}}$	$\frac{1}{\sqrt{3}}$	$\frac{1}{\sqrt{3}}$	$\frac{1}{\sqrt{3}}$	$\frac{1}{\sqrt{3}}$	$-\frac{1}{\sqrt{3}}$	$-\frac{2}{\sqrt{3}}$	$-\frac{2}{\sqrt{3}}$
π^0	$\bar{n}\ n$	$\bar{p}\ p$	$\bar{\Sigma}^-\ \Sigma^-$	$\bar{\Sigma}^+\ \Sigma^+$	$\bar{\Sigma}^0\ \Lambda$	$\bar{\Lambda}\ \Sigma^0$		
	-1	1	-1	1	$\frac{1}{\sqrt{3}}$	$\frac{1}{\sqrt{3}}$		
π^-	$\bar{n}\ p$		$\bar{\Sigma}^0\ \Sigma^+$	$\bar{\Sigma}^-\ \Sigma^0$	$\bar{\Lambda}\ \Sigma^+$	$\bar{\Sigma}^-\ \Lambda$		
	$\sqrt{2}$		-1	1	$\frac{1}{\sqrt{3}}$	$\frac{1}{\sqrt{3}}$		
π^+	$\bar{p}\ n$		$\bar{\Sigma}^+\ \Sigma^0$	$\bar{\Sigma}^0\ \Sigma^-$	$\bar{\Lambda}\ \Sigma^-$	$\bar{\Sigma}^+\ \Lambda$		
	$\sqrt{2}$		-1	1	$\frac{1}{\sqrt{3}}$	$\frac{1}{\sqrt{3}}$		
K^-	$\bar{\Lambda}\ p$	$\bar{\Xi}^0\ \Sigma^+$	$\bar{\Xi}^-\ \Sigma^0$	$\bar{\Xi}^-\ \Lambda$				
	$-\frac{2}{\sqrt{3}}$	$\sqrt{2}$	1	$\frac{1}{\sqrt{3}}$				
K^+	$\bar{p}\ \Lambda$	$\bar{\Sigma}^+\ \Xi^0$	$\bar{\Sigma}^0\ \Xi^-$	$\bar{\Lambda}\ \Xi^-$				
	$-\frac{2}{\sqrt{3}}$	$\sqrt{2}$	1	$\frac{1}{\sqrt{3}}$				
$\bar{K}^0$	$\bar{\Lambda}\ n$	$\bar{\Xi}^-\ \Sigma^-$	$\bar{\Xi}^0\ \Sigma^0$	$\bar{\Xi}^0\ \Lambda$				
	$-\frac{2}{\sqrt{3}}$	$\sqrt{2}$	-1	$\frac{1}{\sqrt{3}}$				
K^0	$\bar{n}\ \Lambda$	$\bar{\Sigma}^-\ \Xi^-$	$\bar{\Sigma}^0\ \Xi^0$	$\bar{\Lambda}\ \Xi^0$				
	$-\frac{2}{\sqrt{3}}$	$\sqrt{2}$	-1	$\frac{1}{\sqrt{3}}$				

Table D.1: Coefficients α for the BBP vertex.

Coefficients β for $(D-F)/2f$								
η_8	$\bar{n}\,n$	$\bar{p}\,p$	$\bar{\Sigma}^-\,\Sigma^-$	$\bar{\Sigma}^+\,\Sigma^+$	$\bar{\Sigma}^0\,\Sigma^0$	$\bar{\Lambda}\,\Lambda$	$\bar{\Xi}^-\,\Xi^-$	$\bar{\Xi}^0\,\Xi^0$
	$-\frac{2}{\sqrt{3}}$	$-\frac{2}{\sqrt{3}}$	$\frac{1}{\sqrt{3}}$	$\frac{1}{\sqrt{3}}$	$\frac{1}{\sqrt{3}}$	$-\frac{1}{\sqrt{3}}$	$\frac{1}{\sqrt{3}}$	$\frac{1}{\sqrt{3}}$
π^0			$\bar{\Sigma}^-\,\Sigma^-$	$\bar{\Sigma}^+\,\Sigma^+$	$\bar{\Sigma}^0\,\Lambda$	$\bar{\Lambda}\,\Sigma^0$	$\bar{\Xi}^-\,\Xi^-$	$\bar{\Xi}^0\,\Xi^0$
			1	-1	$\frac{1}{\sqrt{3}}$	$\frac{1}{\sqrt{3}}$	1	-1
π^-			$\bar{\Sigma}^-\,\Sigma^0$	$\bar{\Sigma}^0\,\Sigma^+$	$\bar{\Sigma}^-\,\Lambda$	$\bar{\Lambda}\,\Sigma^+$	$\bar{\Xi}^-\,\Xi^0$	
			-1	1	$\frac{1}{\sqrt{3}}$	$\frac{1}{\sqrt{3}}$	$\sqrt{2}$	
π^+			$\bar{\Sigma}^0\,\Sigma^-$	$\bar{\Sigma}^+\,\Sigma^0$	$\bar{\Sigma}^+\,\Lambda$	$\bar{\Lambda}\,\Sigma^-$	$\bar{\Xi}^0\,\Xi^-$	
			-1	1	$\frac{1}{\sqrt{3}}$	$\frac{1}{\sqrt{3}}$	$\sqrt{2}$	
K^-	$\bar{\Lambda}\,p$	$\bar{\Sigma}^0\,p$	$\bar{\Sigma}^-\,n$	$\bar{\Xi}^-\,\Lambda$				
	$\frac{1}{\sqrt{3}}$	1	$\sqrt{2}$	$-\frac{2}{\sqrt{3}}$				
K^+	$\bar{p}\,\Lambda$	$\bar{p}\,\Sigma^0$	$\bar{n}\,\Sigma^-$	$\bar{\Lambda}\,\Xi^-$				
	$\frac{1}{\sqrt{3}}$	1	$\sqrt{2}$	$-\frac{2}{\sqrt{3}}$				
$\bar{K}^0$	$\bar{\Lambda}\,n$	$\bar{\Sigma}^0\,n$	$\bar{\Sigma}^+\,p$	$\bar{\Xi}^0\,\Lambda$				
	$\frac{1}{\sqrt{3}}$	-1	$\sqrt{2}$	$-\frac{2}{\sqrt{3}}$				
K^0	$\bar{n}\,\Lambda$	$\bar{n}\,\Sigma^0$	$\bar{p}\,\Sigma^+$	$\bar{\Lambda}\,\Xi^0$				
	$\frac{1}{\sqrt{3}}$	-1	$\sqrt{2}$	$-\frac{2}{\sqrt{3}}$				

Table D.2: Coefficients β for the BBP vertex.

Coefficients of the box integral

The box diagram generates an integral that we have analytically calculated in the general case in Eq. (4.26). The expression has four coefficients (a, b, c and $C_{V_1}C_{V_2}$) which depend on each channel and particles involved in the loop, the baryon B and the three pseudoscalar mesons (B_1, B_2 and B_3). The Tables E.1, E.2, E.3 and E.4, contain those coefficients for each quantum number, channel and loop.

Coefficients for state $S = 0$, $I = 1/2$					
Channel	Box	$(D+F)^2$	$(D-F)^2$	$(D+F)(D-F)$	$C_{V_1}C_{V_2}$
	$BP_1P_2P_3$	a	b	c	
ρN	$N\pi\pi$	1	0	0	$\frac{4}{3}$
	ΣKKK	0	$\frac{1}{4}$	0	1
	ΛKKK	1	$\frac{1}{4}$	-1	1
ωN	ΣKKK	0	1	0	$\frac{3}{4}$
	ΛKKK	1	$\frac{1}{4}$	-1	$\frac{1}{3}$
ϕN	ΣKKK	0	1	0	$\frac{3}{2}$
	ΛKKK	1	$\frac{1}{4}$	-1	$\frac{2}{3}$
$K^*\Lambda$	$NK\pi K$	1	$\frac{1}{4}$	-1	1
	$\Sigma\pi K\pi$	1	1	2	$\frac{1}{4}$
	$N\eta K\eta$	1	1	2	$\frac{1}{4}$
	$NK\eta K$	1	$\frac{1}{4}$	-1	1
$K^*\Sigma$	$NK\pi K$	0	1	0	1
	$\Sigma\pi K\pi$	1	1	-2	$\frac{11}{12}$
	$\Sigma\eta K\eta$	1	1	2	$\frac{1}{4}$
	$\Lambda\eta K\eta$	1	1	2	$\frac{1}{18}$
	$\Sigma\pi K\eta$	1	-1	0	$-\frac{1}{3}$
	$\Sigma\eta K\pi$	1	-1	0	$\frac{1}{3}$
Non-diagonal terms					
Channel	Box	$(D+F)^2$	$(D-F)^2$	$(D+F)(D-F)$	$C_{V_1}C_{V_2}$
	$BP_1P_2P_3$	a	b	c	
$\rho N \to K^*\Lambda$	$\Lambda KK\eta$	2	-1	1	$\frac{1}{4}$
	$\Sigma KK\pi$	0	1	1	$-\frac{1}{4}$
	$N\pi\pi K$	2	0	-1	1
$\rho N \to K^*\Sigma$	$\Lambda KK\pi$	2	-1	1	$\frac{1}{4}$
	$\Sigma KK\eta$	0	1	1	$-\frac{1}{4}$
	$\Sigma KK\pi$	0	-1	1	$-\frac{1}{2}$
	$N\pi\pi K$	0	0	1	$\frac{5}{3}$
$K^*\Lambda \to K^*\Sigma$	$\Sigma\pi K\eta$	1	1	2	$\frac{1}{4}$
	$\Sigma\pi K\pi$	1	-1	0	$\frac{1}{3}$
	$\Lambda\eta K\pi$	1	1	2	$-\frac{1}{4}$
	$NK\pi K$	0	-1	2	$\frac{5}{12}$
	$NK\eta K$	0	-1	2	$-\frac{1}{4}$

Table E.1: Coefficients of the Box Integral for the S=0, I=1/2 states.

Coefficients for state $S = -1,\ I = 0$					
Channel	Box	$(D+F)^2$	$(D-F)^2$	$(D+F)(D-F)$	$C_{V_1}C_{V_2}$
	$BP_1P_2P_3$	a	b	c	
$\bar{K}^*N$	$\Sigma K\pi K$	0	1	0	$\frac{3}{2}$
	$N\pi K\pi$	1	0	0	1
	$\Lambda K\eta K$	1	$\frac{1}{4}$	-1	2
	$N\eta K\eta$	$\frac{1}{4}$	1	-1	2
$\omega\Lambda$	ΞKKK	$\frac{1}{4}$	1	-1	$\frac{2}{3}$
	$NKKK$	1	$\frac{1}{4}$	-1	$\frac{2}{3}$
$\rho\Sigma$	$\Sigma\pi\pi\pi$	1	1	-2	$\frac{10}{3}$
	ΞKKK	1	0	0	$\frac{5}{6}$
	$NKKK$	0	1	0	$\frac{5}{6}$
$\phi\Lambda$	ΞKKK	$\frac{1}{4}$	1	-1	$\frac{4}{3}$
	$NKKK$	1	$\frac{1}{4}$	-1	$\frac{4}{3}$
$K^*\Xi$	$\Sigma K\pi K$	1	0	0	1
	$\Xi\pi K\pi$	0	1	0	$\frac{5}{4}$
	$\Lambda K\pi K$	$\frac{1}{4}$	1	-1	$\frac{1}{3}$
	$\Xi\eta K\eta$	1	$\frac{1}{4}$	0	1
	$\Sigma K\eta K$	1	0	0	$\frac{3}{2}$
	$\Xi\pi K\eta$	0	1	-2	$\frac{1}{2}$
	$\Xi\eta K\pi$	0	1	2	$\frac{1}{2}$

Table E.2: Coefficients of the Box Integral for the S=-1, I=0 states.

Coefficients for state $S = -1$, $I = 1$					
Channel	Box	$(D+F)^2$	$(D-F)^2$	$(D+F)(D-F)$	$C_{V_1}C_{V_2}$
	$BP_1P_2P_3$	a	b	c	
$\bar{K}^*N$	$\Sigma K\pi K$	0	1	0	1
	$\Lambda K\pi K$	1	$\frac{1}{4}$	-1	$\frac{2}{3}$
	$N\pi K\pi$	1	0	0	$\frac{1}{2}$
	$\Sigma K\eta K$	0	1	0	$\frac{3}{2}$
$\rho\Lambda$	$\Sigma\pi\pi\pi$	1	1	2	$\frac{2}{3}$
	ΞKKK	$\frac{1}{4}$	1	-1	$\frac{2}{3}$
	$NKKK$	1	$\frac{1}{4}$	-1	$\frac{2}{3}$
$\rho\Sigma$	$\Sigma\pi\pi\pi$	1	1	-2	1
	$\Lambda\pi\pi\pi$	1	1	2	$\frac{2}{3}$
	ΞKKK	1	0	0	1
	$NKKK$	0	1	0	1
$\omega\Sigma$	ΞKKK	1	0	0	$\frac{1}{2}$
	$NKKK$	0	1	0	$\frac{1}{2}$
$K^*\Xi$	$\Sigma K\pi K$	1	0	0	$\frac{1}{2}$
	$\Xi\pi K\pi$	0	1	0	$\frac{5}{4}$
	$\Lambda K\pi K$	$\frac{1}{4}$	1	-1	1
	$\Xi\eta K\eta$	1	$\frac{1}{4}$	0	1
	$\Lambda K\eta K$	$\frac{1}{4}$	1	-1	2
	$\Xi\pi K\eta$	0	-1	2	$\frac{1}{2}$
	$\Xi\eta K\pi$	0	-1	-2	$\frac{1}{2}$
$\phi\Sigma$	ΞKKK	1	0	0	1
	$NKKK$	0	1	0	1

Table E.3: Coefficients of the Box Integral for the S=-1, I=1 states.

Coefficients for state $S = -2,\ I = 1/2$					
Channel	Box	$(D+F)^2$	$(D-F)^2$	$(D+F)(D-F)$	$C_{V_1}C_{V_2}$
	$BP_1P_2P_3$	a	b	c	
$\bar{K}^*\Lambda$	$\Xi K\pi K$	$\frac{1}{4}$	1	-1	1
	$\Sigma\pi K\pi$	1	1	2	$\frac{1}{4}$
	$\Xi K\eta K$	$\frac{1}{4}$	1	-1	1
	$\Lambda\eta K\eta$	1	1	2	$\frac{1}{4}$
$\bar{K}^*\Sigma$	$\Xi K\pi K$	1	0	0	$\frac{11}{12}$
	$\Sigma\pi K\pi$	1	1	-2	1
	$\Lambda\pi K\pi$	1	1	2	$\frac{1}{12}$
	$\Xi K\eta K$	1	0	0	$\frac{1}{4}$
	$\Sigma\eta K\eta$	1	1	2	$\frac{1}{4}$
	$\Sigma\pi K\eta$	1	-1	0	$-\frac{1}{3}$
	$\Sigma\eta K\pi$	1	-1	0	$-\frac{1}{3}$
$\rho\Xi$	$\Xi\pi\pi\pi$	0	1	0	4
	ΛKKK	$\frac{1}{4}$	1	-1	1
	ΣKKK	1	0	0	$\frac{1}{12}$
$\omega\Xi$	ΛKKK	$\frac{1}{4}$	1	-1	$\frac{1}{3}$
	ΣKKK	1	0	0	$\frac{1}{4}$
$\phi\Sigma$	ΛKKK	$\frac{1}{4}$	1	-1	$\frac{2}{3}$
	ΣKKK	1	0	0	$\frac{1}{2}$

Table E.4: Coefficients of the Box Integral for the S=-2, I=1/2 states.

Appendix F

Evaluation the vertices

The diagonal transition for $\pi\Delta$ (s-wave) and ρN (s-wave) are taken from Refs. [28] and [29] respectively. So we need to evaluate the transition potential of Fig. F.1. When constructing the Kroll-Ruderman term, we shall get the contact term of the type of $\vec{S}^+\vec{\epsilon}$. We must evaluate this matrix element

$$\left\langle 3/2M'|\vec{S}^+\vec{\epsilon}\,|JM\right\rangle \tag{F.1}$$

where

$$|JM\rangle = \sum_m \mathcal{C}\left(1/2, 1, J; m, M-m, M\right)|1/2m\rangle\,|\vec{\epsilon}_{M-m}\rangle \tag{F.2}$$

As $\vec{\epsilon}$ is part of $|JM\rangle$, we get that in the spherical basis

$$\vec{S}^+\vec{\epsilon}_{M-m} \equiv S^+_{M-m} \tag{F.3}$$

then the matrix element becomes

$$\left\langle 3/2M'|S^+_{M-m}|1/2m\right\rangle \equiv \mathcal{C}\left(1, 1/2, 3/2; M-m, m, M'\right)\left\langle ||S^+||\right\rangle \tag{F.4}$$
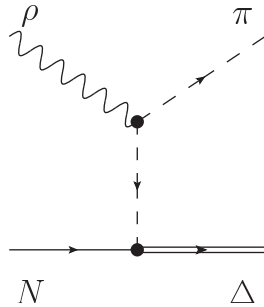
Figure F.1: Diagram of the transition $\rho N \to \pi\Delta$ (s-wave).

where the reduced matrix element is chosen to be 1 by construction, and from the Clebsch-Gordan coefficient we get a $\delta_{MM'}$. Finally we get that

$$\sum_m \mathcal{C}\left(1/2, 1, J; m, M - m\right) \mathcal{C}\left(1/2, 1, 3/2; m, M - m\right) \delta_{MM'} = \delta_{MM'}\delta_{3/2J}$$

(F.5)

Hence, for spin $3/2$ of ρN this operator is unity 1. Getting the Kroll-Ruderman term, we must substitute

$$\vec{\epsilon}\left(\vec{P}_V + 2\vec{q}\right) \frac{1}{(P_V + q)^2 - m_\pi^2} \vec{S}^+ \left(\vec{P}_V + \vec{q}\right) \to \vec{S}^+ \vec{\epsilon}$$

(F.6)

We need to write the states of isospin basis in charge basis, with our sign convention $\rho^+ \equiv - \left|1, 1\right\rangle$.

$$
\begin{aligned}
\left|\rho N, I = 1/2, 1/2\right\rangle &= -\sqrt{\frac{2}{3}} \left|\rho^+ n\right\rangle - \frac{1}{\sqrt{3}} \left|\rho^0 p\right\rangle \\
\left|\rho N, I = 3/2, 1/2\right\rangle &= -\sqrt{\frac{1}{3}} \left|\rho^+ n\right\rangle + \sqrt{\frac{2}{3}} \left|\rho^0 p\right\rangle \\
\left|\pi \Delta, I = 1/2, 1/2\right\rangle &= \sqrt{\frac{1}{2}} \left|\pi^- \Delta^{++}\right\rangle - \sqrt{\frac{1}{3}} \left|\pi^0 \Delta^+\right\rangle - \sqrt{\frac{1}{6}} \left|\pi^+ \Delta^0\right\rangle \\
\left|\pi \Delta, I = 3/2, 1/2\right\rangle &= -\sqrt{\frac{2}{5}} \left|\pi^- \Delta^{++}\right\rangle - \sqrt{\frac{1}{15}} \left|\pi^0 \Delta^+\right\rangle - \sqrt{\frac{8}{15}} \left|\pi^+ \Delta^0\right\rangle
\end{aligned}
$$

(F.7)

For the transition $\rho N \to \pi \Delta$ (s-wave) we have the vertices of Fig. F.2. To evaluate those vertices we need both Lagrangians, one for the VPP vertex and the other one for the lower $\pi N \Delta$ vertex. The first diagram has a vertex

$$t_{\rho^+ \pi^+ \pi^0} = -\mathcal{L} = g\sqrt{2}\left(\vec{P}_V + \vec{q} + \vec{q}\right)\vec{\epsilon}$$

(F.8)

The other coefficients of the diagrams for the different charge combinations are indicated in Fig. F.2. The lower vertex has an isospin coefficient for $\pi N \Delta$, giving a transition vertex for the first diagram

$$-it_{\pi^0 n \Delta^0} = \frac{f_{\pi N \Delta}}{m_\pi} \vec{S}^+ \left(\vec{P}_V + \vec{q}\right) \sqrt{\frac{2}{3}}$$

(F.9)

The other isospin coefficients of the lower vertices are shown in Fig. F.2. Combining the two vertices and the pion propagator, we get the transition potential of the first diagram.

$$-it_{\rho^+ n \to \pi^+ \Delta^0} = -ig\sqrt{2}\, 2\vec{q}\,\vec{\epsilon} \frac{i}{(P_V + q)^2 - m_\pi^2} \frac{f_{\pi N \Delta}}{m_\pi} \vec{S}^+ \vec{q} \sqrt{\frac{2}{3}}$$

(F.10)

As mentioned before, we need to add the Kroll-Ruderman term as $\vec{S}^+\vec{\epsilon}$,

$$-it_{\rho^+ n \to \pi^+ \Delta^0 (KR)} = g\sqrt{2}\frac{f_{\pi N\Delta}}{m_\pi}\sqrt{\frac{2}{3}}\vec{S}^+\vec{\epsilon} \tag{F.11}$$

So in the s-wave for a π-exchange we can sum the momenta products as

$$2\vec{q}\cdot\vec{\epsilon}\,\vec{S}^+\cdot\vec{q} = 2q_i\epsilon_i S_j^+ q_j \to \epsilon_i S_j^+ \frac{2}{3}\vec{q}^2\delta_{ij} = \frac{2}{3}\vec{q}^2\vec{S}^+\cdot\vec{\epsilon} \tag{F.12}$$

And we have shown for $J = 3/2$ that $\vec{S}^+\cdot\vec{\epsilon} = 1$ The sum of the pion propagator and the Kroll-Ruderman for the first diagram gives us

$$-it_{\rho^+ n \to \pi^+ \Delta^0} = g\sqrt{2}\sqrt{\frac{2}{3}}\frac{f_{\pi N\Delta}}{m_\pi}\left(\frac{\frac{2}{3}\vec{q}^2}{(P_V+q)^2-m_\pi^2}+1\right) \tag{F.13}$$

Hence putting all the coefficients of the Clebsch-Gordan and the corresponding vertex factor we get

$$\langle \pi\Delta, I = 1/2, 1/2| - it|\rho N, I = 1/2, 1/2\rangle =$$

$$\langle\sqrt{\frac{1}{2}}\pi^-\Delta^{++} - \sqrt{\frac{1}{3}}\pi^0\Delta^+ - \sqrt{\frac{1}{6}}\pi^+\Delta^0| - it|\sqrt{\frac{2}{3}}\rho^+ n - \frac{1}{\sqrt{3}}\rho^0 p\rangle =$$

$$\left(\frac{1}{\sqrt{2}}\frac{1}{\sqrt{3}}\sqrt{2}(-1) - \frac{1}{\sqrt{3}}\sqrt{\frac{2}{3}}(-\sqrt{2})(-\frac{1}{\sqrt{3}}) - \frac{1}{\sqrt{6}}\sqrt{\frac{2}{3}}\sqrt{2}\sqrt{\frac{2}{3}}\right.$$

$$\left.-\frac{1}{\sqrt{6}}\frac{1}{\sqrt{3}}(-\sqrt{2})\frac{1}{\sqrt{3}}\right) = \frac{2}{\sqrt{3}} \tag{F.14}$$

$$\tag{F.15}$$

The isospin factor is $\frac{2}{\sqrt{3}}$, so finally all together

$$-it_{\rho N(s) \to \pi\Delta(s)} = g\frac{2}{\sqrt{3}}\frac{f_{\pi N\Delta}}{m_\pi}\left(\frac{\frac{2}{3}\vec{q}^2}{(P_V+q)^2-m_\pi^2}+1\right) \tag{F.16}$$

We need also to evaluate the s-wave and d-wave mixing, ρN is in $L = 0$ but $\pi\Delta$ can be in $L = 0$ and $L = 2$ since there is enough momentum for $N^*(1520)$ and $N^*(1700)$. With ρN below threshold there is no need to worry about $L = 2$ for ρN. We want to work with ρN(s), $\pi\Delta$(s) and $\pi\Delta$(d), for this we shall also include the $\rho N \to \pi N(d)$ transition.

Let us evaluate the transition $\rho N(s) \to \rho N(s)$ through an intermediate state $\pi\Delta$ as shown in Fig F.3(a). Let us take the third component of spin $1/2$ and 1 for N and ρ respectively, to get $M = 3/2$ since the result does not depend on the third component. With this choice, both polarizations $\vec{\epsilon}$ and
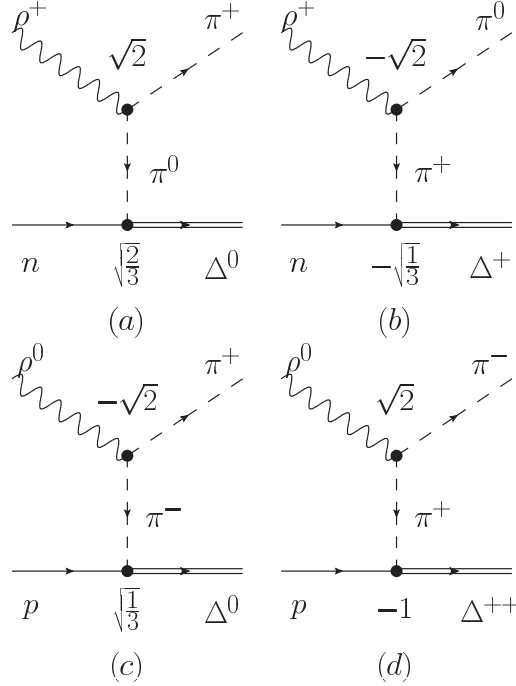
Figure F.2: Diagram of the transition $\rho N \to \pi \Delta$ (s-wave).

$\vec{\epsilon}\,'$ will be the same and we have neglected the momentum $\vec{k}$. The terms of the four vertices are

$$\vec{\epsilon} \cdot 2\vec{q} \ \vec{S} \cdot \vec{q} \ \vec{\epsilon} \cdot 2\vec{q} \ \vec{S}^+ \cdot \vec{q} \tag{F.17}$$

We can put together the polarization terms and the isospin transition operators and use

$$\vec{S} \cdot \vec{q} \ \vec{S}^+ \cdot \vec{q} = S_i q_j \ S_j^+ q_j = (\frac{2}{3}\delta_{ij} - \frac{i}{3}\varepsilon_{ijk}\sigma_k)q_i q_j = \frac{2}{3}\vec{q}^{\,2} \tag{F.18}$$

For the polarization terms we have in the loop integral

$$4\vec{\epsilon} \cdot \vec{q} \ \vec{\epsilon} \cdot \vec{q} = 4\epsilon_i q_i \ \epsilon_j q_j = \frac{4}{3}\delta_{ij}\vec{q}^{\,2}\epsilon_i \epsilon_j = \frac{4}{3}\vec{q}^{\,2}\vec{\epsilon} \cdot \vec{\epsilon} = \frac{4}{3}\vec{q}^{\,2} \tag{F.19}$$

as $\vec{\epsilon} \cdot \vec{\epsilon} = 1$. Now, all together we have

$$\frac{4}{3}\vec{q}^{\,2}\frac{2}{3}\vec{q}^{\,2} \tag{F.20}$$

including both $L = 0$ and $L = 2$ contributions. For s-wave we got $\frac{2}{3}\vec{q}^{\,2}$ for one pion exchange (See Eq. (F.12)) so, the box equivalent operator with only s-wave will be

$$\frac{2}{3}\frac{2}{3}\vec{q}^{\,2}\vec{q}^{\,2} = \frac{4}{9}\vec{q}^{\,4} \tag{F.21}$$
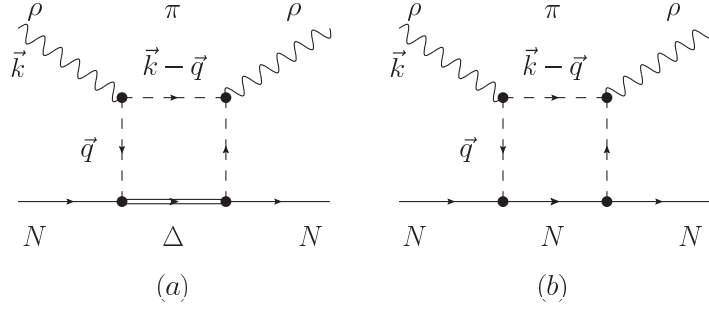
Figure F.3: Box diagrams for the $L = 2$ transition: (a) $\rho N \to \pi \Delta$ and (b) $\rho N \to \pi N$.

subtracting this from the total transition (Eq. (F.20)) we get the d-wave transition in the box

$$\frac{8}{9}\vec{q}^4 - \frac{4}{9}\vec{q}^4 = \frac{4}{9}\vec{q}^4 \tag{F.22}$$

So finally we obtain that for the d-wave transition of one pion exchange the contribution is $\frac{2}{3}\vec{q}^2$, the same one as for the s-wave transition. All the other terms are the same but without the Kroll-Ruderman factor which only comes in $L = 0$. Thus,

$$-it_{\rho N(s) \to \pi \Delta(d)} = g \frac{2}{\sqrt{3}} \frac{f_{\pi N \Delta}}{m_\pi} \left(\frac{\frac{2}{3}\vec{q}^2}{(P_V + q)^2 - m_\pi^2} \right) \tag{F.23}$$

In the case of $\rho N \to \pi N$ (d-wave) transition, the s-wave for $3/2$ does not exist, so whatever comes out will be d-wave. We use the same procedure as for $\pi \Delta$, we chose the third component of spin to be $3/2$. The diagram is shown in Fig F.3(b) and the operators of the vertices are

$$\vec{\epsilon} \cdot 2\vec{q} \, \vec{\sigma} \cdot \vec{q} \, \vec{\epsilon} \cdot 2\vec{q} \, \vec{\sigma} \cdot \vec{q} \tag{F.24}$$
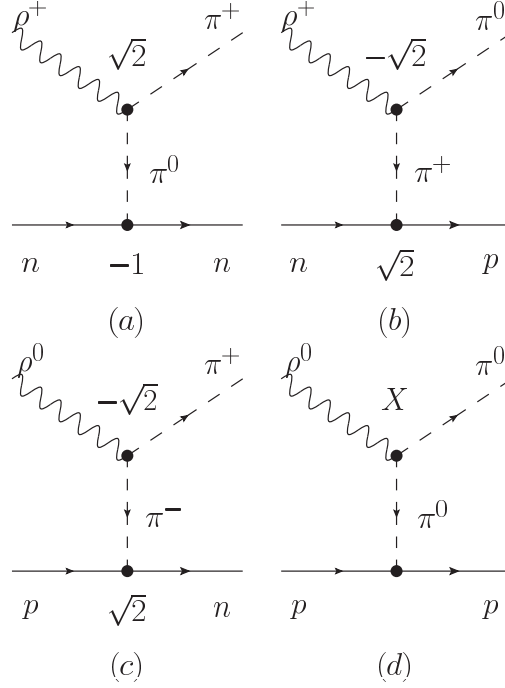
In the same way

$$\vec{\sigma} \cdot \vec{q} \, \vec{\sigma} \cdot \vec{q} = \sigma_i q_j \, \sigma_j q_j = (\delta_{ij} - i\varepsilon_{ijk}\sigma_k)q_i q_j = \vec{q}^2 \tag{F.25}$$

and for the polarization we have the same result as Eq. (F.19). So we get

$$\frac{4}{3}\vec{q}^2\vec{q}^2 = \frac{2}{\sqrt{3}}\vec{q}^2 \frac{2}{\sqrt{3}}\vec{q}^2 \tag{F.26}$$

The result for each vertex in the $\rho N \to \pi N$ (d-wave) is $\frac{2}{\sqrt{3}}\vec{q}^2$.

Figure F.4: Diagram of the transition $\rho N \to \pi N$ (d-wave).

Hence the $\vec{\epsilon} \cdot 2\vec{q} \, \vec{\sigma} \cdot \vec{q}$ operator in one pion exchange can be replaced by

$$\frac{2}{\sqrt{3}} \vec{q}^{\,2} \frac{f_{\pi NN}}{m_\pi} \tag{F.27}$$

which replaces the equivalent contribution $\frac{2}{3} \vec{q}^{\,2} \frac{f_{\pi N\Delta}}{m_\pi}$ that we had for the $\rho N \to \pi \Delta$ (d-wave) transition. Next we must do the isospin combination and the charge factors for each vertex as shown in Fig. F.4.

$$|\rho N, I = 1/2, 1/2\rangle \;=\; -\sqrt{\frac{2}{3}} \, |\rho^+ n\rangle - \frac{1}{\sqrt{3}} \, |\rho^0 p\rangle \tag{F.28}$$

$$|\pi N, I = 1/2, 1/2\rangle \;=\; -\sqrt{\frac{2}{3}} \, |\pi^+ n\rangle - \frac{1}{\sqrt{3}} \, |\pi^0 p\rangle \tag{F.29}$$

Looking at the diagrams, the isospin factor for the transition $\rho N \to \pi N$

(d-wave) will be

$$\langle \rho N, I = 1/2, 1/2 | T | \pi N, I = 1/2, 1/2 \rangle = \tag{F.30}$$

$$\frac{2}{3} \langle \rho^+ n | \pi^+ n \rangle + \sqrt{\frac{2}{3}}\sqrt{\frac{1}{3}} \langle \rho^+ n | \pi^0 p \rangle + \sqrt{\frac{2}{3}}\sqrt{\frac{1}{3}} \langle \rho^0 p | \pi^+ n \rangle = \tag{F.31}$$

$$\frac{2}{3}\sqrt{2}(-1) + 2\sqrt{\frac{2}{3}}\sqrt{\frac{1}{3}}(-\sqrt{2})\sqrt{2} = -2\sqrt{2} \tag{F.32}$$

Finally we have

$$-it_{\rho N(s) \to \pi N(d)} = g(-2\sqrt{6})\frac{f_{\pi NN}}{m_\pi}\left(\frac{\frac{2}{3}\vec{q}^{\,2}}{(P_V + q)^2 - m_\pi^2}\right) \tag{F.33}$$

Bibliography

[1] Murray Gell-Mann. The Eightfold Way: A Theory of strong interaction symmetry. 1961.

[2] Murray Gell-Mann. Symmetries of baryons and mesons. *Phys.Rev.*, 125:1067–1084, 1962.

[3] V.E. Barnes, P.L. Connolly, D.J. Crennell, B.B. Culwick, W.C. Delaney, et al. Observation of a Hyperon with Strangeness -3. *Phys.Rev.Lett.*, 12:204–206, 1964.

[4] L. David Roper and Robert M. Wright. Energy-dependent pion - nucleon phase shift analysis 0-MeV - 700-MeV, l(m) = 4 solution. 1964.

[5] W. Konen and H.J. Weber. Electromagnetic $N \to N^*(1535)$ Transition in the Relativistic Constituent Quark Model. *Phys.Rev.*, D41:2201, 1990.

[6] B. Metsch. The Roper resonance in the constituent quark model. pages 73–82, 2000.

[7] Keitaro Kagata and Atsushi Hosaka. Roper resonance in a quark-diquark model. 2006.

[8] Steven Weinberg. Phenomenological Lagrangians. *Physica*, A96:327, 1979.

[9] J. Gasser and H. Leutwyler. Chiral Perturbation Theory: Expansions in the Mass of the Strange Quark. *Nucl.Phys.*, B250:465, 1985.

[10] A. Dobado and J.R. Pelaez. The Inverse amplitude method in chiral perturbation theory. *Phys.Rev.*, D56:3057–3073, 1997.

185

[11] J.A. Oller and E. Oset. Chiral symmetry amplitudes in the S wave isoscalar and isovector channels and the σ, $f_0(980)$, $a_0(980)$ scalar mesons. *Nucl.Phys.*, A620:438–456, 1997.

[12] D. Jido, J.A. Oller, E. Oset, A. Ramos, and U.G. Meissner. Chiral dynamics of the two $\Lambda(1405)$ states. *Nucl.Phys.*, A725:181–200, 2003.

[13] Masako Bando, Taichiro Kugo, and Koichi Yamawaki. Nonlinear Realization and Hidden Local Symmetries. *Phys.Rept.*, 164:217–314, 1988.

[14] Norbert Kaiser, P.B. Siegel, and W. Weise. Chiral dynamics and the $S_{11}(1535)$ nucleon resonance. *Phys.Lett.*, B362:23–28, 1995.

[15] Norbert Kaiser, P.B. Siegel, and W. Weise. Chiral dynamics and the low-energy kaon - nucleon interaction. *Nucl.Phys.*, A594:325–345, 1995.

[16] Norbert Kaiser, T. Waas, and W. Weise. SU(3) chiral dynamics with coupled channels: Eta and kaon photoproduction. *Nucl.Phys.*, A612:297–320, 1997.

[17] E. Oset and A. Ramos. Nonperturbative chiral approach to s wave $\bar{K}$N interactions. *Nucl.Phys.*, A635:99–120, 1998.

[18] J.A. Oller and Ulf G. Meissner. Chiral dynamics in the presence of bound states: Kaon nucleon interactions revisited. *Phys.Lett.*, B500:263–272, 2001.

[19] C. Garcia-Recio, M.F.M. Lutz, and J. Nieves. Quark mass dependence of s wave baryon resonances. *Phys.Lett.*, B582:49–54, 2004.

[20] C. Garcia-Recio, J. Nieves, E. Ruiz Arriola, and M.J. Vicente Vacas. S = -1 meson baryon unitarized coupled channel chiral perturbation theory and the S_{01} $\Lambda(1405)$ and $\Lambda(1670)$ resonances. *Phys.Rev.*, D67:076009, 2003.

[21] T. Hyodo, S.I. Nam, D. Jido, and A. Hosaka. Flavor SU(3) breaking effects in the chiral unitary model for meson baryon scatterings. *Phys.Rev.*, C68:018201, 2003.

[22] Tetsuo Hyodo, Daisuke Jido, and Atsushi Hosaka. Study of exotic hadrons in s-wave scatterings induced by chiral interaction in the flavor symmetric limit. *Phys.Rev.*, D75:034002, 2007.

[23] E.E. Kolomeitsev and M.F.M. Lutz. On baryon resonances and chiral symmetry. *Phys.Lett.*, B585:243–252, 2004.

[24] Sourav Sarkar, E. Oset, and M.J. Vicente Vacas. Baryonic resonances from baryon decuplet-meson octet interaction. *Nucl.Phys.*, A750:294–323, 2005.

[25] V.K. Magas, E. Oset, and A. Ramos. Evidence for the two pole structure of the $\Lambda(1405)$ resonance. *Phys.Rev.Lett.*, 95:052301, 2005.

[26] D. Jido, E. Oset, and T. Sekihara. Kaonic production of $\Lambda(1405)$ off deuteron target in chiral dynamics. *Eur.Phys.J.*, A42:257–268, 2009.

[27] P. Gonzalez, E. Oset, and J. Vijande. An Explanation of the $\Delta(5/2^-)(1930)$ as a $\rho\Delta$ bound state. *Phys.Rev.*, C79:025209, 2009.

[28] Sourav Sarkar, Bao-Xi Sun, E. Oset, and M.J. Vicente Vacas. Dynamically generated resonances from the vector octet-baryon decuplet interaction. *Eur.Phys.J.*, A44:431–443, 2010.

[29] E. Oset and A. Ramos. Dynamically generated resonances from the vector octet-baryon octet interaction. *Eur.Phys.J.*, A44:445–454, 2010.

[30] M. Bando, T. Kugo, S. Uehara, K. Yamawaki, and T. Yanagida. Is ρ Meson a Dynamical Gauge Boson of Hidden Local Symmetry? *Phys.Rev.Lett.*, 54:1215, 1985.

[31] Masayasu Harada and Koichi Yamawaki. Hidden local symmetry at loop: A New perspective of composite gauge boson and chiral phase transition. *Phys.Rept.*, 381:1–233, 2003.

[32] M. Doring, C. Hanhart, F. Huang, S. Krewald, and U.-G. Meissner. Analytic properties of the scattering amplitude and resonances parameters in a meson exchange model. *Nucl.Phys.*, A829:170–209, 2009.

[33] R. Molina, D. Nicmorus, and E. Oset. The $\rho\rho$ interaction in the hidden gauge formalism and the $f_0(1370)$ and $f_2(1270)$ resonances. *Phys.Rev.*, D78:114018, 2008.

[34] H. Nagahiro, J. Yamagata-Sekihara, E. Oset, S. Hirenzaki, and R. Molina. The $\gamma\gamma$ decay of the $f_0(1370)$ and $f_2(1270)$ resonances in the hidden gauge formalism. *Phys.Rev.*, D79:114023, 2009.

[35] L.S. Geng and E. Oset. Vector meson-vector meson interaction in a hidden gauge unitary approach. *Phys.Rev.*, D79:074009, 2009.

[36] Ju-Jun Xie, M. Albaladejo, and E. Oset. Signature of an h_1 state in the $J/\psi \to \eta h_1 \to \eta K^{*0}\bar{K}^{*0}$ decay. *Phys.Lett.*, B728:319–322, 2014.

[37] M. Ablikim et al. Study of J/Ψ decays into $\eta K^{*0}\bar{K}^{*0}$. *Phys.Lett.*, B685:27–32, 2010.

[38] J.A. Oller, E. Oset, and A. Ramos. Chiral unitary approach to meson meson and meson - baryon interactions and nuclear applications. *Prog.Part.Nucl.Phys.*, 45:157–242, 2000.

[39] Stefan Scherer. Introduction to chiral perturbation theory. *Adv.Nucl.Phys.*, 27:277, 2003.

[40] Ulf G. Meissner. Low-Energy Hadron Physics from Effective Chiral Lagrangians with Vector Mesons. *Phys.Rept.*, 161:213, 1988.

[41] Elizabeth Ellen Jenkins and Aneesh V. Manohar. Chiral corrections to the baryon axial currents. *Phys.Lett.*, B259:353–358, 1991.

[42] E. Oset, A. Ramos, and C. Bennhold. Low lying S = -1 excited baryons and chiral symmetry. *Phys.Lett.*, B527:99–105, 2002.

[43] J.A. Oller and E. Oset. N/D description of two meson amplitudes and chiral symmetry. *Phys.Rev.*, D60:074023, 1999.

[44] Jurij W. Darewych, Marko Horbatsch, and Roman Koniuk. The Photon Decays of Baryons With Strangeness. *Phys.Rev.*, D28:1125, 1983.

[45] M. Warns, W. Pfeil, and H. Rollnik. Electromagnetic properties of hyperons in a relativized quark model. *Phys.Lett.*, B258:431–440, 1991.

[46] Y. Umino and F. Myhrer. Electromagnetic decays of excited hyperons. *Nucl.Phys.*, A529:713–726, 1991.

[47] Yasuo Umino and Fred Myhrer. Electromagnetic decays of excited hyperons. 2. *Nucl.Phys.*, A554:593–619, 1993.

[48] R. Bijker, F. Iachello, and A. Leviatan. Algebraic models of hadron structure. 2. Strange baryons. *Annals Phys.*, 284:89–133, 2000.

[49] Frank E. Close and Zhen-Ping Li. Photoproduction and Electroproduction of N^* in a Quark Model With QCD. *Phys.Rev.*, D42:2194–2206, 1990.

[50] M. Warns, H. Schroder, W. Pfeil, and H. Rollnik. Calculations of Electromagnetic Nucleon Form-factors and Electroexcitation Amplitudes of Isobars. *Z.Phys.*, C45:627, 1990.

[51] Simon Capstick and B.D. Keister. Baryon current matrix elements in a light front framework. *Phys.Rev.*, D51:3598–3612, 1995.

[52] B.D. Keister and S. Capstick. Baryon current matrix elements in a relativistic quark model. pages physics* 58–67, 1997.

[53] M. Aiello, M.M. Giannini, and E. Santopinto. Electromagnetic transition form-factors of negative parity nucleon resonances. *J.Phys.*, G24:753–762, 1998.

[54] E. Pace, G. Salme, and S. Simula. Investigation of N - N^* electromagnetic form-factors within a front form CQM. *Few Body Syst.Suppl.*, 10:407–410, 1999.

[55] Dirk Merten, Ulrich Loring, Klaus Kretzschmar, Bernard Metsch, and Herbert R. Petry. Electroweak form-factors of nonstrange baryons. *Eur.Phys.J.*, A14:477–489, 2002.

[56] M.M. Giannini, E. Santopinto, and A. Vassallo. An Overview of the hypercentral constituent quark model. *Prog.Part.Nucl.Phys.*, 50:263–272, 2003.

[57] Tim Van Cauteren, Dirk Merten, Tamara Corthals, Stijn Janssen, Bernard Metsch, et al. Electric and magnetic form-factors of strange baryons. *Eur.Phys.J.*, A20:283–291, 2004.

[58] Tim Van Cauteren, Jan Ryckebusch, Bernard Metsch, and Herbert-R. Petry. Helicity amplitudes and electromagnetic decays of hyperon resonances. *Eur.Phys.J.*, A26:339–359, 2005.

[59] B. Borasoy, E. Marco, and S. Wetzel. η, η' photoproduction and electroproduction off nucleons. *Phys.Rev.*, C66:055208, 2002.

[60] M. Doring, E. Oset, and Sourav Sarkar. Radiative decay of the $\Lambda(1520)$. *Phys.Rev.*, C74:065204, 2006.

[61] M. Doring. Radiative decay of the $\Delta^*(1700)$. *Nucl.Phys.*, A786:164–182, 2007.

[62] L.S. Geng, E. Oset, and M. Doring. The Radiative decay of the $\Lambda(1405)$ and its two-pole structure. *Eur.Phys.J.*, A32:201–211, 2007.

[63] R. Thompson et al. The $ep \rightarrow e'p\eta$ reaction at and above the $S_{11}(1535)$ baryon resonance. *Phys.Rev.Lett.*, 86:1702–1706, 2001.

[64] V.D. Burkert and T.S.H. Lee. Electromagnetic meson production in the nucleon resonance region. *Int.J.Mod.Phys.*, E13:1035–1112, 2004.

[65] I.G. Aznauryan, V.D. Burkert, H. Egiyan, K. Joo, R. Minehart, et al. Electroexcitation of the $P_{33}(1232)$, $P_{11}(1440)$, $D_{13}(1520)$, $S_{11}(1535)$ at $Q^2 = 0.4$ and 0.65 $(GeV/c)^2$. *Phys.Rev.*, C71:015201, 2005.

[66] T. Branz, L.S. Geng, and E. Oset. Two-photon and one photon-one vector meson decay widths of the $f_0(1370)$, $f_2(1270)$, $f_0(1710)$, $f_2'(1525)$, and $K_2^*(1430)$. *Phys.Rev.*, D81:054037, 2010.

[67] J. Beringer et al. Review of Particle Physics (RPP). *Phys.Rev.*, D86:010001, 2012.

[68] F. Mandl and Graham Shaw. Quantum Field Theory. 1985.

[69] H. Nagahiro, L. Roca, A. Hosaka, and E. Oset. Hidden gauge formalism for the radiative decays of axial-vector mesons. *Phys.Rev.*, D79:014015, 2009.

[70] I.M. Barbour, R.L. Crawford, and N.H. Parsons. An Analysis of Single Pion Photoproduction Between Threshold and 16-GeV. *Nucl.Phys.*, B141:253, 1978.

[71] R.C.E. Devenish, D.H. Lyth, and W.A. Rankin. Determination of Resonance Couplings and High-Energy Amplitudes in $\gamma n \to \pi n$ Using Fixed-t Dispersion Relations. *Phys.Lett.*, B52:227, 1974.

[72] Carl E. Carlson and Christopher D. Carone. Photoproduction of L=1 baryons: Quark model versus large N_c. *Phys.Rev.*, D58:053005, 1998.

[73] Simon Capstick. Photoproduction and electroproduction of non-strange baryon resonances in the relativized quark model. *Phys.Rev.*, D46:2864–2881, 1992.

[74] J. Ahrens, S. Altieri, J.R.M. Annand, H.-J. Arends, R. Beck, et al. Measurement of the helicity dependence for the $\gamma p \to n\pi^+$ channel in the second resonance region. *Phys.Rev.*, C74:045204, 2006.

[75] J. Ahrens et al. Helicity dependence of the $\gamma p \to N\pi$ channels and multipole analysis in the Δ region. *Eur.Phys.J.*, A21:323–333, 2004.

[76] J. Ahrens et al. The Helicity amplitudes $A_{1/2}$ and $A_{3/2}$ for the $D_{13}(1520)$ resonance obtained from the $\vec{\gamma}\vec{p} \to p\pi^0$ reaction. *Phys.Rev.Lett.*, 88:232002, 2002.

[77] Lothar Tiator. Helicity amplitudes and sum rules for real and virtual photons. *GDH 2000 Conference*, pages 57–66, 2000.

[78] Bao-Xi Sun, Garzon, E. J., and E. Oset. Radiative decay into γ-baryon of dynamically generated resonances from the vector-baryon interaction. *Phys.Rev.*, D82:034028, 2010.

[79] Steven Weinberg. Nonlinear realizations of chiral symmetry. *Phys.Rev.*, 166:1568–1577, 1968.

[80] J. Gasser and H. Leutwyler. Chiral Perturbation Theory to One Loop. *Annals Phys.*, 158:142, 1984.

[81] K.P. Khemchandani, H. Kaneko, H. Nagahiro, and A. Hosaka. Vector meson-Baryon dynamics and generation of resonances. *Phys.Rev.*, D83:114041, 2011.

[82] K.P. Khemchandani, A. Martinez Torres, H. Kaneko, H. Nagahiro, and A. Hosaka. Coupling vector and pseudoscalar mesons to study baryon resonances. *Phys.Rev.*, D84:094018, 2011.

[83] D. Gamermann, C. Garcia-Recio, J. Nieves, and L.L. Salcedo. Odd Parity Light Baryon Resonances. *Phys.Rev.*, D84:056017, 2011.

[84] B. Borasoy. Baryon axial currents. *Phys.Rev.*, D59:054021, 1999.

[85] F. Klingl, Norbert Kaiser, and W. Weise. Current correlation functions, QCD sum rules and vector mesons in baryonic matter. *Nucl.Phys.*, A624:527–563, 1997.

[86] G. Chanfray and P. Schuck. The Rho meson in dense matter and its influence on dilepton production rates. *Nucl.Phys.*, A555:329–353, 1993.

[87] M. Herrmann, B.L. Friman, and W. Norenberg. Properties of rho mesons in nuclear matter. *Nucl.Phys.*, A560:411–436, 1993.

[88] F. Antinori et al. Determination of the number of wounded nucleons in Pb + Pb collisions at 158 A GeV/c. *Nucl.Phys.*, A661:357–361, 1999.

[89] D. Cabrera, E. Oset, and M.J. Vicente Vacas. Chiral approach to the rho meson in nuclear matter. *Nucl.Phys.*, A705:90–118, 2002.

[90] E. Oset and A. Ramos. ϕ decay in nuclei. *Nucl.Phys.*, A679:616–628, 2001.

[91] L. Tolos, R. Molina, E. Oset, and A. Ramos. $\bar{K}^*$ meson in dense matter. *Phys.Rev.*, C82:045210, 2010.

[92] E. Oset and A. Ramos. Chiral unitary approach to η' N scattering at low energies. *Phys.Lett.*, B704:334–342, 2011.

[93] B.M.K. Nefkens. Cascade (Ξ) physics: A new approach to baryon spectroscopy. *AIP Conf.Proc.*, 870:405–408, 2006.

[94] J.W. Price et al. Exclusive photoproduction of the cascade (Ξ) hyperons. *Phys.Rev.*, C71:058201, 2005.

[95] R. Castelijns et al. Nucleon resonance decay by the $K^0\Sigma^+$ channel. *Eur.Phys.J.*, A35:39–45, 2008.

[96] D.M. Manley and E.M. Saleski. Multichannel resonance parametrization of πN scattering amplitudes. *Phys.Rev.*, D45:4002–4033, 1992.

[97] M. Batinic, S. Ceci, A. Svarc, and B. Zauner. Poles of the Zagreb analysis partial-wave T matrices. *Phys.Rev.*, C82:038203, 2010.

[98] A.V. Anisovich, R. Beck, E. Klempt, V.A. Nikonov, A.V. Sarantsev, et al. Properties of baryon resonances from a multichannel partial wave analysis. *Eur.Phys.J.*, A48:15, 2012.

[99] R.A. Arndt, W.J. Briscoe, I.I. Strakovsky, and R.L. Workman. Extended partial-wave analysis of πN scattering data. *Phys.Rev.*, C74:045205, 2006.

[100] R.A. Arndt, W.J. Briscoe, I.I. Strakovsky, R.L. Workman, and M.M. Pavan. Dispersion relation constrained partial wave analysis of πN elastic and $\pi N \rightarrow \eta N$ scattering data: The Baryon spectrum. *Phys.Rev.*, C69:035213, 2004.

[101] Ron L. Workman, Mark W. Paris, William J. Briscoe, and Igor I. Strakovsky. Unified Chew-Mandelstam SAID analysis of pion photoproduction data. *Phys.Rev.*, C86:015202, 2012.

[102] R.L. Workman, R.A. Arndt, W.J. Briscoe, M.W. Paris, and I.I. Strakovsky. Parameterization dependence of T matrix poles and eigenphases from a fit to πN elastic scattering data. *Phys.Rev.*, C86:035202, 2012.

[103] D. Drechsel, O. Hanstein, S.S. Kamalov, and L. Tiator. A Unitary isobar model for pion photoproduction and electroproduction on the proton up to 1 GeV. *Nucl.Phys.*, A645:145–174, 1999.

[104] L. Tiator, D. Drechsel, S. Kamalov, M.M. Giannini, E. Santopinto, et al. Electroproduction of nucleon resonances. *Eur.Phys.J.*, A19:55–60, 2004.

[105] D. Drechsel, S.S. Kamalov, and L. Tiator. Unitary Isobar Model - MAID2007. *Eur.Phys.J.*, A34:69–97, 2007.

[106] A.V. Anisovich, R. Beck, E. Klempt, V.A. Nikonov, A.V. Sarantsev, et al. Pion- and photo-induced transition amplitudes to ΛK, ΣK, and $N\eta$. *Eur.Phys.J.*, A48:88, 2012.

[107] U. Thoma, M. Fuchs, A.V. Anisovich, G. Anton, R. Bantes, et al. N^* and Δ^* decays into $N\pi^0\pi^0$. *Phys.Lett.*, B659:87–93, 2008.

[108] R.A. Arndt, W.J. Briscoe, M.W. Paris, I.I. Strakovsky, and R.L. Workman. Baryon Resonance Analysis from SAID. *Chin.Phys.*, C33:1063–1068, 2009.

[109] L. Roca, Sourav Sarkar, V.K. Magas, and E. Oset. Unitary coupled channel analysis of the $\Lambda(1520)$ resonance. *Phys.Rev.*, C73:045208, 2006.

[110] D. Mark Manley, Richard A. Arndt, Yogesh Goradia, and Vigdor L. Teplitz. An Isobar Model Partial Wave Analysis of $\pi N \to \pi\pi N$ in the Center-of-mass Energy Range 1320 MeV to 1930 MeV. *Phys.Rev.*, D30:904, 1984.

[111] R.E. Cutkosky, C.P. Forsyth, R.E. Hendrick, and R.L. Kelly. Pion - Nucleon Partial Wave Amplitudes. *Phys.Rev.*, D20:2839, 1979.

[112] T.P. Vrana, S.A. Dytman, and T.S.H. Lee. Baryon resonance extraction from πN data using a unitary multichannel model. *Phys.Rept.*, 328:181–236, 2000.

[113] M. Shrestha and D.M. Manley. Multichannel parametrization of πN scattering amplitudes and extraction of resonance parameters. *Phys.Rev.*, C86:055203, 2012.

[114] D. Ronchen, M. Doring, F. Huang, H. Haberzettl, J. Haidenbauer, et al. Coupled-channel dynamics in the reactions $\pi N \to \pi N$, ηN, $K\Lambda$, $K\Sigma$. *Eur.Phys.J.*, A49:44, 2013.

[115] K.P. Khemchandani, A. Martinez Torres, H. Nagahiro, and A. Hosaka. Negative parity Λ and Σ resonances coupled to pseudoscalar and vector mesons. *Phys.Rev.*, D85:114020, 2012.

[116] E. Oset, A. Ramos, E.J. Garzon, R. Molina, L. Tolos, et al. Interaction of vector mesons with baryons and nuclei. *Int.J.Mod.Phys.*, E21:1230011, 2012.

[117] Michael Doring. Resonance dynamics in coupled channels. *Int.J.Mod.Phys.Conf.Ser.*, 26:1460054, 2014.

[118] H. Kamano, S.X. Nakamura, T. S. H. Lee, and T. Sato. Nucleon resonances within a dynamical coupled-channels model of πN and γN reactions. *Phys.Rev.*, C88:035209, 2013.

[119] T. Inoue, E. Oset, and M.J. Vicente Vacas. Chiral unitary approach to S wave meson baryon scattering in the strangeness S = 0 sector. *Phys.Rev.*, C65:035204, 2002.

[120] Tetsuo Hyodo, Daisuke Jido, and Atsushi Hosaka. Origin of the resonances in the chiral unitary approach. *Phys.Rev.*, C78:025203, 2008.

[121] E. J. Garzon and E. Oset. Effects of pseudoscalar-baryon channels in the dynamically generated vector-baryon resonances. *Eur.Phys.J.*, A48:5, 2012.

[122] E.J. Garzon, J.J. Xie, and E. Oset. A case in favor of the $N^*(1700)(3/2^-)$. *Phys.Rev.*, C87:055204, 2013.

[123] K.P. Khemchandani, A. Martinez Torres, H. Nagahiro, and A. Hosaka. Role of vector and pseudoscalar mesons in understanding $1/2^-$ N^* and Δ resonances. *Phys.Rev.*, D88:114016, 2013.

[124] Ulf-G. Meissner and J.A. Oller. Chiral unitary meson baryon dynamics in the presence of resonances: Elastic pion nucleon scattering. *Nucl.Phys.*, A673:311–334, 2000.

[125] M. Doring, E. Oset, and M.J. Vicente Vacas. S wave pion nucleon scattering length from pi N, pionic hydrogen and deuteron data. *Phys.Rev.*, C70:045203, 2004.

[126] Richard A. Arndt, Igor I. Strakovsky, Ron L. Workman, and Marcello M. Pavan. Updated analysis of πN elastic scattering data to 2.1-GeV: The Baryon spectrum. *Phys.Rev.*, C52:2120–2130, 1995.

[127] D. Gamermann, J. Nieves, E. Oset, and E. Ruiz Arriola. Couplings in coupled channels versus wave functions: application to the X(3872) resonance. *Phys.Rev.*, D81:014029, 2010.

[128] J. Yamagata-Sekihara, J. Nieves, and E. Oset. Couplings in coupled channels versus wave functions in the case of resonances: application to the two $\Lambda(1405)$ states. *Phys.Rev.*, D83:014003, 2011.

[129] L.D. Faddeev. Scattering theory for a three particle system. *Sov.Phys.JETP*, 12:1014–1019, 1961.

[130] E.O. Alt, P. Grassberger, and W. Sandhas. Reduction of the three - particle collision problem to multichannel two - particle Lippmann-Schwinger equations. *Nucl.Phys.*, B2:167–180, 1967.

[131] A. Martinez Torres, K.P. Khemchandani, and E. Oset. Three body resonances in two meson-one baryon systems. *Phys.Rev.*, C77:042203, 2008.

[132] K.P. Khemchandani, A. Martinez Torres, and E. Oset. The $N^*(1710)$ as a resonance in the $\pi\pi N$ system. *Eur.Phys.J.*, A37:233–243, 2008.

[133] A. Martinez Torres, K.P. Khemchandani, L.S. Geng, M. Napsuciale, and E. Oset. The X(2175) as a resonant state of the $\phi K \bar{K}$ system. *Phys.Rev.*, D78:074031, 2008.

[134] Bernard Aubert et al. A Structure at 2175-MeV in $e^+e^- \to \phi \, f_0(980)$ Observed via Initial-State Radiation. *Phys.Rev.*, D74:091103, 2006.

[135] Bernard Aubert et al. The $e^+e^- \to K^+K^-\pi^+\pi^-$, $K^+K^-\pi^0\pi^0$ and $K^+K^-K^+K^-$ cross-sections measured with initial-state radiation. *Phys.Rev.*, D76:012008, 2007.

[136] Medina Ablikim et al. Observation of Y(2175) in $J/\psi \to \eta\phi f_0(980)$. *Phys.Rev.Lett.*, 100:102003, 2008.

[137] C.P. Shen et al. Observation of the $\phi(1680)$ and the Y(2175) in $e^+e^- \to \phi\pi^+\pi^-$. *Phys.Rev.*, D80:031101, 2009.

[138] C.P. Shen and C.Z. Yuan. Combined fit to BaBar and Belle Data on $e^+e^- \to \phi\pi^+\pi^-$ and $\phi f_0(980)$. *Chin.Phys.*, C34:1045–1051, 2010.

[139] Shi-Lin Zhu. New hadron states. *Int.J.Mod.Phys.*, E17:283–322, 2008.

[140] Zhi-Gang Wang. Analysis of the Y(2175) as a tetraquark state with QCD sum rules. *Nucl.Phys.*, A791:106–116, 2007.

[141] Hua-Xing Chen, Xiang Liu, Atsushi Hosaka, and Shi-Lin Zhu. The Y(2175) State in the QCD Sum Rule. *Phys.Rev.*, D78:034012, 2008.

[142] N.V. Drenska, R. Faccini, and A.D. Polosa. Higher Tetraquark Particles. *Phys.Lett.*, B669:160–166, 2008.

[143] Gui-Jun Ding and Mu-Lin Yan. A Candidate for 1^{--} strangeonium hybrid. *Phys.Lett.*, B650:390–400, 2007.

[144] Gui-Jun Ding and Mu-Lin Yan. Y(2175): Distinguish Hybrid State from Higher Quarkonium. *Phys.Lett.*, B657:49–54, 2007.

[145] T. Barnes, N. Black, and P.R. Page. Strong decays of strange quarkonia. *Phys.Rev.*, D68:054014, 2003.

[146] Susana Coito, George Rupp, and Eef van Beveren. Multichannel calculation of excited vector ϕ resonances and the $\phi(2170)$. *Phys.Rev.*, D80:094011, 2009.

[147] Norbert Kaiser. $\pi\pi$ S wave phase shifts and nonperturbative chiral approach. *Eur.Phys.J.*, A3:307–309, 1998.

[148] J.A. Oller, E. Oset, and J.R. Pelaez. Meson meson interaction in a nonperturbative chiral approach. *Phys.Rev.*, D59:074001, 1999.

[149] V.E. Markushin. The Radiative decay $\phi \rightarrow \gamma\pi\pi$ in a coupled channel model and the structure of $f_0(980)$. *Eur.Phys.J.*, A8:389–399, 2000.

[150] R. Chand and R.H. Dalitz. Charge-independence in K^--deuterium capture reactions. *Annals Phys.*, 20:1–19, 1962.

[151] R.C. Barrett and A. Deloff. Strong interaction effects in kaonic deuterium. *Phys.Rev.*, C60:025201, 1999.

[152] A. Deloff. η d and K^- d zero energy scattering: A Faddeev approach. *Phys.Rev.*, C61:024004, 2000.

[153] S.S. Kamalov, E. Oset, and A. Ramos. Chiral unitary approach to the K^- deuteron scattering length. *Nucl.Phys.*, A690:494–508, 2001.

[154] Ulf-G. Meissner, Udit Raha, and Akaki Rusetsky. The Pion-nucleon scattering lengths from pionic deuterium. *Eur.Phys.J.*, C41:213–232, 2005.

[155] Ulf-G. Meissner, Udit Raha, and Akaki Rusetsky. Isospin-breaking corrections in the pion-deuteron scattering length. *Phys.Lett.*, B639:478–482, 2006.

[156] Ulf-G. Meissner, Udit Raha, and Akaki Rusetsky. Kaon-nucleon scattering lengths from kaonic deuterium experiments. *Eur.Phys.J.*, C47:473–480, 2006.

[157] Avraham Gal. On the scattering length of the K^- d system. *Int.J.Mod.Phys.*, A22:226–233, 2007.

[158] V. Baru, E. Epelbaum, and A. Rusetsky. The Role of nucleon recoil in low-energy antikaon-deuteron scattering. *Eur.Phys.J.*, A42:111–120, 2009.

[159] M. Doring and U.G. Meissner. Kaon-nucleon scattering lengths from kaonic deuterium experiments revisited. *Phys.Lett.*, B704:663–666, 2011.

[160] Ju-Jun Xie, A. Martinez Torres, and E. Oset. Faddeev fixed center approximation to the $N\bar{K}K$ system and the signature of a $N^*(1920)(1/2^+)$ state. *Phys.Rev.*, C83:065207, 2011.

[161] A. Martinez Torres, K.P. Khemchandani, and E. Oset. Solution to Faddeev equations with two-body experimental amplitudes as input and application to $J^P = 1/2^+$, S = 0 baryon resonances. *Phys.Rev.*, C79:065207, 2009.

[162] L. Roca and E. Oset. A description of the $f_2(1270)$, $\rho_3(1690)$, $f_4(2050)$, $\rho_5(2350)$ and $f_6(2510)$ resonances as multi-$\rho(770)$ states. *Phys.Rev.*, D82:054013, 2010.

[163] J. Yamagata-Sekihara, L. Roca, and E. Oset. On the nature of the $K_2^*(1430)$, $K_3^*(1780)$, $K_4^*(2045)$, $K_5^*(2380)$ and K_6^* as K^* - multi-ρ states. *Phys.Rev.*, D82:094017, 2010.

[164] M. Bayar, J. Yamagata-Sekihara, and E. Oset. The $\bar{K}NN$ system with chiral dynamics. *Phys.Rev.*, C84:015209, 2011.

[165] Ju-Jun Xie, A. Martinez Torres, E. Oset, and P. Gonzalez. Plausible explanation of the $\Delta_{5/2^+}(2000)$ puzzle. *Phys.Rev.*, C83:055204, 2011.

[166] A. Martinez Torres and D. Jido. $K\Lambda(1405)$ configuration of the $K\bar{K}N$ system. *Phys.Rev.*, C82:038202, 2010.

[167] Daisuke Jido and Yoshiko Kanada-En'yo. K anti-K N molecule state with I = 1/2 and $J^P = 1/2^+$ studied with three-body calculation. *Phys.Rev.*, C78:035203, 2008.

[168] Akinobu Dote, Tetsuo Hyodo, and Wolfram Weise. Variational calculation of the ppK^- system based on chiral SU(3) dynamics. *Phys.Rev.*, C79:014003, 2009.

[169] Yoichi Ikeda, Hiroyuki Kamano, and Toru Sato. Energy dependence of $\bar{K}$N interactions and resonance pole of strange dibaryons. *Prog.Theor.Phys.*, 124:533–539, 2010.

[170] L. Alvarez-Ruso, J.A. Oller, and J.M. Alarcon. On the $\phi(1020)f_0(980)$ S-wave scattering and the Y(2175) resonance. *Phys.Rev.*, D80:054011, 2009.

[171] L. Alvarez-Ruso, J.A. Oller, and J.M. Alarcon. The $\phi(1020)$ $a_0(980)$ S-wave scattering and hints for a new vector-isovector resonance. *Phys.Rev.*, D82:094028, 2010.

[172] G.E. Brown and A.D. Jackson. The Nucleon-Nucleon Interaction. 1975.

[173] T.C. Rogers, M.M. Sargsian, and M.I. Strikman. Coherent vector meson photo-production from deuterium at intermediate energies. *Phys.Rev.*, C73:045202, 2006.

[174] L. Roca, E. Oset, and J. Singh. Low lying axial-vector mesons as dynamically generated resonances. *Phys.Rev.*, D72:014002, 2005.

[175] Goran Faldt. Binding Corrections and the Pion - Deuteron Scattering Length. *Phys.Scripta*, 16:81–86, 1977.

[176] A. Martinez Torres, Garzon, E. J., E. Oset, and L.R. Dai. Limits to the Fixed Center Approximation to Faddeev equations: the case of the $\phi(2170)$. *Phys.Rev.*, D83:116002, 2011.

[177] S.K. Choi et al. Observation of a narrow charmonium - like state in exclusive $B^\pm \to K^\pm pi^+ pi^- J/\psi$ decays. *Phys.Rev.Lett.*, 91:262001, 2003.

[178] N. Brambilla, S. Eidelman, B.K. Heltsley, R. Vogt, G.T. Bodwin, et al. Heavy quarkonium: progress, puzzles, and opportunities. *Eur.Phys.J.*, C71:1534, 2011.

[179] M.B. Voloshin. Charmonium. *Prog.Part.Nucl.Phys.*, 61:455–511, 2008.

[180] Eric S. Swanson. Short range structure in the X(3872). *Phys.Lett.*, B588:189–195, 2004.

[181] Nils A. Tornqvist. Isospin breaking of the narrow charmonium state of Belle at 3872-MeV as a deuson. *Phys.Lett.*, B590:209–215, 2004.

[182] Eric Braaten and Masaoki Kusunoki. Production of the X(3870) at the $\upsilon(4S)$ by the coalescence of charm mesons from B decays. *Phys.Rev.*, D69:114012, 2004.

[183] D. Gamermann and E. Oset. Axial resonances in the open and hidden charm sectors. *Eur.Phys.J.*, A33:119–131, 2007.

[184] C. Hanhart, Yu.S. Kalashnikova, A.E. Kudryavtsev, and A.V. Nefediev. Remarks on the quantum numbers of X(3872) from the invariant mass distributions of the $\rho J/\psi$ and $\omega J/\psi$ final states. *Phys.Rev.*, D85:011501, 2012.

[185] R Aaij et al. Determination of the X(3872) meson quantum numbers. *Phys.Rev.Lett.*, 110(22):222001, 2013.

[186] Liuming Liu et al. Excited and exotic charmonium spectroscopy from lattice QCD. *JHEP*, 1207:126, 2012.

[187] Gunnar Bali, Sara Collins, and Paula Perez-Rubio. Charmed hadron spectroscopy on the lattice for $N_f = 2 + 1$ flavours. *J.Phys.Conf.Ser.*, 426:012017, 2013.

[188] G. Bali, S. Collins, S. Durr, Z. Fodor, R. Horsley, et al. Spectra of heavy-light and heavy-heavy mesons containing charm quarks, including higher spin states for $N_f = 2 + 1$. *PoS*, LATTICE2011:135, 2011.

[189] Daniel Mohler, Sasa Prelovsek, and R.M. Woloshyn. $D\pi$ scattering and D meson resonances from lattice QCD. *Phys.Rev.*, D87(3):034501, 2013.

[190] Sasa Prelovsek and Luka Leskovec. Evidence for X(3872) from DD* scattering on the lattice. *Phys.Rev.Lett.*, 111:192001, 2013.

[191] Shoichi Sasaki and Takeshi Yamazaki. Signatures of S-wave bound-state formation in finite volume. *Phys.Rev.*, D74:114507, 2006.

[192] T. Yamazaki, Y. Kuramashi, and A. Ukawa. Two-Nucleon Bound States in Quenched Lattice QCD. *Phys.Rev.*, D84:054506, 2011.

[193] Daniel Gamermann and Eulogio Oset. Isospin breaking effects in the X(3872) resonance. *Phys.Rev.*, D80:014003, 2009.

[194] M. Doring, Ulf-G. Meissner, E. Oset, and A. Rusetsky. Unitarized Chiral Perturbation Theory in a finite volume: Scalar meson sector. *Eur.Phys.J.*, A47:139, 2011.

[195] Martin Luscher. Two particle states on a torus and their relation to the scattering matrix. *Nucl.Phys.*, B354:531–578, 1991.

[196] Miguel Albaladejo, Carlos Hidalgo-Duque, Juan Nieves, and Eulogio Oset. Hidden charm molecules in finite volume. *Phys.Rev.*, D88:014510, 2013.

[197] S.R. Beane, P.F. Bedaque, A. Parreno, and M.J. Savage. Two nucleons on a lattice. *Phys.Lett.*, B585:106–114, 2004.

[198] S.R. Beane et al. The Deuteron and Exotic Two-Body Bound States from Lattice QCD. *Phys.Rev.*, D85:054511, 2012.

[199] F. Aceti, R. Molina, and E. Oset. The $X(3872) \to J/\psi\gamma$ decay in the $D\bar{D}^*$ molecular picture. *Phys.Rev.*, D86:113007, 2012.

[200] Steven Weinberg. Evidence That the Deuteron Is Not an Elementary Particle. *Phys.Rev.*, 137:B672–B678, 1965.

[201] A. Martinez Torres, L.R. Dai, C. Koren, D. Jido, and E. Oset. The KD, ηD_s interaction in finite volume and the nature of the $D_{s^*0}(2317)$ resonance. *Phys.Rev.*, D85:014027, 2012.

[202] Damir Becirevic, Svjetlana Fajfer, Sasa Prelovsek, and Jure Zupan. Chiral corrections and lattice QCD results for f_{B_s}/f_{B_d} and $\Delta m_{B_s}/\Delta m_{B_d}$. *Phys.Lett.*, B563:150–156, 2003.

[203] Ting-Wai Chiu, Tung-Han Hsieh, Jon-Yu Lee, Pei-Hua Liu, and Hsiu-Ju Chang. Pseudoscalar decay constants f_D and f_{D_s} in lattice QCD with exact chiral symmetry. *Phys.Lett.*, B624:31–38, 2005.

[204] E. Follana, C.T.H. Davies, G.P. Lepage, and J. Shigemitsu. High Precision determination of the π, K, D and D_s decay constants from lattice QCD. *Phys.Rev.Lett.*, 100:062002, 2008.

[205] B. Blossier et al. Pseudoscalar decay constants of kaon and D-mesons from $N_f = 2$ twisted mass Lattice QCD. *JHEP*, 0907:043, 2009.

[206] C. Bernard, C. DeTar, M. Di Pierro, A.X. El-Khadra, R.T. Evans, et al. B and D Meson Decay Constants. *PoS*, LATTICE2008:278, 2008.

[207] Damir Becirevic, Benoit Blossier, Antoine Gerardin, Alain Le Yaouanc, and Francesco Sanfilippo. On the significance of B-decays to radially excited D. *Nucl.Phys.*, B872:313–332, 2013.

[208] P. Dimopoulos, R. Frezzotti, P. Lami, V. Lubicz, E. Picca, et al. Pseudoscalar decay constants f_K/f_π, f_D and f_{D_s} with $N_f = 2+1+1$ ETMC configurations. 2013.

[209] C.W. Xiao, J. Nieves, and E. Oset. Combining heavy quark spin and local hidden gauge symmetries in the dynamical generation of hidden charm baryons. *Phys.Rev.*, D88:056012, 2013.

[210] R. Molina and E. Oset. The Y(3940), Z(3930) and the X(4160) as dynamically generated resonances from the vector-vector interaction. *Phys.Rev.*, D80:114013, 2009.

[211] R. Molina, D. Gamermann, E. Oset, and L. Tolos. Charm and hidden charm scalar mesons in the nuclear medium. *Eur.Phys.J.*, A42:31–42, 2009.

[212] W.H. Liang, C.W. Xiao, and E. Oset. Baryon states with open beauty in the extended local hidden gauge approach. 2014.

[213] J.R. Pelaez. On the Nature of light scalar mesons from their large N(c) behavior. *Phys.Rev.Lett.*, 92:102001, 2004.

[214] Hua-Xing Chen and E. Oset. The $\pi - \pi$ Interaction in the ρ Channel in Finite Volume. *Phys.Rev.*, D87:016014, 2013.

[215] L. Castillejo, R.H. Dalitz, and F.J. Dyson. Low's scattering equation for the charged and neutral scalar theories. *Phys.Rev.*, 101:453–458, 1956.

[216] E.J. Garzon, R. Molina, A. Hosaka, and E. Oset. Strategies for an accurate determination of the X(3872) energy from QCD lattice simulations. *Phys.Rev.*, D89:014504, 2014.

[217] M. E. Rose. *Elementary Theory of Angular Momentum*. Wiley, New York, 1957.